Background Simulations and WIMP Search with Galactic Signature Dark Matter Experiments

Frédéric Michel Mouton

September 2017

Department of Physics and Astronomy

University of Sheffield

Contents

List of Figures

List of Tables

Acknowledgments

My deepest gratitude goes to my supervisor Neil Spooner for giving me the opportunity to undertake this work. His guidance and benevolence have been invaluable these past three years.

I am also particularly grateful to Daniel Snowden-Ifft, for our really instructive collaborations in my first two years. Each discussion has been a truly educational experience.

I would also like to thank Reina Maruyama for her patience during the long hours she spent listening to me babbling about my results. Despite the initial hardship, I feel that I have learnt a lot from DM-Ice.

Thanks to all the other DRIFTers. Especially Anthony for the frequent physics discussions and his help for the dark matter analysis, and Andrew for his help on various matters. Thanks to Warren for his collaboration on the gamma rejection project. I am also particularly indebted to Matt Robinson who has received more than one "My code is broken. Please fix it." emails.

For DM-Ice, I owe many thanks to Walter Pettus for his help. Not every hero wears a cape. Special thanks to Jay Hyun Jo and Estella de Souza for their help with the COSINE work and during my visit to Daejeon. Without them, I would probably still be lost somewhere in Korea.

Thanks to the Boulby team for their welcome during my few visits, especially to Sean Paling who has kept asking "So when are you coming down to Boulby?" for the past three years.

I would also like to thank Hyun Su Lee and Chang Hyon Ha for their warm welcome at IBS. It has been a really fascinating week.

I would like to express my extreme gratitude to my parents for their encouragements, constant value in my education, and resolve to see things done. They are two giant's shoulders to stand upon.

Last but not least, I owe much to Mathilde for her constant enthusiasm. After eight years of reading my reports, she has probably become a better physicist than I am. I can't thank her enough for her sympathetic ear, and her cheerfulness which never fails to bring back a smile.

Abstract

There is now compelling evidence that ordinary baryonic matter only represents 15% of the matter content of the Universe. Observational results suggest that the remaining 85% may be constituted of dark matter possibly in the form of weakly interacting massive particles (WIMPs). One of the potential ways to detect these WIMPS is to look for their scattering interactions with nuclei. This is the basis of direct detection experiments. In particular, galactic signature direct detection experiments look for the characteristic properties of the WIMP signal.

The current landscape of galactic signature experiments is dominated by two main types of experiments. Firstly, NaI (Tl) detectors are searching for the annual modulation of the WIMP recoil rate induced by the revolution of the Earth. Secondly, directional time projection chambers (TPCs) can reconstruct the momentum of the incoming scattering particle and determinate whether its origin is compatible with the WIMP wind. In this thesis, both types of experiments are addressed.

For these rare-event searches, the performance of the detector is dictated by two linked parameters, the mass of target materials and the rate of background events. A new generation of galactic signature experiments is currently being developed. This work addresses the issue of the background levels through the use of Monte-Carlo simulations to predict the event rate associated with the different backgrounds. In the context of the COSINE experiment, these simulations investigate the neutron background in the detector and compare the associated rate to a theoretical model which proposes that neutrons may be responsible for the positive signal seen by the DAMA experiment. Otherwise, for the proposed CYGNUS experiments,

these simulations are done in a way to facilitate the design effort of the collaboration and orientate the blueprints towards detectors which could potentially achieve background event rates below 1 per year.

These efforts may potentially lead to the creation of background-free experiments larger than the DRIFT-IId TPC. Background-free status was achieved in DRIFT with the discovery of minority carriers in 2013. This thesis presents the current world-leading directional limit on the spin-dependent WIMP-proton cross section achieved with the DRIFT-IId detector. The recent detection of fast neutrons from the rock at the Boulby underground laboratory is also discussed. This is the first ever measurement of the concentration of radioisotopes in an underground laboratory using a TPC. This thesis is considering the impact that this new technique may have on future dark matter searches and how it may provide a new tool for neutron metrology in nuclear physics.

Author's Contribution

In Chapter 3, I wrote the Geant4 simulation for the DM-Ice37 detector at Boulby and did the comparative analysis with the data obtained by the Yale group. For COSINE-100, I participated to some of the modifications of the geometry of the Geant4 simulation. I translated the code to Geant4 version 9.6-p03 to create the Sheffield build on which the simulations presented in this thesis are made. I calculated the neutron production rates for the different materials using SOURCES-4C. I also wrote a parallel code to generate the underground muons. Finally, I took shifts for the surveillance of the detector.

In Chapter 4, I wrote the Geant4 simulation of the DRIFT detector at the JIF laboratory and used the simulation to obtain the data corresponding to the Monte-Carlo section of the nuclear recoil efficiency map. I, then, used this result to analyse 147.48 days of DRIFT data using the Sheffield DRIFT analysis software. I was also regularly on monitoring duty for the DRIFT detector.

In Chapter 5, I calculated the neutron production rates with SOURCES for the steel vessel and the rock. I simulated these backgrounds using the Geant4 simulation I wrote. I tested several designs of neutron shield in a modified version of the Geant4 simulation, which I wrote, upgraded to the new laboratory. Finally, for the radon simulation, I wrote the Geant4 simulation and analysed its data as shown in this chapter.

In Chapter 6, I did the Monte-Carlo simulations associated with the observation of rock neutrons at Boulby. This includes the ^{60}Co, shielded and unshielded neutron

and gamma backgrounds in the detector. I did a review of the different measurements of the concentrations of ^{238}U and ^{232}Th at Boulby for internal discussions. I also wrote the simulation for the UNDER detector and analysed the data obtained from the neutron production rates I calculated with SOURCES for the Gran Sasso underground laboratory. Finally, I generated the data used to investigate the recoil discrimination in UNDER.

In Chapter 7, I wrote the Geant4 simulations for the various CYGNUS models and calculated the neutron production rates for the different materials simulated.

In Chapter 8, I wrote the analysis software used to manipulate the data from CASINO and SRIM. I also wrote a Geant4 simulation aimed at comparing the tracks produced by the different software. Finally, I proposed the discrimination parameters studied in this chapter and participated in the analysis of the Monte-Carlo data.

1 Introduction

It is contrary to reason to say that there is a vacuum or space in which there is absolutely nothing.

René Descartes

The composition of the Universe is a subject which has long been debated. The introduction of the notion of gravity by Newton in his Principia [1] discarded the existence of a "medium that freely pervades the interstices between the parts of bodies". This appreciation rejected the idea of quintessence inherited by Aristotle [2] where the regions of space between cosmic bodies would be inhabited by this strange non-luminous aether. The successes of Newton's theory of gravity helped establish his views on the emptiness of the vacuum and the Universe. The discovery of the Casimir effect in 1948 showed that the vacuum has a non-null zero-point-energy due to quantum fluctuations [3]. While this result contradicted Newton's hypotheses, it did not require the addition of new particles and did not disrupt the assumption that the Universe was believed to be entirely composed of ordinary (baryonic) luminous matter.

1.1 Evidence for Dark Matter

In this section, some of the evidence for the existence of dark matter are presented. While the list discussed below is certainly not exhaustive, this approach is both

historical and one that shows the manifestation of dark matter on a variety of scales in the Universe.

1.1.1 Galactic Rotation Curves

There exists in Astronomy a tradition to look for unseen bodies and phenomena through their gravitational effect on visible matter. One example is the discovery of Neptune by Galle in 1846 from its influence on the orbit of Uranus. In 1922, Jeans' measurement of the vertical motion of stars near the galactic plane suggested that the stellar density was not enough to account for their motion. In [4], he suggested a light to mass ratio of 1/3 due to hypothetical dark stars. In 1933, Zwicky also deduced the existence of a non-luminous component in the Coma cluster by observing the dynamics of its galaxies [5]. In the 1970s, more evidence for the existence of dark matter came from Ford and Rubin's discovery that the rotation curves of galaxies are flat. Their observations, measured in the 21 cm line of hydrogen, showed that the velocities of stars and the gas at large radii did not follow the expected Keplerian decline [6].

Indeed, by equating the gravitational force between a star at a position r within a galaxy with a spherically symmetrical mass profile $M(r)$ and the centripetal force felt by the star, it is possible to obtain the tangential velocity of the star $v_{\tan}$, assuming that all orbits are circular,

$$v_{\tan} = \sqrt{\frac{GM(r)}{r}}. \tag{1.1}$$

Classically, $M(r)$ is constant at large radii since the whole mass of the galaxy is already enclosed in the sphere of radius r and $v_{\tan} \propto \sqrt{1/r}$. However, observations such as the one shown on Fig. 1.1 suggest that the mass profile of the galaxy extends beyond its luminous border with $M(r) \sim r$. If $M(r)$ is expressed as $M(r) = 4\pi \int \rho(r)\, r^2 dr$, the galactic halo density must follow $\rho(r) \propto r^{-2}$. The luminous matter, however, is concentrated in the galactic disk and its density drops

approximately exponentially with radius [7]. The observations in Fig. 1.1 shows a good agreement with the ΛCDM model. This cosmological theory encompasses the Big Bang model with the presence of dark energy (in the form of a cosmological constant Λ) and cold dark matter (CDM) [8].

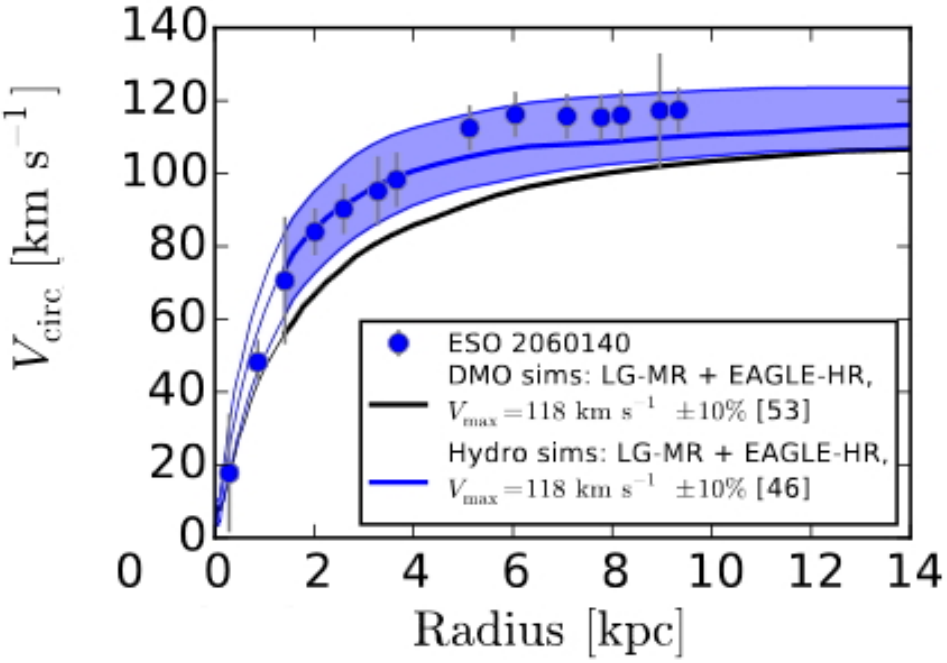

Figure 1.1: Rotation curve of the galaxy ESO 2060140 observed in [9] compared to different ΛCDM simulations. From [9].

It was noted in [9] that not all rotation curves perfectly agree with the model. Several comments can be made about these results. Firstly, N-body simulations suggest a departure from the simple $\rho(r) \propto r^{-2}$ dependence in favour of profiles like the so-called Navarro-Frenk-White (NFW) profile [10] shown in Equation 1.2 where ρ_0 is the local density measured at the radius r_0 for this galaxy,

$$\rho(r) = \frac{\rho_0}{1 + \left(\frac{r}{r_0}\right)^2}. \tag{1.2}$$

In particular, the local density ρ_0 at the Sun's radius r_0 is estimated to be $0.3 \pm 0.1 \frac{\text{GeV}}{c^2}\text{cm}^{-3}$ [11]. This profile assumes a dissipation-less isothermal halo with a

Maxwell-Boltzmann distribution of velocities. The assumptions necessary to make this measurement are however being debated. For example, there are disagreements between Bovy et al. [11] and Bidin et al. [12] due to the assumptions taken in both approaches about the relation between the azimuthal velocities of stars in the Milky Way and their distance to the galactic centre. Results from [12] found a dark matter density lower by a factor 2 to 4, depending on the formalism and the data set used.

Secondly, although there is a good apparent agreement between observations and profiles of dark matter haloes at large radii, the internal galactic dynamics become more complicated in the innermost regions. Near the core, it becomes difficult to efficiently resolve the contributions of dark matter to the density profile from the usual baryonic matter. Indeed, the dark matter profile in the core region of galaxies is not yet fully understood, and discrepancies remain. In particular, NFW profiles show a steep increase in density around the galactic core while observations suggest a flat central density profile. This is known as the cuspy halo problem [13] illustrated in Fig. 1.2 where it can be seen that the NFW profile (in red) overestimates the rotation speed in the inner region by about a factor 2. Similarly, it has been suggested in [14] that the presence of dark matter sub-structures inside the halo could locally increase the dark matter density by up to a factor 2. This value, however, does not agree with more recent simulations [15] in which it is estimated that tidal forces limit the overdensity of subhaloes to $\lesssim 10\%$.

Several possible solutions to this problem have been proposed. Another profile function, derived empirically, has been proposed by Bukert in [16] with a flat core density that better agrees with the current data. Several studies such as [17] have suggested that dark matter profiles are not universal. In particular, simulations in [18] found that the mean halo density depends on the critical density of the Universe at the time of formation. Other simulations such as [19, 20] show that the dark matter profile depends on the baryonic mass of the galaxy implying the existence of baryonic feedback during the formation of the dark matter halo. On the other hand, observations of dwarf spheroidal galaxies in [21] show no statistically

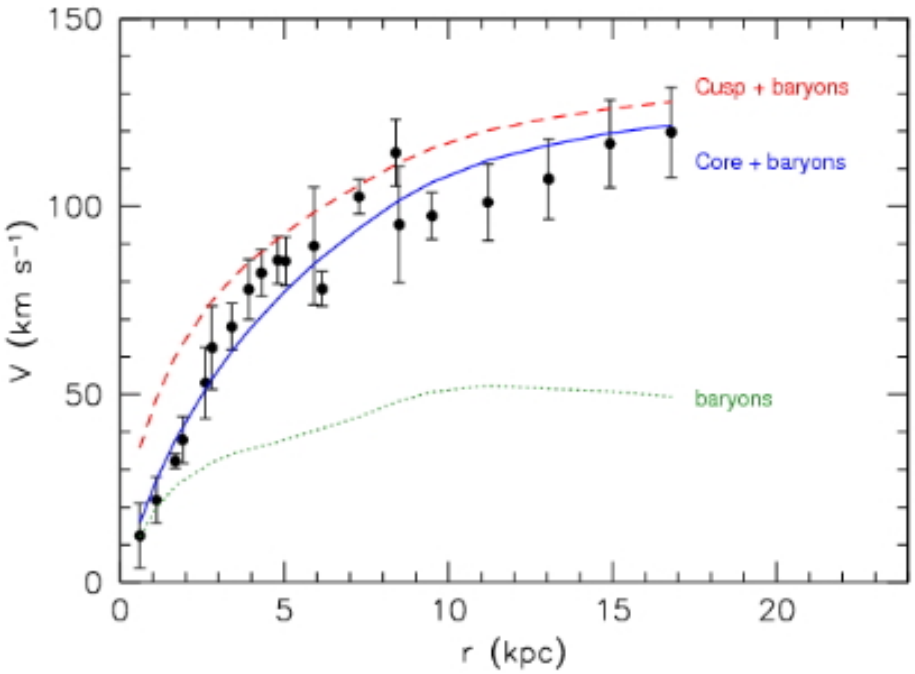

Figure 1.2: Rotation velocities for a cuspy or core dark matter halo compared to data from the F568-3 galaxy. From [13].

significant departures from the standard NFW profile. It could be argued that the (baryonic) mass of dwarf galaxies is too small to create a significant departure from the expected NFW profile. On the other hand, it is possible that the simulations are hinting towards more complicated dark matter models which do not agree with the basic assumption of cold collisionless dark matter used in the NFW profile [9].

There are two strong arguments in favour of cored haloes. Firstly, in [22], the authors obtained cosmological constraints from their N-body simulation. By insisting that dark matter haloes must have cusps, the authors found an upper-limit on the matter density of the Universe (both baryonic and dark matter) $\Omega_m < 0.2$ which is inconsistent with the value obtained by Planck [23], $\Omega_m = 0.316 \pm 0.0014$. No constraints could be obtained for cored haloes. Secondly, some dwarf galaxies and Low Surface Brightness (LSB) galaxies are so faint that they are believed to be mainly composed of dark matter even in the core region. Observations have shown

that these galaxies are dominated by cores [24].

To conclude on the cuspy halo problem, there is a strong evidence for cored profile dark matter haloes supported by cosmological constraints [22], and observations [25]. However, the observed non-universality of dark matter profiles [19, 20, 25], which essentially depends on the galactic mass, may be a clue that both the NFW and Bukert profiles are incomplete descriptions. More detailed models may be required including, for example, the multiple cusps flattening mechanisms such as tidal interactions or galaxy mergers, or other mechanisms discussed in [26].

1.1.2 Galaxy Clusters and Gravitational Lensing

Clusters of galaxies are the largest gravitationally bound objects in the Universe. Using this property, Zwicky measured the velocities of eight galaxies in the Coma cluster [5] where he found an unexpectedly large velocity dispersion. Using the Virial theorem, Zwicky estimated the mass of the cluster M and, by comparing it with the mass L estimated from the luminosity of the nebulae he obtained a mass to light ratio $M/L \simeq 400$. Zwicky concluded that dark matter must be more abundant than the ordinary luminous matter. Another interesting conclusion from this result is that the mass to light ratio in the Coma cluster falls short of the critical mass to light ratio $(M/L)_c \simeq 1390$ which is a hint at the existence of dark energy [27]. The drawback of this method, however, is that it depends on the Hubble parameter for which there was, at the time, a large uncertainty. For example, later measurements of the light to mass ratio in the Coma cluster reported in [27] have found $M/L \simeq 160$, which is substantially lower than the value obtained by Zwicky.

Another evidence for dark matter using galaxy clusters comes from gravitational lensing. Gravitational lensing is the bending of light passing through a gravitational field. This effect was famously used by Eddington during the solar eclipse of 1919 to verify the predictions of Einstein's general relativity in which the deviation of the light-rays is twice the amount predicted by Newtonian mechanics as derived by

von Soldner in 1801 [28]. Gravitational lensing can be divided into three categories: strong, weak and microlensing, depending on the resolution of the instrument and the angular separation between the source and the lens. Each category gives rise to a different phenomenon.

In strong lensing, the photons propagate through a strong gravitational potential causing a large deflection of the light rays. The spherical symmetry of the lensing object means that several images of the lensed object are visible and may form a ring around the massive lensing object. This phenomenon is called an Einstein's ring. Deviations from a perfectly symmetrical lensing object or misalignment between the observer and the two cosmic bodies will instead create arc segments. Strong lensing is often used to estimate the mass of a cluster, or can be used to estimate cosmological parameters (in particular the matter and dark energy densities) such as in [29].

In weak lensing, the lens is not strong enough and the deformation of its image is less dramatic. For example, this occurs when the angular separation between the object, the lens and the observer is large compared to the size of the Einstein ring. Weak lensing is usually used on galaxies to probe the mass distribution of galactic dark matter haloes. The lensing induces shear on the image of the source, turning a spherical source into an ellipsoid image. Non-homogeneity of the lensing halo (such as the presence of internal structures like sub-haloes) adds additional shear on the image which could, in principle, be used to probe inside galactic dark matter haloes [30].

Microlensing happens if the deformation of the image is too small to be resolved, and microlensing only results in the magnification of the lensed object. In particular, the MACHO collaboration [31] has used microlensing in the Large Magellanic Cloud to estimate the number of MACHOs (Massive Astrophysical Compact Halo Objects), a possible dark matter candidate discussed at further length in sec. 1.3.1.

One of the most compelling evidence for the existence of dark matter comes from

gravitational lensing. The observation of the so-called "Bullet cluster" in [32] and the cluster MACS J0025.4-1222 in [33] (both shown in Fig. 1.3) showed that during a collision of two clusters, the hot baryon distribution (shown in pink in the pictures) measured by its x-ray signature by the Chandra telescope [34], is clearly separated from the main mass distribution (shown in blue), when measured using weak gravitational lensing [32]. The population of visible galaxies is following the blue mass distribution. This is explained by the relatively small cross-section of each galaxy compared to the size of the cluster. It is, therefore, a good approximation to treat the galaxies as collisionless. The hot gas in each cluster interacts during the collision while the near collisionless properties of dark matter mean that both dark matter haloes can pass through each other with minimal interactions. The observation of these two cluster collisions is a strong argument in favour of the existence of a dark matter particle and can prove difficult to be explained by the alternative theories as discussed in sec. 1.2.

Figure 1.3: Composite images of the "Bullet Cluster" 1E0657-558 (left, from [32]) and the MACS J0025.4-1222 cluster (right, from [33]) showing the hot baryonic gas distribution in pink and the dark matter distribution in blue.

1.1.3 The Cosmic Microwave Background

ΛCDM cosmology is the model based on the existence of dark energy (in the form of a cosmological constant Λ), cold dark matter, and the Big Bang [8]. The idea that the Universe originated from a single quantum in space-time with near infinite density and temperature where the laws of physics break down, has evolved from Lemaître's primaeval atom [35] thanks to cosmological models. Out of the Big Bang, nearly 14 billion years ago, the Universe evolved as a hot, dense plasma, expanding under the influence of a hypothetic unified force whose successive symmetry breakings led to the physical forces experienced today [36]. From 10^{-37} to 10^{-32} s, the Universe experienced a de Sitter phase of expansion during a period called inflation [8]. The inflationary paradigm can provide a solution to several problems in cosmology [37]. Explaining the scale of temperature anisotropies of the Cosmic Microwave Background (CMB) is one of the solutions provided by inflation [37] which is of particular relevance to dark matter.

The CMB is the remnant radiation from the early hot plasma of the Universe. During inflation, the quantum fluctuations of the vacuum are stretched by the expansion of the Universe [8]. During de Sitter expansion, the Hubble radius cH^{-1} is constant, where H is the Hubble parameter, and the physical wavelength of the density perturbations grows exponentially $\lambda \propto e^{Ht}$. Since these fluctuations are adiabatic, the perturbations are frozen as long as their physical wavelength is larger than the Hubble horizon ($\lambda > cH^{-1}$), [38]. After inflation, the curvature perturbations gradually re-enter the horizon, and the freeze-in conditions are no longer satisfied. The fluctuations evolve as density anisotropies in the early plasma which later became inhomogeneities in the large scale structures [38].

The CMB radiation first observed by Penzias and Wilson [39] in 1964 is made of photons coming from the surface of last scattering 380000 years after the Big Bang [40]. At this moment, the temperature of the plasma had dropped sufficiently to allow the formation of hydrogen. This process is called recombination. The drop

in electron density in the plasma (since the electrons are now bound in hydrogen) meant a reduction of the number of Thomson scatterings and the photons decoupled from the plasma [37]. The photons observed have been freely streaming from the surface of last scattering with the frequency spectrum of a blackbody with a mean temperature of $T = 2.72548 \pm 0.00057$K. [41]

Fig. 1.4 shows the 2015 Planck power spectrum extracted from observations of the CMB [42]. The cosmological parameters can be obtained from the spectrum of CMB photons using a multiparameter fit. Several astrophysical effects must be taken into considerations, these are the Sachs-Wolfe effect and the Sunyaev–Zel'dovich effect [43]. The Sachs-Wolfe effect is the gravitational redshift of CMB photons due to density fluctuations either at the surface of last scattering or along the photon's path between the surface of last scattering and the Earth (integrated effect). The Sunyaev-Zel'dovich effect is the energy boost of CMB photons following inverse Compton scatterings with high energy electrons [44]. These two effects provoke distortions of the CMB spectrum, the dominant effect of the geometry of the manifold results in the position of the first peak, its amplitude is related to the ratio of matter to radiation [27]. The baryon density can be deduced from the ratio of the first two peaks. Since the results found to be coherent with a flat geometry, the total energy density can be calculated. Indeed, by solving the Friedman equation for a flat manifold, it is possible to obtain the critical energy density of the Universe $\rho_c = \frac{3H^2}{8\pi G} \sim 10^{-29}\text{g/cm}^3$, [45] . On the other hand, the height of the second peak implies that baryons represent only 5% of the total energy density. This value is also verified by the estimation of the relative abundance of the light elements in the Universe [45].

Overall, a strong case for non-baryonic dark matter can be made using these two inputs. Again by solving the Friedman equation, the relative densities of each component can be computed, and the density of dark matter was found to be $\Omega_{DM} = \frac{\rho_{DM}}{\rho_c} \sim 0.26$ [45].

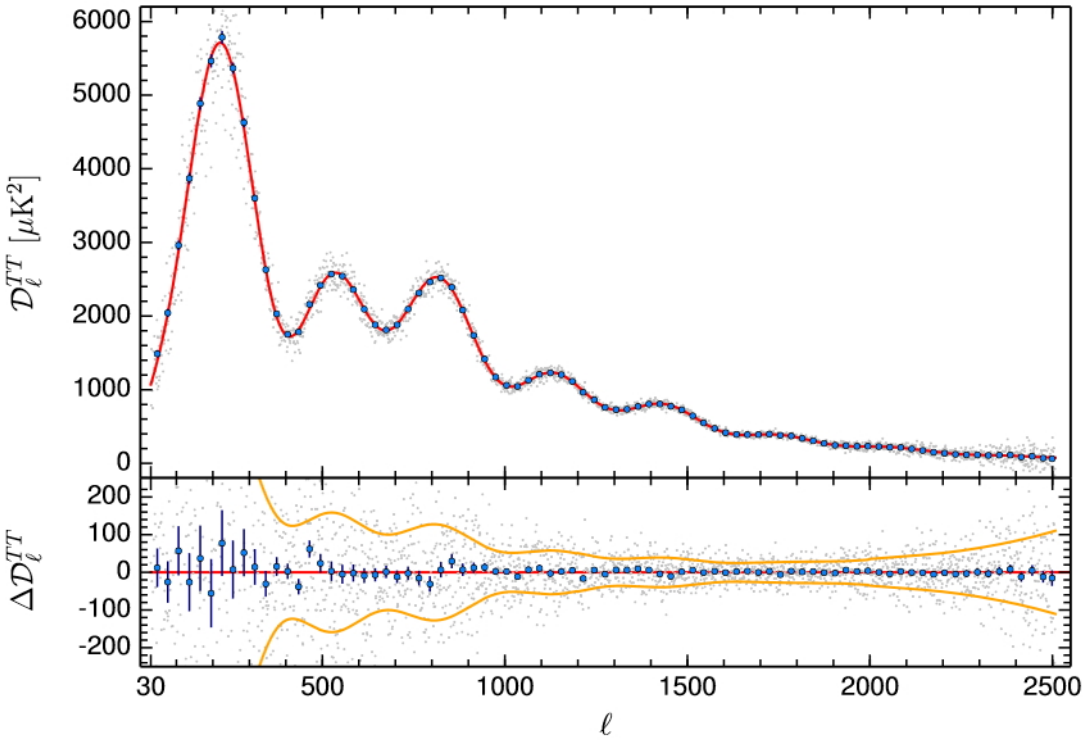

Figure 1.4: Planck 2015 temperature power spectrum (top) showing a good agreement with the ΛCDM prediction. The residuals are plotted on the bottom. From [42].

1.2 Alternatives to Dark Matter

In the previous section, some of the evidence for the existence of dark matter was presented. However, there also exist theories which propose modifications to the theory of gravity in order to explain the observed gravitational phenomena without the need to introduce a new and elusive particle. A difficult obstacle for these theories is to be able to account for the all supposed effects of dark matter from the scale of a simple galaxy to the whole Universe by being able to match the CMB data discussed above. In this section, some of these theories are discussed.

1.2.1 Modified Newtonian Dynamics

Modified Newtonian Dynamics (MOND) is a correction to Newton's second law proposed by Milgrom in 1983 [46] in order to resolve its disagreement with the rotation of galaxies without invoking dark matter. MOND is postulating that the observed acceleration $\overrightarrow{a}$ of an object is not the Newtonian acceleration $\overrightarrow{a_N}$ but that a correction μ must be incorporated [47] such that

$$\overrightarrow{a} = \frac{\overrightarrow{a_N}}{\mu(\chi)}, \tag{1.3}$$

where $\mu(\chi)$ is an empirically determined function of $\chi = \frac{a}{a_0}$, and $a_0 \sim 1.2 \times 10^{-10}\mathrm{m/s^2}$ is a new universal constant which represents the acceleration scale at which MOND become relevant. In the simple interpolation paradigm [48]

$$\mu(\chi) = \frac{\chi}{1+\chi}. \tag{1.4}$$

The MOND paradigm is capable of explaining the rotation curves of galaxies. However, it falls short when trying to explain the dynamics of clusters of galaxies [22] and dark matter is still needed in order to fit the observations (although in lesser quantity). Examples of a mass distribution decoupled from the luminous matter as seen in the "Bullet Cluster" described in sec. 1.1.2 are difficult to explain with models such as MOND which does not require the addition collision-less non-luminous material.

Finally, it is quite evident that a new gravitational paradigm cannot pretend to supersede the current theory without a complete covariant formulation. This is why the relativistic generalisation of MOND called Tensor Vector Scalar gravity (TeVeS) was developed by Bekenstein [49]. However, in [50], the authors found they could not fit both gravitational lensing and galactic rotation curve with a single set of parameters, the covariant equivalent of $\mu(\chi)$ in MOND could either fit rotation curves or gravitational lensing but not both at the same time. Furthermore, fits

to the "Bullet Cluster" [51] have shown TeVeS still requires dark matter in order to fit the data. Although the authors of [51] suggested that neutrinos with masses on the order of 2 $\mathrm{eV/c^2}$ could account for the dark matter needed by TeVeS, this option may be conflicting with the Planck data [52] which constrained the sum of the neutrino masses (using general relativity) as $\sum \mathrm{m}_\nu < 0.136\ \mathrm{eV/c^2}$ at 95% C.L. Furthermore, another comparison between the Planck data and TeVeS done in [53] has obtained a value for the Hubble parameter $H < 50.8\ \mathrm{km\ s^{-1}\ Mpc^{-1}}$ (68% CL) which is substantially lower than the value obtained from supernovae measurements. The necessity to introduce *ad hoc* corrections to the theory as well as limited amounts of dark matter might be a sign that MOND does not form a complete picture.

1.2.2 $f(R)$ gravity

Another alternative theory to dark matter is $f(R)$ gravity [54]. Rather than taking a bottom-up approach like MOND, where the low field approximation is later built into a covariant theory, $f(R)$ gravity is a covariant theory from the start. $f(R)$ gravity is an extension of Einstein's theory of general relativity introduced by modifying the Lagrangian density of the Einstein-Hilbert action S such that [55]

$$S = \frac{1}{2\kappa^2}\int \sqrt{-g}R\mathrm{d}^4x \ \rightarrow\ S = \frac{1}{2\kappa^2}\int \sqrt{-g}\, f(R)\, \mathrm{d}^4x, \tag{1.5}$$

where $\kappa = 8\pi G$ (taking $c = 1$), g is the determinant of the metric tensor $g_{\mu\nu}$ and $R = g^{\mu\nu}R_{\mu\nu}$ is the Ricci scalar. In $f(R)$ gravity, the Ricci scalar is replaced in the Einstein-Hilbert action by a function of itself. Historically, the motivation to further complicate the theory of general relativity came from the possibility of writing a theory without singularities [54]. However, the necessary addition of the inflaton (in the form of a scalar field), as briefly described in sec. 1.1.3, is made in order to solve several issues in early-time cosmology such as the flatness problem [38]. Furthermore, dark energy (possibly in the form of a cosmological constant) is one of the simplest candidates in order to explain the late-time acceleration of

the Universe [56]. These propositions have revived interest in modified gravity [57], especially since both the inflaton and dark energy do not respect the strong energy condition (negative pressure) [58], contrary to dark and ordinary matter.

While the number of possible functions $f(R)$ may seem infinite, many functions will lead to ghosts [57] (non-physical degrees of freedom) which suggest that these choices are unsuitable candidates for a new theory. An important effort has been to try to unite dark energy and the inflaton under a single scalar field which could induce two separate periods of de Sitter expansion, one at early time and the other at late time. Other theories such as [59] have proposed to unite the whole dark sector (dark matter and dark energy) with the inflaton. These theories, however, suffer from a foreseeable drawback, similarly to MOND, which is their difficulty to explain the results obtained through gravitational lensing from the collision of galaxy clusters, such as the "Bullet Cluster" [60]. This is why the authors of [60] have proposed a model in which gravity is written in a tensor-scalar form. When quantised, the theory produces two particles, a massless graviton arising from the tensor part and a new massive particle called the scalaron coming from the scalar part of the theory. A particular feature of the theory is that the scalaron mass is inversely proportional to the scalar curvature of the manifold. During inflation, the scalaron radiates, eventually providing a solution to the inflationary graceful exit and reheating problems. After inflation, the scalaron can regain some of its mass if the curvature index k is not exactly zero since

$$|\Omega - 1| = \frac{|k|}{a^2 H^2}. \tag{1.6}$$

Unfortunately, the scalaron mass predicted in [60] is around 10^{119} eV, making the dark matter particle larger than the Planck mass ($\sim 10^{19}$ GeV) but especially as heavy as roughly 10^{55} Milky Ways!

1.3 Dark Matter Candidates

In the previous section, the alternative theories of dark matter were presented. It was shown that these theories either cannot explain all of the evidence, require fine-tuning to explain at least one of them, or predict improbable dark matter candidates. Some well-motivated dark matter candidates are now presented.

1.3.1 MACHOs

MACHOs (Massive Astrophysical Compact Halo Objects) include all small faint stellar objects. This includes faint stars, sub-stellar objects, stellar remnants (white dwarfs or neutrons stars), planets, black holes [61] present in galaxies. Since these objects emit little or no radiations, they can be dark matter candidates. One of the appeals of this theory is that it proposes a solution to the missing mass problem without the need to expand the standard model by including some new yet undiscovered particles. Several experiments such as the MACHO and EROS collaborations [31, 62] used micro gravitational lensing. This is done by monitoring the brightness of distant stars. However, both experiments found that the number of micro-lensing observed could not account the total density of dark matter. The combined analysis of these two experiments has shown that MACHOs cannot account for more than 25% of the dark matter present in the Milky Way halo [63].

Furthermore, the study of primordial nucleosynthesis can also rule out MACHOs and other baryonic candidates (gas, dust) as the main dark matter candidate [45]. As the primordial plasma cooled, light elements began to form. At $t \sim 1$ s, ($T \sim 10$ MeV), weak interactions are no longer at thermal equilibrium, and the number of free neutron becomes Boltzmann suppressed due to neutron decay, until the ratio of neutron to proton becomes frozen around $n/p \sim 1/6$ [64]. Around $t \sim 100$ s, ($T \sim 0.1$ MeV), the temperature is low enough to stop the photodisintegration of deuterium [64]. As the temperature cooled further, heavier elements became stable such as deuterium, helium, lithium. Elements heavier than lithium (in particular carbon, nitrogen and

oxygen) were formed in the first generations of stars [45]. The predicted abundances of these materials can be compared to measurements. For example, the abundance of ^{4}He is determined through the measurement of He emission lines in extragalactic regions [65], the abundance of deuterium is measured using the absorption lines of high redshift quasar [65]. It was found that for these measurements to agree with the Big Bang nucleosynthesis model, baryonic matter could not exceed 5% of the energy density of the Universe [45].

Other candidates for MACHOs are primordial black holes resulting from the collapse of density fluctuations in the early Universe. However, black holes dissipate energy through Hawking radiation. If dark matter were primarily made of black holes, they would have evaporated if their mass was less than 10^{14}g [66], above this mass it should still be possible to detect the radiation of these black holes. The observation of neutron stars in [67] has ruled out primordial black holes as the main dark matter candidate above 10^{16}g. The authors looked at the numbers of neutrons stars in globular clusters. If a black hole is gravitationally captured by a neutron star, the star will be destroyed as its material is gradually stolen by the black hole. Therefore, the number of neutron stars today must be inversely proportional to the mass of the black holes and their density. Lighter black holes have smaller Schwarzschild radii and can be treated as collisionless. In [67], the authors found that primordial black holes could not account for more than 5% of the dark matter density.

1.3.2 Characteristics of Non-baryonic Dark Matter

The previous sections have given some valuable insights about the elusive nature of dark matter. In particular, it was shown that the modifications of general relativity could not explain the evidence for dark matter and in particular the observation of the "Bullet Cluster". From these results, it can be deduced that there must exist an yet unobserved particle, or a class of astrophysical objects to account for the missing mass. Furthermore, it has been shown that dark matter must be non-

baryonic; otherwise, it would not be possible to explain the different behaviour of dark matter compared to the baryonic matter in the "Bullet Cluster". Besides, there would be disagreement with the Big Bang nucleosynthesis. The baryonic dark matter has also been shown to be unable to give rise to structure formation in the early Universe due to interaction with the baryonic matter [27].

Secondly, the search of MACHOs through the observation of microlensing has shown that the density of these objects is not sufficient to explain the dark matter problem [63]. It can be deduced from this that dark matter must be a particle (or form an object too small for it to be resolved by gravitational lensing with the current technology).

Thirdly, dark matter must be electrically neutral; otherwise, it would interact with photons. It must have no colour otherwise it would interact with baryons through the strong force.

Fourthly, dark matter must be stable (at least on the timescale of the Universe). This can be done by requiring the conservation of a quantum number as it will be discussed in the following sections

Finally, dark matter must be cold (non-relativistic at decoupling) [68]. This argument is due to the role of dark matter in structure formation. It has been shown that hot dark matter can smooth the primordial density perturbations described in sec. 1.1.3 and stop the formation of large structures. This process is called Silk damping [69].

In the next sections, the review below will present some of the well-motivated cold dark matter candidates which satisfy these conditions.

1.3.3 Axions

Axions have been proposed in the Peccei-Quinn solution of the strong CP problem [70]. The strong CP problem is the lack of strong interaction violating CP [71].

CP violation has been observed for the weak force, in particular, through kaon decays [72]. However, experiments have shown no sign of CP violation in strong interactions, despite its natural presence in the theory in the case of massive quarks [73]. The relevant term for CP violation in the QCD Lagrangian can be expressed as [27]

$$L_{QCD} = \frac{\Theta g^2}{32\pi^2} G^{a\mu\nu}\tilde{G}_{a\mu\nu}, \tag{1.7}$$

where $G^{a\mu\nu}$ is the gluon field tensor and g is a coupling constant. Any non-zero choice of the angle Θ will break CP symmetry. This induces a large electric dipole moment on the neutron $|d_n| \sim 10^{-16} e\,\mathrm{cm}$, where e is the electric charge [73], while experimental limits have placed an upper-bound at $|d_n| < 5.6\times10^{-25} e\,\mathrm{cm}$, [74]. This means that either Θ must naturally be zero, but such arrangement requires fine-tuning, or there must be another term in the QCD Lagrangian effectively cancelling the Θ term. The Peccei-Quinn solution assumes that the spontaneous breaking of a $\mathrm{U}(1)$ global symmetry at an energy scale f_A drives the Θ term to zero. The resulting pseudo Nambu-Goldstone boson is called the axion, whose mass depends on the energy scale f_A such that

$$m_a \simeq 6 \times 10^{-6}\mathrm{eV} \times \left(\frac{10^{12}\mathrm{GeV}}{f_A}\right). \tag{1.8}$$

There exist several bounds on the axion mass. Observation of the supernovae 1987A has placed an upper-limit on the axion mass as $m_a < 4.4\times10^{-10}$eV [75], while the advanced LIGO detector has placed an upper-limit of $m_a < 6\times10^{-13}$eV based on black hole radiation [76]. Another constraint comes from the ADMX collaboration which is looking at the possible interaction of axions with photons from the experiment's magnetic field through a process called the Primakoff effect [77]. This method is used to search for axions with masses in μeV range [78]. Despite their expected low mass, axions can still be cold dark matter candidates if they are produced non-thermally [79]. This is possible thanks to a process called the misalignment mechanism [79]. If the axion field has an initial value which is not a local minimum, the fluctuations of the field cause the particle to lose energy [80], hence reducing the energy of axions

to non-relativistic levels.

1.3.4 Sterile neutrino

Standard model neutrinos have been excluded as the main dark matter candidate since N-body simulations have shown that hot (relativistic) dark matter results in accretion models which differ from our Universe [81]. However, the existence of heavy sterile neutrinos is motivated as an explanation for the masses of neutrinos through the "see-saw mechanism" [82]. The idea is that every left-handed neutrino is associated to a right-handed chiral neutrino which does not interact through the weak force. These particles are combined in the Lagrangian to form a mass term. However, the mass eigenstates are linear combinations of the chiral eigenstates. The "see-saw mechanism" lies in the fact the mass of left-handed active neutrino mass eigenstates is linked to the mass of the right-handed sterile neutrinos since they are eigenvalues of the neutrino mass matrix [83]. In this case, it is possible to obtain light neutrino masses without fine-tuning [84] since it simply implies that there also exist heavy sterile neutrinos.

Sterile neutrinos can be constrained based on different experiments and observations. For example, sterile neutrinos can have an impact on the composition of the elements ejected during supernovae explosions as well as the composition of the Universe during nucleosynthesis [85]. Gamma-ray telescopes such as Fermi [86] are searching for the decay of sterile neutrinos with masses in the $20 - 50$ keV range. The Karlsruhe Tritium Neutrino Experiment (KATRIN) is examining the energy spectrum of electrons produced by the β-decay of tritium. It is expected that KATRIN will provide the most sensitive results on the search for sterile neutrinos with sensitivity up to masses in the eV range [87].

1.3.5 Weakly Interacting Massive Particles (WIMPs)

WIMPs are cold dark matter candidates with masses in the GeV to TeV range. These particles are defined to interact through the gravitational and weak forces [45]. WIMPs have gained some particular attention due to a phenomenon known as the "WIMP miracle". In the early Universe, WIMP particles and antiparticles were produced and annihilated thermally. As the Universe cooled down, when $T \approx m_{\mathrm{WIMP}}$, the production of WIMPs froze out. At this point, WIMPs were not created anymore, but their number density continued to decrease due to self-annihilation until the WIMP density became low enough and annihilation became marginal. This means that the relic density of WIMPs is inversely proportional to its annihilation cross-section. The WIMP relic density is predicted as [88]

$$\Omega_{\chi} h^2 = \frac{3 \times 10^{-27} \mathrm{cm}^3/\mathrm{s}}{\langle \sigma v \rangle_{\mathrm{ann}}}, \tag{1.9}$$

where h is the reduced Hubble constant and $\langle \sigma v \rangle_{\mathrm{ann}}$ is the averaged of the WIMP annihilation cross-section times the speed. The WIMP miracle is the coincidence that if $\langle \sigma v \rangle_{\mathrm{ann}}$ is of the order of the weak scale then the correct WIMP relic abundance is predicted [45]. Another strong advantage in favour of WIMP dark matter is the fact that they are independently predicted by several theories such as Supersymmetry (SUSY), and higher dimensional theories such as the Kaluza Klein (KK) theory.

1.3.5.1 SUSY WIMPs

Maxwell's equations have shown that electricity and magnetism are two aspects of the same force, the electromagnetic force. The physical landscape is then divided between four fundamental forces, the weak, strong, electromagnetic forces and gravity, which together can explain every physical interaction. In 1979, Weinberg, Salam and Glashow were awarded the Nobel Prize for the prediction of the unification of the weak and electromagnetic forces. The unification principle at hand suggests that

the standard model cannot be a final theory [89]. However, in the standard model, the extrapolation of the coupling constants measured at LEP does not show any sign of unification between gravity α_3, the electroweak force α_2, and the strong force α_3, as shown in Fig. 1.5. This is, in part, due to the hierarchy problem [89]. This is the fact that the gravitational force is about 10^{34} times weaker than the weak force. If these interactions are different manifestations of the same force, why should one be so much weaker than the others?

SUSY is one of the most highly motivated theories beyond the standard model [90] which attempts to solve the hierarchy problem. Its primary purpose is to propose an answer to the hierarchy problem, the large (10^{24}) difference between the electroweak and Planck energy scales [27, 91]. The solution proposed in SUSY is to introduce a new Fermi-Bose symmetry where every fermionic particle has a bosonic partner and vice versa such that

$$Q\,|\text{fermion}\rangle = |\text{boson}\rangle \text{ and } Q\,|\text{boson}\rangle = |\text{fermion}\rangle\,, \tag{1.10}$$

where Q is the supercharge operator related to SUSY. In the standard model, all particles get radiative corrections to their masses. However, the corrections to the fermion masses only increase as the logarithm of the energy, while for scalar particles such as the Higgs boson, these corrections increase quadratically with energy [91, 92]. Hence, in the standard model, the Higgs boson mass is highly sensitive to the new physics scale, and radiative corrections would push the masses of the gauge bosons through their coupling to the Higgs towards the Planck scale and ruin electroweak stability [27]. In SUSY, this problem is solved since fermionic and bosonic loop contributions differ by a minus sign, the radiative corrections cancel each others and the correction to the Higgs mass $\delta m_H^2 \sim m_b^2 - m_f^2$ is canceled at all orders of perturbation theory provided that $\left|m_b^2 - m_f^2\right| < 1$ TeV [91].

Another evidence in favour of SUSY is the prospect of unification of the forces due to the unification of the gauge couplings around 10^{16} GeV [92] as seen in Fig. 1.5. The unification of the forces in SUSY is considered a hint in favour of a Grand

Unified Theory (GUT) [91].

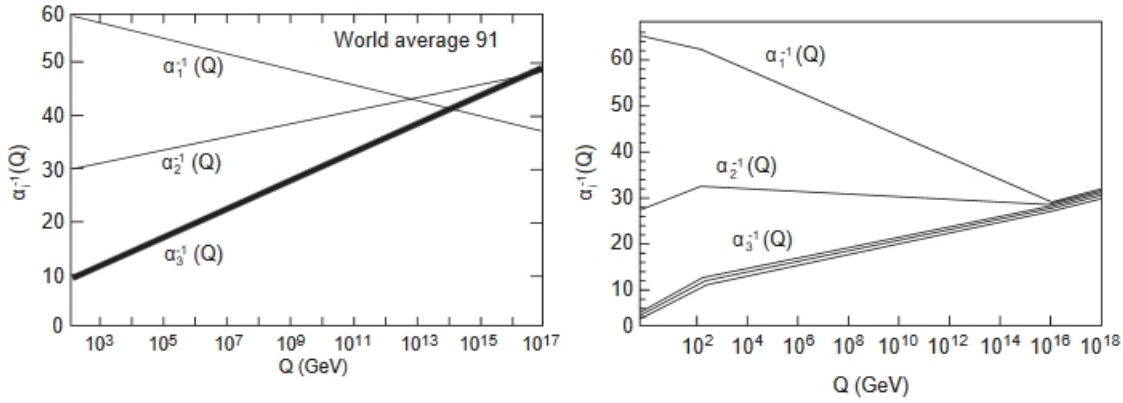

Figure 1.5: Extrapolation of the gauge couplings in the standard model (left) and in SUSY (right). From [91].

Finally, the third advantage of SUSY is that it provides a natural dark matter candidate. Doubling the number of particles through the fermion-boson symmetry can allow or enhance certain reactions. In particular, the possible existence of terms in the superpotential violating baryon and lepton numbers in SUSY is problematic. For example, squarks would mediate rapid proton decay [92, 27]. The introduction of R-parity in the theory ensures that interactions violating B or L do not happen. R is given by

$$R = (-1)^{3B+L+2s}\,, \tag{1.11}$$

where sparticles have $R = -1$ while standard model particles have $R = 1$. The conservation of R-parity implies that sparticles can only be produced or annihilated in pairs. Consequently, there must exist a lightest supersymmetric particle (LSP) which must be stable since it has no lighter sparticle to decay into. If the LSP is electrically neutral, its interaction with ordinary matter is very weak and is, therefore, a natural candidate for non-baryonic dark matter [91].

1.3.5.2 Kaluza Klein Dark Matter

The standard model can be completely described using a 3+1 dimensional manifold. However, extra dimensions may exist at higher energy scales [93]. The concept of extra-dimensions originates from the work of Kaluza and Klein, where the addition of an extra dimension into Einstein's field equations led to the unification of electromagnetism with gravity by identifying the extra components of the metric tensor to the gauge fields [91]. This work has evolved into higher dimensional theories in which the $3+1$ dimensional spacetime is called the brane, which is embedded into the $3+1+n$ bulk.

Similarly to SUSY, extra-dimensional theories can propose a solution to the hierarchy problem. If the standard model fields are limited to the brane, while the graviton has a non-zero expectation value in the bulk, then gravity's apparent strength is reduced from the point of view of an observer limited to the brane [94].

In order to explain the difference between the brane and the rest of the bulk, extra-dimensional theories require that the additional dimensions are compactified [95]. There is an upper-limit on the size of the extra dimensions due to their modifications of the inverse square law of gravity. In [96], the authors exclude compactification radii larger than 1mm. However, assuming that a field propagates in the bulk, its field equation can be rewritten. For example, following the process described in [97], if a massless scalar field $\phi(x^\mu)$ which satisfies the Klein-Gordon equation is considered then

$$\partial^\mu \partial_\mu \phi(x^\mu) = 0, \tag{1.12}$$

where the 5-dimensional d'Alembertian is given by

$$\partial^\mu \partial_\mu = \frac{\partial^2}{\partial t^2} - \nabla^2 - \frac{\partial^2}{\partial x_4^2}, \tag{1.13}$$

then the Fourier expansion of $\phi(x^\mu)$ is

$$\phi\left(x^{\mu}\right)=\sum_{n}\phi_{n}\left(x^{\nu}\right)\exp\left(\frac{inx_{4}}{R}\right), \tag{1.14}$$

where ν runs from 0 to 3.

If this result is substituted into the Klein-Gordon equation, then

$$\frac{\partial^{2}\phi_{n}\left(x^{\mu}\right)}{\partial t^{2}}-\nabla^{2}\phi_{n}\left(x^{\mu}\right)+\frac{n^{2}}{R^{2}}\phi_{n}\left(x^{\mu}\right)=0, \tag{1.15}$$

which from the point of view of an observer in the brane is the Klein-Gordon equation for a particle with mass $m=n/R$, [27]. The momenta of the fields are quantised in units of $p^{2}\sim 1/R^{2}$ in the compactified dimension. As viewed from the brane, the series of the Fourier modes of each bulk fields form a "tower" of states (called KK states) with different masses but identical quantum numbers [91]. One consequence is that, if the assumption of Universal Extra Dimension theories is verified, and all fields propagate in the bulk, then masslessness cannot be achieved from the point of view of an observer on the brane [98]. In particular, this result has led the study of the phenomenology of a massive KK photon such as in [99].

In Universal Extra Dimension theories, since there is no separation of the fields between the brane and the bulk, momentum must be conserved in the bulk since it is conserved in the brane [27]. This property introduces KK-parity which stabilises the lightest Kaluza-Klein (LKK) state through a similar mechanism as the LSP in SUSY since the LKK cannot decay to standard model particles only [100].

1.4 Conclusion

In this chapter, the main evidence for the existence of dark matter was presented. It was shown, in particular, that gravitational lensing and the Big Bang nucleosynthesis have brought irrefutable proofs that dark matter must be non-baryonic. The shortfalls of alternative theories of gravity were highlighted and it was shown that,

despite fine-tuning, these theories still require the addition of dark matter. Finally, the main dark matter candidates were review and the theories which independently motivated their existence were presented. Finally, it should be emphasised that there are many more dark matter models. For example, a light scalar dark matter particle has been proposed in [101] in order to explain the excess 511 keV line observed in the Milky Way. In Little Higgs models, the Higgs boson is a pseudo-Nambu-Goldstone boson originating from the breaking of time parity. These models can produce a scalar dark matter candidate [102]. In a third model, WIMPzillas are heavy dark matter candidates with mass $> 10^7$ GeV produced before the end of reheating at the end of inflation. They arise in Grand Unified Theories and possess a small colour charge in order to produce proton decay [103]. In the same way, there also exist many more theories of alternative scenarios to dark matter such as mimetic dark matter for example [104], where the inhomogeneous adiabatic fluctuations of the inflaton mimic the effects of cold dark matter on large scale structures.

2 Dark Matter Detection

There are a myriad of experiments searching for dark matter. These complementary experiments can be divided into three categories depending on the interaction between dark and baryonic matter. These categories are illustrated in Fig. 2.1. The Feynman diagram represents the interaction between dark matter particles (denoted χ) and standard model particles (denoted p). At colliders, the collision of standard model particles may produce dark matter particles. Indirect detection, on the other hand, is searching for evidence of dark matter annihilation or decay resulting in standard model particles. Direct detection, finally, is the search of scattering interactions between dark matter and standard model particles. In this chapter, each strategy is briefly reviewed with a particular emphasis on direct detection. Some of the experiments which chose this approach are presented and the properties of the WIMP-nucleon cross-section are discussed in order to highlight the potential of galactic signature experiments.

2.1 Collider Searches for Dark Matter

Particle colliders are searching for the production of dark matter particles from the collision of standard model particles. The Large Hadron Collider (LHC) accelerates protons up to a centre of mass energy of 13 TeV. As the two proton beams collide in the 27 kilometer ring, the high centre of mass energy recreates conditions closer to the early Universe. In a sense, the LHC tries to reach energies high enough to break the freeze-in condition and produce a WIMP pair from standard model particles.

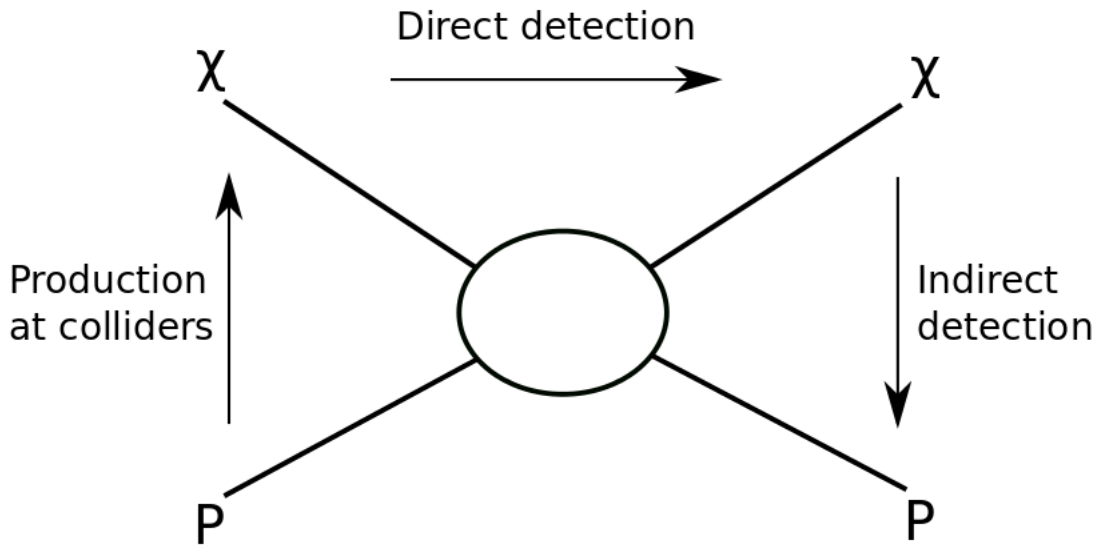

Figure 2.1: Feynman diagram illustrating the three strategies of dark matter detection.

Since the LHC is not a facility dedicated specifically to dark matter, the approach taken is to constrain the theories which produce dark matter candidates. In the case of SUSY for example, the conservation of R-parity can lead to mono-jet events [105]. In these scenarios, the recorded missing transverse energy can be used to deduce the mass of the undetected particles. The issue with this technique is that the operator related to the interaction between dark matter and baryonic matter is unknown and theory-dependent. To this effect, an effective field theory approach has been taken [106]. By using this technique, it is not necessary to know the exact Lagrangian in order to interpret the results. Instead, effective field theories aim to obtain the Lagrangian by comparing the experimental data to the phenomenology calculated using generic operators.

So far, no evidence for dark matter was found at the LHC [45, 105] as shown in Fig. 2.2. For example, the first quadrant of the table shows the current limit on the energy scale of different higher dimensional theories. This is a constraint on the Kaluza-Klein WIMP models. However current collider searches cannot completely

rule-out new physics [45]. For example, if SUSY is not found at 13 TeV, then the mass of super-symmetric particles can be set to be higher than 13 TeV. Similarly, if there is no sign of higher-dimensions at 13 TeV, then these dimensions may be more compactified than what was assumed. Essentially, it could be argued that until the Planck scale is reached, a null result from collider experiments cannot rule out SUSY, it only makes its existence less likely. On the other-hand, the detection of new particles at the LHC as missing transverse energy would produce limited information about the stability of the dark matter candidates. For example, a particle which is long-lived enough to escape the detector at the LHC but is not stable on a cosmological timescale would not be a suitable dark matter candidate. This argument illustrates the complementarity of the dark matter searches since an astrophysical detection is required to verify the dark matter models.

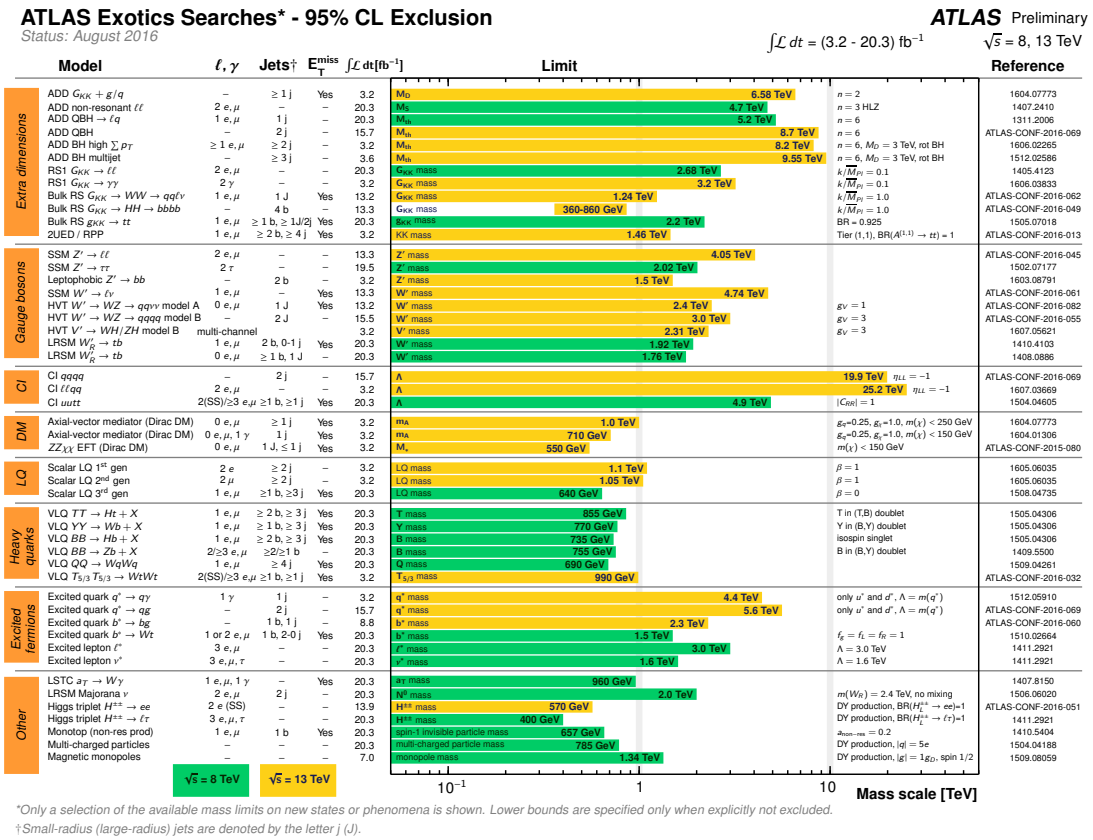

Figure 2.2: Summary of ATLAS reach to new physics.

2.2 Indirect Searches

Indirect searches look for the decay products of dark matter annihilations. Although the present day dark matter annihilation rate is extremely small, annihilation can still occur locally where WIMPs over-densities exist [45]. The final products of WIMP annihilation are electron positron pairs, photons and neutrinos. The problem of this technique is that is may be difficult to estimate in a model independent way the origin of the signal observed. For example, assyming that WIMP annihilations near the galactic core would produce an excess of positrons. The particles would eventually be annihilated themselves due to interactions with electrons in the interstellar medium. This would result in a 511 keV line emission which would be consistent with the results observed by the INTEGRAL gamma ray observatory [107]. However, it is not possible to ascertain that these gamma rays are due to the annihilation of dark matter, since large quantities of positrons can also be produced in β-decays of unstable elements created through stellar fusion or supernovae explosion [108]. A possible stellar origin of the signal cannot be excluded but the detected luminosity is reportedly concentrated in the bulge rather than the galactic disk where most of the baryonic matter lies [109].

Another lead followed by indirect detection experiments is to detect neutrinos from WIMP annihilation. As stars rotate around the galactic centre and through the dark matter halo, it is expected that some dark matter will become trapped inside the gravitational wells of stars [110]. In this case, photon detection is not a viable option since photons take a long time to reach the surface of the Sun, but neutrinos from the Sun could, however, be detected. Using this method, the neutrino detectors IceCube/DeepCore located at the South Pole are sensitive to WIMP with masses between 50 GeV to 1 TeV [111]. However, no evidence for dark matter annihilation in the Sun or the Earth has yet been found in IceCube [112]. Overall, indirect detection is capable to exclude WIMP interaction cross-section competitively with direct detection experiments. For example, in Fig. 2.3, the exclusion of the spin-

independent cross section obtained by IceCube is of the same order of magnitude as Xenon100.

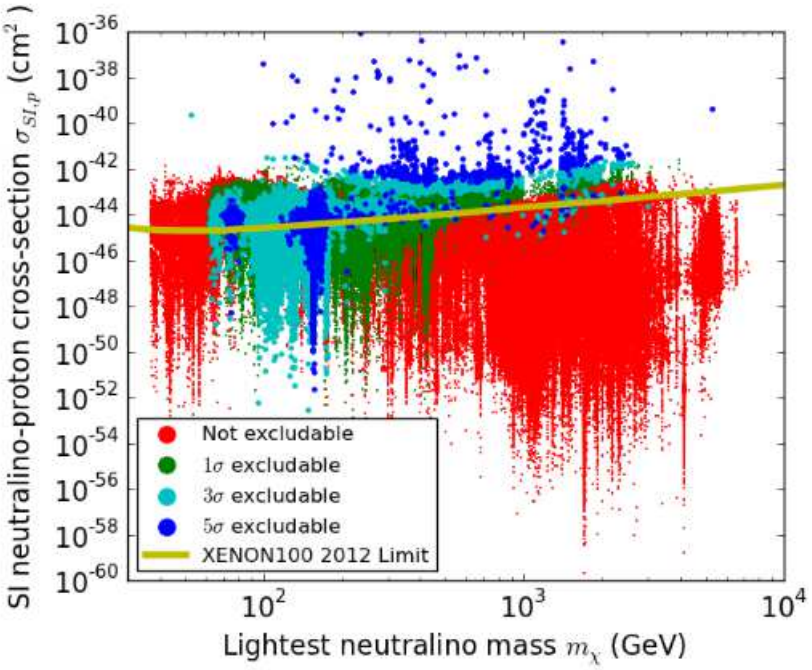

Figure 2.3: Spin-independent results from IceCube showing excludable neutralino models using Minimal Supersymmetric Standard Model (MSSM). The calculation of the MSSM parameter space was done using the DarkSUSY program [113] to compute the neutralino masses. Each dot corresponds to a MSSM model. The results are compared to the XENON100 results [114] excluding all MSSM models above the gold line. From [115].

2.3 Direct Detection

Direct detection experiments look for the scattering of a dark matter particle with standard model particles. In these interactions, the dark matter particle transfers some of its energy to the standard model particle, and its recoil is detected by the experiment through different processes (ionisation, scintillation and phonon production). The scattering of a WIMP with mass 10 GeV to 1 TeV would produce nuclear

recoils in the range of 1 to 100 keV$_r$ [116]. One of the advantages of direct detection is its ability to distinguish the galactic origin of the signal observed compared to Earth based backgrounds. This technique revolves around the annual modulation of the dark matter flux and the change of direction during the day for an Earth-based observer.

Direct detection experiments record the recoil spectrum of scattering events. However, given the small cross-section of dark matter, the probability of multiple scatterings within a detector volume is negligible. Using the approach in [117, 116], the differential recoil spectrum of WIMPs $\frac{\mathrm{d}R}{\mathrm{d}E}(E,t)$ can be written as

$$\frac{\mathrm{d}R}{\mathrm{d}E}(E,t) = \frac{\rho_0}{m_\chi m_\mathrm{A}} \int v \times f(\vec{v},t) \times \frac{\mathrm{d}\sigma}{\mathrm{d}E}(E,v)\,\mathrm{d}^3 v, \tag{2.1}$$

where $\rho_0 \approx 0.3$ GeV/cm^3 is the local dark matter density , m_χ is the WIMP mass and m_A the target nucleon mass. $\frac{\mathrm{d}\sigma}{\mathrm{d}E}(E,v)$ is the differential cross section and $f(\vec{v},t)$ is the dark matter velocity distribution. ρ_0 and $f(\vec{v},t)$ are astrophysical parameters and have associated uncertainties as discussed in chapter 1 for the case of ρ_0. The study of these parameters can be used to provide a galactic signature of dark matter interactions, as shown in the next two sections

2.3.1 Annual Modulation

One particular galactic signature is the annual modulation of the dark matter signal. The dark matter velocity profile $f(\vec{v},t)$ is commonly described by an isotropic Maxwell-Boltzmann distribution truncated at the galactic escape velocity since WIMPs with velocities higher than this value would not be gravitationally bound in the halo. The escape velocity was estimated by the RAVE survey [118] to be 498km/s $< v_\mathrm{escape} <$ 608km/s (90%CL). The velocity distribution enters the equation with a time dependence because of annual modulation. As the Sun revolves around the galactic centre, our motion in the dark matter halo effectively creates a dark matter wind. However, due to the motion of the Earth around the Sun, the

addition of both velocities creates an annual modulation of the WIMP wind velocity which in turns leads to an annual modulation of the recoil rate according to 2.1 and as visible in Fig. 2.4.

As seen in Fig. 2.4, the WIMP velocity distribution should peak in June when the Earth's displacement in the direction of rotation of the galactic disk is the fastest, and be at its minimum in December when the Earth is moving the fastest in the opposite direction [119]. Then following [119], for an observer in the lab frame $f(\vec{v},t) = f(\overrightarrow{v_{\text{obs}}},t)$ with $\overrightarrow{v_{\text{obs}}} = \overrightarrow{v_{\odot}} + \overrightarrow{v_{\oplus}}(t)$, where $\overrightarrow{v_{\odot}}$ is the vector representing the motion of the Sun around the galaxy, and $\overrightarrow{v_{\oplus}}(t)$ represents the motion of the Earth around the Sun. For a smooth, virialized halo with no substructures, $\overrightarrow{v_{\odot}}$ has no time dependence on the timescale of a dark matter experiment and its norm is around the commonly accepted value of 220km/s, although there is some minor uncertainty between different measurements [120]. The $\overrightarrow{v_{\oplus}}(t)$ term, on the other hand, varies throughout the year and neglecting the ellipticity of the Earth's orbit, the time dependence can be explicitly written as [119]

$$\vec{v_{\oplus}}(t) = v_{\oplus}\left[\hat{\epsilon_1}\cos\omega\left(t-t_1\right) + \hat{\epsilon_2}\sin\omega\left(t-t_1\right)\right], \tag{2.2}$$

where $\omega = \frac{2\pi}{1\text{year}}$, $\hat{\epsilon_1}$ and $\hat{\epsilon}_2$ are unit vectors such that they point in the direction of the Earth's motion at a time t_1 and $t_2 = t_1 + 0.25$ year. Using this expression and the Galilean transformation of $f(\vec{v},t)$, the differential recoil rate can be expressed as a Fourier series [119]. However, since the modulation amplitude is smaller than the time averaged rate , $S_m \ll S_0$, annual modulation can be treated as a perturbation and the differential recoil rate can be expressed as [116]

$$\frac{\mathrm{d}R}{\mathrm{d}E}(E,t) \approx S_0(E) + S_m(E) \times \cos\left(\frac{2\pi\left(t-t_0\right)}{1\text{ year}}\right). \tag{2.3}$$

Annual modulation could be a strong tool to demonstrate the galactic origin of an observed dark matter signal and is being used by several dark matter experiments as discussed in sec. 2.4.1.

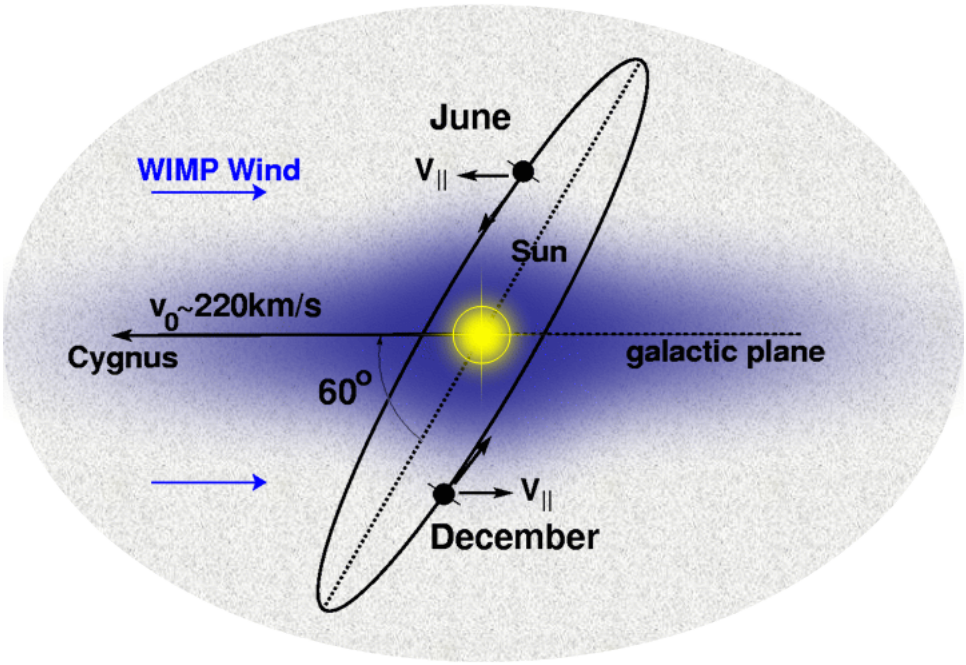

Figure 2.4: Schematic view of the WIMP velocities and the effect of the Earth's motion around the Sun. From [121].

2.3.2 Directionality

The underlying principle of directionality is that in addition to the annual modulation described above, the Earth also rotates on its axis with a period of one day. If an experiment would be capable of reconstructing the direction of an incoming WIMP before it scatters on the target, the observed dark matter signal would show a preferred direction towards the constellation Cygnus due to the solar motion. In a sense, while annual modulation relies on the $\overrightarrow{v_\oplus}$ term of observed velocity, directionality is based on the $\overrightarrow{v_\odot}$ part. It could be argued that this is a more potent technique than annual modulation since it relies on the bulk of the velocity $v_\odot = 220$ km/s [119] rather than on a smaller perturbative effect $v_\oplus = 29.8$ km/s [119]. The idea to create dark matter detectors with a strong angular resolution was pioneered in [122, 123] as the nuclear recoil rate can be expressed as a function of the recoil angle γ compared to the direction of the solar motion [116]

$$\frac{\mathrm{d}R}{\mathrm{d}E\mathrm{d}\cos\gamma} \propto \exp\left[\frac{-\left[(v_\oplus + v_\odot)\cos\gamma - v_{\min}\right]^2}{\frac{3}{2}v_\odot^2}\right], \tag{2.4}$$

where $v_{\min}$ is the low energy cut-off under which a nuclear recoil of energy E cannot be produced. This shows that the number of recoils in the direction of the solar motion will exceed the number of recoils in the opposite direction due to the change of sign of the $\cos\gamma$ term. In effect, this phenomenon creates a "WIMP wind" coming from the direction of the constellation Cygnus. This technique can be used to statistically discriminate WIMP recoils from Earth based background which should either be isotropic or appear at a fixed position in the case of a point-like comoving background. There is no known laboratory background which is expected to mimic this signal [123]. The amplitude of this modulation depends on the latitude of the detector, where no modulation happens for directions parallel to the orientation of the Earth spin axis [123]. The amplitude of the signal is illustrated in Fig. 2.5.

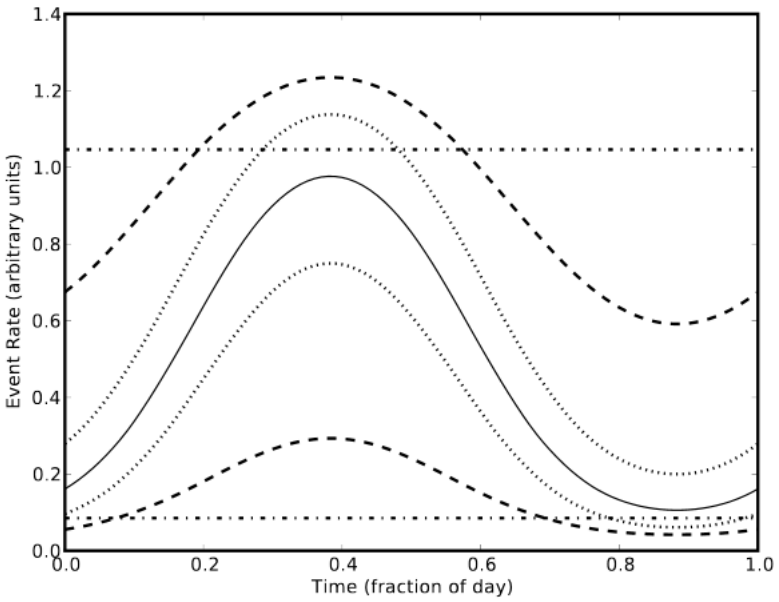

Figure 2.5: Modulation of the event rate in a directional detector at zero degree (solid line), ±18ř(dotted lines), ±54ř (dashed lines), ±90ř (dashed-dot lines) from the equatorial plane. From [123].

Furthermore, a detector with sufficient angular resolution could be able to resolve sub-structures in the dark matter halo as theoretically demonstrated in [124]. For example, it is expected that the halo of the Milky Way contains at least 10^5 sub-haloes above 5 solar masses [125]. A directional detector with enough sensitivity and exposure could be compared to a "WIMP telescope" capable of pointing towards halo substructures in the galactic vicinity.

2.3.3 Spin-dependence and Nuclear Physics Effects

The interpretation of the dark matter cross-section depends on the target used. For spin-independent WIMP interactions, each nucleon is assumed to contribute equally under isospin conservation [116] and the scattering amplitude of each nucleon adds coherently. Dark matter detectors looking for spin-independent interactions tend to use high-A targets which can be deployed with a high density. For example, several large experiments such as PandaX-II [126] or Xenon1T [127], are based on liquid xenon (^{128}Xe is the main stable xenon isotope). Sodium iodide (NaI) or caesium iodide (CsI) have also been considered due to the presence of iodine (^{127}I is the only naturally occurring stable iodine isotope). Alkali halides have been particularly popular with experiments looking for annual modulation such as DAMA/LIBRA for NaI [128] and KIMS for CsI [129].

For spin-dependent searches, only unpaired nucleons contribute to the scattering and the cross-section depends on the spin of the unpaired nucleon with a different coupling between protons and neutrons [116]. In the spin-dependent case, the target nucleus must, therefore, have an odd number of nucleons. Iodine is still a suitable target, and liquid xenon experiments have some sensitivity to spin-dependent interaction due to the presence of ^{129}Xe and ^{131}Xe which together represent around 50% of naturally occurring xenon. Fluorine (^{19}F) has been a popular target choice for gaseous detectors with CF_4 being used by all major time projection chamber experiments [130, 131]. Recently, there has been growing interests for SF_6 [132] due to its

higher fluorine content and negative ion properties as will be discussed in sec. 7.1.

In general, experiments can investigate both regimes and the WIMP-nucleus cross section $\frac{\mathrm{d}\sigma}{\mathrm{d}E}$ can be written as the sum of both the spin-dependent and independent cross sections for a nucleus with mass number A [116]

$$\frac{\mathrm{d}\sigma}{\mathrm{d}E} = \frac{m_{\mathrm{A}}}{2\mu_{\mathrm{A}}^2 v^2} \times \left(\sigma_0^{\mathrm{SI}} \times F_{\mathrm{SI}}^2(E) + \sigma_0^{\mathrm{SD}} \times F_{\mathrm{SD}}^2(E)\right), \tag{2.5}$$

where the σ_0 are the cross sections when no momentum is transferred. The momentum dependence is instead in the form factors F. When the transferred momentum q is such than the de Broglie wavelength of the recoiling target nucleus $\frac{2\pi\hbar}{q}$ is less than the nuclear radius $r_0 \approx 1.25\mathrm{fm} \times \mathrm{A}^{1/3}$, the reaction can no longer be approximated as the scattering of two hard spheres. The nuclear form factors are corrections to the cross-sections in scenarios where the reaction is suppressed [117]. If both the incoming and outgoing particles are approximated at plane waves (Born approximation), the form factor is the Fourier transform of the distribution of the scattering surface $\rho(r)$ [117], giving

$$\begin{aligned}
\mathrm{F}(q) &= \int \rho(\vec{r})\, e^{i(\vec{q}\cdot\vec{r})} \mathrm{d}^3 r \\
\mathrm{F}(q) &= \int_0^{2\pi} \mathrm{d}\phi \int_0^{\infty} \rho(r)\, r^2 \mathrm{d}r \int_{-1}^{+1} e^{iqr\cos\theta} \mathrm{d}\cos\theta \\
\mathrm{F}(q) &= \frac{4\pi}{q} \int_0^{\infty} r \sin(qr)\, \rho(r)\, \mathrm{d}r.
\end{aligned} \tag{2.6}$$

In the low energy case, the incoming WIMP does not have a sufficient energy to penetrate deeply in the Wood-Saxon potential [133] of the atom and the scattering region is the surface of the target nucleus, hence $\rho(r) = \frac{\delta(r-r_0)}{4\pi r_0^2}$ and this gives $\mathrm{F}(q) = j_0(qr_0)$, where j_0 is the zeroth order Bessel function of the first kind [117].

For spin-dependent interactions, the form factors are more complicated due to the effects of nuclear structures [134] and are determined by nuclear shell model calculations [116]. Using Galilean (non-relativistic) effective field theory, a more complete

formalism of the coupling between WIMPs and dark matter was formulated in [135] where the scattering cross-section is not only considered in terms of spin-dependent or independent terms, but additional terms are included in order to account for potentially more complex coupling to dark matter. For example, particles are not treated as point-like and the model also takes in consideration the different treatment required between scalar and vector dark matter particles.

2.4 Galactic Signature Experiments

In the previous section, it was shown that the dark matter recoil rate can be written in different ways so as to show explicitly the dependence on the direction of the dark matter wind and the time of the year in the case of annual modulation. This section contains a review of some of the experiments which make use of this techniques to search for dark matter.

2.4.1 Scintillating Crystal Detectors

Several galactic signature experiments rely on inorganic crystals for their dark matter search. Inorganic scintillators are known to have a higher stopping power due to their density and high atomic number, with a high light output which enables the experiment to have a low energy threshold and a good energy resolution [136]. The scintillation mechanism is based on the luminescent properties of these materials. If the material is exposed to energy, this energy can be absorbed by raising the atom to an excited state. The energy is later released in the form of light. However, the time delay before relaxation is dictated by the meta-stability of the excited state [136]. During a nuclear scattering, the crystal can either be ionised by liberating a valence electron to the conduction band, creating a free electron. Or in the other case, the atom is simply raised to an excited state. The valence electron is promoted to a higher energy state, from the valence band to the exciton band. In this case, the

electron and electron hole remain bound together (in a state called an exciton) and can travel through the crystal. If the pair reaches impurities in the crystals (such as thallium doping in sodium iodide crystals), the exciton can ionise the impurity atom [136]. This method can be used to increase the luminosity of the crystals and make the detector more efficient.

2.4.1.1 The DAMA problem

The DAMA (DArk MAtter) [128] experiment is an annual modulation experiment using ultra-low background sodium iodide crystals (NaI) activated with thallium (Tl) to increase their scintillation properties as described above. The DAMA experiment has accumulated an exposure of 1.33 tonne × year over 14 years [137]. The DAMA/LIBRA experiment shown in Fig. 2.6 is composed of NaI (Tl) crystals in their protective copper casings. These encapsulation units serve both as a gamma shield against external radiation and to protect the crystals since NaI crystals can be damaged by moisture [136]. The outer shielding is made of copper, lead, cadmium, and paraffin [138].

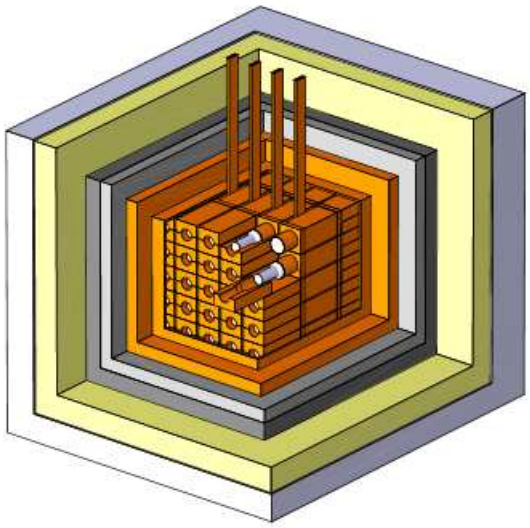

Figure 2.6: Schematic view of the DAMA/LIBRA experiment. From [138].

Instead of seeking a background-free region of parameter space, DAMA is searching for an annual modulation of the detected signal above the background pedestal. Background levels are being contained through the use of low radioactivity materials, pulse-shape analysis of the data and mutual vetoing between the crystals. For example, the 3 keV peak of potassium-40 (^{40}K) is a problematic source of background for DAMA since it lies inside its $2-6$ keV region of interest. ^{40}K decays to ^{40}Ar with a 10.7% branching ratio producing a 1460 keV gamma and a 3 keV X-ray or Auger electron. While the 3 keV X-ray is not energetic enough to escape the crystal in which it was created, the 1460 keV gamma ray can deposit energy in the neighbouring crystals [139]. Mutual vetoing between the crystals can help reject some of this background.

The cumulative exposure of the DAMA/LIBRA collaboration during 14 annual cycles at the Gran Sasso underground laboratory (LNGS) has shown an annual modulation of the signal in the single event channel with an amplitude of $A = (0.0110 \pm 0.0012)$ dru $\left(1 \text{ dru} = 1 \text{ event kg}^{-1} \text{ day}^{-1} \text{ keV}^{-1}\right)$ corresponding to a 9.2σ C.L. [128]. The period of the oscillation $T = (0.998 \pm 0.002)$ year and its phase $t_0 = 144 \pm 7$ days are consistent with the expectations of a dark matter signal. The DAMA collaboration has verified that this signal modulation is absent outside of the dark matter region of interest [137] and is also unseen in the multiple event channels [128].

The results of DAMA have created controversy since the annual modulation of their signal would be consistent with dark matter interaction cross sections which are already excluded by several other experiments, as ilustrated in Fig. 2.7. Several explanations have been put forward to resolve the issue. Addenda to the theory have been proposed in order to fit the data by modifying the properties of the dark matter candidates or the mediators involved [140], or by creating models in which dark matter couples preferably to leptons at tree-level [141]. The DAMA collaboration itself has been investigating possible other origins of the signal. In particular, the cosmic muon flux has been measured to fluctuate by the Borexino

experiment also located at LNGS [142]. The muon flux is expected to depend on the temperature of the atmosphere with a maximum around June 28th, but this hypothesis has been rejected by the DAMA collaboration [143]. Furthermore, the neutron background is also known to fluctuate at LNGS due to varying levels of water in the concrete [144]. The concrete walls can act as moderators of neutrons either produced in the rock or in the concrete itself. If the water content depends on the temperature of the laboratory, then the dry concrete in the hot summer months will have a lesser impact on the ambient neutron flux.

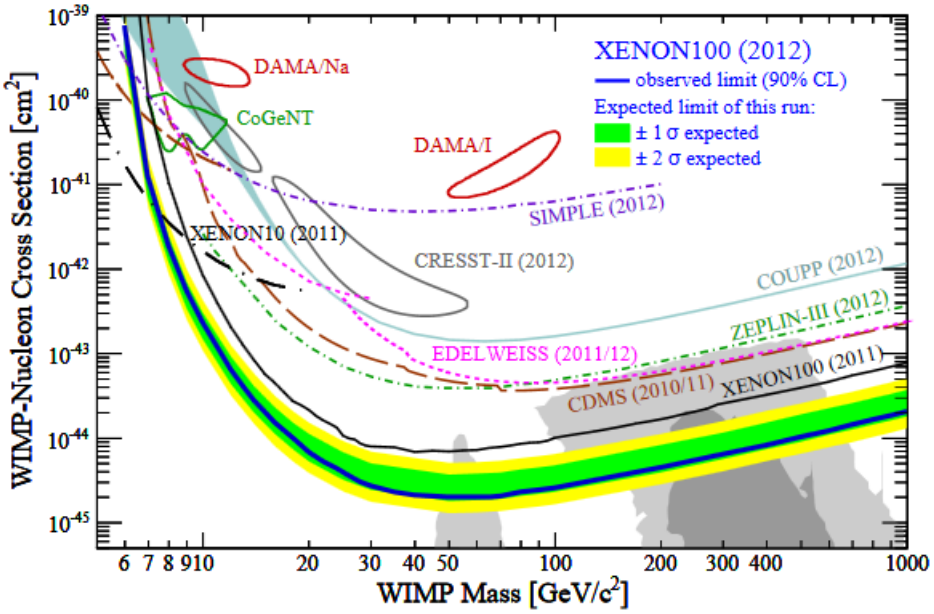

Figure 2.7: Spin independent limits from several experiments, including the XENON100 2012 limit [114], excluding the DAMA-allowed regions (in red). From [114].

The solution to the DAMA problem can be twofold. Firstly, several experiments are attempting to reproduce the DAMA signal using similar NaI(Tl) crystals. In particular, the DM-Ice experiment [145], which will be described in greater details in the next chapter, could investigate the galactic nature of the DAMA signal. Indeed, since the DM-Ice crystals are placed at the South Pole, the modulation of backgrounds caused by cosmic rays should have an inversion of phase compared to

LNGS while the dark matter signal should remain the same. Furthermore, local background sources, such as humidity, or temperature-related backgrounds may have different phases since the experiments are conducted in far away laboratories. A second possible solution to the DAMA problem would be to investigate this region of parameter space with a directional detector. Should the DAMA signal be indeed due to dark matter, a directional detector could provide a definitive proof of its galactic origin. At the time of writing, the most sensitive directional spin-dependent exclusion limits are from the DRIFT detector. One such limit is published in [146], while the current world leading directional limit is presented in sec. 4.3.2. However, both limits are only partially probing the DAMA allowed regions at the moment.

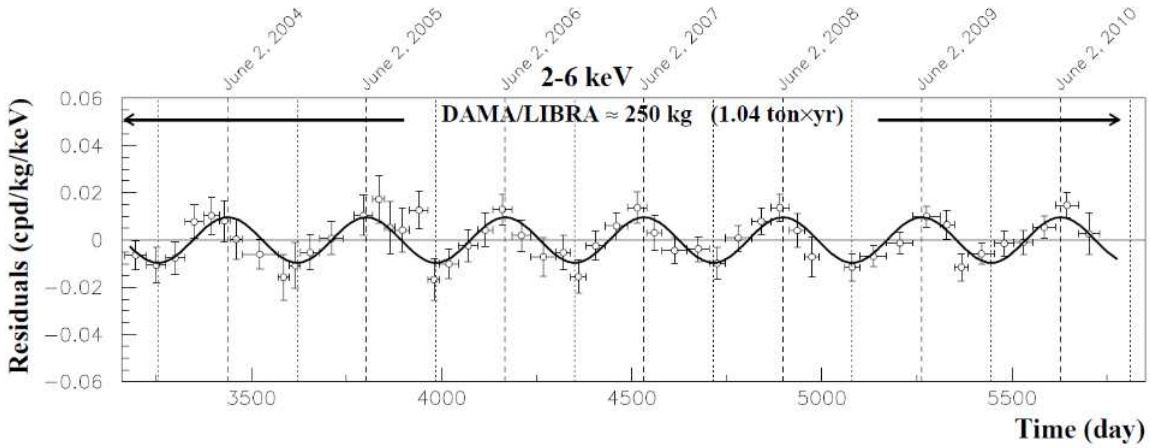

Figure 2.8: Experimental residual rate in the single event channel in DAMA. From [128].

2.4.1.2 Testing the DAMA Signal

Several experiments are currently trying to test or reproduce the annual modulation reported by DAMA. However, the observed signal is already conflicting with several other experiments. For example, the XMASS detector [147] is an 800 kg detector filled with ultra-pure liquid xenon situated in the Kamioka underground laboratory in Japan. As discussed in sec. 2.3.3, xenon has been a target chosen by several dark

matter experiments for spin-independent search, but its properties also make it an interesting material to search for annual modulation. In particular, liquid xenon has a high light yield similar to NaI(Tl) which means that both are sensitive to low energy scatterings. As a coincidence, both liquid xenon (3.06 g/cm^3) and NaI (3.67 g/cm^3) have similar densities so both materials can be used to create the large experiments required to observe an annual modulation signal. Furthermore, xenon's high atomic number (Z=54) can provide efficient gamma background self-shielding as the XMASS collaboration has developed [147]. This method consists in using the outer-regions of the active volume as a shield and veto to reject external background. Weakly interacting particles (such as WIMPs or neutrinos) on the other hand, will be able to interact in the core region of active volume. In [148], the authors analysed the results of 359.2 live days of exposure accumulated with 832 kg of target mass and found no evidence of annual modulation.

Similar measurements, such as the one performed by XMASS, have been done by LUX [149], XENON-100 [114], and Super-CDMS [150]. All of them have excluded the regions of parameter space allowed by DAMA as shown in Fig. 2.7 for LUX and XENON. This discrepancy is highlighting the need for further investigation using the same target material as DAMA with a method relying on the galactic signature to discriminate background events from a true WIMP signal. This is the goal of the SABRE [151] and COSINE experiment described in sec. 3.3.

SABRE is developing an array of low background NaI crystals to look for annual modulation. In particular, ^{40}K is the main background isotope as discussed previously due to its 3 keV X-ray or Auger electron. SABRE has developed crystals with ^{40}K levels 4 times inferior to DAMA [151]. The full-scale experiment will comprise two twin detectors, one placed at the Gran Sasso laboratory (LNGS) in Italy, the other at the Stawell underground physics laboratory (SUPL) in Australia. In the northern hemisphere, the annual modulation of the WIMP flux with its maximum in June is in phase with the temperature fluctuations linked to the seasons. Since there is an inversion of phase in the southern hemisphere, SABRE will be able to discrim-

inate between a true WIMP signal and temperature related background. Similarly to the other NaI experiments, each crystal is placed in a low background copper encapsulator between two photomultiplier tubes, and the copper encapsulators are placed inside a volume of liquid scintillator in order to reject external background events.

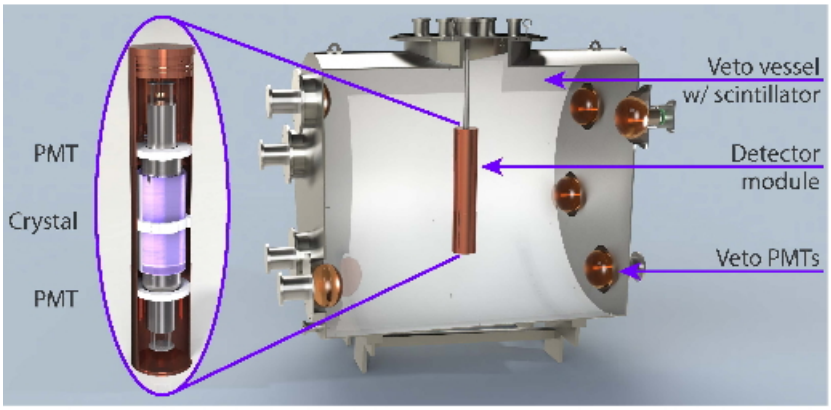

Figure 2.9: Schematics of the SABRE experiment. From [151].

2.4.2 Directional Detectors

In the previous section, it was shown how a directional detection of dark matter may be one of the few ways to provide a definitive proof of the detection of dark matter. Directionality relies on the ability to reconstruct the WIMP direction and as such has so far mainly been explored by low-density gases in Time Projection Chambers (TPCs). The study of the ionisation density ($^{\mathrm{d}E}/_{\mathrm{d}x}$) requires that the density of the medium is small enough to be able to reconstruct the direction of the recoiling nuclei. For example, the typical track length for a 100 GeV/c^2 WIMP in a TPC with pressure under 100 Torr is on the order of $1 - 2$ mm [116]. The asymmetry in the number of events pointing towards the Cygnus constellation can be used to prove that the signal observed is indeed due to dark matter. Different experiments have evolved around different gas mixtures and readout technologies. However, CF_4 is one of the most commonly used target material because of its unpaired

nucleon which gives it sensitivity spin-dependent interaction. ^{3}He has also been investigated by the MIMAC collaboration [152] for low mass WIMP spin-dependent interactions, but its dissuasive cost forbids its use in any large scale TPCs. The DRIFT experiment has pioneered the use of negative ions (in particular CS_2^-), to reduce the thermal diffusion of the ionisation along the drift distance. The DRIFT experiment is reviewed in greater details in sec. 4.1.

D^3 [153], NEWAGE [154] and MIMAC [152] are detectors which are developing full 3D track reconstruction. In particular, the NEWAGE detector is placed at Kamioka underground laboratory in Japan. NEWAGE has perfected its track reconstruction technique and has demonstrated its ability to create a map of nuclear recoil directions. In Fig. 2.10, the reconstructed origins of the scattering particles are plotted as a function of their positions for WIMP like events. The purple circle marks the direction of Cygnus during the experiment. The figure also illustrates the limitations of NEWAGE. Without a significant reduction of its current background level, a small WIMP signal could easily be hidden by a large number of background events. While directional detectors can provide an indisputable dark matter signal, efforts should be made to reduce their intrinsic background levels in order to support their unique capabilities. In sec. 7.1, the attempts of the CYGNUS collaboration to develop a large scale background-free directional detector are discussed.

2.4.2.1 Directional crystal detectors

Besides low-pressure TPCs, crystal based experiments are also being considered to create a directional detector. Organic (carbon based) crystals have been proposed as directional dark matter detectors [155]. This technique makes use of the anisotropic properties of organic crystals since their scintillation efficiency depends on the direction of the scattering particle with respect to the crystals axes [155]. Using this method, the authors investigate the possibility to create a directional dark matter detector by aligning a crystal of stilbene $(C_6H_5CH)_2$ in the direction of Cygnus. The results from Monte-Carlo simulations in [155] show a 7% anisotropy in favour of the

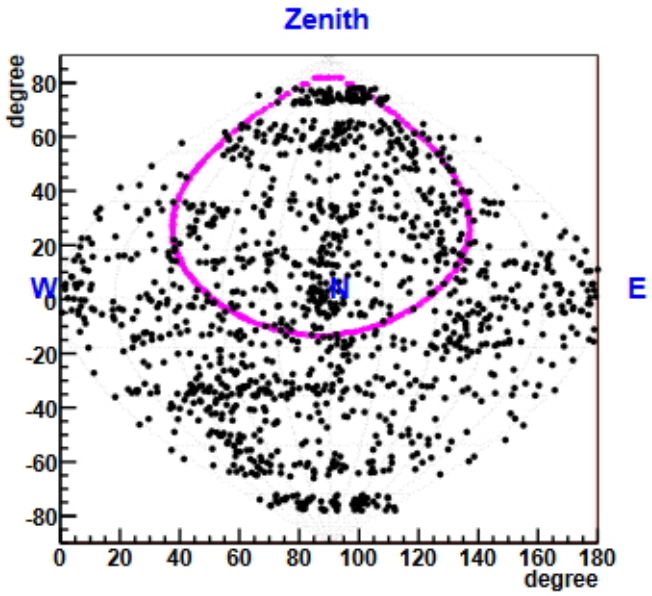

Figure 2.10: Distribution of nuclear recoil tracks in local altitude-azimuth coordiantes at the Kamioka Underground Laboratory. The purple line is the track of the direction of Cygnus. From[154].

preferred direction during a comparison with neutron induced nuclear recoils. In [156], the same authors tested a small 116 g organic crystal at the Kamioka underground laboratory but their attempts to prove their detection of a directional signal were limited by both the crystal mass and its high background levels ($>$ 2000 dru). Improvements are needed to develop this technology into an efficient dark matter detector. The authors report that background levels below 0.3 dru would be sufficient to observe an anisotropy in the signal.

The ADAMO [157] collaboration is developing a dark matter detector based on zinc tungstate $ZnWO_4$. $ZnWO_4$ is an inorganic crystal which as been studied for its anisotropic properties similar to stilbene described above. Its high density (7.8 g/cm^3) make it a prime material for directional detection. Furthermore, background levels obtained in $ZnWO_4$ are comparable to the contamination levels in NaI (Tl). For example, the background levels in the crystals studied in [158] are around 0.5 ppt for ^{232}Th, 0.2 ppt for ^{238}U and 0.6 ppb for ^{40}K, assuming secular

equilibrium. This is extremely competitive with the levels obtained in KIMS-NaI [159] 0.5 ppt for ^{232}Th, 0.14 ppt for ^{238}U and 25.3 ppb for ^{40}K. The ADAMO collaboration has also demonstrated its ability to discriminate some of the backgrounds in their crystals by doing pulse shape analysis [158] in particular in order to distinguish βs and αs. Finally, the ADAMO collaboration expects to be able to probe most of the DAMA allowed regions at the 90% C.L. over 5 years with 200 kg for crystal mass as shown in Fig. 2.11.

These results show that there is a potential for creating a directional detector based $ZnWO_4$ crystals. However, the axial measurements tested in [158] are based on gamma and alpha signals not nuclear recoils. Furthermore, the anisotropic response of the $ZnWO_4$ crystals can give the detector some directional sensitivity but it is only limited to the angle of the recoil. In a sense, $ZnWO_4$ crystals can be used to build detectors with axial sensitivity rather that directional sensitivity. In order to truly determine the origin of the incident particle as shown in Fig. 2.10, the detector needs to sensitive to direction of signal. In low pressure gas TPCs, such as NEWAGE, this is done through the head-tail effect. The head-tail effect is the fact that nuclear recoil tracks deposit more energy at the beginning of the track that at the end [160]. Several gas TPCs has demonstrated sensitivity to head-tail such as DRIFT [161] and DMTPC [162] for example. However, there is no equivalent of this head-tail parameter in scintillation experiments.

2.4.2.2 Directionality with Noble Elements

The noble elements are used extensively in dark matter searches for their scintillation properties. When exposed to radiation, the noble elements emit ultra-violet light which can be captured by a photomultiplier tube coated with a wavelength shifting material such as P-terphenyl (PT) and tetraphenyl-butadiene (TPB) [163]. In the large noble liquid dark matter detectors such as LUX or XENON, the directional information is lost due to Rayleigh scattering. In these detectors, the Rayleigh scattering length is of the order of a few dozen of centimetres and does not exceed

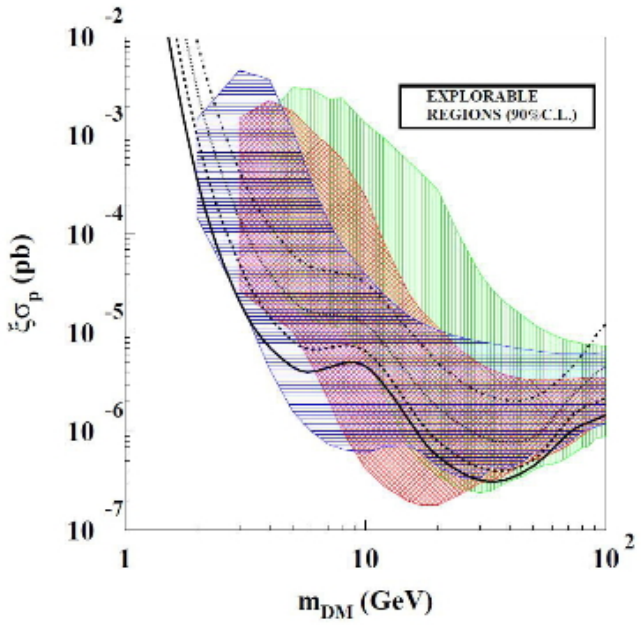

Figure 2.11: Projected exclusion curve of the ADAMO detector with a 2keV_{ee}threshold (solid black) compared to the DAMA-allowed regions (colored). The green region neglects the channeling effect in the crystal, this is included in the blue region. The red region neglects channeling but includes energy dependent quenching factors for Na and I. From [157].

one metre [164, 165]. This means that a detected photon will have scattered several time before reaching the PMTs. For this reason, noble liquid detectors are unsuitable to look for a directional signature of dark matter recoils.

The directional capabilities of high-pressure noble gases TPCs have been studied, notably by the NEXT collaboration [166, 167]. NEXT-100 is a TPC filled with 100 kg of enriched ^{136}Xe in order to search for neutrinoless double-β decays. It is not yet entirely certain that in a similar configuration, nuclear recoils would retain enough directional sensitivity. Moreover, low mass WIMPs may not produce xenon recoils with sufficient energy to be detected, or at least for any directional information to be extrapolated [166]. Simulations have shown that most of the directional sensitivity comes from the reconstruction of the direction of the tracks

through the head-tail effect [168]. However, columnar recombination has also been proposed in order to extract directional information in a high pressure noble gas TPC if the detector is properly aligned [169]. Columnar recombination happens when the ionisation tracks are parallel to the electric field. In this case, electrons and ions drift in a column which enhances the probability of recombination of the signal. In this case, the ionisation signal is reduced compared to the primary scintillation pulse. Axial information may be extracted from the sum and the ratio of both signals [169, 170].

In conclusion, new directional dark matter detectors may be developed from the high- pressure noble gases experiments currently searching for neutrinoless double-β decays. While the choice of target material will influence the sensitivity of the detector to different WIMP masses, simulations have shown that a noble gas TPC with axial sensitivity could demonstrate the anisotropy of the dark matter signal with as few as $10 - 20$ events [170]. This result is comparable with the conclusions of similar simulations done in [171] for low pressure directional TPCs. This result makes high pressure noble gases TPCs with axial sensitivity a potentially viable option to detect a galactic signature of the dark matter signal.

2.4.2.3 Nuclear Emulsion

Nuclear emulsion has been used in particle physics for a long time. In particular, nuclear emulsion was used in the discovery of pions [172]. The OPERA experiment [173] is a fixed target neutrino experiment searching for neutrino oscillations. The collaboration has developed a detector with a $0.3\,\mu$m 3D resolution composed of crystalline silver bromide (AgBr) in a gel matrix. This technology has been adapted for dark matter searches [174] by surrounding the silver bromine by a neutron shielding. The detector has no time information since the data is analysed by cutting the gel into thin slices after exposure. These slices are then studied with an electron microscope. To palliate to this issue, the detector is mounted on an equatorial telescope oriented in the direction of Cygnus.

When a particle crosses the emulsion plate, it ionises the medium along its path. These ionised regions act as crystallisation centres and Ag atoms align along the tracks as shown in Fig. 2.12. WIMP-induced nuclear recoils are expected to produce recoil tracks of less than 1 μm length [175]. This resolution is not sufficient for directional dark matter search. This is currently the main issue in dark matter searches using nuclear emulsion techniques. For this effect, finer grained silver halide crystal have developed with a 40 nm resolution [176], while more techniques are expected to go as low as 20 nm [177].

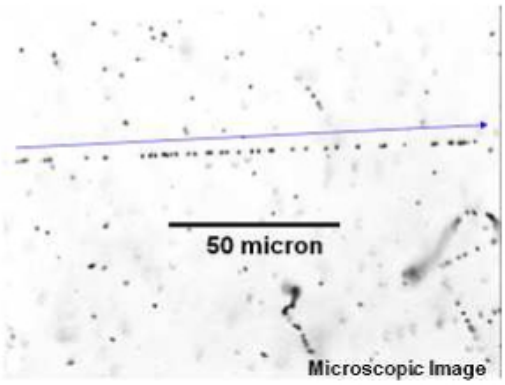

Figure 2.12: A charged particle track in nuclear emulsion. From [173].

The NEWS collaboration is developing a dark matter detection experiment based on nuclear emulsion [178]. Based at the Gran Sasso underground laboratory (LNGS), the proposed 1 kg detector would be mounted with its external shielding on an equatorial mount orientated towards Cygnus. Assuming zero backgrounds, the detector is expected to exclude most of the DAMA allowed region in one year of exposure depending on the resolution obtainable. The detector is limited to 1 kg of target mass due to its internal neutron background. This constraint is currently an important limitation for nuclear emulsion experiments. Separate γ-spectroscopy of the AgBr crystal and the gelatin matrix has shown that the level of purity which can be obtained during the manufacturing process are poor [179]. This is added to the fact that nuclear emulsion experiments only have axial sensitivity rather than head-tail.

The matrix is the primary contributor to the uranium and thorium background, but the AgBr crystal represents 25% of the contamination levels. Simulations of fast neutrons with SOURCES [179] have shown that the expected neutron rate is 1.2 ± 0.4 kg^{-1}year^{-1}. Unless future nuclear emulsion experiments can achieve higher purity levels, the size of these detectors will be limited at the kilogram scale and may be unable to compete will other directional technologies.

2.5 Conclusion

In this chapter, it has been shown how the dark matter recoil rate can be rewritten in order to show its dependence on galactic variables explicitly. In this way, it is possible to design and operate experiments which use annual modulation an directionality as a way to prove the dark matter origin of a potential signal. The DAMA controversy has shown that annual modulation may be not sufficient to provide by itself a definitive proof of the detection of dark matter. Several experiments such as SABRE are using the properties of a galactic signal to investigate the DAMA signal using NaI(Tl) crystals. In this situation, directional detectors may be the best hope to provide an irrefutable galactic signature. However, there is no doubt that both approaches can be improved. In the case of annual modulation, a better understanding of the background signals and sources may allow other NaI experiments to refute or confirm the DAMA signal. Thorough background studies are being undertaken by the DM-Ice and COSINE experiments as described in the next chapter. For directional detection, promising research is underway to develop an array of directional technologies. However, it was shown that the current background levels, for neutrons in particular, are one of the main limiting factors to the development and operation of successful large scale directional detectors. In the case of gaseous TPCs in particular, a collaborative approach may be required. The DRIFT experiment has demonstrated its successful handling of its intrinsic background, but its use of directional information is limited. Few detectors are taking full advantage

of their directional capabilities in a way like NEWAGE does, partially due to the high neutron output of its readout materials. Next generation directional detectors such as the CYGNUS project should aim to combine both approaches in order to create a reliable detector capable to reach the current limits of the large liquid xenon detectors.

3 Background Simulations in Annual Modulation Experiments

This chapter discusses the first method used by direct detection experiments to extrapolate a galactic signal. The annual modulation of the dark matter signal can provide experiments with the potential to differentiate between the galactic signal induced by the WIMP wind and the Earth-based background. This is why a complementary group of NaI experiments has been created and many of them are going through a period of upgrades. One example is the DM-Ice series of detectors which are the subject of this chapter. In particular, the problem of the backgrounds of these experiments is addressed, with an emphasis on the neutron background. This chapter presents the results of background simulations for the DM-Ice37 and COSINE-100 experiments.

3.1 DM-Ice17

The DM-Ice series of detectors is composed of NaI(Tl) dark matter detectors designed to observe the annual modulation of the WIMP signal. DM-Ice17 is the only operational direct detection experiment currently deployed in the Southern hemisphere. The SABRE collaboration is expected to deploy a copy of its northern hemisphere detector to the Stawell underground laboratory in Australia currently in construction. As described in sec. 2.4.1.1, the modulation of background levels is

expected to be out of phase between the northern and southern hemispheres while the modulation of the WIMP signal should remain unchanged. This principle is illustrated in Fig. 3.1 with the example of the variation of the muon rate caused by the seasonal change in the mean density of the atmosphere (see sec. 3.4). In this figure, the muon flux in shown to peak in the summer in both hemisphere, which corresponds to a maximum in July in the northern hemisphere as measured by Borexino [142], and a maximum in January in the southern hemisphere as measured by IceCube [180]. The DAMA signal presented in sec. 2.4.1.1 reaches its peak in June in agreement with a theoretical WIMP signal. The small phase difference can easily be masked by statistical fluctuations or imprecisions in the fitting process. A reproduction of the DAMA signal in the southern hemisphere could constitute an unambiguous proof of the galactic origin of the signal.

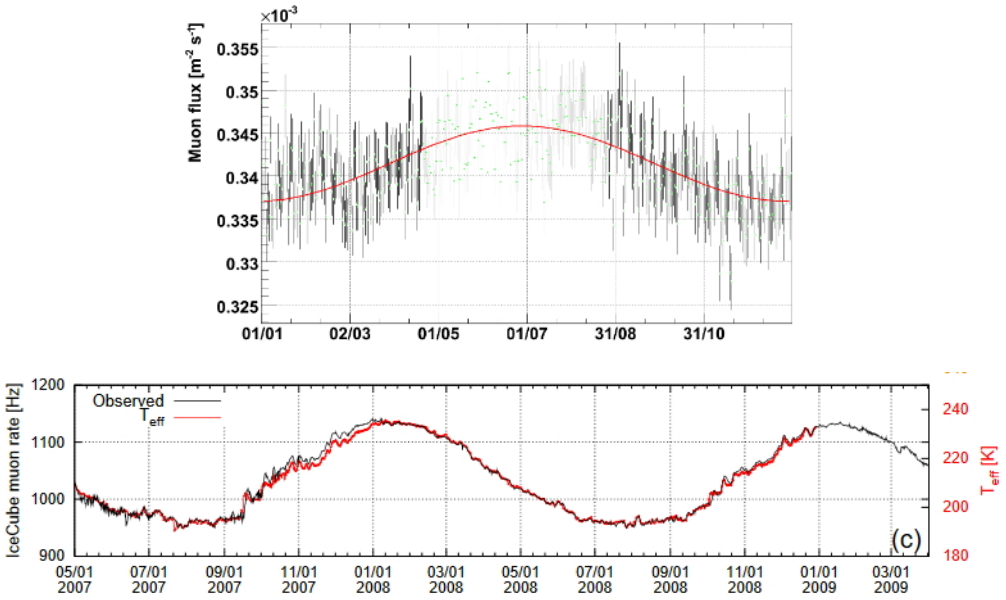

Figure 3.1: Top: Muon rate in the northern hemisphere as measured by Borexino [142]. Bottom: Muon rate in the southern hemisphere measured in IceCube [180].

DM-Ice17 is the first phase of the DM-Ice experiment, operating continuously since its deployment in December 2010. It is composed of two 8.47 kg NaI(Tl) crystals originally used by the NaIAD [181] experiment. The crystals are wrapped in

polytetrafluoroethylene (PTFE) to limit the loss of light, and enclosed in copper encapsulators. Quartz windows and photo-multiplier tubes (PMTs) are placed on either end of both crystals. The setup shown in Fig. 3.2 is enclosed into a copper-lined stainless steel pressure vessel for protection. The steel cases were lowered into two drilled shafts of the IceCube array. The surrounding ice acts as a shield to protect the experiment by blocking background radiations. Geological surveys [182] have shown that the ice surrounding the DM-Ice crystals, 2450 m under the surface is 90000 to 100000 years old. The background levels of the Antarctic ice are extremely small [183] ($\sim$ 1 ppt ^{40}K contamination and $\sim 10^{-2}$ ppt for ^{238}U and ^{232}Th). These background levels are much lower than what can be achieved in the different underground laboratories. The radioactive contamination in Boulby, for example, is around 6 orders of magnitude greater. Furthermore, DM-Ice can take advantage of the efficient muon tagging by IceCube DeepCore [184] to reject these events. However, the two main limitations of DM-Ice17 are its small crystal mass and the high background rate of its crystal which is at least a factor 10 higher than the current purity levels achievable in NaI(Tl) [183, 185]. Nonetheless, DM-Ice17 has produced the first dark matter exclusion limit in the Southern hemisphere [145].

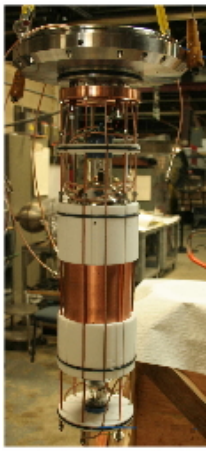

Figure 3.2: Open view of the DM-Ice17 pressure vessels.

3.2 DM-Ice37

After the successful deployment and continuous operation of the DM-Ice17 prototype at the South Pole, progress is being made towards the development of a full-scale 250 kg detector which is expected to be deployed at the South Pole conjointly with the installation of the PINGU experiment [186]. PINGU is a proposed extension and refitting of IceCube to create a larger neutrino detector with better sensitivity. This arrangement would continue to provide DM-Ice with complementary data in order to improve its muon veto. DM-Ice37 is a transitional state of the detector as part of a collaborative effort with the crystal growing company Alpha Spectra to develop and test new NaI(Tl) crystals with background levels similar to those reported by DAMA ($\sim$ 1 event/kg/keV/day in the region of interest). DM-Ice37 is not expected to be deployed at the South Pole. DM-Ice37 is made of two copper-wrapped crystals (labelled AS1 and AS2) with a mass of 18.3 kg each. Following a previous test at Fermilab from April to November 2014, the detector was installed at the Boulby underground laboratory in November 2014 and started taking data on December 10^{th}. Boulby offers a significant reduction in the muon flux thanks to its 1070 m of rock overburden, corresponding to 2850 m.w.e. [187].

A photography of the detector is shown in Fig. 3.3. A representation of the DM-Ice37 setup, simulated using Geant4, is shown in Fig. 3.4. The detector is placed inside a copper-lined lead castle (green) flushed with nitrogen. In the centre, the two NaI(Tl) crystals can be seen in their copper capsule (orange), while on both sides of each crystal a PMT has been modelled. The figure shows the detector setup after its January 2015 upgrade when the quartz light guides were removed and the previously used Hamamatsu R877 PMTs [188] were replaced by the Hamamatsu R12669 model [189] which has a lower background level. These upgrades significantly reduced the overall noise as seen in Fig. 3.5, even below the levels of DM-Ice17 in ice. In particular, trigger rates in crystal AS1 fell from 3.04 ± 0.01 Hz to 2.37 ± 0.01 Hz and from 2.27 ± 0.01 Hz to 2.17 ± 0.01 Hz in crystal AS2.

Figure 3.3: DM-Ice37 in its copper castle at Boulby. Photo courtesy of W. Pettus.

3.2.1 Background simulations for DM-Ice37

This section presents the background simulations of the DM-Ice37 detector. DM-Ice17 was limited by its size and its internal background, especially from the PMTs. The purpose of these simulations is to show that the DM-Ice37 detector has been able to reduce its background and that the main contributions are well understood. The reduction of the overall background is a s key aspect towards the development of large NaI (Tl) experiments capable to verify the annual modulation claims of DAMA.

The simulations of the DM-Ice37 detector were performed using the Geant4 package [190] and the ROOT analysis framework [191]. Geant4 is an object-oriented toolkit, written in C++, used to simulate the interaction of particles through matter. The object-oriented nature of Geant4 allows for the addition of specific models into the simulation. The group of these models, called physics list, is composed of particular libraries which contain the required data, cross-sections or branching ratio to reproduce the necessary physical processes faithfully. The DM-Ice37 simulation was carried on Geant4 version 9.6-p03 using a custom made analysis and the

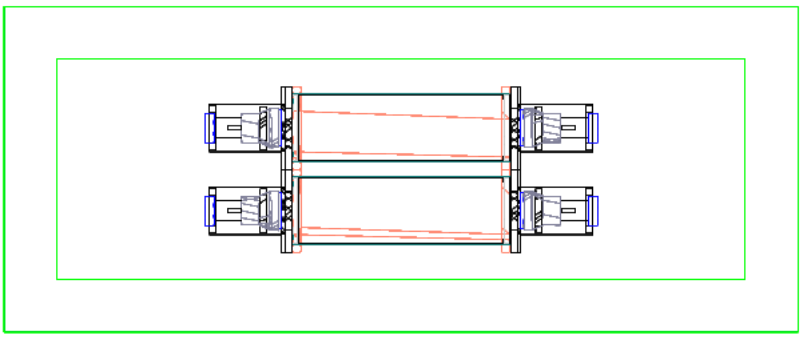

Figure 3.4: Simulated representation using Geant4 of the DM-Ice37 experiment at Boulby.

FTFP_BERT physics list [192] which is designed for the simulation of particles with energies below 10 GeV. Furthermore, the simulation also included the G4Shielding libraries which are designed to simulate absorption and ion-ion collisions and are widely used in the simulation of underground and rare events searches. The low energy libraries for Rayleigh and Compton scattering were added, as well as the photoelectric effect, gamma ray conversion and the emission of Auger electron. The libraries also include ionisation, Bremsstrahlung, pair production, scattering (including multiple scattering) for electrons, positrons, and muons, as well as muon capture. Libraries related to radioactive decays of unstable nuclei were extensively used to simulate the decay chain of the radioactive isotopes present in the detector.

Geant4 requires the input of a Detector Construction class in which the user draws the different volumes which form the experiment and assigns a material to these volumes. For the DM-Ice37 simulation, it was assumed that the external gamma background produced outside of the lead shield is negligible, so a complete simulation of the Boulby underground laboratory was not required. The principal volume is made of salt rock, modeled as NaCl with density 2.17 kg m^{-3}. The DM-Ice lead shield is placed inside this volume allowing for 1 m for air. Backgrounds originating outside of lead shield were not considered in the simulation, but the experimental setup was faithfully reproduced using the technical drawings made during the

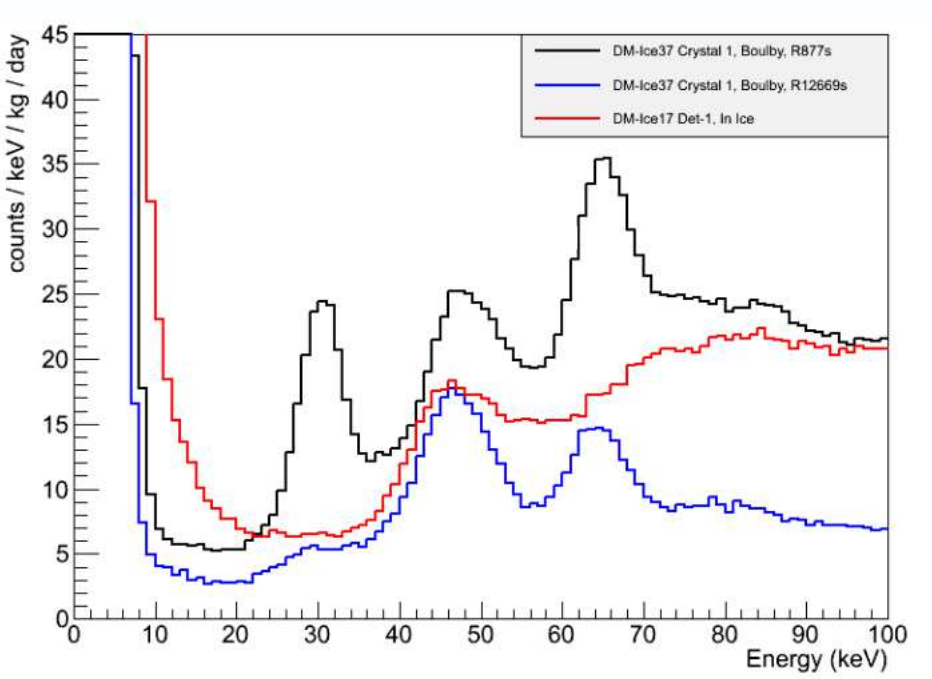

Figure 3.5: Background levels in the low energy region for DM-Ice17 (red), DM-Ice37 before (black) and after (blue) the January 2015 update.

commission of the detector.

Background levels for identical PMTs and the crystals issued from the same powder had already been measured and published by the KIMS collaboration [185] and are shown in Tab. 3.1. These values were used in the Geant4 simulation of DM-Ice37 in order to calculate the Monte-Carlo live-time. For each volume and each isotope, the number of radioactive decays to be simulated was calculated such that it represents one year of operation of DM-Ice37. In the case where Tab. 3.1 reports upper-limits on the activity of a particular isotope, the maximum value was simulated assuming secular equilibrium. When the chain was explicitly broken, for example for ^{226}Ra which is part of the ^{238}U chain, the required additional amount of ^{226}Ra was added to the simulation. To populate the materials with radionuclides, the Geant4 primary particles generator called "G4GeneralParticleSource" (or GPS) was used. GPS enables the user to populate a volume homogeneously in order to simultaneously model bulk and surfaces background. If the volume of interest has a complex shape (such

as a PMT for example), the user can draw a simple volume (a cube for example) around the region of interest. GPS will automatically sample up to 100000 randomly chosen coordinates inside the user-drawn volume until it finds the region of interest. Furthermore, a list of known radioactive decays and their branching ratios are listed in a Geant4 library called "G4RadioactiveDecay" which can be linked to GPS. In this way, the user can input the mass number A and the atomic number Z of a particular radio-nucleus, and Geant4 will automatically and homogeneously distribute the radio-nuclei throughout the volume of interest and simulate its whole decay chain with the correct branching ratio.

Element	Radioactivity (mBq/PMT)
U (^{214}Bi)	25 ± 5
Th (^{228}Ac)	12 ± 5
K (^{40}K)	58 ± 5
^{226}Ra	60 ± 10
^{208}Tl	4 ± 1

Radionuclei	NaI-001 (mBq/kg)	NaI-002 (mBq/kg)
U (^{214}Bi)	< 0.0003	< 0.0015
^{228}Th (^{216}Po)	< 0.013	0.002 ± 0.001
^{40}K	1.25 ± 0.09	1.49 ± 0.07
^{210}Pb	3.28 ± 0.01	1.76 ± 0.01
Total alphas	3.29 ± 0.01	1.77 ± 0.01

Table 3.1: Background levels for the Hamamatsu R12669 (top) and Alpha Spectra crystals (bottom) as measured in [185]

Similarly to DM-Ice17, the energy resolution function of each crystal was measured using the width of internal contamination peaks. These functions were measured during a previous deployment of the detector at Fermilab [193]. For both crystals,

two energy resolution functions were calculated, one for the low energy region (up to 100 keV), the second one for energies above 100 keV. At low energy, the resolution function is based on the width of the ^{210}Pb peak. For energies above 100 keV, the resolution function is based on the width of the fitted Gaussian peaks over a linear background such that

$$\frac{\sigma}{E} = \sqrt{\frac{a}{E} + b}, \tag{3.1}$$

where a is the width of the Gaussian distribution and b is the value of the linear background. In order to recreate the energy smearing in the simulation, the Monte-Carlo true energy E_{MC} is modified such that

$$E = E_{\mathrm{MC}} + E_{\mathrm{MC}} \times \left(\frac{\sigma}{E}\right) \times R, \tag{3.2}$$

where R is a random number chosen from a Gaussian distribution with mean 0 and variance 1. In the low energy case, $\sigma/E \approx 0.096$ keV for both crystals. In the high energy case, the parameters a and b are given in Tab. 3.2.

Crystal	a	b
AS1	0.6404	-4.351×10^{-5}
AS2	0.5363	-2.81×10^{-5}

Table 3.2: Parameters a and b from the energy resolution of the DM-Ice37 crystals. From [193].

Fig. 3.7 and Fig. 3.6 show a comparison between the Monte-Carlo results and the experimental data. At high energy, there is some agreement between the data and the simulation, with the exception of the missing ^{208}Tl peak from the ^{232}Th chain above 2500 keV. At low energy, however, the 3 keV peak of ^{40}K is broader in the simulation than in the data. The constant resolution function at low energy, which was determined using ^{210}Pb, may not be fully adapted below 10 keV. The divergence from the $1/\sqrt{E}$ term of the high energy resolution function would result in a sharper,

less spread peak. Furthermore, the resolution function of the crystals were determined at Fermilab before the crystals were shipped to Boulby. Levels of ^{210}Pb had been reported to vary during the Fermilab run due to ^{222}Rn decays. Since ^{210}Pb has a half-life of 22.3 years, it is possible that the simulation underestimates the amounts of ^{210}Pb because the contamination of the crystals at Fermilab has not yet completely decayed. Furthermore, above 60 keV, the discrepancies are due to ^{125}I and ^{212}Pb from the thorium chain [183]. No measurements for the KIMS crystals originating from the same powder were published in [185] for several radio-nuclei, including ^{125}I. This results in a missing peak at 65.3 keV. The experimental data, however, shows no evident sign of the contribution of nuclear de-excitation in ^{125}I at 37.7 keV where the Monte-Carlo already overestimates the background levels. No measurements were done by the KIMS group for the X-ray emission of ^{121m}Te visible in the experimental data at 26 keV or for ^{212}Pb. Unfortunately, the short lifespan of DM-Ice37 at Boulby means that the detector was dismantled before these issues could be resolved. The two crystals were shipped Spring 2016 to the YangYang Underground Laboratory in South Korea to form part of the COSINE-100 experiment.

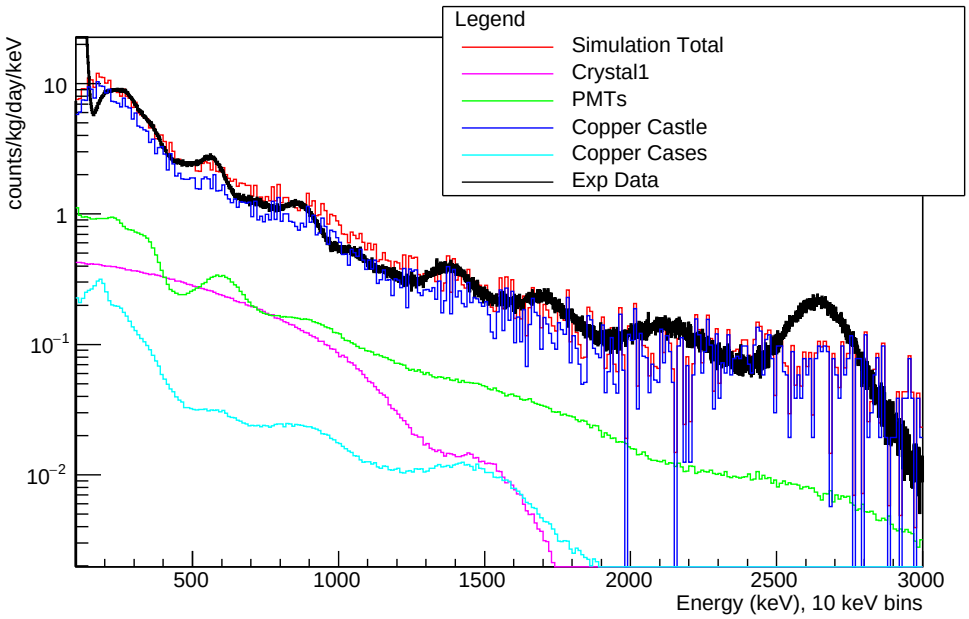

Figure 3.6: Comparison between data and simulation in the high energy region for DM-Ice37.

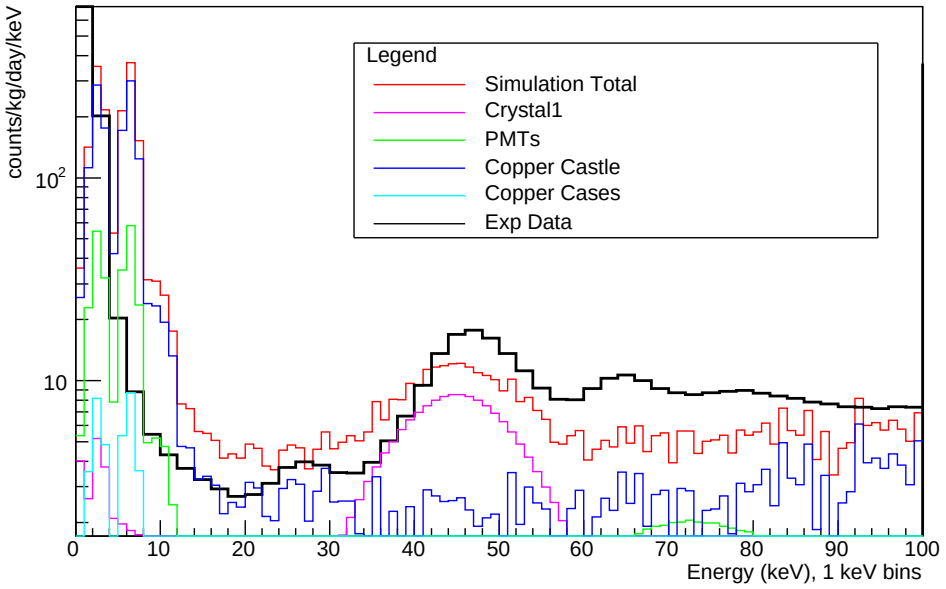

Figure 3.7: Comparison between data and simulation in the low energy region for DM-Ice37.

3.3 COSINE-100

The COSINE-100 experiment is a collaborative effort between the KIMS [159] and DM-Ice [145] groups to operate a large scale NaI(Tl) detector and develop methods to grow ultra-low background NaI(Tl) crystals with purity comparable to DAMA. In 2016, both experiments delivered around 50 kg of crystals each. The resulting total crystal mass of 106 kg has been installed at the YangYang underground laboratory in Korea as shown in Fig. 3.8. The detector is kept in a controlled clean air environment to limit the amount of dust and radon around the experiment. In particular, the ventilation system reduced the large amount of radon in the air (1.20 ± 0.29 pCi/L ≈ 33 Bq/m) by a factor 100. The crystal detector is submerged in a scintillating liquid used to veto external particles. This liquid has a high heat capacity which shields the crystals and PMTs from significant fluctuations in thermal noise. The principal components of the detector shielding are outlined in Fig. 3.9. COSINE-100 has inherited a similar shielding structure as KIMS [139]. On the outside, plastic scintillator panels linked to PMTs and placed on each side of the detector are used for muon tagging. The muon panels were tested on the surface previously to being deployed underground. The surface tests have shown a detection efficiency of 99.95% with the remaining 0.05% being due to misalignment of the PMTs. Going inwards, two steel frames encircle the high 99.99% purity Pb shield used to stop the external gamma background. The copper box serves as a second moderator for gammas and X-rays. Its inner surfaces are covered with a reflective foil and are lined with an acrylic frame which supports a volume filled with liquid scintillator. Facing Hamamatsu R877 PMTs are placed on two opposite sides of the detector and are used to collect scintillation light generated in the veto. The liquid scintillator is mostly composed of Linear Alkyl-Benzene. This organic liquid is also being used by the SNO+ collaboration for its low background and good scintillation properties. Diphenyloxazole and p-bis-(o-methyl-styryl)-benzene are mixed to act as wavelength shifters to increase the veto detection efficiency. Finally, the crystals

are hermetically encased in a case made of an oxygen free copper alloy. Quartz windows are placed on each end of the crystals facing an Hamamatsu R12669SEL PMT also enclosed in their protective copper casing. The crystals and their PMTs are put on a high-purity acrylic table submerged in liquid scintillator as shown in Fig. 3.8 before the detector was closed.

Figure 3.8: The COSINE-100 crystals inside the detector.

3.3.1 Pulse shape discrimination in COSINE-100

COSINE-100 aims to detect WIMP-nucleus scatterings in the NaI (Tl). However, the crystals responds differently to nuclear recoils than to gamma or electron interactions. The KIMS collaboration has used these properties in order to develop a pulse shape discrimination analysis so as to distinguish between nuclear and electron recoils [194]. Several groups, including KIMS, had previously developed similar techniques for CsI(Tl) [195]. Previous attempt to implement this analysis on NaI(Tl) had been less successful [194] since the obtainable light yield was less than what could be achieved with CsI(Tl). Furthermore, in the case of [196] for example, the analysis was hindered by many background events, in particular surface alphas due to radon decays. This sections presents the technique used by the COSINE-100 col-

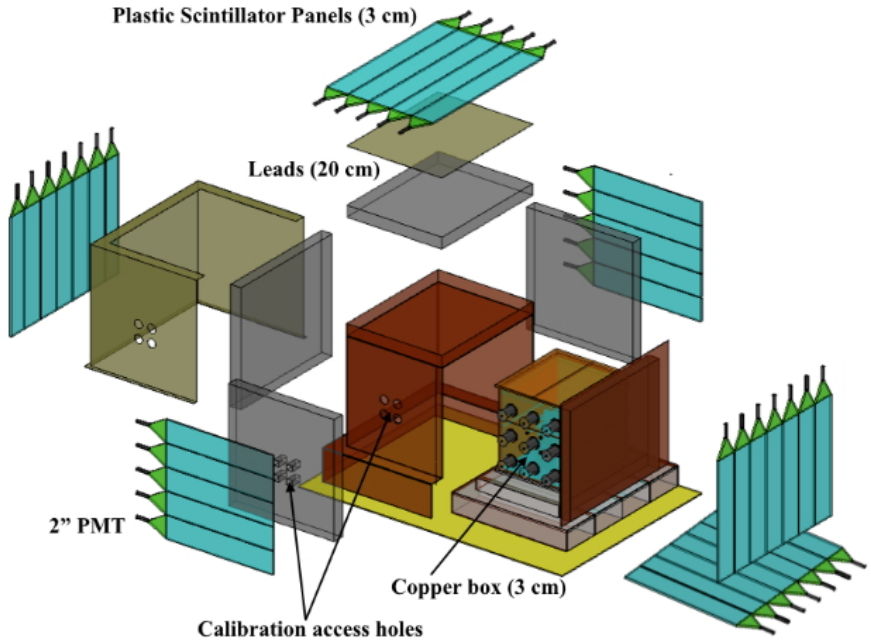

Figure 3.9: Schematics of the COSINE-100 Shield.

laboration to separate nuclear from electron recoils in the crystals, and shows how this technique can be used to reduce the background levels in the detector.

The KIMS collaboration performed its neutron-nuclei elastic scattering measurements using and 300 mCi Am and a Be source of the same strength surrounded by liquid scintillator (of the same composition as described for COSINE-100). A smaller NaI(Tl) crystal issued from the same ingot as some of the COSINE-100 crystals are used to detect events in coincidence. The ^{241}Am source provides an energy calibration with its 59.54 keV gamma ray. ^{9}Be, on the other hand, is a neutron emitter. When struck by an initial neutron, ^{9}Be undergoes a (n,2n) reaction. ^{9}Be can also produce neutrons through (α,n) reactions. The two processes summarised in equation 3.3 can produce an avalanche of neutrons.

$$ {}^{9}_{4}\mathrm{Be} + \mathrm{n} \rightarrow 2\alpha + \mathrm{n} \quad ; \quad {}^{9}_{4}\mathrm{Be} + \alpha \rightarrow {}^{12}_{6}\mathrm{C} + \mathrm{n} \tag{3.3} $$

The pulse shape discrimination described in [194] is based on three different cuts.

A preliminary cut consists in rejecting events that deposit energy in several crystals. WIMPs are weakly interacting particles, so they are not expected to interact in more than one crystals.

1. In order to remove the occasional dark noise events above the 1keV threshold, a cut is placed on the number of photoelectrons per single PMT. If less than two photoelectrons are recorded, the event is rejected.

2. To reject PMT noise, the DAMA collaboration [197] developed a series of parameters based on the time duration of the pulse. PMT noise usually gives rise to short pulse, where crystal events tend to last longer due to the decay time of scintillations in NaI. DAMA defines the slow charge ratio parameter X_1 and fast charge ratio X_2 as

$$X_1 = \frac{Q_{100\to600\text{ns}}}{Q_{0\to600\text{ns}}} \quad ; \quad X_2 = \frac{Q_{0\to50\text{ns}}}{Q_{0\to600\text{ns}}}, \tag{3.4}$$

where Q is the charge deposited during the specified time range. Scintillation events are expected to have $X_1 > X_2$, while PMT noise have $X_1 < X_2$. The DAMA selection cut consists of choosing WIMP like events by requiring large values of $X_1 - X_2$.

3. An asymmetric distribution of charge between two facing PMTs can be an indicator of the position of the interaction in the crystal. Noise signals produced in the PMTs will have a large charge asymmetry. This cut can also be used to remove some of the surface background events in the crystals. The asymmetry parameter is defined as

$$\text{Asymmetry} = \frac{Q_1 - Q_2}{Q_1 + Q_2}, \tag{3.5}$$

where $Q_{1,2}$ is the charge collected in each PMT. Using both condition 3 and the prerequisite that energy should not be deposited in several crystals , Fig. 3.10 shows that it is possible to isolate a population of events which satisfies the criteria for WIMP-like events. The populations of events with a small $X_1 - X_2$ corresponds to short pulse events incompatible with nuclear recoils in NaI (Tl). Furthermore the

fact that the asymmetry parameter for these events is approximately ±1 demonstrate that these events are produced at the extremities of the crystals. The conjunction of the two cuts demonstrates that these events are noise from the PMTS. The authors of [194] estimate the efficiency of the cut to be 45% at 3keV and 60% at 6keV . This corresponds to a reduction of the backgrounds levels by approximately a factor 2.

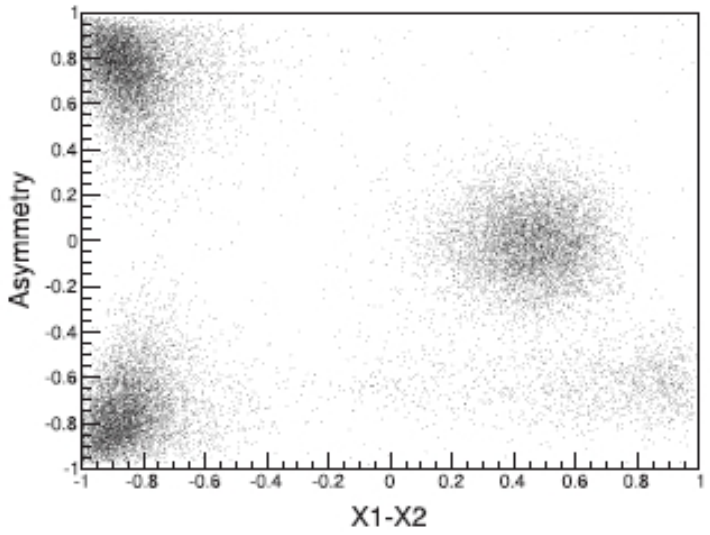

Figure 3.10: Asymmetry parameter versus $X_1 - X_2$ between 4 and 5 keV. From [194].

3.4 Neutron background in COSINE-100

In the previous section, it was shown that the pulse shape analysis developed for the COSINE-100 experiment is able discriminate around half of the non-WIMP-like events. However, the cuts are targeted towards short pulses originating from the PMTs. Neutron background events, on the other hand, cannot be rejected using a similar analysis since neutrons will produce nuclear recoils anywhere in the crystals. However, neutrons can create nuclear recoils similar to WIMPs. This means that COSINE-100 requires an accurate simulation of its neutron background in order to use appropriate shielding when possible or to account for the presence

of neutron-induced nuclear recoils in their results. This section concentrates on fast neutrons. Thermal neutrons can activate materials through neutron capture, but nuclear recoils of thermal neutrons are at the moment below the threshold of NaI (Tl).

There are two main contributions to the fast neutron flux. The first one is from spontaneous fissions or (α,n) reactions of radioactive isotopes present in the materials. The second contribution comes from atmospheric muons. These particles are a significant background source for underground dark matter experiments. They originate from the interaction of cosmic rays in the atmosphere. The cosmic rays, which are primarily protons, will produce hadronic showers comprising pions and kaons, which in term will decay to muons. These muons can propagate through the atmosphere and the rock to trigger the experiment. However, while going through the rock, these high energy muons can induce spallation in the rock (or any other material near to the detector). The resulting neutrons can then undergo scattering in the crystals. Variations of densities in the atmosphere can induce a variation of the muon flux, as measured in other laboratories (for example, in [142] or by DM-Ice17 at the South Pole in [198]). Simulation studies have suggested that this modulation should induce a variation in the flux of muon-induced neutrons [199, 200]. This variation needs to be accounted for when searching for the annual modulation of the dark matter signal. The fast neutron flux from spontaneous fissions and (α,n) reactions has also been postulated to fluctuate. While the activity of radioactive materials is independent of seasonal variation, the authors of [144] suggest that changing levels of humidity in the construction materials of the underground laboratory will affect the moderating properties of the material. This, eventually, would lead to a seasonal modulation of the neutron flux. The Geant4 simulation of the neutron background in the COSINE-100 experiment is presented in the following sections.

3.4.1 Neutron High Precision Models and SOURCES-4C

The simulation of neutrons from (α, n) reactions and spontaneous fission was performed with Geant4 using the same library as the DM-Ice37 simulation. The NeutronHP libraries were used for the simulation of neutrons. This physics model can simulate neutron interactions from the thermal range up to 20 MeV. The NeutronHP model includes the following interactions.

Elastic Scattering- Elastic scattering applies to the collision of a neutron with a nucleus. The nucleus remains in its ground state since it has no excited states with energies below the centre of mass energy. This is the most significant interaction of neutrons in dark matter detector since WIMPs are expected, in most models, to interact in this way with nuclei. Geant4 includes cross-section tables for different nuclei, the approach taken by Geant4 depends on whether the particle simulated is included in the tables of the model [201]. In both cases, the final state of the interaction is obtained by sampling the differential scattering cross-section. If the data is available, Geant4 samples the differential neutron cross-section as a function of the scattering angle and the kinetic energy of the neutron. In the second case, when the data is unavailable, Geant4 represents the normalised cross-section as a series of Legendre polynomials where the Legendre coefficients are tabulated as a function of the energy of the incoming neutron.

Inelastic Scattering- Inelastic scattering is another form of collisions between a neutron and a nucleus. However, this time the nucleus is transferred to an excited state. The final state is composed of the scattering neutron, the recoil nucleus and its daughter particles issued from the nuclear de-excitation. These daughter particles include gamma rays, neutrons, or alpha particles. Geant4 include the possibility that one of several or these particles may be emitted during the decay of the recoiling nucleus. The energy spectrum and angular distribution of the final state particles are handled by the same mechanism as radiative capture described below.

Radiative Capture- Radiative capture is a physics process in which the target

nucleus captures a slow neutron. The daughter nucleus latter returns to its ground state energy via the emission of a photon. While this process is negligible for dark matter detectors given the type of target used, it can be relevant for the simulation of the thermal neutrons flux. Geant4 will take into account the possibility to have several gamma-rays emitted, similarly to the simulation of inelastic scatterings. The energy of the emitted gamma ray depends on the multiplicity of the particles emitted and the discrete energy of each allowed transition. If the data is available, Geant4 will use the full transition probability array. If not, the normalised emission probability is expressed as a weighted sum of the different allowed transitions.

Fission - During a fission, the neutron is captured by a nucleus. The daughter nucleus then decays into two or more fragments. Geant4 can simulate both spontaneous fission and neutron induced fission, but only the latter depends on the NeutronHP libraries. When several channels exist, Geant4 includes up to the four most likely fission channels. As previously, the neutron yield is simulated by two methods. If the libraries include the required data, the neutron energy and angular distribution are tabulated using the model's data. Where there are no data available, the model assumes an isotropic emission in the centre of mass system of the collision. However, the fission libraries are not used in the COSINE (or subsequent neutron) simulation since the neutron energy spectra are produced outside of Geant4.

The production of neutrons through (α, n) reaction is a process for which the cross section is small. This means that it would require a large statistics (which would translate into a large running time) to simulate this process with Geant4. This is the reason why this process is not included in the NeutronHP models. Another program was used to generate the primary neutrons. SOURCES-4C [202] is a computer code written in Fortran which can be used to obtain the fast neutron energy spectrum due to spontaneous fission and (α, n) reaction from the decay of isotopes. SOURCES requires two main inputs. Firstly, the user must enter a list of the radioactive isotopes. For the case of the COSINE simulations, these are the isotopes from the uranium or thorium decay chains which decay through α decays. In the

case of uranium, the natural ratio of ^{238}U to ^{235}U is assumed. For thorium, only ^{232}Th is considered since it represents 99.08% of the natural abundance of thorium [203] and is the only isotope with a particularly long half-life. For each isotope, the user must input a number density (in number of atoms per cm^3). This method allows the user to manually break the equilibrium in the decay chain, however, in all the simulations, secular equilibrium was assumed. If the inputted number density is properly normalised and secular equilibrium is assumed, SOURCES will return the normalised neutron energy spectrum up to 10MeV, as well as the neutron production rate in neutrons/s/g/ppb. The second input required by SOURCES is a list of the different atoms, including their different isotopes, which compose the studied material. Each isotope is matched to its corresponding relative fraction in the material. This is due to the fact that different isotopes of a similar species produce different neutron rates (this is the case between ^{16}O, ^{17}O and ^{18}O for example), or that some isotopes do not undergo (α, n) reaction because their Q value is negative (this is the case for ^{12}C which do not produce neutrons, while its other stable isotope ^{13}C can undergo (α, n)).

3.5 Neutron background simulation in COSINE-100

3.5.1 (α, n) reactions and spontaneous fission

3.5.1.1 Neutrons from the rock

The different components of the COSINE-100 detector described in sec. 3.3 are reproduced in the Geant4 simulation as accurately as possible. The simulated detector, shown in Fig. 3.11 , is placed centrally in a volume of air representing the room in which the detector is placed at YangYang. A volume of rock of varying thickness is placed around the volume of air to represent the cavern rock. The rock is simulated as silica SiO_2 with density 2.7 g/cm^3. Measurements of the concentration of uranium and thorium in the rock at YangYang were performed by the KIMS group in [204].

Concentration of ^{238}U are reported to vary between $1770 - 2820$ ppb, while the concentration of thorium is estimated to be between $11100 - 14500$ ppb. To compensate for these large uncertainties, the simulations were performed separately for ^{238}U and ^{232}Th. Using SOURCES, the neutron production rate was estimated to be 4.787×10^{-11} neutron/s/cm^3/ppb (^{238}U) and 6.040×10^{-12} neutron/s/cm^3/ppb (^{232}Th). The neutron energy spectra for both isotopes are shown in Fig. 3.12 assuming the minimal concentrations $\left(1170 \text{ ppb of } ^{238}\text{U and } 11100 \text{ ppb of } ^{232}\text{Th}\right)$.

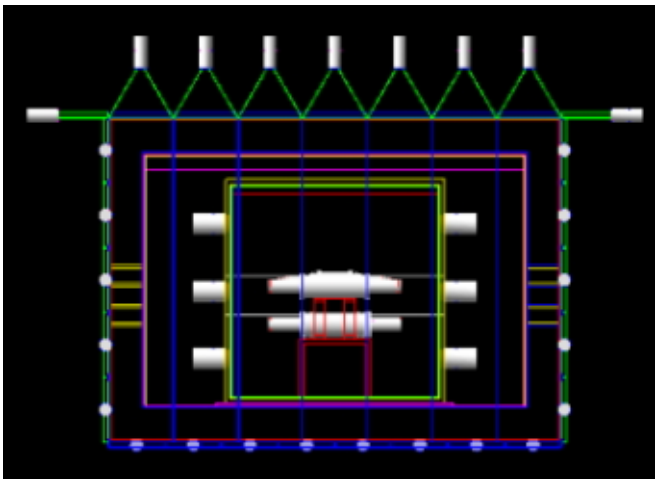

Figure 3.11: Visualisation of the geometry of the COSINE-100 detector in Geant4.

Geant4 imports the neutron energy spectra, the simulation then generates neutrons isotropically and homogeneously within the rock volume. An additional step is required to measure the attenuation of the neutron flux in the rock in order to estimate how much rock should be simulated. This simulation is based on the fact that the ^{238}U spectrum is similar to the ^{232}Th spectrum and it was, therefore, assumed that both neutron fluxes are moderated similarly in the rock. The impact of moderation was simulated by drawing a volume of rock in Geant4 next to a volume of air representing the cavern. Neutrons penetrating into the cavern are recorded and accounted for in the calculation of the neutron flux. Neutrons are produced homogeneously and isotropically in the volume of rock, but the active volume of rock is gradually increased. Fig. 3.13 shows that the neutron flux saturates at about

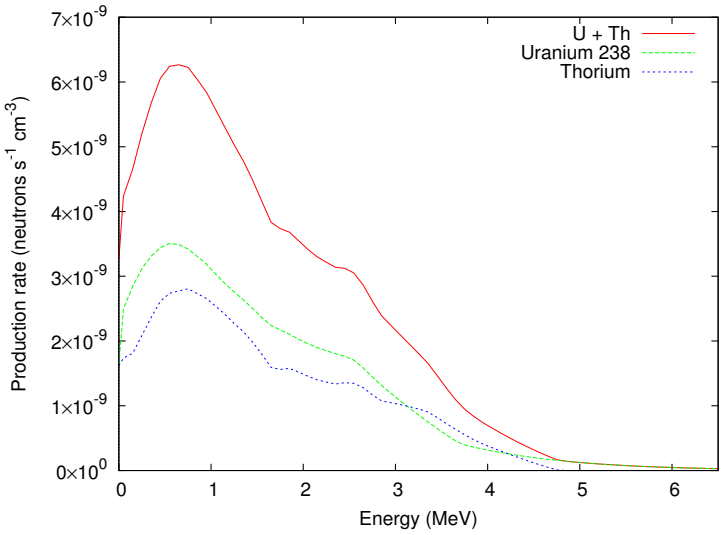

Figure 3.12: Neutron energy spectra in the rock for ^{238}U and ^{232}Th.

1 m depth. This result means that neutrons produced further than 1 m are stopped in the rock and do not contribute to the neutron flux. For the simulation of rock neutrons at YangYang, 1.5 m of rock were simulated on each side of the detector.

In the simulation, each crystal is registered as a sensitive detector, so particles which deposit energy in these volumes are recorded. Energy deposited in the liquid scintillator is also recorded. Geant4 associates a number to each primary particle called the event number. This number was used in order to determinate coincident events. For example, if an event deposits energy in two or more crystals, this event will be rejected from the analysis, the same rejection criteria are applied to the Monte-Carlo data. WIMP-like events (referred to as single events) are nuclear recoils in a single crystal with no energy deposited in the liquid scintillator veto.

3.6×10^9 neutrons were sampled from the ^{238}U neutron spectrum, but only events depositing energy in a single crystal were considered. Using the method of [205], the null result corresponds to an upper limit on the rate single events due to rock neutrons from the ^{238}U decay chain of $< 2.72 \times 10^{-8}$ Hz (90% C.L.) if the minimal concentration of ^{238}U is assumed, corresponding to 1770 ppb. If the maximal concentration is used instead (corresponding to 2820 ppb), the upper limit becomes

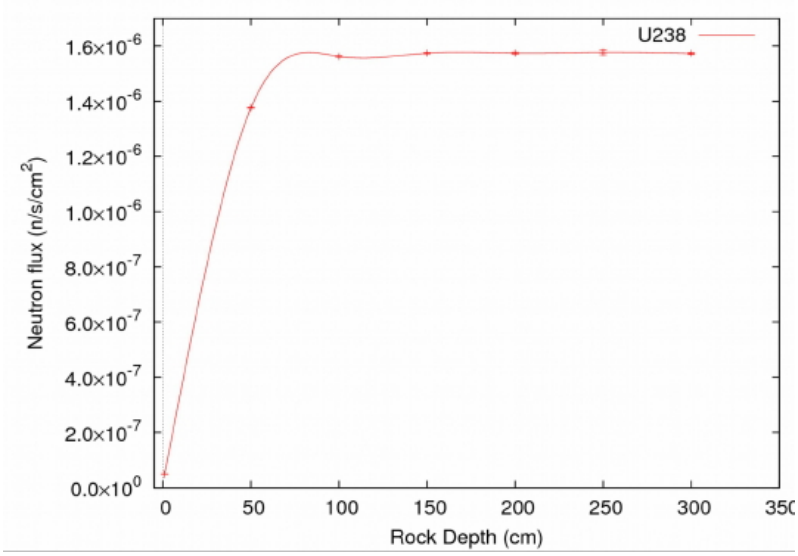

Figure 3.13: ^{238}U rock neutron flux as a function of depth.

$< 4.33 \times 10^{-8}$ Hz (90% C.L.). This corresponds to < 1.4/year (90% C.L.) for the maximal concentration and is below the self-imposed limit of < 3 events/year. This arbitrary limit was created to select backgrounds to which the detector might be sensitive during its exposure.

The neutron production rate for ^{232}Th is smaller than the ^{238}U rate so less neutrons are required in order to obtain similar results. 6.21×10^8 neutrons from the ^{232}Th spectrum were simulated. Similarly, no single events were recorded and the upper limit on the event rate was calculated as $< 1.35 \times 10^{-8}$ Hz (90% C.L.) if the concentration of ^{232}Th is assumed to be 11100 ppb. Instead, if the concentration of ^{232}Th is assumed to be 14500 ppb, the event rate becomes $< 1.77 \times 10^{-8}$ Hz (90% C.L.). At the maximal concentration, this corresponds to < 0.56/ year (90% C.L.) .

Overall, adding the contribution of ^{238}U and ^{232}Th, the total upper-limit of the rate of single events due to neutrons in the rock is between 0.99 event/year and 1.93 event/year. If using the results of [144], it is assumed that of the level of humidity varies by up to 8%, then the modulation of the moderating properties of the rock should be of the same order. A seasonal modulation of the flux of rock neutrons of 8% would not be detected by the COSINE-100 experiment. To accurately

reproduce these estimations, it will be necessary to monitor the parameters in the detector room over several years. For example, the different climates between Italy and Korea may result in different variations of the level of humidity. However, it will also be necessary to take into account the effect of the air conditioning unit which is maintaining the humidity to a roughly constant level. Additional information about the material used in the construction of the detector room will also be required. These were not available at the time of writing.

3.5.1.2 Neutrons from the external shield

The KIMS group performed a background assay in order to estimate the radioactive activities of the material which would constitute the COSINE-100 detector. Tab. 3.3 contains the measured concentration of ^{238}U and ^{232}Th for the shielding materials. For the lead shield, no neutrons are expected to be produced from (α, n) reaction. This is due to the high-Z value of lead (Z=82). The α particle must be able to tunnel through the Coulomb barrier of the nucleus for the reaction to happen. The chances for the reaction to happen decrease as the electric charge of the nucleus inceases. The contribution of the lead shield can therefore be neglected.

For the copper vessel, the neutron production rate calculated with SOURCES was 6.27×10^{-11} neutron/s/cm^3. The neutron energy spectrum is shown in Fig. 3.14. The uranium decay chain produces more neutrons than the thorium decay chain, so at equal concentration, the uranium chain dominates the production of neutrons. The simulation recorded no single events corresponding to an upper limit on the single events rate of $< 3.10 \times 10^{-13}$ Hz (90% C.L.). This is similar to $< 9.78 \times 10^{-6}$/ year (90%C.L.) and corresponds to well below 1 event in the expected duration of the experiment.

Similarly, for the steel parts of the shield, the neutron production rate calculated using SOURCES is 1.787×10^{-10} neutron/s/cm^3. For the outer part of the steel shield (outside of the lead shield), no single events were recorded leading to an upper limit

of $< 1.81 \times 10^{-12}$ Hz (90% C.L.). For the inner part of the steel shield (situated between the lead shield and the copper vessel), no single events were recorded as well giving an upper limit of $< 1.20 \times 10^{-12}$ Hz (90% C.L.). There are two explanations for these null results. Firstly, when the simulation was performed with a full tracking in order to follow the neutrons between volumes, multiple scatterings were observed between the different parts of the shield. This effect, which is naturally more prominent for the outer parts of the shield, results in the moderation of the neutrons, or even to some neutrons leaving the detector due to backscattering. Secondly, the high fraction of hydrogen in the organic compounds of the liquid scintillator resulted in a large fraction of neutrons scattering inside the LS Veto region, hence reducing the number of single events.

Material	Concentration ^{238}U	Concentration ^{232}Th
Copper	0.5ppb	0.5ppb
Steel	1ppb	0.4ppb
LS Veto	7ppt	4ppt

Table 3.3: Concentration of radioactive isotopes in the COSINE-100 shielding materials.

Finally, the simulation neutrons originating inside the liquid scintillator veto region is presented. The high level of purity of the liquid scintillatior gives a small neutron production rate of 6.72×10^{-14} neutron/s/cm^3. As expected, the results shown in Tab. 3.4 are nearly constant for each of the eight crystals.

Overall, the large fraction of hydrogen in the liquid scintillator increases its neutron veto efficiency hence reducing the neutron background from the outer parts of the shield. Thanks to its high purity, the neutron background induced by the liquid scintillator itself remained low, and the summed neutron background from the shielding components remain largely negligible with only ~ 0.1 event/ year on average for each crystal.

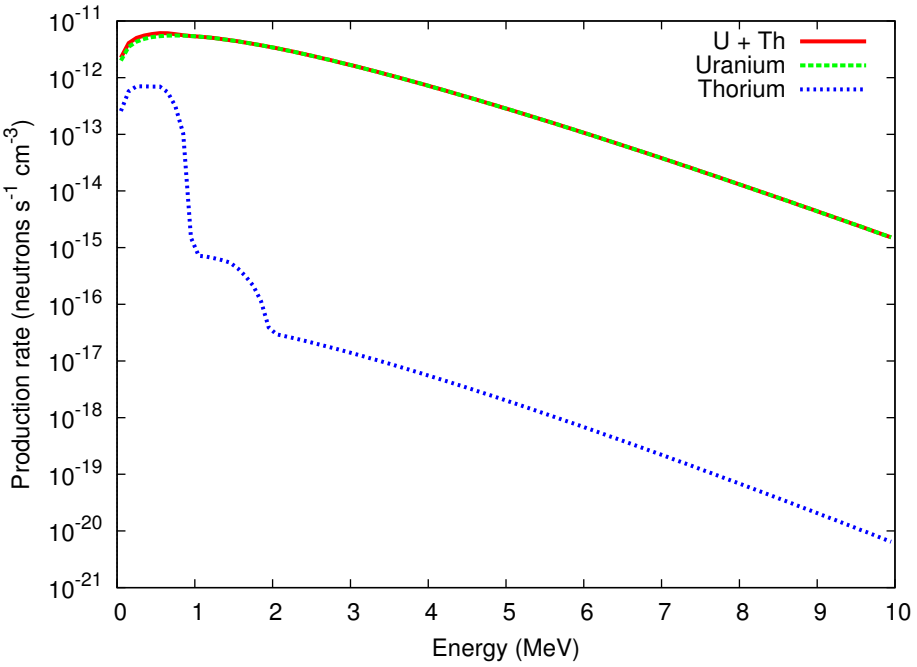

Figure 3.14: Neutron energy spectra from ^{238}U and ^{232}Th in copper.

3.5.1.3 Neutrons from the crystals

The previous section presented the neutron background from the shield and veto components. This section contains the simulation of neutrons from the crystals and copper encapsulation units. The neutron background originating from the PMTs will depend on the activities of the different internal components of the PMT. Furthermore, each material will produce neutrons with a different energy spectrum. The simulation of the neutron background from the PMTs are ongoing based on the information provided by the manufacturer.

The purity levels of the copper in the crystal capsules are similar to that of the copper vessel, so the same neutron production rates were used. Each capsule unit was populated with neutrons separately. Most of the single events in each crystal were due to neutrons originating in this crystal own encapsulation unit, but cross-contamination between neighbouring crystals has been observed, even for single events. These cross-contamination events should be more frequents in the crystals

Volume	Single event rate (counts/kg/day)
Crystal 1	$(5 \pm 1) \times 10^{-9}$
Crystal 2	$(3.5 \pm 0.9) \times 10^{-9}$
Crystal 3	$(4 \pm 1) \times 10^{-9}$
Crystal 4	$(5.0 \pm 0.8) \times 10^{-9}$
Crystal 5	$(3.7 \pm 0.7) \times 10^{-9}$
Crystal 6	$(4.5 \pm 0.9) \times 10^{-9}$
Crystal 7	$(3.4 \pm 0.8) \times 10^{-9}$
Crystal 8	$(3.6 \pm 0.7) \times 10^{-9}$

Table 3.4: Single event rate due to fast neutrons originating from the LS Veto.

which are near the centre of the experiment (Crystals 2 and 3 on the top row, and Crystals 6 and 7 on the bottom row). Nonetheless, these events remain relatively rare since, in most of the cases, energy is also deposited in the liquid scintillator.

Finally, the simulation of fast neutrons originating from the crystals is presented. Most crystals were produced from different manufacturers and from different ingots so background levels differ between crystals. Tab. 3.6 gives a list of the background levels in the different crystals. With SOURCES, the neutron production rates were calculated as 6.57×10^{-10}neutron/s/cm^3/ppb (^{238}U) and 2.97×10^{-10}neutron/s/cm^3/ppb (^{232}Th). The rates of single events in each crystal are summarised in Tab. 3.7.

3.5.1.4 Conclusion for (α, n) and Spontaneous Fission

Using SOURCES and Geant4, the fast neutron background from spontaneous fissions and (α, n) reactions were simulated. It was shown that the liquid scintillator veto is able to reject the external neutron background down to rates below 3 events/ year. Comparatively, its action on the internal neutron background is more limited. For each crystal, the neutron-induced background remains low and

Volume	Single event rate (counts/kg/day)
Crystal 1	$(3.63 \pm 0.04) \times 10^{-7}$
Crystal 2	$(2.91 \pm 0.04) \times 10^{-7}$
Crystal 3	$(3.48 \pm 0.05) \times 10^{-7}$
Crystal 4	$(3.57 \pm 0.04) \times 10^{-7}$
Crystal 5	$(3.66 \pm 0.05) \times 10^{-7}$
Crystal 6	$(4.14 \pm 0.05) \times 10^{-7}$
Crystal 7	$(3.35 \pm 0.04) \times 10^{-7}$
Crystal 8	$(3.86 \pm 0.5) \times 10^{-7}$

Table 3.5: Single event rate due to fast neutrons originating from the Copper encapsulation units.

dominated by the copper encapsulation units, apart from Crystal 5 and 8, for which the NaI powder was of a lower quality. Overall, the neutron induced background in each crystal does not exceed $\sim 10^{-6}$ counts/kg/day for the most radioactive crystals, and remains negligible compared to the current levels of gamma background observed in NaI (Tl) experiments, even with pulse shape discrimination. The neutron backgrounds from spontaneous fission and (α, n) reactions are expected to modulate as a function of ambient temperature and humidity for external sources. For materials inside the detector shield, the neutron rate should remain mostly constant, and the current NaI (Tl) experiments should be blind to these variations given their current sensitivity levels.

3.5.2 Muon-induced Neutrons in COSINE-100

In [206], it is suggested that DAMA could be sensitive to muon-induced neutrons and neutrons produced by the interaction of ^{8}B solar neutrinos in the rock or the surroundings of the detector. The flux of solar neutrinos also varies annually due

Crystal	Concentration ^{238}U	Concentration ^{232}Th
Crystal 1	0.02ppt	3.17ppt
Crystal 2	1.04ppt	0.48ppt
Crystal 3	0.04ppt	0.20ppt
Crystal 4	0.04ppt	0.20ppt
Crystal 5	7.5×10^{-2}ppb	2.5×10^{-1}ppb
Crystal 6	0.018ppt	0.079ppt
Crystal 7	0.018ppt	0.079ppt
Crystal 8	7.5×10^{-2}ppb	2.5×10^{-1}ppb

Table 3.6: ^{238}U and ^{232}Th levels in the COSINE-100 crystals.

to the changing distance between the Earth and the Sun. Atmospheric muons are produced in the atmosphere from the decays of pions produced by the decay of cosmic radiations (primarily protons). Muons have a mean lifetime of 2.2 μs [207], but since atmospheric muons are highly relativistic, time dilation allows these particles to travel up to the Earth surface and to penetrate the crust. The flux of atmospheric muons has been measured in the different underground laboratories, for example in [208] for the YangYang laboratory. The interactions of muons in materials can create a flux of neutrons issued from spallation or interactions with hydrogen atoms [209]. Muon-induced neutrons and radioactive decays are the two natural sources of fast neutrons in underground laboratories. Muon-induced neutrons have been proposed as a solution to the DAMA problem in [206]. This hypothesis is based on the annual modulation of the muon flux measured in Borexino [142] and Icecube [180] shown in Fig. 3.1. However, in [143], the DAMA collaboration showed that the muon flux reaches its maximum roughly a month after the DAMA signal. Furthermore, it is proposed in [210] that DAMA should be sensitive to the long term variations of the muon flux. This analysis was performed in [143] where the DAMA collaboration reports than the proposition of [210] only accounts for less than 2% of the amplitude

Volume	Single event rate (counts/kg/day)
Crystal 1	$(3.9 \pm 0.3) \times 10^{-8}$
Crystal 2	$(2.6 \pm 0.2) \times 10^{-8}$
Crystal 3	$(1.0 \pm 0.3) \times 10^{-8}$
Crystal 4	$(1.0 \pm 0.2) \times 10^{-8}$
Crystal 5	$(5.16 \pm 0.05) \times 10^{-6}$
Crystal 6	$(3.7 \pm 0.2) \times 10^{-7}$
Crystal 7	$(3.7 \pm 0.2) \times 10^{-7}$
Crystal 8	$(5.23 \pm 0.05) \times 10^{-6}$

Table 3.7: Rate of single events nuclear recoils from neutrons in the crystals.

of the DAMA signal.

[206] shows that the sum of the two contributions results in an annual oscillation which is well in phase with the DAMA signal. The author claims that, in particular, neutrinos with energies above > 7.37 MeV can liberate neutrons through spallation in the Pb gamma shield of the detector. Best fits of the model from [206] estimate a near equal contribution between muons and neutrinos. However, simulations of the muon-induced neutron background for DAMA in [200, 199] both agree that muons-induced neutron cannot account for more than 0.3% of the modulation of the DAMA signal.

As another NaI dark matter experiment, the COSINE-100 detector is also potentially subject to detecting the annual modulation of the muon-induced neutron flux. To understand the muon-induced neutron background in COSINE, a simulation of muons at YangYang was done using Geant4. Libraries dedicated to the interaction and transport of muons were added to the Geant4 physics list. In particular, these are G4MuonNuclearProcess which is related to the emission of photons (or π^0 at high energy) which then interact with nuclei. G4VDNuclearModel handles the nuclear scattering of muons, and finally, G4MuonMinusCaptureAtRest which contains

the parameter for the nuclear capture of muons.

The muons are produced on the surface of a hemisphere of 30 m radius in air. The muons which pass through a square area of 20×20 m^2 are recorded. The muon flux at sea level at YangYang is 0.019 cm^2/s [211]. This method allows for a first calculation of the simulated live time. The muons which passed through the active square of 20 m are propagated through 660 m of rock where they are again recorded. The rock overburden at YangYang is 680 m corresponding to 1.8 km.w.e . The last 20 m of rock are simulated in a different code with the detector. This separation is due to the fact that the muon generator is shared between some of the different experiments at YangYang. The remaining muons at 660 m depth are inputted into the Geant4 simulation described in sec. 3.4 where the physics list has been modified to incorporate the necessary muon libraries described above. The last 20 m of rock are simulated together with the detector. A cubic volume of air of 5 m side is placed around the experiment in order to simulate the detector room. The muon flux in the A5 tunnel at YangYang has been measured [211] as $(3.98 \pm 0.09) \times 10^{-7}$ cm^{-2}s^{-1}. This flux can be compared to the number of muons which are recorded when they enter the cavern in order to obtain a second estimation of the Monte-Carlo live time. This technique showed that the simulation corresponds to 597 ± 18 days. Muons reaching the detector are recorded in the muon panels. Every two hours, at the end of each analysis run, the data saved by the detector can be checked against a reference run. In particular, the reference run estimate that on average 245 muons pass through the muon veto during a two-hour run. This number is above the number of muons recorded by the simulation. Muons passing through the plastic scintillator of the muon veto are recorded. The average number of muons observed in the veto is 206 ± 4 muons/run.

The energy spectrum of muons entering the detector room is shown in Fig. 3.15. Neutrons penetrating in the A5 cavern are also recorded, the simulated flux of neutrons above 1 MeV is $(3.1 \pm 0.5) \times 10^{-9}$ neutrons/s/cm^2. This is below the results found in [199] for the A6 cavern (where the KIMS detector is located). However,

it has been measured that A5 and A6 have different muon flux [211]. When this difference is taken into account, we found that both results are in good agreement. The muon-induced neutron energy spectrum is shown in Fig. 3.16.

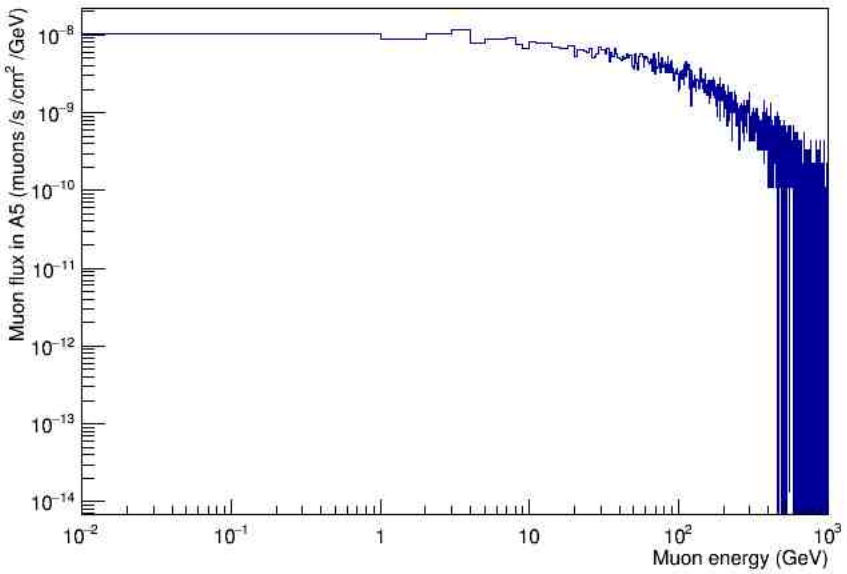

Figure 3.15: Simulated energy spectrum of muons entering the A5 room at YangYang.

A series of cuts are applied to the events registered inside the detector. Firstly, if a particle deposits energy in the crystal but shares the same event number as muon in the veto, this event will be rejected in the analysis. Secondly, muons (or other ionising particles) can be detected in the liquid veto around the crystals. Similarly to the previous neutron simulations, if an event deposits energy in both the liquid scintillator veto and a crystal, this event is rejected. Thirdly, events which deposit energy in two or more crystals can be identified in the analysis as background by using a coincidence analysis. These events are, therefore, also rejected. Finally, due to the pulse shape analysis presented in sec. 3.3.1, only nuclear recoils are selected from the events which have not been rejected by the other selection cuts. It was found that no events could satisfy all these conditions during the simulated 597 ± 18 days. This places an upper-limit on the rate of nuclear recoils in the crystals due to muon-

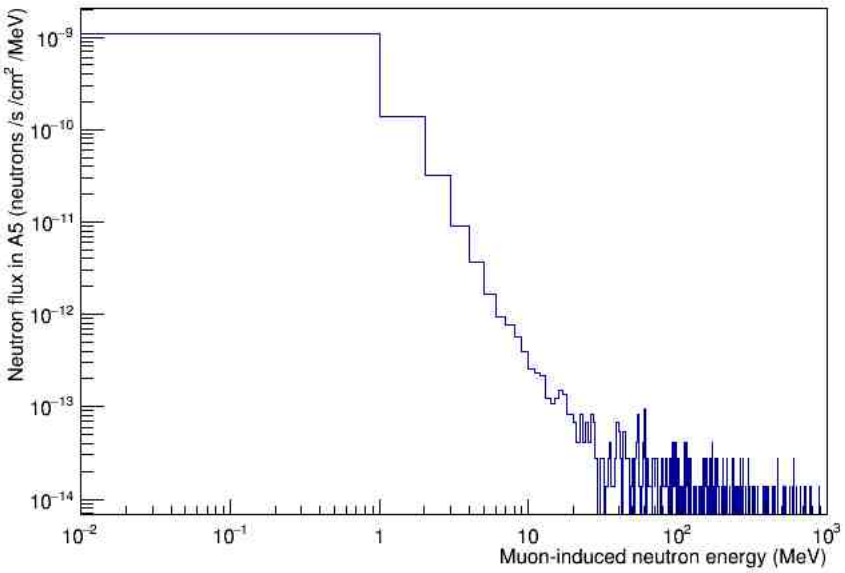

Figure 3.16: Simulated energy spectrum of the muon-induced neutrons entering the A5 room at YangYang.

induced neutrons of $< 4.73 \times 10^{-8}$/s (90% C.L.) or < 1.49/ year (90% C.L.). This result corresponds to 0.5% of the rate of nuclear recoils predicted in DAMA in [199]. It can, therefore, safely be concluded that the muon-induced neutron background will not play a significant role in the search for dark matter with the COSINE-100 experiment.

3.6 Conclusion

DM-Ice17 has demonstrated the feasibility of operating a dark matter detector at the South Pole. This new location offers the possibility to question the galactic origin of the annual modulation signal reported by the DAMA experiment. However, DM-Ice17 is limited by the mass of its crystals and their background levels. Reducing the background levels has been the primary objective of the DM-Ice37 detector, which is the next iteration within the DM-Ice family. In particular, the background tests performed at Boulby with a new set of lower background PMTs

have shown a reduction in the overall background rate. The COSINE collaboration is a joint effort between the KIMS and DM-Ice experiments. COSINE has developed a detector with 106 kg of low background NaI(Tl) crystals. The pulse shape discrimination developed by the KIMS group enables the analysis software to differentiate between electron recoils and nuclear recoils. In this case, it becomes vital to understand the neutron background of the detector since neutrons can produce nuclear recoils and imitate a WIMP signal. Using SOURCES and Geant4, fast neutrons originating from the spontaneous fission and (α, n) reactions from radioisotopes in the uranium and thorium chains were simulated. However, the event rate of nuclear recoils passing all the veto conditions is on the order of $10^{-6} - 10^{-8}$ counts/kg/day (corresponding to < 0.03 events/ year) depending on the radioactivity of the crystals. Finally, the muon-induced neutron background at YangYang was investigated. So far no Monte-Carlo simulation of a NaI dark matter detector has corroborated the claim of [206] that muon-induced neutrons could play an important part in explaining the annual modulation observed by DAMA. The results found in sec. 3.5.2 suggest that COSINE-100 should detect less than 1.5 events/ year. Therefore, it can be concluded that in its current mode of operation, COSINE-100 will not be sensitive to the annual modulation of the muon flux.

4 Improved Detection Efficiency and WIMP search with DRIFT

The previous chapter discussed the issue of the background levels in annual modulation experiments. This chapter focuses on the more powerful technique for galactic signature which is directionality. This technique was pioneered by the DRIFT [146] (Direction Recoils Identification From Tracks) experiment which remains at the moment the most sensitive directional detector. The DRIFT experiment is a UK-US collaboration operating a family of direct directional dark matter detectors, in particular at the Boulby underground laboratory, already described in section 3.2. The DRIFT collaboration has pioneered the development of time-projection chambers (TPCs) for their directional potential and is currently the only directional detector operating at the m^3 scale. In this chapter, the structure of the DRIFT detectors is reviewed, with a particular emphasis on the DRIFT-IId model on which the work described below was performed. This chapter also contains the description of the Geant4 simulation which lead to the calculation of the nuclear recoil detection efficiency of the detector. This efficiency map is used in the analysis of the data presented in this chapter and chapter 5 in order to obtain the true rate of nuclear recoils in the detector. In this chapter, the nuclear recoil efficiency map is used in the analysis of 147.48 live days of unblind dark matter search leading to the current best directional spin-dependent limit on the WIMP-proton cross section from a directional detector.

4.1 DRIFT-IId detector technology

The DRIFT-IId detector shown in Figure 4.1 is composed of back to back negative ion time projection chambers (NITPCs) with a drift length of 50 cm each. The two chambers are enclosed in a vacuum sealed stainless steel vessel. The steel vessel itself is protected by a neutron shield composed of polypropene pellets with a minimum thickness of 67 cm on each side of the detector to reduce the ambient neutron flux. These neutrons are discussed in greater details in section 6.2. The under-floor space below the detector was dug such that an equivalent thickness of shielding was placed on each side of the detector. The 1100 m rock overburden (equivalent to 2800 m.w.e.) of the Boulby Laboratory ensures that the flux of cosmic ray particles is minimised.

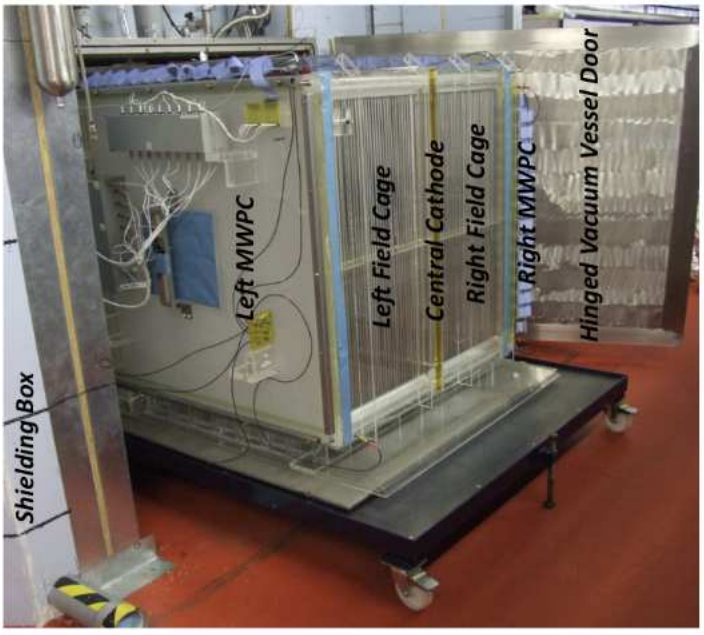

Figure 4.1: The DRIFT-IId detector at Boulby. From[212].

On each side of the detector, two identical multi-wire proportional chambers (MWPCs) are used to read the signal. Each MWPC is composed of three orthogonal planes of steel wires. In the center, the grounded anode plane is composed of 512 vertical

(y-orientated) wires of 20 μm thick stainless steel with a 2 mm spacing. Each anode is located between two grid planes at 2800 V. These planes are also made of 512 stainless steel wires with a 2 mm spacing. However, these wires are 100 μm thick and orientated horizontally in the x-direction [212]. The simultaneous deposition of charge onto anode and grid wires can be used as an indicator of the location of the event in the $(x - y)$ plane. The outermost regions of the MWPCs can, therefore, be used as veto regions to reject a fraction of the external background or surface background induced by radon daughters from the surface of the vessel.

The central cathode separating the two back to tack TPCs can be used as another way to reject Radon Progeny Recoils (RPRs). In some cases, some events can be detected in coincidence between the two back to back TPCs. The cathode has been specifically developed to reduce the rate of this problematic radon background. It is composed of a 0.9 μm thick custom made sheet of aluminised Mylar held at a voltage of -31.9 kV [213]. Microscopic (sub-micron) wrinkles on the surface of the cathode increase the chance of detecting the alpha particles. This technique has shown a 23% increase in detection efficiency [214] compared to the previous flat cathode. An example is shown in Figure 4.2 where the left part of the picture shows the signal read by the anode wires in the left TPC, and the right section of the plot contains the signal read by the anode wires in the right TPC. These events, nicknamed "Gold-Plated Cathode Crosser", are alpha particles detected in both TPCs. The signal is recorded firstly on the left anode where the successive peaks are seen because every 8^{th} wires are linked together into the same reading channel to reduce the required number of digitisers. The first signal is read on the dark blue line for the left anode and moves to the following line with a time increment corresponding the the distance between the anode wires. The signal repeats itself once the particle has travelled a full octave (a group of 8 consecutive wires) and, therefore, deposits energy on two wires linked to the same readout channel. Slightly below 8000 μs, the signal disappears on the left anode but is now read on the right anode. This means that the particle has moved to the other TPC and has, therefore,

crossed the cathode. These events are of particular relevance in DRIFT, the only way for these events to be produced is by alpha decay of radon, so the rate of these events is proportional to the concentration of radon in the detector. These events are regularly counted in order to monitor the quantity of radon in the detector and, if necessary, adjust the rate at which gas is flown in the detector.

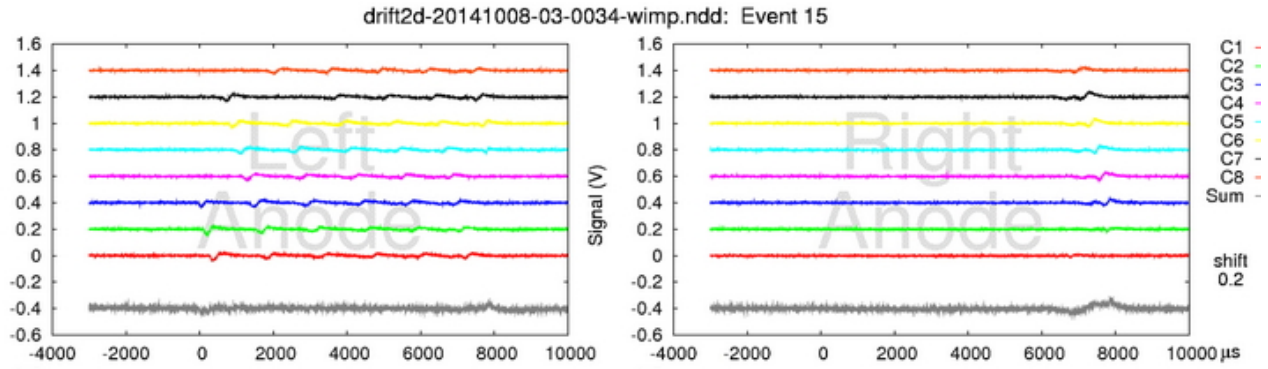

Figure 4.2: Gold-Plated Cathode Crosser event in DRIFT

DRIFT is operated using a dilute mix of $CS_2 - CF_4 - O_2$ following a ratio of 30 : 10 : 1 Torr. Directional TPCs must find a balance between the need to expose more target mass, and the ability to reconstruct mm-scaled tracks for directionality. The ability to reconstruct tracks also depends on the read-out employed. The DMTPC detector, for example, operates at 75 Torr of pure CF_4. In DMTPC, the electron drifts towards the mesh where the avalanche of electron produces photons which are detected by the CCD cameras [215]. Instead, the negative-ion technology used in DRIFT has the advantage of reducing diffusion. The electron is captured by a CS_2 molecule to form a CS_2^- ion. Since both species have the same electric charge, they are both accelerated by the same Lorentz force in the detector's electric field. Graham's law, however, predicts that the thermal diffusion rate scales as $1/\sqrt{M}$, where M is the molar mass of the diffusing species. In the presence of an electric field, the electrons or electronegative ions are accelerated towards the anode. The acceleration is interrupted by the repetitive collisions in the gas, so the molecules do not reach their maximal velocities but instead tend towards an average drift velocity. In the

case of ions, their drift speed is slow compared to their thermal velocities [136]. For electrons, the drift speed can be higher because of their smaller mass due to the $^1/\sqrt{\mathrm{m}}$ dependence of the mean thermal velocity $\mathrm{v} = \sqrt{^{8kT}/_{\pi \mathrm{m}}}$, [136].

The addition of O_2 in the DRIFT gas mixture resulted in the appearance of minority carriers, first observed in [216]. The origin of these new species, shown in Figure 4.3, is still currently under investigation. However, for DRIFT, it is enough to note that the drift velocities of the minority carriers are constant between events and that each minority carrier has a slightly different drift velocity. Therefore, the time difference between the minority peaks is a measure of the z-projection of the distance to the MWPCs. In this case, GPCC events such as Figure 4.2 can be used as a guide to determinate the z-coordinate of the event since it is known that GPCCs happen at the cathode. This process of determinaning the z coordinate using minority carriers is known as z-fiducialisation.

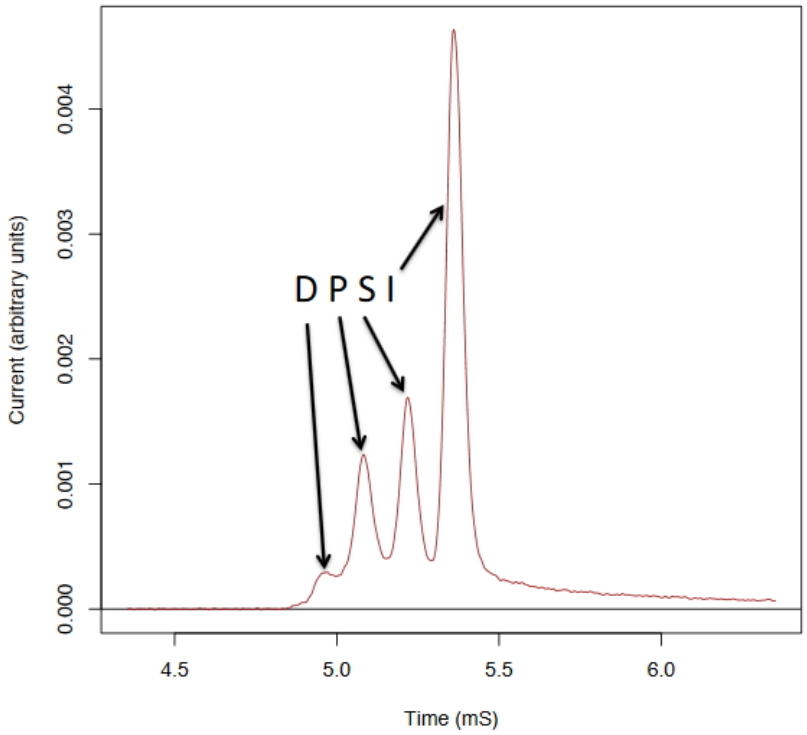

Figure 4.3: Time arrival distribution of negative ions in a DRIFT-like gas mixture showing the presence of minority carriers. From [216].

The mechanism by which minority carriers are created is still being investigated at the time of writing. A possible experiment would be to collect a sample of the gas mixture before and after exposure in the detector to test, by gamma spectroscopy, for the appearance of new species. This hypothesis, however, implies that the minority carriers survive after the stripping of their electric charge and if they do survive, that their energy levels are not degenerate compared to the parent species. Another possible lead is the Bloch-Bradbury mechanism [217]. The thermal capture of electrons in oxygen due to this mechanism has been widely documented (see [218, 219] for example). For electron captures in oxygen, the Bloch-Bradbury mechanism is a two-stage process [220]. Firstly, the electron is captured by the oxygen atom

$$e^- + \mathrm{O_2} \rightarrow \left(\mathrm{O_2^-}\right)^*, \tag{4.1}$$

where the asterisk denotes the fact that the $\mathrm{O_2^-}$ is not in its ground-state. The second stage consists of the relaxation of the ion by scattering on a third body M

$$\left(\mathrm{O_2^-}\right)^* + \mathrm{M} \rightarrow \mathrm{O_2^-} + \mathrm{M}, \tag{4.2}$$

or the collisional decay of the unstable ion

$$\left(\mathrm{O_2^-}\right)^* + \mathrm{M} \rightarrow \mathrm{O_2} + e^- + \mathrm{M}. \tag{4.3}$$

It was shown in [219] that the electron capture cross-section differs between isotopes, especially between ^{16}O and ^{18}O. It is conceivable that this difference in cross section would result in different rates of electron capture (Equation 4.1) and oxygen decay (Equation 4.3). These modulations could induce a change of drift velocity between the different isotopes as the charge is repeatedly lost and recaptured along the drift path.

4.2 DRIFT-IId Neutron Calibration

In this section, the Geant4 simulation of the DRIFT-IId detector is presented. In particular, the simulation of the ^{252}Cf exposure is discussed, and the steps which lead to the nuclear recoil detection efficiency published in [146] are detailed. The DRIFT-IId detector is regularly exposed to different radioactive sources for its calibration. A ^{60}Co source is used to calculate the gamma rejection ability of the detector. This is discussed in more details in subsection 6.2.2. Every 6 hours, data taking is halted to perform simultaneous ^{55}Fe calibration in each TPC. During this time, the software threshold is removed, and the detector operates with continuous triggering. ^{55}Fe produces 5.9 keV X-rays, this corresponds to 234 NIPs (number of ion pairs) when calculated using the W value in [221]. The W value corresponds to the amount of energy required to form one ion pair. The measured W value for gamma interactions in 30 : 10 Torr of CS_2 and CF_4 is 25.2 ± 0.6 eV [221]. It is assumed that this value does not vary significantly due to the addition of 1 Torr of oxygen in the gas. This calibration allows for the monitoring of the gain and the purity of the gas by looking for variations of the W value. The purpose of the ^{55}Fe analysis is to verify that the signals read by the wires are consistent and remain comparable over long exposures. However, to calibrate the detector to the detection of nuclear recoils, it is necessary to use a neutron emitting source. This is the role of the ^{252}Cf source.

4.2.1 ^{252}Cf calibration

^{252}Cf is an unstable element used in a wide range of domains, including medicine and to initiate nuclear reactions in power stations. These applications ensue from the neutron emitting properties of ^{252}Cf. The DRIFT detector is regularly exposed to a ^{252}Cf source for calibration, once every 12 days on average [146]. Neutrons emitted from ^{252}Cf induce nuclear recoils with a nearly identical energy spectrum to WIMPs [222]. These similitude are used to calibrate the detector and to calculate its nuclear recoil detection efficiency. During a ^{252}Cf exposure, the source is placed

10 cm above the steel vessel along the central cathode, 37 cm away from the edge of the vacuum vessel. This standard position, corresponding to (43 cm, 90 cm, 0 cm) in the coordinate system shown in Figure 4.1, is kept constant for the successive ^{252}Cf exposures. The source is placed inside a protective lead canister which is lowered into a plastic tube inside the neutron shielding. The polypropene pellets inside the tube were removed for the duration of the calibration run.

During the different source exposures which will be discussed in subsection 4.2.3, the ^{252}Cf source was replaced by a more recent source. This new source was calibrated using the DRIFT-IId detector by comparing the trigger rate of the detector between the two exposures. It was found that the new source is 27 ± 1 times stronger than the previous ^{252}Cf source , corresponding to a neutron output of 28000 ± 2000 neutrons/s.

4.2.2 Detector simulation

The following paragraphs provide a description of the simulation of the detector at its former location in the JIF underground laboratory at Boulby. The simulations of the DRIFT-IId detector were performed using Geant4 [190] and ROOT [191]. The simulation presented in section 3.4 was derived from the same base code as the Monte-Carlo program introduced here. As such, they share the same set of physical libraries, especially the NeutronHP models for the simulation of neutron interactions. In this section, we describe the main volumes of the geometry.

4.2.2.1 Laboratory

The organisation of a Geant4 geometry can be compared to Russian dolls. A single volume, the mother volume, is drawn. Daughter volumes can then be enclosed inside the mother volume, but the daughter volumes can, themselves, act as mother volumes to the "granddaughter volumes". The first volume drawn in the geometry is the rock volume around the laboratory cavern. The halite around the laboratory is simulated as pure NaCl with a density of 2.17 kg/m^3. At the centre of the rock

volume, the laboratory is modelled as a volume of air with dimensions $6.5 \times 4.5 \times 80$ m^3. 3 m of rock are simulated on each side of the laboratory. The walls, floor and roof of the laboratory are modelled as 3 cm thick plaster boards made of gypsum. The gypsum is simulated as pure calcium sulphate $CaSO_4$ and the water content of the plaster boards is neglected. Pure calcium sulfate has a density of 2.32 g/cm^3, well below the density of commercially available plaster boards [223]. In the simulation, the density was fixed at 708.25 kg/m^3, this value was calculated from the mass of plaster boards with similar thicknesses. Below the detector, the simulation includes the under-floor CH_2 shielding.

4.2.2.2 Detector

The detector is placed in the centre of the laboratory volume. The simulation includes a complete geometrical rendition of the inner detector as shown in Figure 4.4. A lead canister containing the ^{252}Cf source is drawn on top of the vacuum vessel (not visible on the picture), towards the front of the detector. The polypropene pellets that form the neutron shielding (including the underfloor shielding) are included in the simulation. Polypropene has a density of 0.946g/cm^3. The neutron shielding, however, is less dense than this value due to the space between pellets. To accurately described the effects of the neutron shield, its density was reduced to 0.6g/cm^3. The roughly 40% packing fraction was determined during previous simulations of the detector [224], but can easily be obtained by weighting some pellets. The pellets are held by a 1 cm thick wooden frame on the lateral sides of the detector. Next to the detector, a similar frame was drawn to represent the stocking area of the pellets. In the case of the ^{252}Cf simulation, its effects can be neglected since it is further than the neutron source, but it may influence the event rate due to external backgrounds during unshielded exposures.

4.2.2.3 Fiducial volume

The gas volume inside the detector is set as a "sensitive detector". This means that Geant4 will record the interaction of particles inside this volume. The gas volume is composed $CS_2 + CF_4 + O_2$ following the typical ratio 30 : 10 : 1 Torr used in DRIFT. In a previous simulation when the detector was filled with only 40 Torr of CS_2 [224], it was found that the probability for a neutron to scatter twice was negligible up to 6000 Torr. This simulation confirmed there is a linear relation up to 6000 Torr between the recoil rate and the pressure of the gas. This relation can be used to increase the pressure of the gas as an artificial way to increase the simulation live time. In the simulations described in [224], the pressure was increased by a factor 25, from 40 Torr of CS_2 to 1000 Torr. It was verified that this relation remains true for composite gas mixtures and that the ratio of recoils is not skewed towards a particular element. Furthermore, it was also verified that increasing the pressure does not increase the nuclear recoil rate in the outer regions of the detector by a factor greater than in the centre of fiducial volume. Therefore, in the simulation, the density of each gas was increased by a factor 25 in all the DRIFT neutron simulations described below.

4.2.3 Simulation of ^{252}Cf neutrons

In this section, the results of the simulation of ^{252}Cf exposure described in subsection 4.2.1 are presented. 900 million neutrons were fired isotropically from the ^{252}Cf source using Geant4. The neutron energy spectrum was obtained from SOURCES-4C, similarly to the neutron Monte-Carlo simulations described in section 3.4. The spectrum is shown in Figure 4.5. The production rates per bin are calculated for the source strength reported by the manufacturer in September 1994 [224]. To generate neutrons with the correct energies, only the relative height of each bin is relevant. The integrated neutron rate is used to calculate the Monte-Carlo live time. This number scales as the activity of the old source, which can be calculated using the half-life of

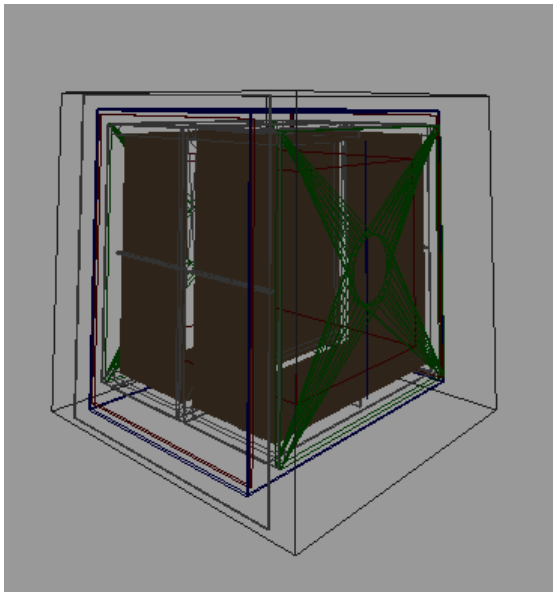

Figure 4.4: Graphical representation of the simulated DRIFT-IID detector in Geant4.

^{252}Cf, and the ratio of the strength of the old source to the new, which is proportional to the ratio of the rate of events in the detector, as described in subsection 4.2.1. According to the manufacturer's measurements in September 1994 [224], the old ^{252}Cf source had an activity of 1.8×10^6 Bq with a half-life of 2.645 years but also contained 3% of ^{250}Cf, corresponding to 5.6×10^4 Bq with a half-life of 13.1 years. The spontaneous fission branching ratio of ^{250}Cf is 0.08% compared to 3.09% for ^{252}Cf.

900 million neutrons sampled from the ^{252}Cf spectrum were simulated and tracked. This corresponds to 9.4 days live-time, more than a factor 10 longer than the duration of the neutron calibration runs [146]. In Geant4, it is also possible to extract the identity of the recoiling nucleus. A sample of the Monte-Carlo events is shown in Figure 4.6. The letters C, S, F, O, represent the corresponding nuclei. The region inside the tan square corresponds to the fiducial region, events outside of this square are either rejected or unseen by the DRIFT analysis software. The second tan rectangle at 50 cm corresponds to the 2 cm exclusion zone around the cathode used

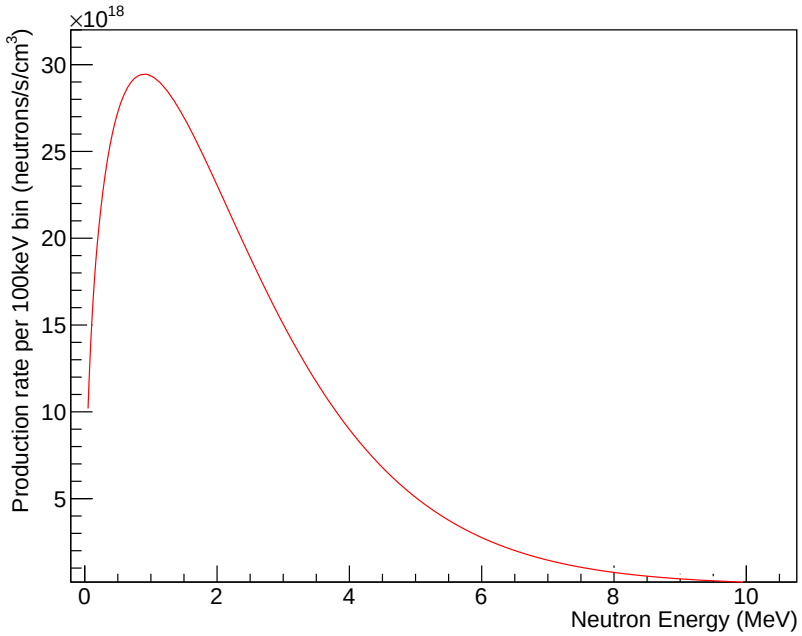

Figure 4.5: Simulated neutron energy spectrum from a 50μCi ^{252}Cf with SOURCES-4C.

to reject RPRs as described in section 4.1. Figure 4.6 only shows nuclear recoils. Geant4, however, also recorded neutron-electron scatterings but these events can be rejected in the analysis. Two principles are used to reject electron recoils. Firstly, at equal ionisation, electron recoils have 10 times longer tracks than nuclear recoils [146], this means that the energy deposited per wires is 10 times lower. Many electron recoils are not detected because the energy deposited per wire remains below threshold. Secondly, if the energy is deposited along more than one octave (a group of 8 consecutive wires), the signal will be repeated on the same channel (as seen in Figure 4.2) and the event is rejected, this is primarily a selection cut applying to higher energy electron tracks.

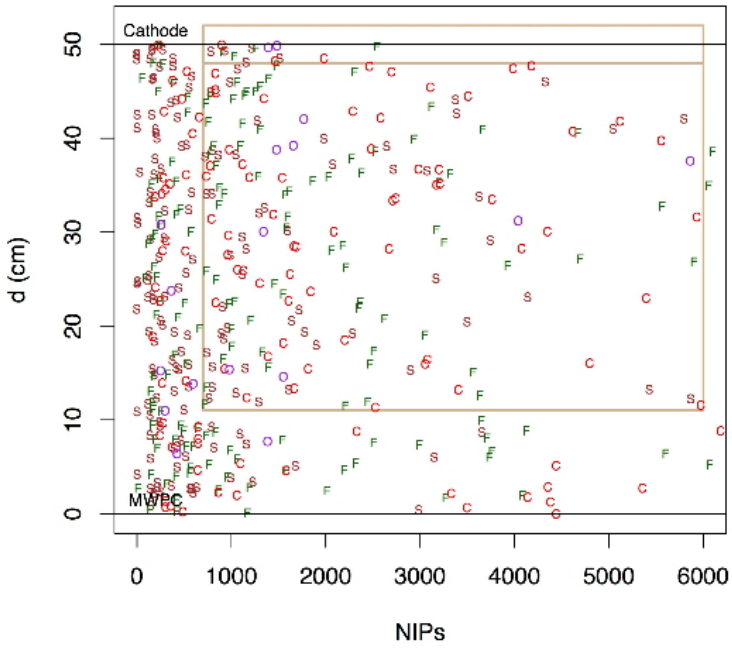

Figure 4.6: A sample of ^{252}Cf neutron induced nuclear recoils simulated in Geant4.

4.2.4 Nuclear efficiency map

The nuclear recoil efficiency map is required to calculate the efficency of the detector as part of the calculation of limits of the dark matter cross section. In order to calculate the neutron detection efficiency, the results obtained from the ^{252}Cf neutrons are compared to the experimental data shown in Figure 4.7. Only the 14240 neutron-induced nuclear recoils which successfully passed the cuts are shown in Figure 4.7. The event selection criteria create two regions of lower detection efficiency in the distribution of events which are not reproduced in the Monte-Carlo. These regions are delimited by green lines in Figure 4.7. In the first zone, there is a linear rise at low energy which becomes more pronounced as the event is further away from the readout plane. This is due to diffusion. Events which happen far from the MWPC have more time to diffuse, so the minority peaks are less pronounced. For low energy events, the minority peaks can be concealed by the background fluctuations. The event selection algorithm neglects the smaller (often undetected) D-peak and tries

to fit 3 Gaussian peaks to the signal to locate the P, S, and I peaks. In the case where the peak finding routine cannot identify at least 1 of the 3 peaks, the event is rejected.

The second region of lower efficiency (number 2) is more pronounced for small distances and increases with energy. In this case, the small relative difference in drift velocities between the peaks over the short drift distance results in peaks which are not fully resolved. In this case, the effect is more pronounced at high energy where a significant amount of ionisation results in broader peaks which require more drift distance to be fully resolved.

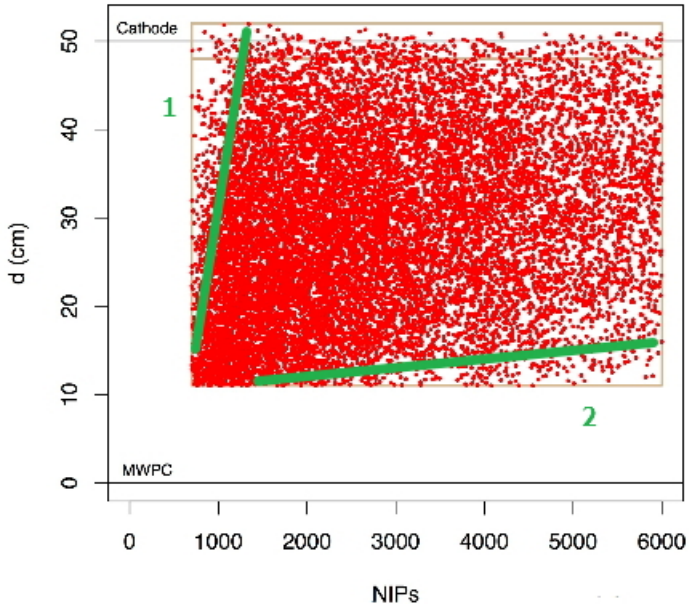

Figure 4.7: Plot of d vs NIPs for all accepted, shielded neutron events.

The neutron detection efficiency map shown in Figure 4.8 is obtained by taking the ratio of the observed nuclear recoils shown in Figure 4.7 with the Monte-Carlo events shown in Figure 4.6. The strengths of the ^{252}Cf sources are also taken into account, as well as the difference in live time and the pressure factor used in the Monte-Carlo to accelerate the accumulation of statistics. The fiducial volume is split into equal bins. The energy region of interest, between 700 and 6000 NIPs,

was divided into 20 equal parts, while the drift region between 11 and 48 cm is divided into 19 bins. The large quantity of data assembled allows for a much finer-grained efficiency map compared to the previous bin of 500 NIPs $\times$ 5 cm [131]. The nuclear recoil detection efficiency is shown in false colour in Figure 4.8, where white represents 100% detection and red 0%. The tan square delimits the fiducial volume as previously. The two slopes in the efficiency described above can be seen more clearly as well.

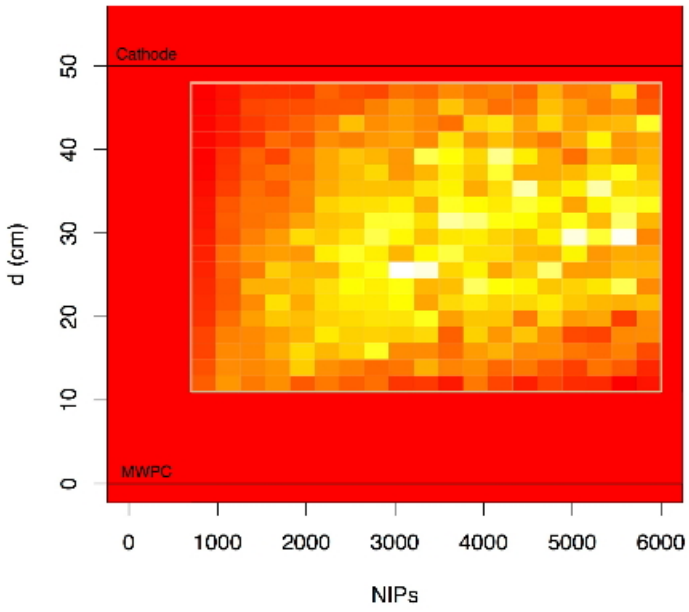

Figure 4.8: Nuclear efficiency map of the detector. From [146].

The projected efficiency, shown in Figure 4.9, represents the average detection efficiency at a fixed NIPs value. The pink band represents the uncertainty on the activity of the source. Thanks to the lower threshold applied in the latest analysis, the detector reaches near full efficiency at lower energies compared to the previous results published in [131]. The lower-limit of the fiducial volume was extended from 1000 NIPs in [131] to the current threshold of 700 NIPs. This new efficiency map published in [146] was first used in the lower threshold dark matter search published in the same article. Figure 4.9 shows a decrease of efficiency at large energy, this is due to the rejection of events with track lengths longer than one octave. In this

case, the signal repeats itself on the same channel and is rejected in the analysis as described in section 4.1.

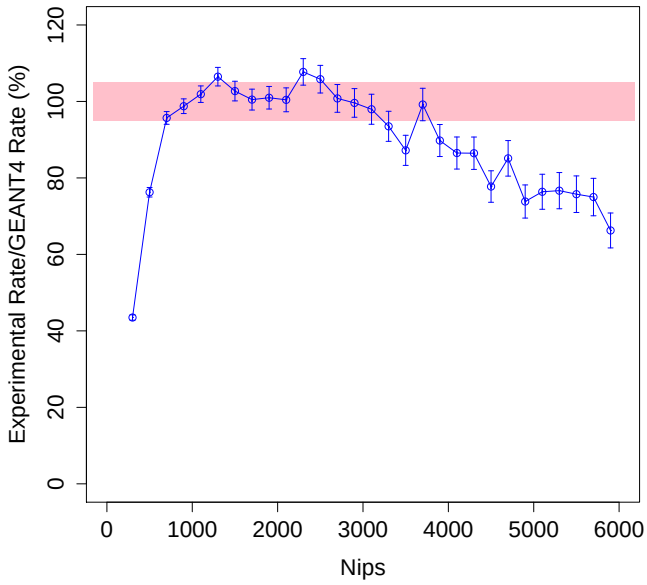

Figure 4.9: Projected detection efficiency for the DRIFT-IId detector.

4.3 WIMP search analysis

The purpose of this section is present the results of 147.48 live days of WIMP search with the DRIFT-IId detector. The approach of [225, 117] is followed to expand on the equations presented in chapter 2 and show how one can obtain the equation for the differential event rate of WIMP-nuclear recoils, with a particular emphasis on the spin-dependent case.

4.3.1 Theoretical calculation

4.3.1.1 Nuclear Recoil Differential Event Rate

Assuming that WIMP-nucleus recoils can be described as the collision of a hard sphere on independent nuclei, the classical scattering cross section σ is the surface of disc $\sigma = \pi R^2$, where R is the sum of the radii of the particles. The total cross section for this interaction is the sum of individual cross sections, so given that the detector is filled with N identical atoms, the cross section is Nσ. If the nuclei are occupying the cubical volume $L^3\,(\mathrm{m}^3)$ of a detector, then a WIMP travelling at a speed v will take $^L/_v$ to go across the detector with an interaction cross section $^{N\sigma}/_{L^2}$. Assuming that there is always one WIMP only in the detector at any given time, the classical recoil rate in the detector is [225]

$$R = \frac{Nv\sigma}{L^3}. \tag{4.4}$$

In reality, the number of WIMP crossing the detector at each instant depends on the local dark matter density (estimated at $\rho_{\mathrm{W}} = 0.3$ GeV/ cm^3, [117]) and the WIMP mass M_{W} (GeV/c^2). In this case, the number of WIMP in the detector is $N_{\mathrm{W}} = 10^6 \mathrm{L}^3 {}^{\rho_{\mathrm{W}}}/_{\mathrm{M_W}}$, when using the aforementioned units. By changing the number of nuclei in the detector N to a measurable quantity such as the mass the detector M_{D}(kg), using Avogadro's number $N_{\mathrm{A}} = {}^{N}/_{1000\times M_{\mathrm{D}}}$,the classical recoil rate can be written as

$$R = 10^9 M_{\mathrm{D}} \times N_{\mathrm{A}} \times \frac{\rho_{\mathrm{W}} v\sigma}{M_{\mathrm{W}}}. \tag{4.5}$$

However, there are two approximations made in Equation 4.5. The first one is that WIMPs of different energies can interact in the detector. Secondly, Equation 4.5 assumes that every WIMP travels at the same velocity, while the WIMPs are expected to follow a Maxwellian distribution [117]. Therefore, the recoil rate can be expressed as

$$R = \int_{E_{\min}}^{E_{\max}} \int_{v_{\min}}^{v_{\text{esc}}} \frac{\mathrm{d}R}{\mathrm{d}E}(v)\,\mathrm{d}v\mathrm{d}E, \tag{4.6}$$

where the differential recoil rate $\frac{\mathrm{d}R}{\mathrm{d}E}(v)$ is a function of the velocity distribution.

To address the dependence of R on the recoil energy first, the recoil energy of a WIMP scattering at an angle θ with a target nuclei of mass M_{N} in the centre of mass frame is given by [225]

$$E = \frac{\mu^2 v^2}{M_{\mathrm{N}}}(1 - \cos\theta), \tag{4.7}$$

where $\mu = \frac{M_{\mathrm{W}} M_{\mathrm{N}}}{M_{\mathrm{W}} + M_{\mathrm{N}}}$ is the reduced mass of the WIMP and the target nucleus. Equation 4.7 has two extrema. The minimum $E_{\min} = 0$ is obtained when $\theta = 0$, while the maximum recoil energy $E_{\max} = \frac{\mu^2 v^2}{M_{\mathrm{N}}}$ is achieved for head-on collisions when $\theta = 180$ degrees. The recoil energy can take any values between 0 and $E_{\max}$, but the probability density $\mathrm{p}(E)$ of having a recoil of energy E is given by [225]

$$\mathrm{p}(E) = \frac{M_{\mathrm{N}}}{2\mu^2 v^2}, \tag{4.8}$$

so using $\frac{\mathrm{d}R}{\mathrm{d}E} = R \times \mathrm{p}(E)$, the differential recoil rate becomes

$$\frac{\mathrm{d}R}{\mathrm{d}E}(v) = 10^9 M_{\mathrm{D}} \times N_{\mathrm{A}} \times \frac{\rho_{\mathrm{W}} M_{\mathrm{N}} \sigma}{2 M_{\mathrm{W}} \mu^2 v}. \tag{4.9}$$

Some uncertainty remains regarding the velocity distribution of dark matter. One set of assumptions is that the dark matter halo has had time to reach thermal equilibrium and the velocity hence follow a Maxwell-Boltzmann distribution [226]. On the other hand, halo simulations suggest large departure from a Maxwellian distribution [227]. For the purpose of the calculations shown here, it is assumed that dark matter follows a Maxwell-Boltzmann distribution. In this case, the distribution of velocities is given by [225]

$$f(\mathrm{v}) = \frac{4\pi v^2}{\left(\pi v_0^2\right)^{3/2}} \exp\left(\frac{-v^2}{v_0^2}\right), \tag{4.10}$$

where v_0 is proportional to the root mean squared velocity:$v_0 = \sqrt{2/3} \times v_{\mathrm{rms}}$. To take into account this distribution the sum over the possible velocities in Equation 4.6 transforms as

$$\int_{v_{\mathrm{min}}}^{v_{\mathrm{esc}}} \frac{\mathrm{d}v}{v} \rightarrow \int_{v_{\mathrm{min}}}^{v_{\mathrm{esc}}} \frac{f\left(v\right)}{v} \mathrm{d}v. \tag{4.11}$$

The upper-limit of the integral is the galactic escape velocity estimated at $v_{\mathrm{esc}} = 533^{+54}_{-41}$ km/s (90% C.L.) [228]. WIMPs with velocities higher than the escape velocity have enough energy to leave the gravitational potential of the galaxy. However, to simplify the computation, the upper limit of the integral can be changed to $v_{\mathrm{esc}} \rightarrow \infty$ [117] under the assumption that the detector is sensitive to most of the velocity range and that the contribution of $f\left(v\right)$ between v_{esc} and $+\infty$ is minimal. In this case, the integral over the velocities in Equation 4.6 becomes

$$\int_{v_{\mathrm{min}}}^{\infty} \frac{f\left(v\right)}{v} \mathrm{d}v = \frac{2}{\sqrt{\pi} v_0} \exp\left(-\frac{v_{\mathrm{min}}}{v_0}\right), \tag{4.12}$$

which substituted into Equation 4.9 gives

$$\frac{\mathrm{d}R}{\mathrm{d}E} = 10^9 \mathrm{M_D} \times N_{\mathrm{A}} \times \frac{\rho_{\mathrm{W}} M_{\mathrm{N}} \sigma}{M_{\mathrm{W}} \mu^2 v} \times \frac{1}{v_0 \sqrt{\pi}} \times \exp\left(-\frac{v_{\mathrm{min}}}{v_0}\right)^2. \tag{4.13}$$

Equation 4.13 is the expression for the theoretical differential scattering rate of isothermal WIMPs in a direct detection experiment in the limit of $\mathrm{v}_{esc} \rightarrow \infty$.

4.3.1.2 Nuclear form factor

The nuclear form factor discussed in subsection 2.3.3 is a correction required when the approximation that the scattering particles are two hard spheres is no longer valid. This is only true when the de Broglie wavelength $\lambda = \mathrm{h}/\mathrm{p}$ is small compared to the nuclear radius which is approximately given by 1.25 fm $\times \mathrm{A}^{1/3}$ [117]. For fluorine, the nuclear radius is around 3.3 fm while the de Broglie wavelength of a 100 GeV

WIMP is approximately 16 fm [225]. The fact that the de Broglie wavelength of the WIMP is 5 times larger than the fluorine radius is an indication that the hard sphere approximation is not correct.

The first order Born approximation can be used to model the interaction of soft objects [225]. In this case, the WIMP can be considered as a plane wave $\psi = Ae^{i(\vec{k}.\vec{r})}$, where $\vec{k}$ is the particle momentum. In an elastic scattering, there is no loss of kinetic energy in the center of mass frame so the scattering amplitude at the position of overlap $\vec{\mathrm{r}}$ between the WIMP initial state ψ_i and the final state ψ_f is given by [225]

$$\psi_f^* \psi_i = Ae^{i(\vec{k}.\vec{r} - \vec{k'}.\vec{r})} = Ae^{i\vec{q}.\vec{r}}, \tag{4.14}$$

where $\vec{q}$ is the momentum transferred to the fluorine nucleus. The scattering objects are not classical hard sphere but the particle scatters of a potential $V(r)$, the inclusion of these quantum mechanical effects modify the expression of the effective cross-section into [117]

$$\sigma \to F^2(\vec{q})\,\sigma_0, \tag{4.15}$$

where $F(q)$ is the nuclear form factor and

$$F(\vec{q}) = \int V(r)\,\psi_f^* \psi_i \mathrm{d}^3 r \tag{4.16}$$

which can be solved as done in Equation 2.6. If the potential $V(r)$ is assumed to be a thin shell of charge as is the case in subsection 2.3.3, then the form factor is $F(qr_n) = j_0(qr_n) = {}^{\sin(qr_\mathrm{n})}/_{qr_\mathrm{n}}$, where j_0 is the zeroth order Bessel function of the first kind and r_n is the nuclear radius.

For spin-dependent interactions, calculations done in [134] show that a more realistic form factor can be obtained when the distribution of all nucleons of the same type as the unpaired one is taken into account. In this "odd-group" model, the first zeros of the Bessel functions are filled in the new distribution and a better approximation

of the form factor is [117]

$$F^2\left(qr_n\right) = \begin{cases} j_0^2\left(qr_n\right) & \left(qr_n < 2.55,\, qr_n > 4.5\right) \\ 0.047 & \left(2.55 \leq qr_n \leq 4.5\right) \end{cases}. \tag{4.17}$$

For each case in Equation 4.17, the departure from the hard sphere approximation to include the quantum mechanical effects of the potential has resulted in a decrease of the effective cross section since $F^2\left(qr_n\right) \leq 1$. In the limit of no transferred momentum, $j_0\left(0\right) = 1$, and the classical hard sphere approximation is recovered.

4.3.1.3 WIMP- nucleon cross section

Different dark matter experiments are based on various target materials. To be able to compare the results of different experiments, the WIMP-nucleon cross section can be written in terms of the cross section between a WIMP and a free proton or neutron in a model-independent way [229]. In each case, it as assumed that the spin of the nucleus is dominated by either one of the neutron or proton contribution. Overall, this usually depends on the target used. Odd proton targets usually get low WIMP-proton cross section limits, and reciprocally for odd neutron targets [229]. With Z = 9, this is the reason why fluorine is a sought target material in dark matter experiments.

The total WIMP-nucleus cross section σ_{WN} can be decomposed into a WIMP proton contribution σ_p and a WIMP-neutron cross section σ_n [229] such that

$$\sigma_{WN} = \left(\sqrt{\sigma_{WN}^{p}} + \sqrt{\sigma_{WN}^{n}}\right)^2, \tag{4.18}$$

where $\sigma_{WN}^{p,n} = 4\mathrm{G_F}\mu^2 C_{WN}^{p,n}$, $\mathrm{G_F} = 1.1663788 \times 10^{-5}\mathrm{GeV}^{-2}$ is the Fermi coupling constant [230] and $C_{WN}^{p,n}$ are the proton and neutron contributions to the total enhancement of the cross section. $C_{WN}^{p,n}$ are defined as [229]

$$C_{WN}^{p,n} = \frac{8}{\pi}\left(a_{p,n}\left\langle S_{p,n}\right\rangle\right)^2 \frac{J+1}{J}. \tag{4.19}$$

$\langle S_{p,n} \rangle$ are the expectation values for the spin of the proton or neutron in the nucleus and J is the nuclear spin. The values of these parameters are given for different targets in [229]. The factor $a_{p,n}$ is the theoretical coupling between the WIMP and a proton or neutron. The value of the parameter depends on the WIMP theoretical model considered. The total WIMP-nucleus enhancement factor C_{WN} is given by

$$C_{WN} = \frac{8}{\pi} \left(|a_p \langle S_p \rangle \pm a_n \langle S_n \rangle| \right)^2 \frac{J+1}{J}. \tag{4.20}$$

By applying the assumption that the proton cross section dominates $\sigma \simeq \sigma^p_{WN}$, the effective WIMP-proton cross section σ_{Wp} can be expressed in terms of the measurable WIMP-nucleus cross section σ_{WN} such that [229]

$$\sigma_{Wp} = \sigma_{WN} \frac{\mu_p^2}{\mu^2} \frac{C_{Wp}}{C^p_{WN}}, \tag{4.21}$$

where C_{WP} is the enhancement factor for the WIMP scattering of a free proton, corresponding to the case $J = \langle S_p \rangle = 1/2$ in Equation 4.20 and where μ_p is the reduced mass of the WIMP-proton system. In this way, σ_{Wp} can be expressed in a model-independent way since the ratio $\frac{C_{Wp}}{C^p_{WN}}$ is independent of the parameter a. In this case,

$$\frac{C_{Wp}}{C^p_{WN}} = \frac{3}{4} \langle S_p \rangle^{-2} \frac{J}{J+1}. \tag{4.22}$$

The values of J and $\langle S_p \rangle$ for different target nuclei are given in [229]. In this way, the ratio C_{Wp}/C^p_{WN} can be determined to solve Equation 4.21. Finally, by incorporating the form factor and Equation 4.21 into the expression of the differential recoil rate obtained in Equation 4.13 , the final expression for the spin-dependent differential recoil rate is [231]

$$\frac{\mathrm{d}R^{SD}}{\mathrm{d}E} = 10^9 N_\mathrm{A} M_\mathrm{D} M_\mathrm{N} \times \frac{4}{3} \langle S_p \rangle^2 \frac{J+1}{J} \times \frac{F^2(E)\, \sigma_{Wp}}{M_\mathrm{W} \mu_p^2} \times \frac{\rho_\mathrm{W}}{\mathrm{v}_0 \sqrt{\pi}} \exp\left(-\frac{v_\mathrm{min}}{v_0} \right)^2 \tag{4.23}$$

4.3.2 Data Analysis

This section presents the results of 147.48 days of unblind dark matter search with the DRIFT-IId detector in underground JIF laboratory at Boulby. The runs included are all between December 4^{th} 2014 and November 2^{nd} 2015 and analysed for the first time in this work. The raw data is subjected to a series of cuts designed to reduce the number of background events recorded in the detector. A summary of the cuts is shown in Table 4.1. These cuts are separated into 3 categories called stages. Table 4.1 presents a summary of the stage 1 and 2 cuts which purpose is to remove non-nuclear recoils events. For example, high energy alpha particles which can deposit energy in more than 8 wires are rejected by cut 2.3.2. Cuts 1.2, 1.3, 1.5, 1.7 are aimed at selecting short-timed events such as nuclear recoils. The true energy of events which saturates the analogue to digital counters (ADCs) cannot be accurately measured. These events are removed in cuts 1.4 and 1.7. Cut 2.5 ensures that the events exhibit an ionisation pattern which is consistent with the use of minority carriers. This is done to reduce the failure rate of the final stage (number 3) of the analysis.

The purpose of the stage 3 analysis is to ensure that the correct number of minority peaks are detector in order to perform the calculation of the z-coordinate [146]. This is done by comparing the integral of minority peaks to the main I peak as in cut 2.5. The ratio of the height of each minority peak must be consistent with the height of the I peak, and their temporal position must be correct. For example, if the main I peak is not the last peak to be read by the MWPC as shown in Figure 4.3, then the event is rejected.

These event selection cuts were applied to the experimental data. Furthermore, the region of interest was restricted to $700 \leq \text{NIPs} \leq 6000$, corresponding to $30 - 205$ keV$_r$ [232]. As shown in Figure 4.10, two events in the fiducial volume (delimited in blue) passed the cuts. The events at $Z \approx 50$ cm in the red rectangle are radon progeny recoils (RPRs). This source of background is discussed in greater

Cut	Description
-	Raw trigger data
1.1	NIPs > 0 on the anode
1.2	No charge on the anode within $+5\,\mu$s of the region of interest
1.3	No charge on the anode within $-5\,\mu$s of the region of interest
1.4	No saturation of the digitizer for the anode
1.5	No grid charge within $+5\,\mu$s of the region of interest
1.6	No grid charge within $-5\,\mu$s of the region of interest
1.7	No saturation of the digitizer for the grid wires
1.8	No activity in the veto region
2.1	Remove events with $>$ 10000 NIPs
2.2	Charge is only deposited in one side (anode + grid)
2.3	Anode hits are contiguous
2.3.2	Remove events that ionise more than an octave of wires
2.4	Remove events with anode.min.risetime$<3\,\mu$s
2.5	Minority peaks integral $> 0.4\times$ majority peak integral

Table 4.1: Summary of the stage 1 and 2 cuts in the DRIFT analysis software. Adapted from [231].

details in section 5.2. Regarding the two events in the fiducial volume, they will be referred to by their event number for simplicity, the first event around $Z = 30$ cm will be referred as event 3494, while the second event around $Z = 40$ cm is named event 35. The events are shown in Figure 4.11 and Figure 4.12. For each figure, the left quadrant represents the signal read by the left TPC, while the right quadrant corresponds to the signal in right TPC. The 8 channels on the top called L/RG1, L/RG2... corresponds to the left (right) grid wires of the MWPC. The channel L/RGS represents the sum of all 8 channels. Simillarly, the L/RA channels corresponds to the anode wires of each MWPC. The L/RVG channels corresponds to the

grid veto wires on the outer part of the MWPC, while the L/RVA channel is linked to the anode veto wires. L/RVS is the sum of the veto signal for the left (right) MWPC. The close observation of the two events in Figure 4.11 and Figure 4.12 shows the presence of minority carriers. They are particularly visible on the 6^{th} anode channel in the left MWPC (LA6) for event 35 and the 5^{th} anode channel of the right MWPC (RA5) for event 3494. The absence of visible minority peaks on the veto channels (LV and RV channels) suggests that the signals detected on the veto wires may possibly be an induced signal rather than actual ionisation. Nonetheless, the veto signals prove that these events occurred in the outer regions of the fiducial volume. Interestingly, the Geant4 simulation of the rock neutron background at the JIF laboratory predicted an event rate of $(7 \pm 2) \times 10^{-3}$ events/ day in the fiducial volume of the shielded detector. This rate corresponds to 1.1 ± 0.3 event during the total duration of this exposure. However, given the that only two events were detected, it is not possible to confirm whether these events are indeed due to nuclear recoils from rock neutrons in the shielded detector.

For this WIMP search, events 35 and 3464 can be rejected on the ground that a signal has been recorded by the veto wires for both events. It can, therefore, be concluded that this is the 3^{rd} successful background-free dark matter search of the DRIFT-IId detector with an exposure time about 3 times longer than the published results in [131] and [146]. This result can be used to compute the upper-limit on the expected number of WIMP events in the detector at the 90% confidence level during the exposure time. Using the calculations of [205], the 90% confidence interval of the Poisson statistic for 0 WIMP event observed and no background events detected corresponds to an upper-limit of 2.44 events. Assuming the detector's efficiency shown in Figure 4.8, Equation 4.23 can be solved for 100 arbitrary WIMP masses in the range $10 < M_{\mathrm{W}} < 10^4$ GeV/c^2, using 34.2 g of ^{19}F as the spin-dependent target in a fiducial volume, and using $v_{\mathrm{min}} = \sqrt{\frac{M_{\mathrm{N}}E}{2\mu_p^2}}$ [233]. However, the detector efficiency shown in Figure 4.9 was obtained without any separation between the fluorine, carbon, sulphur and oxygen recoils. The nuclear recoil detection efficiency

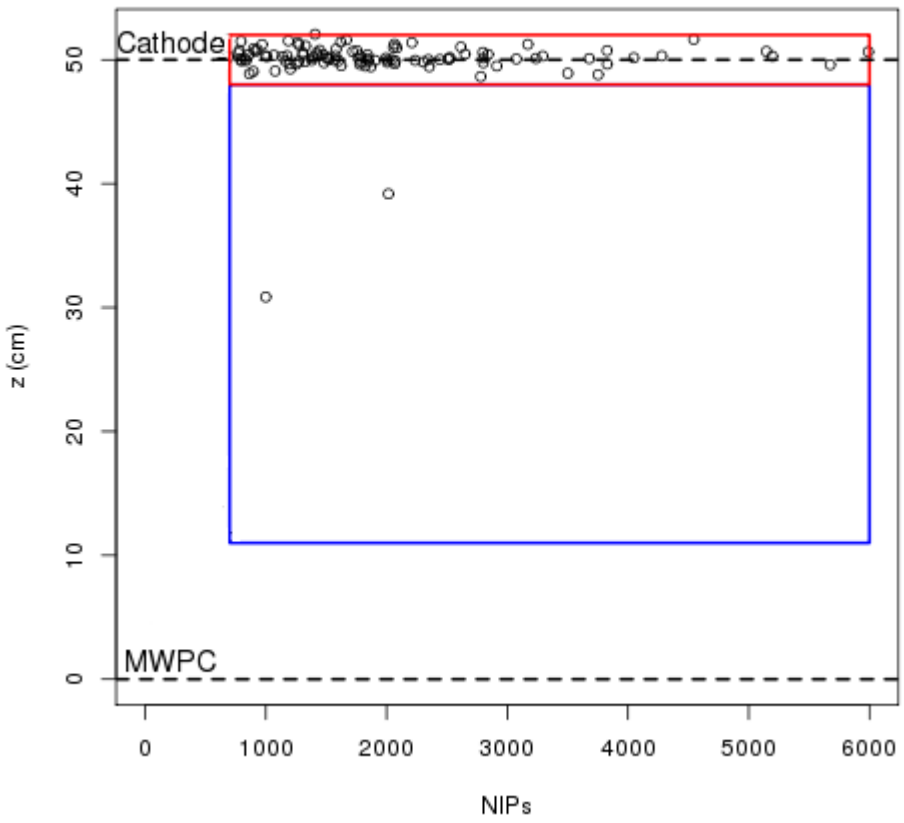

Figure 4.10: Results from 147.48 live days of shielded exposure in the JIF laboratory at Boulby.

used is, therefore, an averaged value obtained from the different atomic constituent of the gas mixture. The equation is solved for a fixed arbitrary cross section of 1 pb [234] and the results are scaled up to the number of events predicted in [205] to achieve the 90% C.L. upper-limit on the cross section.

The 90% C.L. upper-limit on the spin-dependent WIMP-proton cross section for this analysis is shown (in red) in Figure 4.13. Also included in the plot are in green the latest published DRIFT limit [146] for 54.7 live-days of exposure, the (non-directional) PICO-60 results [235] obtained with a C_3F_8 bubble chamber are shown in blue. Shown in purple is the DAMA/LIBRA allowed region for spin-dependent

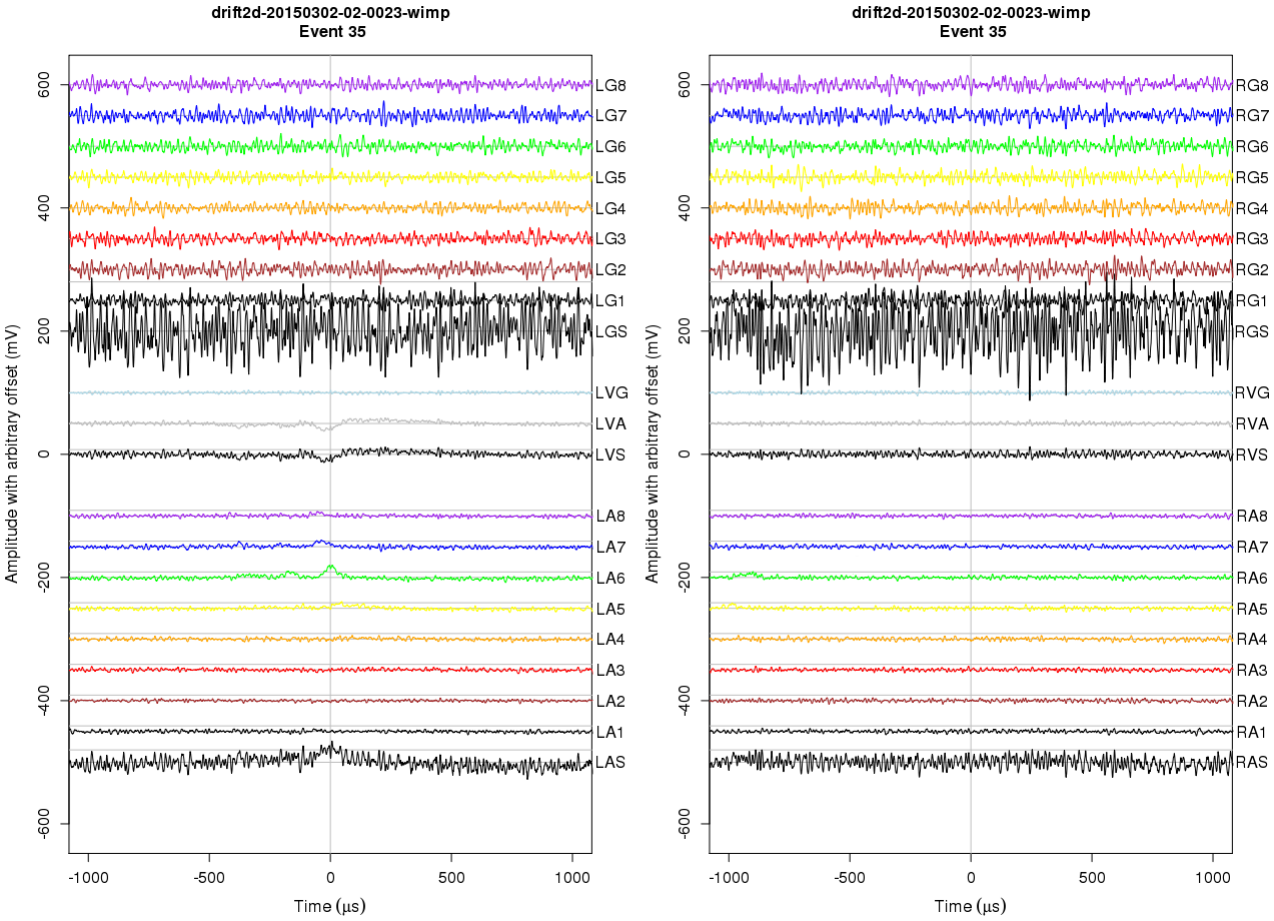

Figure 4.11: Registered signal for event 35 with a signal on the left anode wires (LA5to LA8) and the left veto (LVA and LVS).

interactions as interpreted in [236].

Compared to DRIFT, the PICO detector benefits from a larger quantity of ^{19}F primarily since it is in a liquid state. The detector is also capable of probing lower mass WIMP thanks to its 3.3 keV threshold [235]. However, the DRIFT results presented here are, at the time of writing, the most sensitive limit on the spin-sensitive WIMP-proton cross section from a directional detector. The DRIFT detector had started to probe the DAMA allowed region in [146]. In this work, the current progress of the detector is shown.

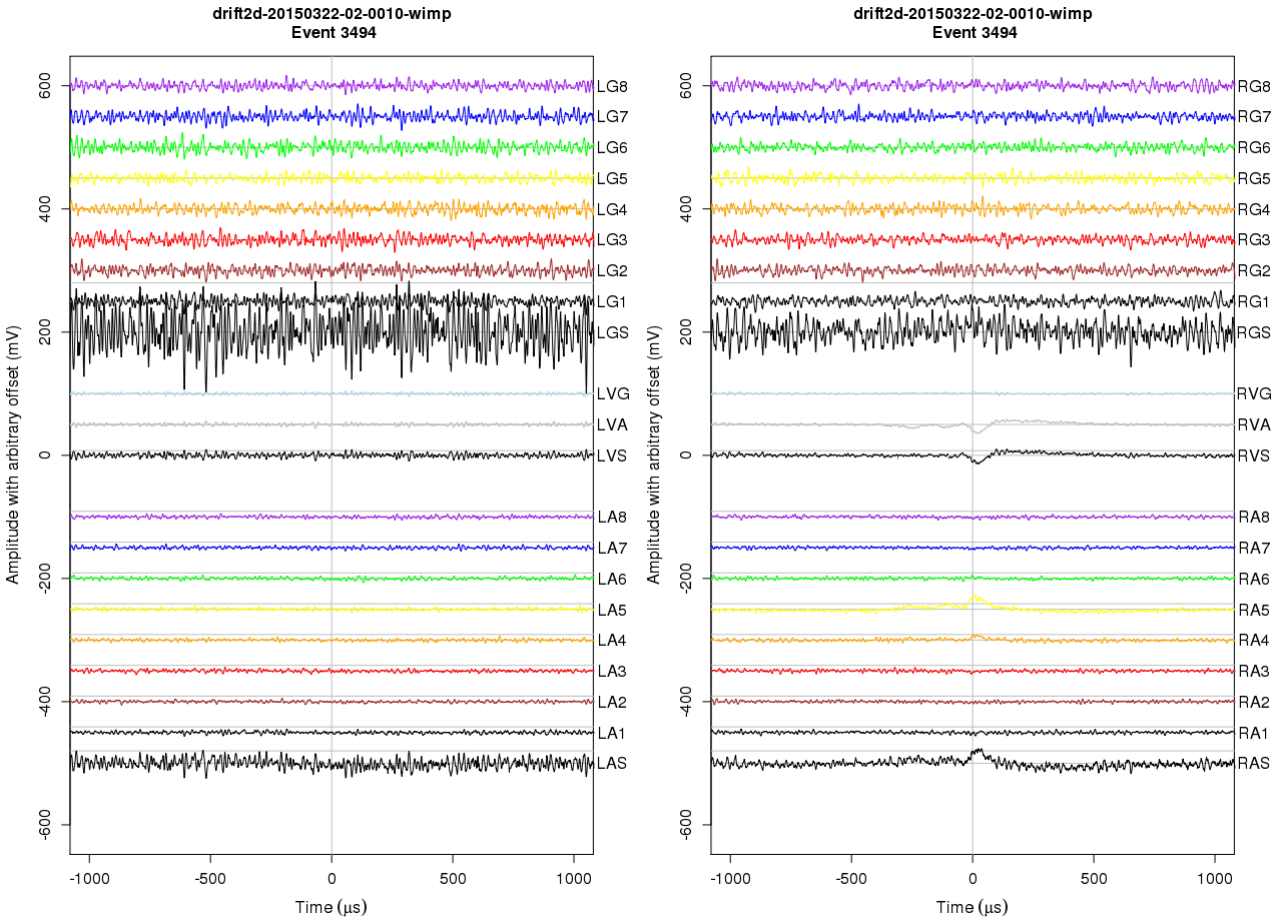

Figure 4.12: Registered signal for event 3494 with a signal on the right anode wires (RA4 and RA5) and the right veto (RVA and RVS).

4.4 Conclusion

Negative ions can be used in time projection chambers to reduce diffusion by using a heavier and slower charge carrier. The simultaneous operation of back to back TPCs can increase the rejection of radon progeny recoils when the events are detected in coincidence between the two chambers. This rejection rate can be increased further by the development of ultra-thin cathode as tested in the DRIFT detector. The addition of textures on the surface of the cathode also reduces the chance of the α-particle being trapped in the cathode, which further increases the rejection capabilities of the detector. Z-fiducialisation, finally, has been used in DRIFT to

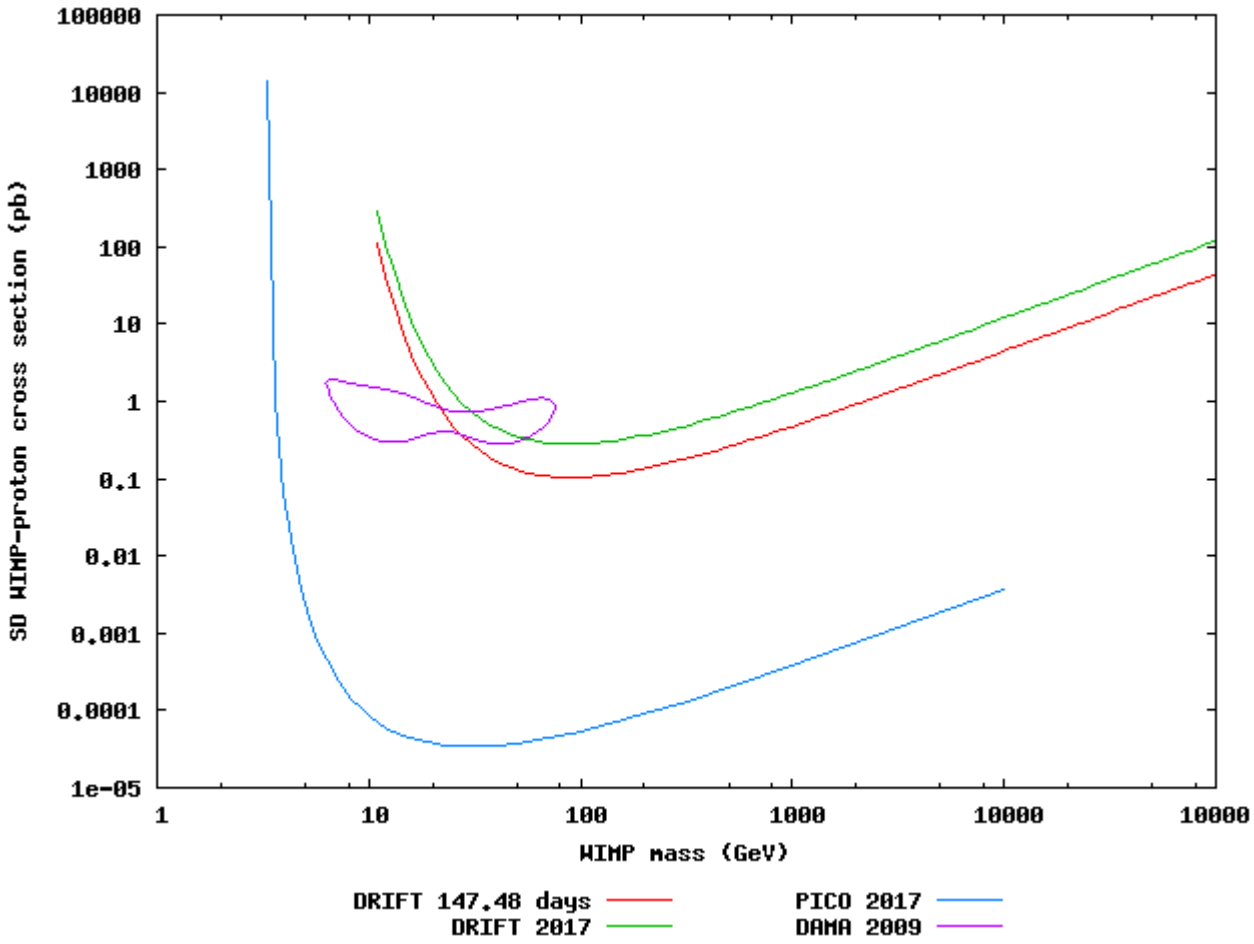

Figure 4.13: Spin-dependent WIMP-proton cross section limit at the 90% confidence level for this analysis (red) and other dark matter detectors.

reject RPRs by drawing an exclusion zone around the cathode. However, cathode crossers are used as calibration events to measure the drift velocities of the charge carrier. Using this technique, the DRIFT collaboration has demonstrated that fiducialisation can be achieved using the minority carriers induced by the introduction of oxygen into the gas mixture. Several tests are planned to investigate the origin of the minority carriers both in the DRIFT gas mixture and in other electronegative gases. In particular, the first hint at the presence of minority carriers in pure SF_6 [132] would suggest that several mechanisms could produce minority carriers, in addition to the suggested Bloch-Bradbury mechanism in $CS_2 + O_2$.

The changes in the composition of the gas mixture of the DRIFT detector required that the nuclear recoil detection efficiency map used for dark matter search be redrawn. This chapter presented the Geant4 simulation of the detector used to estimate the number of neutron events when the detector is exposed to a radioactive ^{252}Cf source. This efficiency map is used in all neutron measurements when a comparison with the Monte-Carlo simulation is required. It was shown that the DRIFT detector can achieve on average near full detection efficiency close to its new low energy threshold at 700 NIPs. However, improved sensitivity to nuclear recoils at lower energy also means that the DRIFT detector is now also more sensitive to its neutron background. The simulations of these backgrounds are presented in chapter 5.

In subsection 4.3.2, it was demonstrated that the DRIFT detector can continue to be operated background-free at its current 700 NIPs for 147.48 live-days. This constitutes an improvement of almost a factor 3 compared to the latest results published in [146]. The DRIFT detector has obtained an upper-limit on the spin-dependent WIMP-proton cross section of 0.1 pb at 100 GeV. This is currently the best result from a directional detector, and DRIFT is, at the time of writing, the only directional detector which has started to probe the DAMA-allowed regions for spin-dependent interactions.

5 Background simulations for the DRIFT detector

In the last chapter, the background-free results from the operation of the DRIFT detector during 147.48 live-days were presented. These results are made possible by the use of minority carriers, the careful selection of materials with low radioactive contamination, and the simulation of the irreducible background. However, it was found that the expected rate of nuclear recoils during the 147.48 days of exposure was above 1 event per year. This is because the DRIFT neutron shield at the JIF underground laboratory was designed at the time when the threshold was 1000 NIPs [224]. This chapter discusses the internal background of the detector and the construction of a new neutron shield for the detector. Over the course of December 2015, the DRIFT-IId detector was turned offline, meticulously disassembled to be transported to its new location in a newly built underground laboratory at Boulby. This chapter describes how the collaboration used this opportunity to ensure that the dominating internal and external sources of neutron background do not contribute above 1 event per year in the fiducial volume.

5.1 Background from the steel vessel

Neutrons originating inside the detector are a potential source of limitation on the sensitivity of the detector to dark matter since no shielding materials are reducing the internal flux. The choice of material to create an internal shielding can be

limited, since it requires that this material produces less neutrons that it can stop. This makes the careful simulation of the backgrounds induced by the detector components necessary to make sure that their contribution is below 1 event per year. The stainless steel vacuum vessel is the most massive component of the detector and is expected to be the main contributor to the background. The vacuum vessel contains rods and hinges for structural support. The total mass approximates 867 kg. The support sections have been measured to have different concentrations of radioactive isotopes [237]. For simplicity, the thickness of the vacuum vessel is averaged in Geant4 to take into account these extra components, the density of the steel was assumed to be 8.027 g/cm^3. Since the vessel itself represents the bulk of the mass, it was assumed that its concentrations of radioactive isotopes apply to the whole simulated vessel. These concentrations are 0.81 ppb (^{238}U), 0.51 ppb (^{232}Th) [237]. Using SOURCES-4C [202], the neutron output from the steel was simulated assuming secular equilibrium in both decay chains. The calculated combined neutron production was 1.44×10^{-10}neutron/s/cm^3, 1.20×10^{-10}neutron/s/cm^3 of which are due to the uranium decay chains, and the remaining 2.4×10^{-11} neutron/s/cm^3 are due to decays from the ^{232}Th chain. The neutron energy spectra are shown in Fig. 5.1.

Geant4 was used to simulate neutrons originating homogeneously and isotropically in the steel vessel. No decays were simulated in the 3 feet of the vessel. The rate of events in the fiducial volume (i.e. all nuclear recoils events with 700 < NIPs value < 6000 and 11 < Z (cm) < 48) amounts to $(5.46\pm0.07)\times10^{-3}$ year^{-1}. However, it was necessary to replace the former external neutron shield because its efficiency was below the target of the experiment once the threshold was lowered. For this reason, it is interesting to calculate the total rate of nuclear recoils predicted by Geant4 which is $(5.58\pm0.03)\times10^{-2}$ year^{-1}. The energy spectrum of nuclear recoils events in the detector for this simulation is shown in Fig. 5.2. Similarly to previous simulations for DRIFT-like detectors, the authors of [187] have shown that the steel vessel is overwhelmingly the main contributor to the internal neutron background.

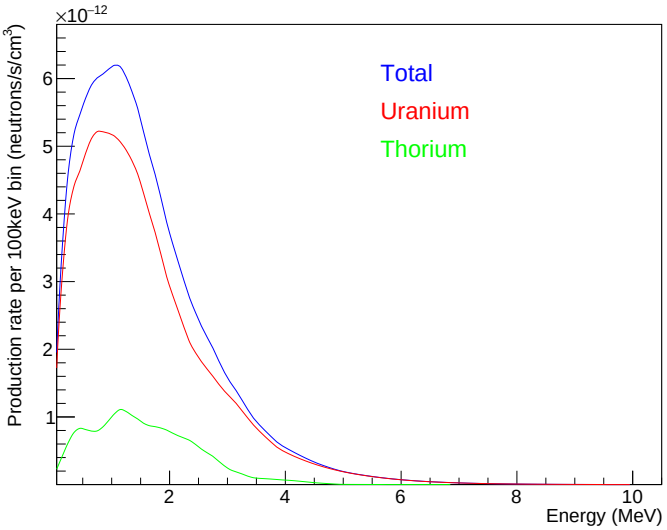

Figure 5.1: Simulated energy spectra of neutrons emanating from the steel due to decays from the uranium and thorium chains.

This simulation, therefore, shows that the neutron background from the rock remains the principal source of neutron background even when the detector is protected by the polypropene pellets.

The gamma background from the vacuum vessel is simulated by populating the steel with ^{238}U, ^{232}Th and ^{40}K at rest. These particles decay using the branching ratios recorded in Geant4 until the last daughter nucleus in each chain is stable. The concentrations of ^{238}U and ^{232}Th are those used in the neutron background simulation. The concentration of ^{40}K reported in [237] for the vacuum vessel is 0.05 ppm. Geant4 records the number of electron recoils in the fiducial volume and convert their energies to NIPs using a work function of W = 25.2 eV. For this simulation, the rates of events in the region of interest are $(1.238 \pm 0.002) \times 10^{-2}$ Bq for uranium, $(1.958 \pm 0.003) \times 10^{-3}$ Bq for thorium and $(1.392 \pm 0.007) \times 10^{-4}$ Bq for potassium. This gives a total rate of $(1.448 \pm 0.002) \times 10^{-2}$ Bq in the fiducial volume between 700 and 6000 NIPs. The conversions calculated assuming secular equilibrium are 1ppb $= 1.23 \times 10^{-1}$ Bq/kg for uranium, 1ppb $= 4.07 \times 10^{-3}$ Bq/kg for the thorium chain and finally, 1ppm $= 3.10 \times 10^{-2}$ Bq/kg for ^{40}K. Fig. 5.3 shows

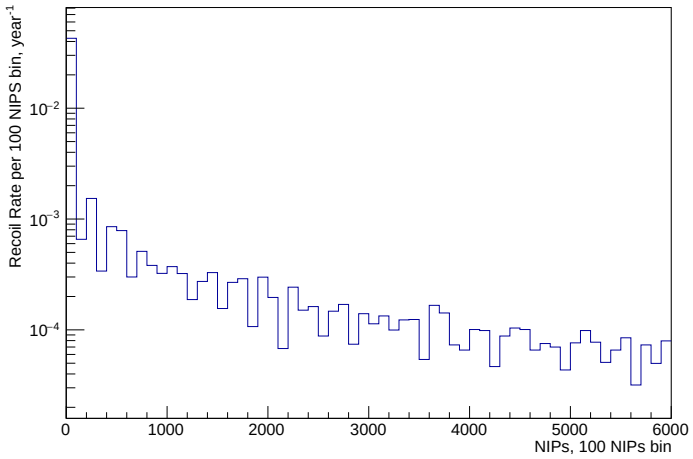

Figure 5.2: Energy spectrum of nuclear recoils in DRIFT due to neutrons from the steel vessel.

that the event rate is dominated by the contribution of ^{238}U. The shoulder in the spectrum seen for each element slightly below 1000 NIPs is due to events which are not entirely contained in the fiducial volume. The Geant4 simulation shows that electron tracks can have vastly different ranges for similar energy deposited in the fiducial volume. A possible explanation for this is that some events are not fully contained in the fiducial volume and their energy is underestimated. However, if these events are actually detected in DRIFT (and are above threshold), they are easily rejected in the analysis. For example, events which are not fully contained in the (x-y) plane will deposit energy on the veto wires and will, therefore, be rejected. If the electron penetrates inside the fiducial volume perpendicularly to the MWPC, this will induce a long waveform which is inconsistent with nuclear recoils. Most importantly, these high energy electron tracks will deposit energy on more than one octave of wires and will be discarded by the analysis due to the repeating signal.

In both simulations presented here, it was shown that the rate of nuclear and electronic recoils due to radioactive decays in the vacuum vessels are small and substantially negligible. This background is proportional to the size of the vacuum vessel and might be a limiting factor for future large size directional detectors. The careful se-

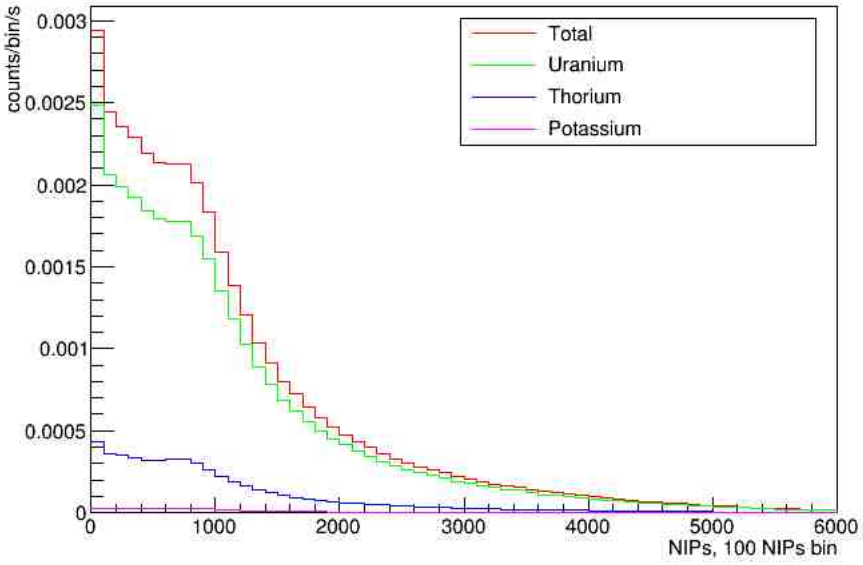

Figure 5.3: Energy spectrum of electronic recoils in DRIFT due to decays in the steel vacuum vessel.

lection of high purity materials can, at the m^3 scale, reduce the neutron background sufficiently to be ignored and remove the need for internal shielding. Similarly, the rate of electron recoils in the region of interest is well below the gamma rejection factor presented in sec. 6.2.2, so both contributions can be neglected.

5.2 Radon background

Radon Progeny Recoils (RPRs) are another internal source of background which may hinder the good operation of the detector. They originate from the emanation of gaseous radon due to the decay of ^{238}U in materials. Since radon is a gas, it can spread throughout the fiducial volume and is, therefore, a primary concern for rare-event searches such as dark matter detection or neutrino-less double beta decay searches. ^{220}Rn has a half-life of 56 s so its ability to diffuse is limited. This means that ^{220}Rn daughters cannot accumulate on the cathode and this background can safely be ignored. This study is, therefore, concentrated on ^{222}Rn which has a half-

life of 3.8 days and can accumulate in the detector. Dark matter experiments have developed different strategies to reduce their radon background. Firstly, a careful background assay is done to select materials with the lowest ^{238}U concentration. Secondly, a continuous flow of target material is created to limit the accumulation of radon. These two methods are employed in DRIFT. Radon monitoring was done by adding a specialised radon detector to the gas circuit which is detecting the α particles from radon decays [238]. Similar measurements have been carried out in MIMAC [239]. The decreasing rate of α decays in a separated closed system is consistent with the half-life of ^{222}Rn as shown in Fig. 5.4.

Several experiments have developed or investigated methods to recycle their target materials after purification with some success. For example, the distillation method used by the XENON and XMASS collaborations to separate the radioactive ^{85}Kr from the liquid Xe have shown that successive distillation of Xe can reach a reduction of the radon content by a factor 27 [240]. This technique relies on repeatedly liquefying and evaporating the target to separate Xe from ^{85}Kr and ^{222}Rn using the fact that they have different boiling points. The XMASS collaboration [241] has tested filtering the gaseous xenon using charcoal but only found a small improvement of a factor of 0.07. Other studies have suggested that this method is limited by the emission of radon from decays in the ^{238}U in the charcoal [240].

Radon decays in the bulk of the gas volume can be vetoed as the α tracks would be detected. Radon daughters, on the other hand, accumulate on the surface of materials. In this case, the α particle can be trapped in the material while the daughter nucleus recoils in the gas. For DRIFT, these regions are situated too far away from the fiducial volume to have an impact on the results. Radon events near the readout planes are already rejected by the cut Z $>$ 11 cm which is based on the separation of the minority carriers. This is not the case for events near the cathode. In sec. 4.1, the installation of a new 0.9 μm thick cathode is described. The textures on the surface of this new cathode are used to reduce the occurrence of unvetted RPRs. α tracks perpendicular to the cathode have only a small chance of being

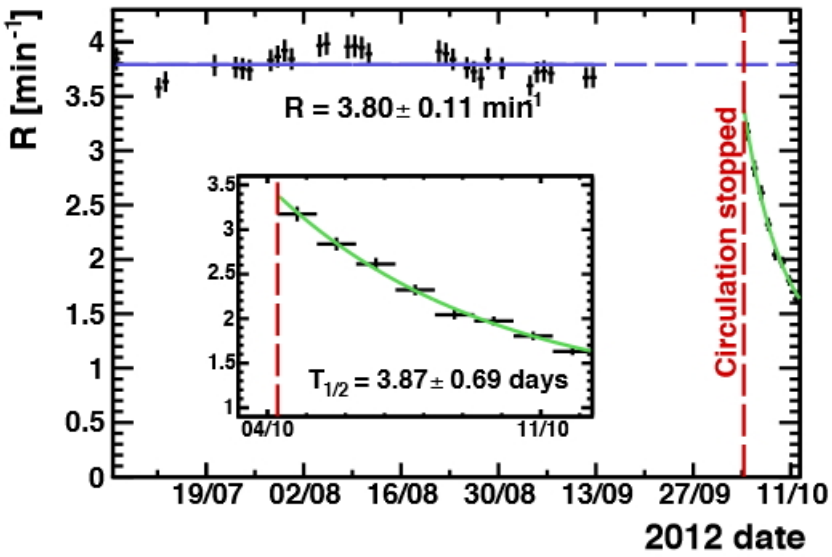

Figure 5.4: Radon monitoring in MIMAC. From [239].

stopped in the Mylar and these events form GPCCs (gold-plated cathode crossers) as shown in Fig. 4.2. Only longitudinal α tracks moving along the cathode plane have a chance to be trapped. The addition of curvature increases the chance that the α particle ionises the gas between its incursions in the Mylar as schematised in Fig. 5.5.

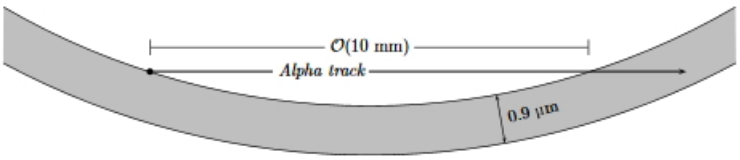

Figure 5.5: α rejection from the textures on the surface of the Mylar cathode in DRIFT. From [213].

The fraction of α particles which remain undetected are limiting the extension of the fiducial volume in the centre of the detector. In the analysis, the cut Z < 48cm excludes events which are less than 2cm away from the cathode. The value 48cm was chosen empirically by observing the spread of RPRs around the cathode in

previous datasets. While all radon events originate from the surface of the cathode, there is a systematic uncertainty in the determination of the Z origin of the events. The resolution of Z calculations is discussed in [216]. The Z position of the events is calculated using the difference of time arrival between the main I peak and the minority carriers. However, this technique relies on the goodness of the fitting of the minority carriers. The smaller the amplitude of the minority peak, the harder it will be for the fitting algorithm to identify the peak above the signal noise. Although, the dominant effect comes from the separation of the peaks. This is why the inference of the Z position returns a better result when it is based on the separation between the minority P peak and the main I peak, rather than between the neighbouring S and I peaks. The resolutions reported in [216] are $\sigma_P = 0.33$ cm and $\sigma_S = 0.67$ cm.

Using Geant4, the effect of the analysis cut Z $>$ 48cm were tested and it was estimated the probability associated with finding an RPR further than 2 cm away from the cathode. ^{222}Rn atoms are simulated at rest at a fix position (x_0, y_0, z_0) in the fiducial volume, the final position of the recoiling particles are recorded. The 3D range shown in Fig. 5.6 is defined as

$$\text{Range} = \sqrt{(x - x_0)^2 + (y - y_0)^2 + (z - z_0)^2}, \tag{5.1}$$

while the Z range is the Z component of the 3D $-$ range and the variable on which the cut is applied.

The sample of 510385 events corresponds to $(1.5 \pm 0.2) \times 10^5$ days $\approx$ 410 years, using the current rate of RPRs detected around the cathode in DRIFT which is 3.41 ± 0.40 RPRs/ day. To simulate the uncertainty in Z, the variable Z_{exp} was calculated. This variable corresponds to the Z position of the event as inferred by the analysis, its expression is is

$$Z_{\text{exp}} = |Z + \text{G}(0, \sigma_P)| \,, \tag{5.2}$$

where $\text{G}\,(0, \sigma_{\text{P}})$ is a random number selected from a normal distribution with mean 0 and variance σ_{P}. The distribution of Z_{exp} is shown in Fig. 5.7.

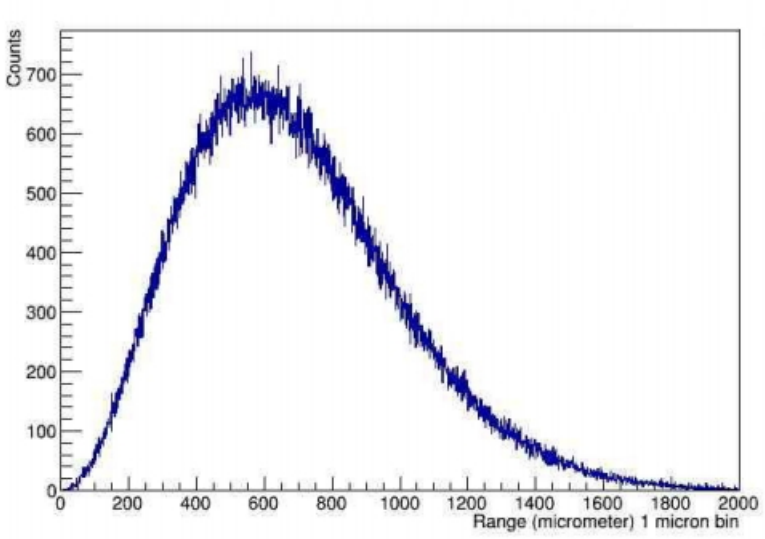

Figure 5.6: Sample of range for nuclear recoils from the decay of ^{222}Rn in the DRIFT mixture.

To reduce the computational burden, an exponential function is fitted to Z_{exp} in Fig. 5.7 using ROOT. The fit function of the form

$$\exp\left(p_1 \times Z_{\text{exp}} + p_0\right), \tag{5.3}$$

has its parameters p_0 and p_1 equal to $p_0 = 1.0893 \pm 0.0003$ and $p_1 = (-1.066 \pm 0.002)\ \text{mm}^{-1}$. The number of events above the cut $Z > 2$ cm is therefore given by the integral

$$\int_{2\text{ cm}}^{39\text{ cm}} \exp\left(p_1 \times Z_{\text{exp}} + p_0\right) \mathrm{d}Z_{\text{exp}}, \tag{5.4}$$

where the lower bound of the integral corresponds the beginning of the fiducial event (close to the cathode) and the upper-bound corresponds to the end of the fiducial event (close to the MWPCs). This corresponds to $(2.6 \pm 0.1) \times 10^{-5}$ events within the fiducial volume in the simulated sample. Using the Monte-Carlo live-time calculated previously, this is equivalent to rate of $(1.7 \pm 0.2) \times 10^{-10}$ RPRs/ day beyond the analysis cut.

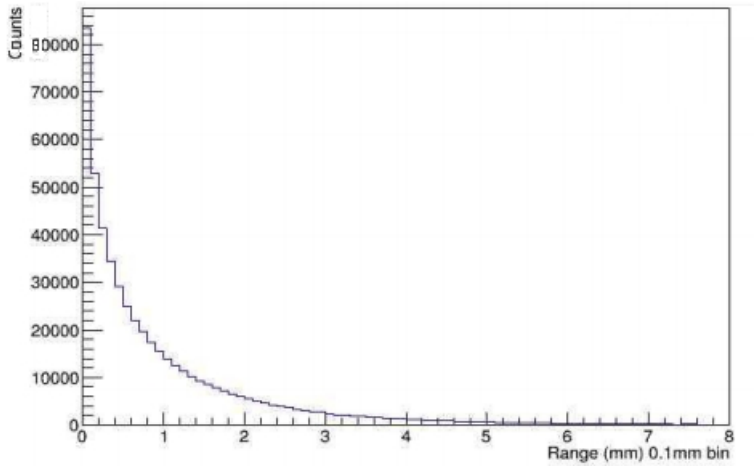

Figure 5.7: Sample of smeared Z_{exp} position of RPRs in DRIFT.

This result demonstrates the high efficiency with which RPRs can be easily rejected. Before z-fiducialisation, the reduction of radon background relied primarily on selecting materials with the lowest radon emanation rates possible or using the diffusion of the charge cloud to identify events emitted from a long distance. The first technique was especially orientated towards porous materials such as the insulating plastic coating of electronic cables which are known to important emitters. Other techniques can be employed. For example, the continuous gas flow in the DRIFT vessel is done such that the entire gas volume in the detector is flushed in a period shorter than the half-life of radon (3.8 days). Noble liquid TPC experiments are constrained by the cost of their target materials. For this reason, they have developed high-efficiency traps to separate radon from liquid argon or xenon. Tests on the recycling mechanism in DEAP have shown that less than one atom of radon can escape the cryogenically cooled activated carbon filters for each refill of the detector [242]. For the current gas TPCs, the results presented here show that precise z-fiducialisation, either through the use of minority carriers as in DRIFT or by reading a positive cathode signal (as investigated by MIMAC [243]), can reject radon events with sufficient accuracy. In the case of DRIFT, this result, in combination with the two previously published background-free analysis [131, 146], proves that

the radon background is under control and that the remaining RPRs do not impede the detector's ability to perform background-free dark matter searches. Finally, this simulation concludes the series of radon-related measurements undertaken in [238], in which the radon emissions of the different components of the detector were measured and where it was determined that the DRIFT detector is sensitive to radon levels up to 2.5 μBq/ l.

5.3 Background from the rock

The previous sections showed that the internal background of the DRIFT detector has been sufficiently minimised by selecting low background material with small radon emanation. The results above have shown that z-fiducialisation can be used to reject the remaining radon background events with efficiency well above the life expectancy of the experiment. The goal of this section is to simulate the background from external sources. For the DRIFT detector, the principal external source of background is the rock surrounding the JIF laboratory at Boulby. The nuclear decays of the radioactive isotopes naturally present in the rock at Boulby produce a flux of neutrons and gamma rays which can penetrate the detector and cause interactions in the gas. In the case of gamma rays, the DRIFT detector is not expecting to detect the ionisation caused by the recoil of Compton scattered electrons. This is because electrons have longer tracks, and hence a smaller $^{dE}/_{dx}$ than a nuclear recoil at the same energy, resulting in the fact that most electrons do not trigger individual wires. The gamma background rejection capabilities of the detector will be discussed in greater details in sec. 6.2.2. In this chapter, only the predicted event rate in the detector, before any analysis cuts is discussed. In particular, the simulation concentrates on the current location of the DRIFT detector. The DRIFT detector was shut down and dismantled in December 2016 to be transported to its present location in the new laboratory at Boulby mine. The structure of the JIF (old) and the new laboratory are different, and so it was found that two separates simulations were

required to account for the environmental moderation of the neutron and gamma fluxes in each case.

5.3.1 Environmental conditions

The new underground laboratory was built after the JIF laboratory was damaged by the geological movement of the salt rock along a fault line. The new laboratory has a stainless steel frame design to absorb the stress induced by the shifting of blocks of rock. Every one metre, a steel I-beam wraps around the laboratory and acts like vertebrae as shown in Fig. 5.8. The walls of the laboratory are made of 2.5 cm thick medium-density fibreboards (MDF). The inner face of the MDF planks are covered with 3 mm of polypropene [244]. This setup was reproduced in Geant4 where the DRIFT detector was placed in the center of the hall with dimensions 50 m $\times$ 7 m $\times$ 4 m (L $\times$ W $\times$ H). In the simulation, only the hallway containing the DRIFT detector was modelled as it was assumed that the rest of the geometry does not contribute to the neutron or gamma fluxes reaching the detector.

Figure 5.8: General view of the new underground laboratory in Boulby. (Photo courtesy of S. Paling).

The detector is placed in the centre of a rectangular space of approximately 6×4 m.

The floor panels covering this surface were lifted to allow for the excavation of the rock as shown in Fig. 5.9. The wooden block placed below the steel beams for structural support are not represented in the Geant4 geometry. The excavated volume was filled with polypropene pellets identical to those used in the former DRIFT neutron shield. Small variations in the thickness of the underfloor shielding were measured between cells. In Geant4, this was approximated by using an averaged thickness of 31 cm for every cell.

Figure 5.9: Excavation of the rock at Boulby before the installation of the underfloor shielding. (Photo courtesy of S. Paling).

5.3.2 New neutron shield design

The density of polypropene is slightly below the density of water at 0.946 g/cm^3. However, for loose pellets as in the DRIFT shield at the JIF laboratory, there always remains space between the beads which reduces the average density of the shield and therefore its efficiency. For the underfloor shielding, an average density of 0.62 g/cm^3

was assumed [146]. For the new DRIFT shield, loose pellets represented a certain encumbrance. If the pellets are not kept loose, the average density of the shield will decrease further to account for the additional spaces between the bags of pellets. On the other hand, a shield based on loose pellets make quick access to the detector difficult, and their transfer has been an untidy process. This option was no longer possible due to the increased clean room standards of the new laboratory.

For these reasons, it was decided to abandon the previous design in order to start anew and build a new shield based on water as shown in Fig. 5.10. This sections descibes the Geant4 simulations which were performed to verify the effectiveness of the different drawings. The design is based on hollow plastic blocks filled with water. Each perspex block is 1 cm thick on each side. Once filled, the block is sealed to be made watertight. Since every block can be moved by the roof crane of the laboratory, the detector can be quickly accessed by removing only the front side of the shield without ever emptying the water blocks. Furthermore, each block has a tab and a blank end, similar to a piece of a jigsaw puzzle. This form strengthens the structural strength of the shield and reduces the probability of letting a neutron pass through the gap.

4 holes have been pierced in the shield on the top and bottom of the left and right face of the shield. Each hole is linked to a plastic tube of 5 cm of diameter bent in a Z shape to minimise the risk of particle crossing the shield without interacting. The top holes are used to pass cables and other necessary piping outside of the shield, up to the DAQ electronic for example. The bottom holes are used for ventilation. The near 31 cm of pellets installed below the floor only provide half of the necessary neutron shielding on this side. Below the detector, perspex sheets have been cut to size to absorb external neutrons further. These sheets will block the air flow below the detector and force the air to go around the detector for better cooling. This is particularly important since four Peltier coolers have been placed on the top of the detector. The Peltier coolers rely on the assumption that the vacuum vessel is in thermodynamic equilibrium with the inner detector. By applying a current to

two thermally connected semiconductor plates, thermodynamic cooling induces a temperature difference between the two plates [245]. The hot sides of the Peltier coolers are linked to their respective CPU fans to evacuate the accumulated heat.

The roof of the shield is composed of 2 cm thick plaques of solid polypropene which cover the whole 3×3 m base of the shield. These plates sit 2.25 m high and cover the hole left for the detector inside the shield which is a square of 2 m side. The polypropene plates do not provide enough shielding by themselves, so another water block is placed on top of them to complete the roof. This block is 3.15 m (L) $\times$ 2.76 m (W) and 42 cm tall. The roof block is larger than the detector hole to provide complete protection. The total height and width of the shield are, however, limited by the space required by the crane suspended to the roof. With this design, 20 cm of space remain between the roof and the crane.

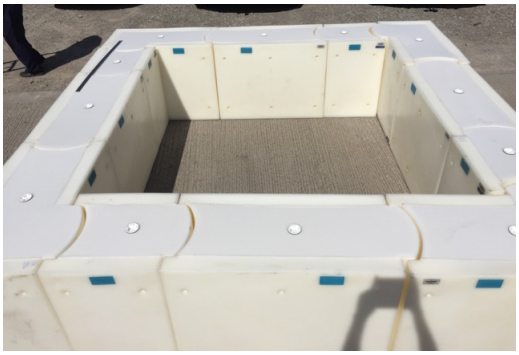

Figure 5.10: Surface assembly test of one stage of the new neutron shield for DRIFT. (Photo courtesy of A. Cole)

5.3.2.1 Test of the neutron shield design

Different shield designs have been exposed to fast neutrons from the rock using Geant4. In particular, the shield presented in the previous section was considered, but it was also envisaged the possibility to place both the DRIFT-IId and DRIFT-IIe detectors in the same shield. A second identical vacuum vessel is underground next to the current detector. While it is currently used to perform R&D tests on

new hardware, this vacuum vessel could be used to house the DRIFT-IIe prototype currently in surface testing in Los Angeles. In this case, the modularity of the design allows the shield to expand on one side by only changing the corner pieces for T-shaped blocks. The possibility of joint shielding of DRIFT detectors has been studied for polypropene shielding in [187]. In this study, the authors suggest that minimal amount of shielding (equivalent to 20 g/cm^2) is required between the detectors to block cross contaminating events between the modules. By sharing a full-size panel between them, the two DRIFT vessels would retain their optimal protection against neutrons while reducing the total quantity of water required.

SOURCES-4C was used to simulate fast neutrons from (α, n) and spontaneous fission, in the same way as described in sec. 3.4 for the simulation of the neutron background in COSINE. Boulby is a salt mine so the rock was approximated as pure NaCl with a density of 2170 kg/m^3. SOURCES was used to verify the neutron production rates quoted in [224] using the background levels presented in [237]. The concentration levels are 70 ppb of uranium and 125 ppb of ^{232}Th. The total neutron production rate for these concentrations is 6.3×10^{-8} neutrons/s/cm^3, split such that 3.1×10^{-8} neutrons/s/cm^3 are due to uranium decays and 3.2×10^{-8} neutrons/s/cm^3 are to due ^{232}Th decays. These results are illustrated in Fig. 5.11.

Similarly to the rock neutron simulations for COSINE, it was determined using Geant4 that only the first 3 m of rock are relevant as neutrons created beyond this distance have a near 100% chance of being stopped in the rock. The saturation of the flux was measured by homogeneously and isotropically populating the rock with neutrons sampled from the sum of the uranium and thorium spectra. For a fixed ratio of uranium to thorium, using the sum of the spectra can reduce the CPU time as the simulation only needs to run one set of neutrons. For the test, the active region of rock is gradually increased until the neutron flux on the rock cavern surface remains constant. The results are shown in Fig. 5.12 and are consistent with previous simulations of a previous version of the DRIFT detector at Boulby, presented in [224]. Similarly to the simulation of ^{252}Cf neutrons, the mean free path

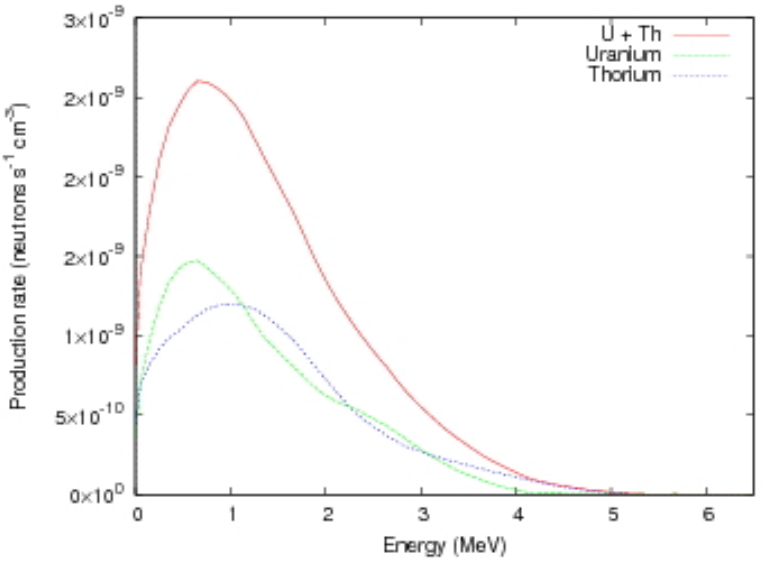

Figure 5.11: Neutron production rates in Boulby rock using uranium and thorium concentrations in [246].

of neutrons in the gas is longer than the size of the detector so the pressure can be increased as long as the probability of double scatterings remains small enough. In this simulation, the pressure was increased by a factor 25 from 41 Torr to 1025 Torr where no corrections are needed [187, 224].

Following the recent background-free dark matter searches, the requirements on the capabilities of the neutron shield have significantly increased. The exercise is to simulate the different backgrounds originating from the rock and to verify that they induce acceptable event rates in the detector. While the simulations have been an iterative process as the new shield was slowly taking shape, only the results obtained with the final model are discussed here. Simulations of the neutron flux for 70 ppb of uranium and 125 ppb of ^{232}Th found that the neutron flux in the laboratory is $(7 \pm 2) \times 10^{-7}$ neutrons/s/cm^2. This result differs from previously measured flux quoted in [224]. In [224], the neutron flux above 0 keV is 4.53×10^{-6} neutrons/s/cm^2, but this simulation does not include the walls of the laboratory. The flux is, therefore, measured at the rock/air interface. Measurements of the simulated flux before the laboratory walls gave a flux of 1.13×10^{-6}neutrons/s/cm^2. The discrepancy was

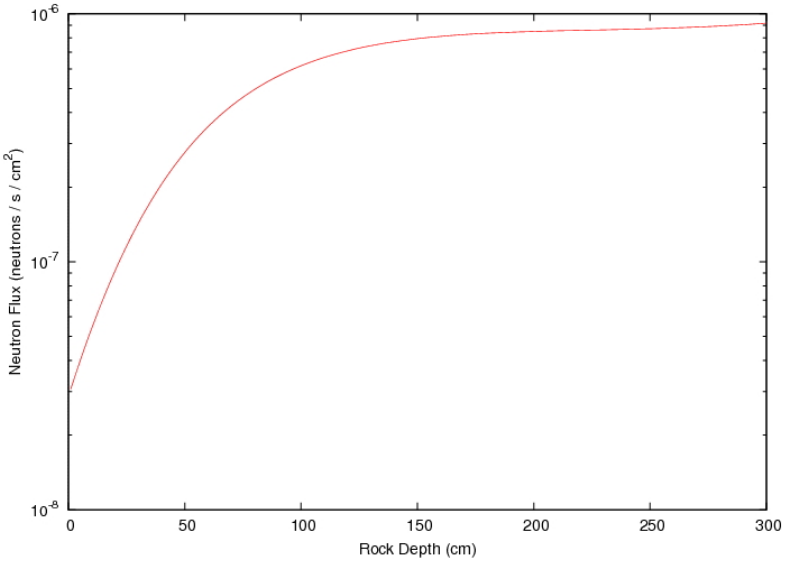

Figure 5.12: Neutron Flux in the rock at Boulby as a function of depth.

explained when the exact simulation of [224] was reproduced (with the help of its author). In this case, Geant4 produced a neutron flux of 1.157×10^{-6}neutrons/s/cm^2. This result suggests that the difference between the flux measured in this work at the rock/air interface, and the flux presented in [224] is simply due to the modifications of the NeutronHP physics list which happened during the last 10 years. The impact of the walls and laboratory structures and the event rate will be discussed at a longer length in sec. 6.2.3.

Similarly to the results obtained in [224], it was found that the neutron flux measured at the air/steel boundary for the unshielded DRIFT vessel is higher than the laboratory flux. This is due to multiple scattering of the rock neutrons which therefore undergo several traversals of the laboratory. In this case, it was found that the flux is $(1.216 \pm 0.002) \times 10^{-6}$ neutrons/s/cm^2. However, for a shielded detector, the neutrons cannot pass through the shield multiple times as the energy loss per traversal is too great. In this case, the vessel flux falls to $(4.5 \pm 0.1) \times 10^{-9}$ neutrons/s/cm^2. The ratio of the two fluxes can be interpreted as a figure of merit on the effectiveness of the shield. The most significant result from the simulation of rock neutrons is the prediction of the nuclear recoil event rate. The simulation of 60.36 days

of shielded exposure with a pressure factor of 25 returned no events. This result places an upper-limit on the rate of nuclear recoils due to rock neutrons at $\leq 6.63 \times 10^{-4}$/day (90% C.L.), corresponding to a maximum of ≤ 0.73 recoils/3 years. This rate is below the self-imposed maximal rate of 1 event per 3 years and is a validation of the new neutron shield currently being installed at Boulby.

5.3.3 Gamma rays from the rock

The DRIFT detector is insensitive to gammas since the energy deposited per wire (similar to $^{dE}/_{dx}$) is below the threshold, and also since the ionisation tracks of high energy electrons will be longer than one octave of wires. However, for completeness, the rock gamma background in the new laboratory at Boulby was also simulated. The estimation of the theoretical rate of interactions in the detector due to gamma rays originating from the rock follows a similar protocol as the DM-Ice simulation presented in sec. 3.2. The volume of rock was populated with 70 ppb of ^{238}U, 125 ppb of ^{232}Th and 1130 ppm of ^{40}K [237]. The nuclei are placed homogeneously and at rest in the rock. Similarly to the neutron simulation, a test is required to quantify the thickness of the active volume of rock. Fig. 5.13 shows that the gamma flux saturates after 25 cm of rock. Furthermore, it was found that the linear relationship at low pressure between density and the nuclear recoil rate does not hold true for electron recoils. This means that the simulation of gamma rays must be done at nominal pressure.

The simulation of the gamma flux inside the laboratory returned a gamma flux of 0.015 ± 0.002 cm^{-2}s^{-1}. The gamma ray flux at the rock / cavern has been measured as 0.09 cm^{-2}s^{-1} [246]. This result compares well with the results obtained from our simulation which returned a flux of $(8.44 \pm 0.01) \times 10^{-2}$ cm^{-2}s^{-1}. The breakdown of the flux by isotope is given in Tab. 5.1. The difference between the flux at the rock interface and inside the laboratory can be attributed to walls and structures of the laboratory. In particular, the set of steel beams around the laboratory can act

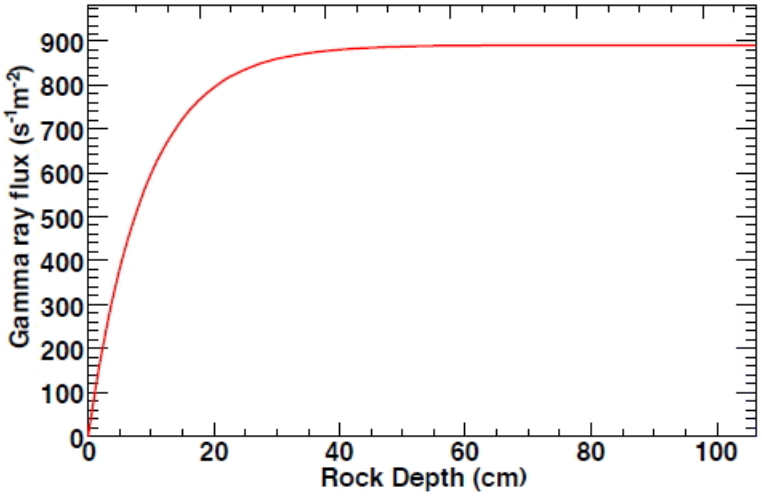

Figure 5.13: Gamma ray flux from the rock as a function of depth at Boulby.

as partial gamma shield, moderating the energy of gamma rays.

^{238}U (cm^{-2}s^{-1})	^{232}Th (cm^{-2}s^{-1})	^{40}K (cm^{-2}s^{-1})	Total (cm^{-2}s^{-1})
$(2.2 \pm 0.4) \times 10^{-2}$	$(1.04 \pm 0.08) \times 10^{-2}$	$(5.2 \pm 0.9) \times 10^{-2}$	$(8.44 \pm 0.01) \times 10^{-2}$

Table 5.1: Gamma ray flux per isotope at the rock / cavern boundary.

Finally, the simulations for the shielded and unshielded detector were performed and events in the signal region of the fiducial volume were counted. These events satisfy the conditions $700 \leq$ NIPs ≤ 6000 , 11 cm $\leq$ Z $\leq$ 58 cm and are susceptible to be registered as potential events by the analysis software. Overall, the 50 cm of water only provide a reduction of factor 10 of the gamma event rate. This result can be explained by the fact that the shield is entirely designed in low-Z materials. These materials are effective at moderating fast neutrons but have poor performances with regards to gamma rays. This simulation concludes that the rejection of the gamma background depends primarily on the capabilities of the analysis to reject electron recoils. In the next chapter, the gamma rejection power of the DRIFT analysis will be discussed at a greater length.

Isotope	^{238}U (s^{-1})	^{232}Th (s^{-1})	^{40}K (s^{-1})	Total (s^{-1})
Shielded rate	$(3.3 \pm 0.5) \times 10^{-2}$	$(1.4 \pm 0.2) \times 10^{-2}$	$(7 \pm 3) \times 10^{-2}$	$(1.1 \pm 0.3) \times 10^{-1}$

Isotope	^{238}U (s^{-1})	^{232}Th (s^{-1})	^{40}K (s^{-1})	Total (s^{-1})
Unshielded rate	$(4.3 \pm 0.5) \times 10^{-1}$	$(1.7 \pm 0.1) \times 10^{-1}$	$(7 \pm 2) \times 10^{-1}$	1.30 ± 0.04

Table 5.2: Event rate in the signal region due to gamma rays from the rock in the shielded (top) and unshielded (bottom) case.

5.4 Conclusion

In this chapter, the different background simulations performed using Geant4 for the DRIFT detector were presented. The simulation of fast neutrons from the steel vacuum vessel showed that internal backgrounds do not currently limit the capabilities of the detector. Although there is no experimental data regarding the vessel, the results and spectra obtained are in good agreement with the previous simulations carried out for the prior DRIFT-I detector [187]. Furthermore, the simulations presented here are a useful complement to the radon assay published in [238]. The simulation of radon events in the fiducial volume has shown that the analysis cuts in place can veto RPRs with excelling reliability as long as z-fiducialisation is maintained. Given the fact that it has been shown in [187] that the steel vessel is the primary source of internal background, and given the two published background-free dark matter searches [131, 146], the results presented in this chapter prove that the DRIFT detector is not limited by its background but by its size, provided that it is suitably shielded. Since DRIFT is the first directional detector to reach this position, the results presented here can be seen as the motivational basis for the development of larger detectors. This is the goal of the CYGNUS collaboration, and the prototype CYGNUS detectors are described in chapter 7.

Obtaining a good level of neutron (and potentially gamma) shielding is a key issue

in order to develop larger TPCs. In this chapter, it was shown that the new neutron shield currently being installed at Boulby is able to provide adequate shielding given the current sensitivities of the detector. The new design, based on water blocks, has proved to be more modular than the previous shield based on loose polypropene pellets. Furthermore, it is also a more compact design with no need to account for an effective density as it is the case for the pellets. This property will be especially advantageous when larger TPCs will require thicker neutron shields. A 40% reduction in size compared to polypropene pellets may allow for the deployment of a larger detector without the need to dig a new cavern underground. Finally, germanium measurements performed by the DRIFT collaboration [247] have shown that clean water and polypropene pellets have similar concentrations of uranium, thorium and potassium. This result would suggest that the transition to a water shield can be done with no increase in the gamma or neutron output of the shield.

6 Negative Ion TPCs as neutron detectors

The previous chapter presented the results of background simulations for the DRIFT aimed at minimising the impact of the neutron background during the dark matter exposures. In this chapter, a different approach is taken. The results of 45.4 live-days of unshielded exposure in the JIF laboratory at Boulby are presented. During this time, 14 nuclear recoil-like events were observed. The detailed analysis of the events will be presented and it will be shown that the detected event rate is consistent with the detection of fast neutrons originating in the rock, similarly to the rock neutrons modelled in the previous chapter for the design of the new DRIFT shield. This is the first purposely made detection of fast neutrons originating from the rock with a negative ion TPC. These results could provide a new tool for the different metrology groups, and it will be shown that, if developed, this new technique may provide certain advantages over some of the experimental techniques already in use. Finally, the proposed UNDER experiment (Underground Neutron DEtection through nuclear Recoils) is introduced. UNDER is expected to repeat and improve on the technology and sensitivities obtained with the DRIFT detector. This is done by performing a similar measurement at the Gran Sasso underground laboratory (LNGS) but with the potential to reach a lower threshold and to make use of its directional capabilities.

6.1 Motivations

Several tools are currently in use to measure the flux of ambient neutrons or the activity of a neutron emitting radioactive source. A NITPC has the potential to do both. A manganese bath can be used to measure the strength of a radioactive source emitting neutrons such as a ^{252}Cf or an ^{241}Am source. One such example is the manganese bath at the National Physical Laboratory (NPL) in the UK [248] illustrated in Fig. 6.1. The source and its protective container can be lowered into the central cavity of the manganese sulfate ($MnSO_4$) bath through the control rod as shown in Fig. 6.1. The neutron emitted by the source will activate the ^{55}Mn in the bath to form the unstable ^{56}Mn through (n,γ) reaction. The gamma ray flux emitted by the bath is proportional to the strength of the source. Using calibrations and Monte-Carlo simulations, the absolute neutron emission rate of the source can be measured. The radiation emitted by the bath is captured by two NaI crystals situated on opposite ends of the bath in recesses of the stainless steel vessel. Scintillation in the NaI crystals is continuously read, even when no measurement is being done. This is a way to continuously calibrate the detector by measuring the gamma ray flux due to radioactive impurities in both the bath and the crystals as well as cosmogenic activations (the apparatus is not situated in an underground laboratory). During measurements, a pump is creating a vacuum in the central container to limit the moderation of the emitted neutrons and limit the accumulation of thermal neutrons in the bath. A de Pangher long counter is placed outside of the stainless steel sphere to estimate the flux of neutrons escaping the bath [248].

De Pangher counters are used by different laboratories to measure the fluence of fast neutrons. The principle is to have concentric annuli of neutron moderators to stop the ambient thermal neutrons and decrease the energy of the fast neutrons passing through the detector. For a model such as the one presented in Fig. 6.2, the borated polyethene can absorb thermal neutrons thanks to the boron in the material, while polyethene is a plastic similar to the plastic from which the pellets of the previous

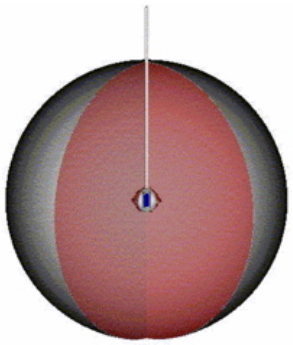

Figure 6.1: Schematic of the manganese bath. From [249].

DRIFT neutron shield was made. Cadmium rods are used in nuclear reactors for their neutron absorbing properties, so the thin cadmium cylinder also moderates the flux on the counter situated in the light blue region in the core of the detector. The counter developed at AMANDE [250] captures thermal neutrons using ^{3}He while the original design from Pangher [251] uses BF_3. In both cases, boron and helium-3 have a distinctive reaction when a thermal neutron is captured. For boron 10 for example, the absorption of the neutron produces a ^{7}Li atom and an alpha particle

$$^{10}\mathrm{B} + \mathrm{n} \rightarrow^{7} \mathrm{Li} + \alpha, \tag{6.1}$$

where the alpha energy depends on whether the ^{7}Li remains in the ground state or if its energy is raised to the first excited state. This can lead to the detection of two alpha particle peaks, one at 2.792 MeV, the second at 2.310 MeV. For ^{3}He on the other hand, the capture of a thermal neutron leads to the fission of nucleus into tritium and hydrogen,

$$^{3}\mathrm{He} + \mathrm{n} \rightarrow^{3} \mathrm{H} +^{1} \mathrm{H}. \tag{6.2}$$

The Q-value of equation 6.2 is 763 keV shared as kinetic energy between the daughter particles and the signal can be read as ionisation in the gas.

The simultaneous use of the manganese bath and the de Pangher counter as described in [248] can provide a verification of the Monte-Carlo when the absolute strength of a radioactive source is measured. However, this technique relies on

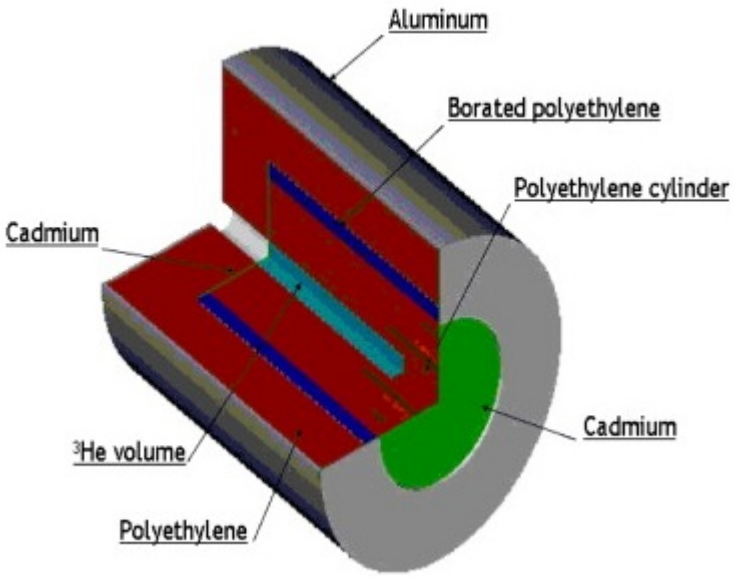

Figure 6.2: Schematic of a de Pangher long counter. From [250].

isotropy as it requires that the fluence measured over the solid angle subtended by the de Pangher counter is constant throughout the surface of the vessel of the manganese bath. A modified setup was used in [252] to alleviate this issue, where the de Pangher counter is placed on a motorised rail and revolves around the manganese bath where it can measure the neutron fluence in different directions. If the source at the centre of the manganese bath in Fig. 6.3 is also rotated but in a direction perpendicular to the de Pangher's plane, then it is possible to measure the anisotropy of the neutron flux.

So far, the experiments described can measure the activity of a radioactive source from the neutron fluence but have no spectral information. The ambient neutron energy spectrum can be obtained using Bonner spheres. Each sphere is made of a neutron moderator (usually polyethene) with a varying thickness. Each sphere is filled with ^{3}He and has a central proton counter tube [253]. Monte-Carlo simulations and calibrations can be used to estimate the neutron energy before it reached the polyethene. Since each sphere has a different thickness of moderator, they are not sensitive to the same energy range. If there is too little plastic, the neutron energy

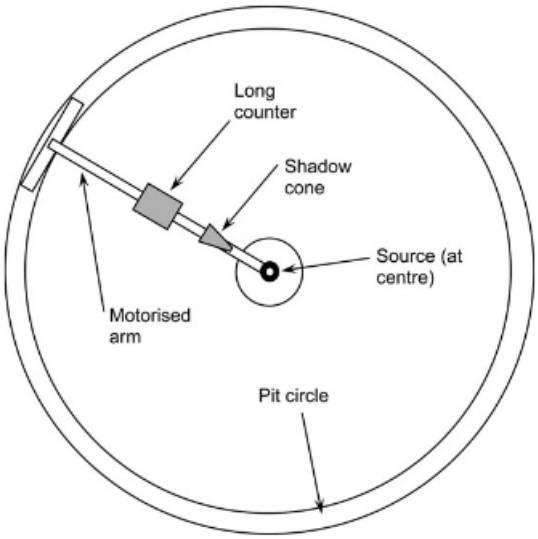

Figure 6.3: Manganese bath with a revolving de Pangher counter. From [252].

is too high to be absorbed by the ^{3}He and there is an upper-limit on the energy at which the Bonner sphere is sensitive. Similarly, if the polyethene is too thick the neutron will be stopped before it reaches the ^{3}He and the Bonner sphere has an energy threshold. By using several spheres, the neutron energy spectrum can be measured from the thermal range up to 20 MeV [253]. Special Bonner spheres have been developed to extend the window at high energy up to 800 MeV using external layers of high-Z material to enhance the response of the detector through neutron multiplication [254]. Overall, because Bonner spheres rely on the capture of a thermal neutron, they remain better suited to detect low energy neutrons. Bonner spheres are one of the ways the neutron flux is measured in underground physics laboratories. For example, the neutron flux in the Jinping underground laboratory in China was measured to be $(2.69 \pm 1.02) \times 10^{-5}$/cm/s and this measurement was sensitive neutron energies in the order of $\mathcal{O}\,(10^{-2}$ eV $-$ 10 MeV) [255].

This comparison of technology has shown that there exist a whole variety of tools in neutron metrology to measure the neutron fluence of a radioactive source. However, there are fewer experimental methods capable of outputting an energy spectrum or to perform a directional measurement. The results presented in the following

sections are the first measurement of the concentration of ^{238}U and ^{232}Th in an underground laboratory using a NITPC. If successfully developed and enhanced, this technique could be equivalent to using Bonner spheres, at least in low background environments.

6.2 DRIFT Unshielded Exposure

This section presents the analysis of 45.4 live days of unshielded data using the DRIFT-IId detector, which ultimately led to the detection of fast neutrons from the rock as published in [146]. Overall, the 45.4 live-days of data were divided into two continuous runs, the first one containing 24.3 live-days, and the second 21.1 live-days. The two unshielded runs were separated by 402 days.

During these two exposures, the polypropene pellets around the detector were removed and stocked in the former pellet reservoir in the JIF Underground Laboratory. The reservoir is a wooden crate opened on the top with dimensions 2.3m $\times$ 2.3m $\times$ 1.98m, nearly 4 m away from the detector. The thickness of the wood is approximated as 1 cm. Metal rods go across the crate, and wooden backings are nailed on the outer sides for support, but these elements are not represented in the Geant4 simulation of the environment. The reservoir of the external shield is simulated as it accounts for a large mass of neutron moderating materials. This may induce a small difference in neutron rate between the left and the right TPC. However, given the small statistical sample obtained during the 45.4 live-days, this effect was not seen.

Underneath the detector, 15 cm of polypropene pellets were placed below the floor. The pellets expand over 10 m along the laboratory and 3.3 m across. The underfloor shielding was purposely made longer than necessary to accommodate the possibility to add a second neutron shielding for the empty DRIFT-IIe vessel, should it become instrumented.

The walls of the laboratory are made of 3 cm thick gypsum plaster boards. In the simulation, it will be shown that the plaster boards play a significant role in the moderation of the neutron flux. This is due to the high water content of the gypsum which is modeled in Geant4 as $CaSO_4 + 2H_2O$ with a density of 0.708 g/cm^3.

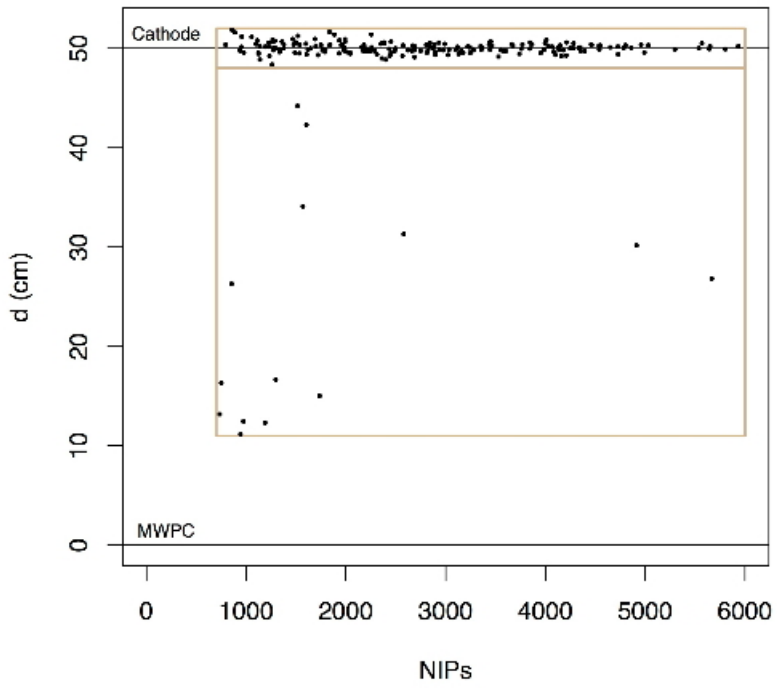

Figure 6.4: Nuclear recoil-like events seen with DRIFT-IId during 45.4 live-days unshielded. From [146].

Fig. 6.4 shows the 14 nuclear recoil-like events seen during the two unshielded exposures combined. These events successfully passed all the cuts applied to the dark matter data as in sec. 4.3.2. In total, 8 events were seen during the first 24.3 days, and 6 events during the second run of 21.1 days. Since the two runs are more than a year apart, it is necessary to ensure that they were recorded under the same experimental conditions. To do this, a comparison between the rate of fiducial events and rate of occurrence of radon events around the cathode is done [256]. These results are shown in Tab. 6.1. The rate of fiducial events is consistent within statistical error. This means that it is likely that the events originate from the same source. The cathode rate is constant between the two exposures when corrections are applied to

compensate for the fact that the average flow speed of the gas in the detector had increased between 2014 and 2015. Furthermore, the gamma calibration obtained from the ^{55}Fe exposure showed that no change affected the detector. It can be concluded from these results that the data were recorded in the same experimental conditions and that no corrections are required. Furthermore, no events were seen during longer shielded exposures so the origin of these events must be external to the shield. The salt rock around the detector is the primary emitter of background radiations and neutrons due to its sheer size. In the following sections, the effect of the rock backgrounds on the detector are discussed.

	Fiducial rate $\left(\text{day}^{-1}\right)$	Cathode rate $\left(\text{day}^{-1}\right)$
Run 1 (2014)	0.33 ± 0.12	3.55 ± 0.33
Run 2 (2015)	0.28 ± 0.12	3.11 ± 0.36

Table 6.1: Fiducial rate and RPR rate in DRIFT during the two unshielded exposures.

6.2.1 Gamma background from the rock

During the unshielded exposures, the detector was subjected to a higher flux of gamma rays emanating from the rock. One possible explanation for the detected events is Compton scattering of these gamma rays in the detector. The aim of this section is to discount this possibility. The approach to verify this hypothesis is twofold. Firstly, the results of a Geant4 simulation of the rock gamma background are presented in order to quantify the gamma fluence during the exposure. Then, the ^{60}Co source runs are presented. From these runs, the gamma rejection factor of the detector is determined. If the gamma rejection power is sufficiently high compared to the simulated number of electron recoils in the rock gamma simulation, then gamma rays can be ruled out as the cause of the 14 events.

To simulate the gamma background from the rock, the same technique described in sec. 5.3.3 was used. The first 25 cm of salt rock are populated with 70 ppb of ^{238}U, 125 ppb of ^{232}Th and 1130 ppm of ^{40}K. It was shown in the previous rock gamma simulation at Boulby that gamma rays originating beyond 25 cm have little chance to escape the rock. The whole decay chains are simulated assuming secular equilibrium. The following fiducial cuts 11 cm < Z < 48 cm, and 700 < NIPs < 6000 were applied to the results and the rate of events passing these cuts was counted. For electron recoils, the conversion factor between NIPs and energy loss, called the " W-factor", used was W = 25.2 eV/NIPs [221]. This value represents the averaged energy loss of the incident particle by electron pairs.

Geant4 predicted a rate of 7.8±1.3 Hz of fiducial events with the detector unshielded. Over 45.4 live-days, this corresponds to 3.1×10^7 events. The breakdown of the flux per decay chains is given in Tab. 6.2. The gamma ray flux at the rock / cavern was measured in Tab. 5.1 with a total flux of $(8.44 \pm 0.01) \times 10^{-2}$ Hz/ cm^2 in good agreement with the measured flux 0.09 s^{-1}/ cm ^{2} reported in [246].

Isotope	^{238}U	^{232}Th	^{40}K	Total
Rate (s^{-1})	2.0 ± 0.1	1.0 ± 0.2	4.8 ± 1.3	7.8 ± 1.3

Table 6.2: Rate of fiducial events in the unshielded detector due to the gamma background from the rock.

^{238}U Flux (s^{-1}cm^{-2})	^{232}Th Flux (s^{-1}cm^{-2})	^{40}K Flux (s^{-1}cm^{-2})	Total Flux (s^{-1}cm^{-2})
$(2.2 \pm 0.4) \times 10^{-2}$	$(1.04 \pm 0.08) \times 10^{-2}$	$(5.2 \pm 0.9) \times 10^{-2}$	$(8.44 \pm 0.01) \times 10^{-2}$

Table 6.3: Simulated gamma ray flux at the rock / cavern boundary at Boulby.

6.2.2 ^{60}Co Exposure

To interpret the results of the gamma ray simulations, the gamma rejection factor of the detector must be calculated. This is done using radioactive ^{60}Co sources. This is possible because it will be shown that after Compton scattering, ^{60}Co and rock gammas produce similar electron recoil spectra which only differ by their rates in the detector. ^{60}Co decays produce two mono-energetic and isotropic gamma rays with energies 1.17 MeV and 1.33 MeV. Three radioactive sources with a total activity of 56 kBq were placed directly above the vacuum vessel. One source was placed above the centre of each TPC while the third source was placed directly above the central cathode. The central source labeled B032 is placed in a plastic cylindrical container with dimensions 4.3 cm (L) $\times$ 1 cm (Ø). The thickness of the plastic case is 2 mm on each side. The side sources with references B016 and B017 are placed inside plastic cylinders of 2.5 cm (Ø) and 0.5 cm (H). The sources are a sphere of approximately 0.3 cm located in the centres of the containers. Each source is placed in an identical plastic cup, 1 mm thick, with dimensions 9.5 cm (H), 4.3 cm (lower diameter), 6.7 cm (upper diameter). The plastic containers and cups are also represented in the Geant4 simulation, where the ^{60}Co sources are approximated as a point in the centre of each containers, inside the neutron shielding at the position mentioned above.

The analysis of 2.90 live-days of ^{60}Co returned no events [146]. This result must now be compared to the Geant4 simulation to estimate the number of Compton scatterings which happened during the exposure. It was found that the relationship between pressure and the recoil rate used for the simulation of neutrons does not hold true in this case. When the simulation is performed at pressures 25 times higher, the recoil rate above 0 keV threshold was 32.4 ± 0.1 Hz while the same recoil rate at the true pressure was 199.0 ± 0.1 Hz. For consistency, it was verified that the same phenomenon appears in the simulation of gamma rays from the rock. This result suggests that there is self-shielding from the gas. The increase of pressure

drastically reduces the mean free path of the electrons, and most of the energy is, therefore, deposited outside of the fiducial volume. It was also verified whether having several sources with a smaller strength spread across the volume induced a change of rate compared with a single source placed above the central cathode. In this case, for a fixed total activity of 56 kBq, the rate induced by a single source is 192.68 ± 0.20 Hz above 0 keV. This result shows that the position of the source has little effect on the total recoil rate, but that the pressure must be accurately simulated.

Finally, Geant4 predicted a rate of 46.26 ± 0.07 Hz in the fiducial window from the decays of ^{60}Co. The energy spectra in Fig. 6.5 show that, when accounted for the difference of rate, gamma rays from the rock induce electron recoils in the unshielded detector with a similar energy spectrum that ^{60}Co gamma rays in the shielded detector. This result means that ^{60}Co is a good replacement to determine the rejection efficiency of unshielded gamma rays. The fact that no events were seen during the 2.90 live-days of ^{60}Co run gives an upper-limit on the new gamma rejection factor of 1.98×10^{-7} (90% C.L.), published in [146] and obtained using the predicted rate of fiducial events of 46.26 ± 0.07 Hz. This result is an improvement by more than one order of magnitude compared to the previous result obtained with the DRIFT-IIa detector in [257] with a threshold of 1000 NIPs compared to the present threshold of 700 NIPs.

By applying this rejection factor to the gamma rays from the rock and the predicted rate of events in the fiducial region of 7.8 ± 1.3 Hz gives an upper-limit on the gamma contamination of 6 events (90% C.L.). This is less than half of the events detected. Furthermore, all events are well contained in X, Y, Z [146] which is inconsistent with the larger track lengths of electrons. More ^{60}Co exposures are required to confirm that the 14 events seen in the detector are not caused by gamma interaction by lowering the upper-limit on gamma interactions. However, for the section, it was assumed that none of these events is due to Compton scattering in the gas.

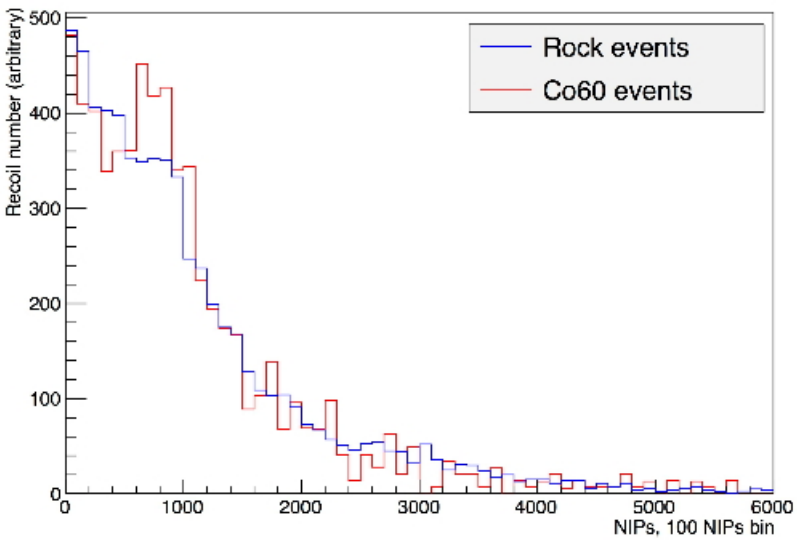

Figure 6.5: Simulated energy spectra of events created by gamma rays in the rock (blue) and ^{60}Co decays (red).

6.2.3 Measurement of ^{238}U and ^{232}Th in the rock

The previous section has shown that most of the 14 events seen in the detector cannot be due to the interaction of gamma rays from the rock. To investigate the contribution from fast neutrons from the rock, a Geant4 simulation similar to the one describe in sec. 5.3.2 was used. Although this time, rather than to scale the neutron production rate from SOURCES in order to match the concentrations of uranium and thorium from [246], the concentration for ^{238}U and ^{232}Th was fixed to 10 ppb each. The neutron production rates for both isotopes obtained with SOURCES are 2.08×10^{-10} neutrons/s/g/ppb(^{238}U) and 9.85×10^{-11} neutrons/s/g/ppb(^{232}Th). Geant4 was used to sample 5.5×10^{8} neutrons from both energy spectra separately. For the design of the neutron shield in the new laboratory at Boulby in sec. 5.3.2, Geant4 sampled neutrons from the sum of the spectra, using the sum of the production rates to calculate the simulation live-time. In this case, two distinct simulations are done so as to be able to change the ratio of uranium to thorium. In each case, the neutrons are produced homogeneously and isotropically in 3 m of salt rock.

A sample of the simulated nuclear recoils in the gas is shown in Fig. 6.6. Compared to Fig. 4.6, Fig. 6.6 shows a larger accumulation of nuclear recoils at low energy below threshold. This is because the rock neutrons have to travel a longer distance (potentially through denser materials) and hence enter the fiducial volume with statistically less kinetic energy. This result illustrates the importance of an accurate description of the detector surroundings. For example, a comparison between the results presented in this work and the results of previous simulations [224] done in bare rock marks the importance of the gypsum boards on the wall of the JIF laboratory. The measurement of the predicted neutron flux at the rock/cavern boundary done with this simulation returned a neutron flux of 1.13×10^{-6} neutrons/s/cm^2 above 0 keV, in good agreement with the result found in [224]: 1.157×10^{-6} neutron/s/cm^2. When the 3 cm thick plaster boards are taken into account in the simulation, the neutron flux decreases to $(7.076 \pm 0.002) \times 10^{-7}$ neutron/s/cm^2, this is a 39% reduction! The explanation for such a large difference is that most of the neutrons have already been moderated in the rock before reaching the laboratory. Since the neutrons have already lost most of their kinetic energy, only a minimal amount of shielding is required. This result also shows that the 14 events detected in DRIFT probably originates on or near the surface of the rock.

For the measurement of the concentrations of ^{238}U and ^{232}Th in the rock, the nuclear recoil detection efficiency map presented in Fig. 4.8 is applied to the Monte-Carlo data in order to estimate how many of the simulated recoils would be correctly detected by the experiment. The number of remaining events, when normalised for the correct exposure time, represent how many nuclear recoils should be seen in the detector due to rock neutrons from ^{238}U chain or ^{232}Th with a fixed concentration of 10 ppb. Experimentally, however, there is no way to distinguish between neutrons from the ^{238}U chain and those from the ^{232}Th chain. DRIFT is only sensitive to the sum of the contributions. In effect, there is two unknowns but only one equation. To solve this issue, the ratio of ^{238}U to ^{232}Th was fixed using several previous measurements shown in Tab. 6.4. On average, all the measurements show

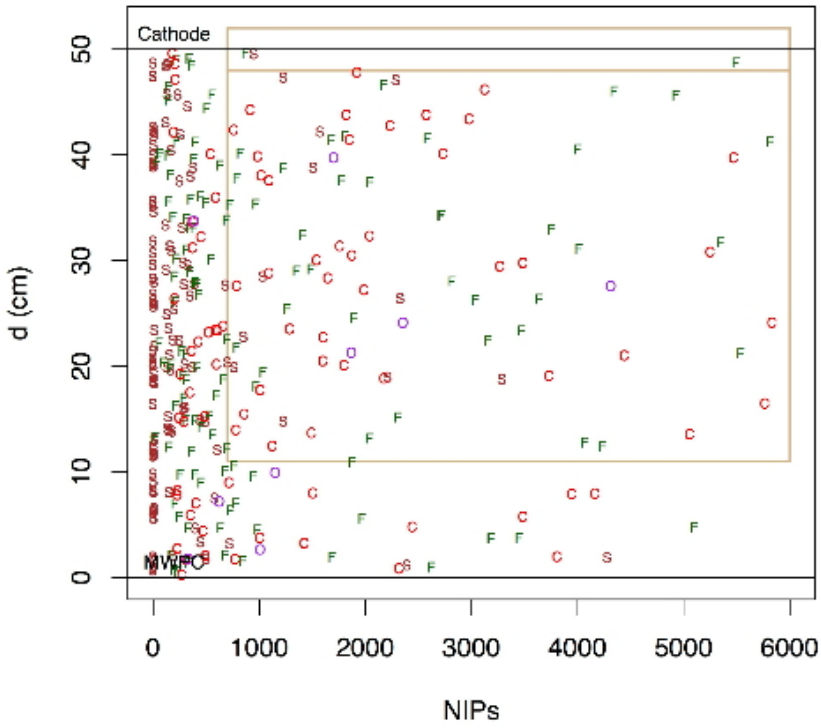

Figure 6.6: Sample of simulated nuclear recoils in DRIFT due to rock neutrons. From [146].

$C_{^{232}Th} = 2 \times C_{^{238}U}$. Using this ratio, the Monte-Carlo simulations can provide the number of nuclear recoils detected by DRIFT for 10 ppb of ^{238}U and 20 ppb of ^{232}Th during 45.4 live-days. If this number is scaled to 14 events, it represents the first measurement of the concentration of ^{238}U and ^{232}Th in an underground laboratory with a negative ion TPC. The results obtained are 77 ppb$\pm$20 (stat)$\pm$7 (sys) of ^{238}U and 150 ppb$\pm$40(stat) $\pm$10(sys) of ^{232}Th as published [146]. These results compare well with the other measurements done in the vicinity of the former location of the DRIFT detector in the JIF underground laboratory at Boulby. Other measurements exist in locations further away in the mine in [237] or in the survey carried out by the authors of [258]. The wide range of concentrations published in different locations (from as low as 10 ppb (^{238}U) up to $\sim$ 130 ppb (^{238}U)) suggests that the concentration of isotopes in the rock at Boulby could vary significantly from one location to another. Although the results in and around the JIF laboratory in Tab. 6.4 are all

consistent with each others, it may prove useful to repeat these measurements in the cavern where the new laboratory has been built. At the time of writing, however, no such measurement has been planned so the concentrations of ^{238}U, ^{232}Th and ^{40}K used in sec. 5.3.2 for the design of the new neutron shield for DRIFT are still the most accurate value at this point.

Source	Method	^{238}U (ppb)	^{232}Th (ppb)
Smith [259]	Ge $\gamma-$ ray	67 ± 6	127 ± 10
JIF lab [237]	γ spectroscopy	70 ± 10	125 ± 10
Plank [260]	Ge $\gamma-$ ray	66 ± 8	145 ± 13
ILIAS [258]	Ge $\gamma-$ ray	132 ± 5	463 ± 15
Tziaferi [261]	Gd detector	$95 \pm 34\,(\text{stat}) \pm 21\,(\text{sys})$	$169 \pm 69\,(\text{stat}) \pm 42\,(\text{sys})$
DRIFT [146]	NITPC	$77 \pm 20\,(\text{stat}) \pm 7\,(\text{sys})$	$150 \pm 40\,(\text{stat}) \pm 10\,(\text{sys})$

Table 6.4: Concentrations of ^{238}U and ^{232}Th in the salt rock in Boulby. The ILIAS measurements were taken in a different location at Boulby mine and are presented to illustrate potential variations in the concentrations of isotopes.

6.3 Measurement of the fast and thermal neutron flux at LNGS with UNDER

It has been shown in the previous section that negative ion TPCs can successfully be used for the detection of fast neutrons in low background environments. Provided that they are sufficiently made insensitive to other backgrounds, NITPCs can be used to determinate the concentration of neutron emitting radioisotopes. So far, the DRIFT experiment has only demonstrated sensitivity to fast neutrons. Furthermore, the results obtained in [146] are limited by their statistical uncertainties. This is due to the fact that the analysis was done with only a small sample of 14 events.

The aim of the Underground Neutron DEtection through nuclear Recoil experiment (UNDER) is twofold. Firstly, UNDER can operate as a NITPC dedicated to dark matter searches and the development of new readout technologies or gas mixtures. Secondly, UNDER can double as a neutron detector to improve the technique and detector sensitivity achieved in [146]. This experiment aims to develop a m^3 scale NITPC to test the triple thin gas electron multipliers (GEMs) readout currently being developed in Sheffield or by the collaborating research groups in Italy. The transition from a wire readout to a GEM based system may be required since insufficient gain was obtained with SF_6 using a DRIFT-like readout. SF_6 has been investigated since the first hints of a potential fiducialisation through minority carriers have been shown in [132]. If these properties are confirmed, SF_6 would present several advantages compared to a DRIFT-like gas mixture. First of all, SF_6 is a non-toxic electronegative gas. This alleviates the need for toxic and corrosive CS_2. It has been shown to less prone to sparking in regions of high electric field. This reduces the risk of accident compared to the $CS_2 + O_2$ combination, even if the risk due to only 1 torr of O_2 is minimal. Finally, SF_6 presents the substantial advantage of having a large target fraction of fluorine (78%) compared to only 20% in the DRIFT gas mixture. This means that the exposure of the detector can easily be increased during spin-dependent dark matter searches. SF_6 could result in more sensitive dark matter detector for spin-dependent WIMP interactions.

With regards to the detection of rock neutrons, the Gran Sasso laboratory (LNGS) offers some interesting possibilities. Firstly, it was found that there exists a significant amount of previous measurements of the neutron flux but at the thermal (shown in Tab. 6.5) and fast range (shown in Tab. 6.6). However, many of these measurements are about twenty or thirty years old, while some are in contradiction with each other. A possible explanation is proposed in [144], where it is suggested that the change of humidity in the concrete of the walls of the cavern fluctuates during the seasons. This argument resonates with the results shown in sec. 6.2.3 where 3 cm of plaster boards reduced the neutron flux by around 40%. At LNGS,

the minimal thickness of concrete walls is 40 cm. This is why it will be shown in the simulation described below that the concrete is the primary contributor to the fast neutron flux. Although the seasonal fluctuation of the fast neutron flux at LNGS has never been measured experimentally, one could imagine that the flux should be higher in the summer when the temperatures are hotter. If this is the case, the annual modulation of the neutron flux should be in phase (or more realistically nearly in phase) with the dark matter annual modulation. In that scenario, annual modulation experiments would need to reconsider the importance of their neutron backgrounds. Furthermore, simulation studies as the one presented in sec. 3.4 could include this effect if the proper environmental measurements are done.

Energy Range (eV)	Thermal Neutron Flux $10^{-6}\mathrm{cm}^{-2}\mathrm{s}^{-1}$			
	Ref [262]	Ref [263]	Ref [264]	Ref [265]
$0 - 0.05$	5.3 ± 0.9	1.08 ± 0.02	0.54 ± 0.13	0.32 ± 0.09

Table 6.5: Thermal neutron flux measurements at LNGS. Adapted from [144].

In this section, the potential of a DRIFT-sized UNDER detector is investigated, supposing that it is placed in the Hall B of LNGS. This hall was specifically chosen because all but one of the measurements shown in Tab. 6.5 and Tab. 6.6 are done in Hall A. Only [267] was done in Hall C. If placed in Hall B, the UNDER experiment could maximise its impact. Specifically it has been proposed that the UNDER vessel could sit on top of the LUNA-MV shield in Hall B, next to the XENON experiment as shown in Fig. 6.7.

Using Geant4, an UNDER vessel was simulated in this location. The experimental hall is simulated as an ellipsoid of 15 m width, 14 m height and 62.5 m length. The true length of Hall B is 125 m but, in order to reduce the computational burden, this size was reduced by a factor 2. It was assumed that neutrons produced more than 30 m away from the detector have little chance to interact with the detector.

<table>
<tr><td rowspan="2">Energy (MeV)</td><td colspan="6">Fast Neutron Flux 10^{-6}cm^{-2}s^{-1}</td></tr>
<tr><td>Ref [266]</td><td>Ref [267]</td><td>Ref [263]</td><td>Ref [262]</td><td>Ref [268]</td><td>Ref [269]</td></tr>
<tr><td>$0.1-1$</td><td rowspan="3"></td><td></td><td rowspan="2">0.54 ± 0.01</td><td rowspan="2"></td><td rowspan="2"></td><td rowspan="4">2.56 ± 0.27</td></tr>
<tr><td>$1-2.5$</td><td>0.14 ± 0.12</td></tr>
<tr><td>$2.5-3$</td><td rowspan="2">0.13 ± 0.04</td><td rowspan="2">0.27 ± 0.14</td><td rowspan="5">3.0 ± 0.8</td><td rowspan="5">0.09 ± 0.06</td></tr>
<tr><td>$3-5$</td><td rowspan="4">0.78 ± 0.3</td></tr>
<tr><td>$5-10$</td><td>0.15 ± 0.04</td><td>0.05 ± 0.01</td><td rowspan="3"></td></tr>
<tr><td>$10-15$</td><td>$(0.4 \pm 0.4) \times 10^{-3}$</td><td>$(0.6 \pm 0.2) \times 10^{-3}$</td></tr>
<tr><td>$15-25$</td><td></td><td>$(0.5 \pm 0.3) \times 10^{-6}$</td></tr>
</table>

Table 6.6: Fast neutron flux measurements at LNGS. Adapted from [144].

On each side of the ellipsoid, 40 cm of concrete separate the rock from the cavern filled with air. The composition of the concrete and the rock are taken from [144] and shown in Tab. 6.7 and Tab. 6.8. The density of the rock in the simulation is 2.71 g/cm^3 [144] mainly composed of $CaCO_3$ and $MgCO_3$, the density of the concrete fluctuates between 2.3 and 2.5 g/cm^3 according to [144] depending on the assumed water content. For the simulation, the density of the concrete was set at 2.3 g/cm^3. The vessel was composed of stainless steel with density 8.027 g/cm^3 and is identical in shape and size to the DRIFT vessel. Inside the vessel, the central cathode is represented by a sheet of Mylar with a thickness of 0.9 μm, similar to the DRIFT cathode. Two 0.5 mm thick sheets of copper are placed 50 cm away from the cathode, one on each side to represent the GEM readout. The design of the inner detector was purposefully left crude to retain generality and avoid slowing down the simulation. The internal parts of the detectors have been showed to have no effects on the results of these simulations [224]. A graphical representation of the detector made with Geant4 is shown in Fig. 6.8.

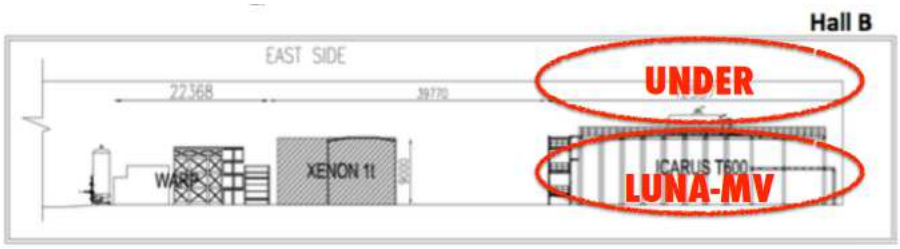

Figure 6.7: Proposed location for the UNDER experiment.

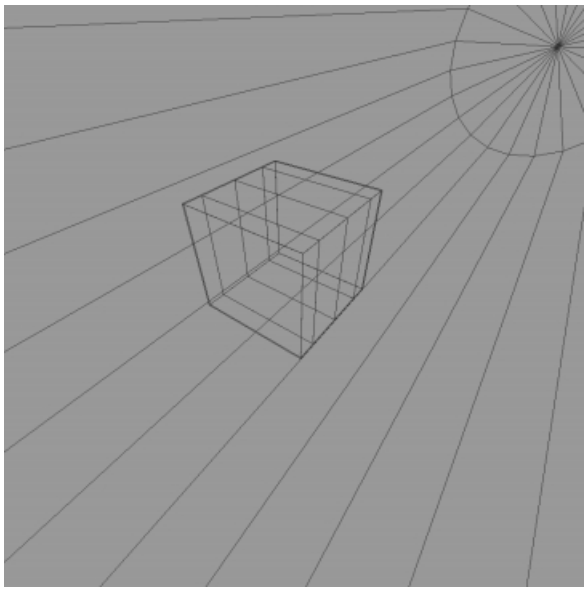

Figure 6.8: Geant4 representation of the UNDER vessel in Hall B using VRML.

For the gas mixtures, UNDER is expected to operate in two operation modes. In the first mode, the gas mixture is composed of ^{3}He :^{4} He : SF_6 at 1 : 659 : 100 Torr. This combination of gases corresponds to what the typical gas mixture in UNDER would be for dark matter searches. In this case, most of the mass fraction of the gas is SF_6 for the search of WIMP-proton interaction. UNDER is also expected to have a good sensitivity in the low mass WIMP region for spin-independent interactions thanks to the large molar fraction of He. Finally, 1 torr of ^{3}He was added to the gas mixture to gain sensitivities to thermal neutrons. As discussed in sec. 6.1, ^{3}He is used in the de Pangher counters and Bonner spheres to detect fast neutrons which have

Element	Fraction in rock (%)
C	11.88
O	48.92
Mg	5.58
Al	1.03
Si	1.27
K	1.03
Ca	30.29

Table 6.7: Composition of the rock (top) and concrete (bottom) in LNGS. Adapted from [144].

been moderated down to the thermal range. In UNDER, since there is no significant moderation of the neutron energies in the detector, discrimination between fast and thermal neutrons can easily be achieved. In the second gas mode, the fraction of SF_6 is reduced and the proposed gas mixture is ^{3}He :^{4} He : SF_6 at 1 : 749 : 10 Torr. This second option is considered to palliate for the potential loss of directionality in the first gas option. It is important to stress that the development of NITPCs based on SF_6 is still quite at an early stage. SF_6 is a heavier charge carrier compared to CS_2 so one should expect to observe less diffusion in SF_6 under isobar conditions. However, no directional TPC has yet successfully operated at 1 atmosphere, and it is possible that at this pressure, the density of the gas mixture is such that any directional information would be lost. If this is the case, the NITPC would lose one of its main arguments over Bonner sphere. More importantly, the successful measurement of a neutron flux in a TPC relies on a zero background hypothesis. Assuming that UNDER can be made insensitive to gammas in the same manner as DRIFT, the diffusion in a high-pressure NITPC might be such that the minority carriers are no longer discernible. In this scenario, UNDER would be subject to radon background events. Making progress towards the development of successful

Element	Fraction in concrete (%)
Si	3.86
O	49.64
H	0.89
Ca	34.06
Al	0.9
Fe	0.43
C	7.99
Mg	0.85
Na	0.6
K	0.54
S	0.16
P	0.4
Ti	0.4

Table 6.8: Composition of the concrete in LNGS. Adapted from [144].

high-pressure NITPC for dark matter search is one of the goals of the CYGNUS collaboration. As one of the CYGNUS demonstrator, UNDER will participate to the research effort. For the time being, it is sufficient to assume that the zero background hypothesis holds for UNDER and that z-fiducialisation through the use of minority carriers is possible for the gas mixtures proposed. Furthermore, since the efficiency of the detector cannot be estimated yet, all results presented in this section assume 100% nuclear recoil detection efficiency.

The fast neutron production rates in the rock and concrete in the Hall B of LNGS were calculated using SOURCES-4C based on the concentrations of ^{238}U and ^{232}Th given in [144]. For the concrete, a total neutron production rate of 3.23×10^{-8} neutron/s/g was found. This rate is split between 2.82×10^{-8} neutron/s/g due to 1.05 ppm of uranium and 4.11×10^{-9} neutron/s/g due to 0.656 ppm of ^{232}Th. For the rock, the total

neutron production rate is 3.69×10^{-8} neutron/s/cm^3. 3.56×10^{-8} neutron/s/cm^3 are due to 420 ppb of uranium, while the remaining 1.32×10^{-9} neutron/s/cm^3 are due to the 62 ppb of ^{232}Th present in the rock. The neutron energy spectra for the rock and the concrete are shown in Fig. 6.9 and Fig. 6.10.

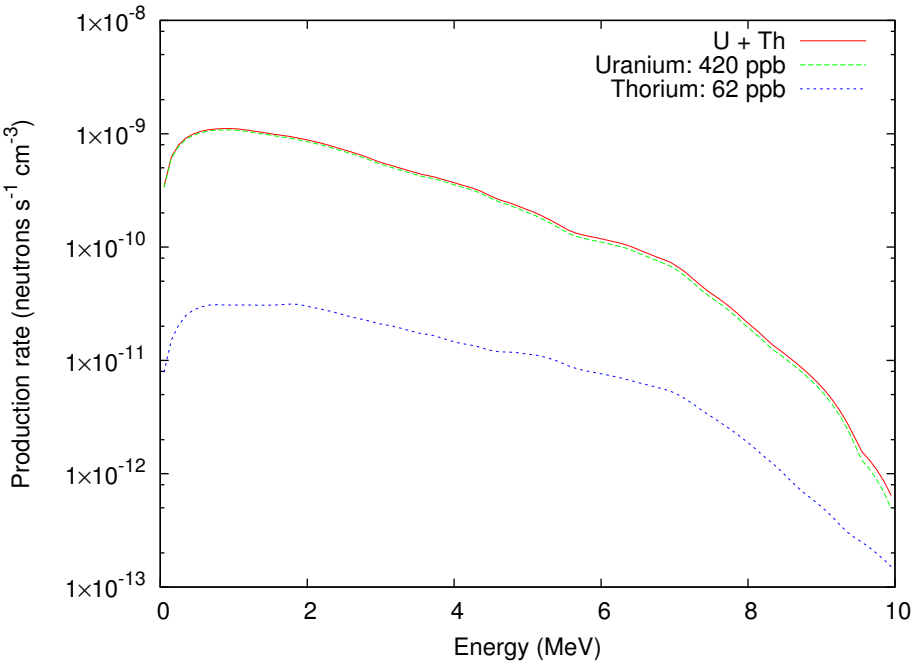

Figure 6.9: Neutron production rate in LNGS rock for Hall B.

In the simulation, 3 m of rock were included on each side of the cavern. The neutrons are produced isotropically and homogeneously in either the concrete or the rock with an energy sampled from the relevant distribution. Nuclear recoils were counted in the fiducial volume of UNDER using the similar selection cuts as DRIFT. This means that only events satisfying 11 cm $<$ Z $<$ 48 cm were selected. Furthermore, the NIPs selection cut in DRIFT 700 $<$ NIPs $<$ 6000, was replaced by a energy threshold of 30 keV. Since the quenching factors in DRIFT are different for each species, 700 NIPs of fluorine recoils do not correspond to the same energy as 700 NIPs of sulphur recoil. However, 30 keV was found to be a good average between the different elements. This approximation was necessary because no measurements of the W-factor were found for SF_6 + He. In any case, a more detailed simulation will be

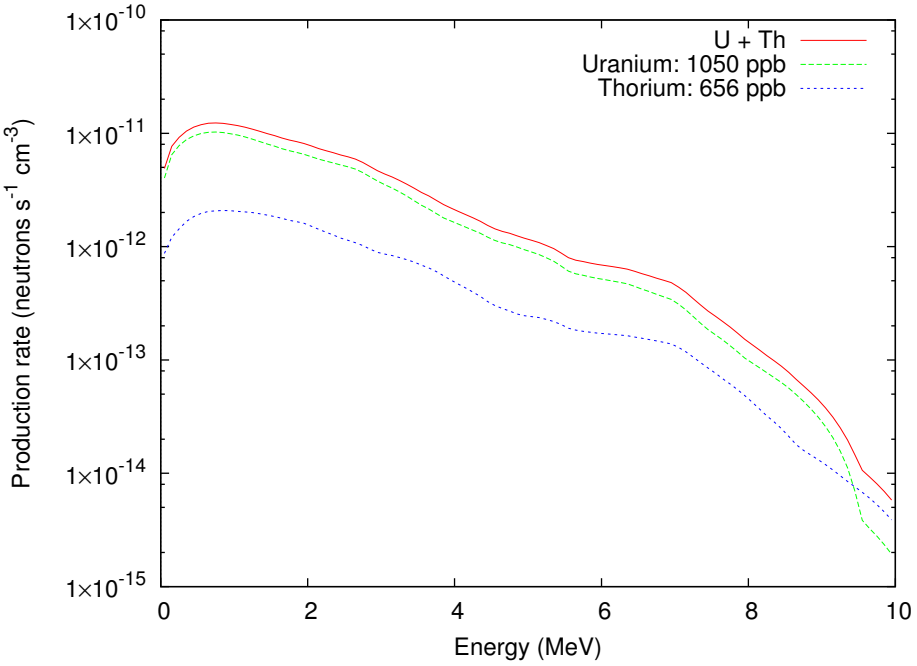

Figure 6.10: Neutron production rate in the concrete at LNGS.

required when the UNDER will perform its neutron flux measurement. The rate the fiducial events in the detector is shown for both gas mixture in Tab. 6.9 assuming 100% nuclear recoil detection efficiency.

^{3}He : He : SF_6	1 : 659 : 100	1 : 749 : 10
Nuclear recoils from the rock $\left(\text{month}^{-1}\right)$	76 ± 13	< 21 (90% C.L.)
Nuclear recoils from the concrete $\left(\text{month}^{-1}\right)$	9331 ± 519	804 ± 181
Total $\left(\text{month}^{-1}\right)$	9407 ± 519	< 825 (90% C.L.)

Table 6.9: Nuclear recoils in UNDER from fast neutrons in Hall B at LNGS.

The results from Tab. 6.9 show that the concrete is the main contributor to the nuclear recoil rate. The moderating effect from the concrete can easily explain the low rate of nuclear recoils from the rock. This is consistent with the fast neutron flux determined by the simulation. Geant4 returned a flux of $(3.784 \pm 0.002) \times 10^{-6}$ neutron/s/cm^2 in Hall B, of which $(3.643 \pm 0.002) \times 10^{-6}$ neutron/s/cm^2 are

due to neutrons from the concrete. The total flux obtained from the simulation is in good agreement with the measured flux $(3.81 \pm 0.11) \times 10^{-6}$ neutron/s/cm^2 from [263]. The simulation presented here shows that UNDER would be capable of making a time-dependent measurement of the neutron flux at LNGS. This would be the first measurement of this kind and could be a significant asset for dark matter experiments which are based on the annual modulation of the WIMP flux. Given a certain modulation of the neutron flux, Monte-Carlo simulations will be able to quantify the change of water content in the concrete. These simulations could then be confronted to the measurements of a hygrometre. Finally, if the annual modulation of the neutron flux is not sufficient to explain the discrepancies between the results quoted in Tab. 6.6 and Tab. 6.5, the directional capabilities of UNDER could provide a solution. For example, fast neutrons emitted from the materials of neighbouring experiments could potentially be detected as a deviation from isotropy. The combination of a directional and time-dependent measurement of a neutron flux, both at fast and thermal energies, could create even more possibilities for NITPCs in the future.

6.4 Conclusion

This chapter has presented a review of some the widely used experimental apparatus used to measure the flux of ambient neutron, either at fast energies or the thermal range. It was shown that the zero background operation of the DRIFT detector and its capacity to reject internal background such as radon events can be used to turn the dark matter detector into an instrument to measure the concentration of ^{238}U and ^{232}Th in the salt rock of the Boulby underground laboratory. This measurement was possible thanks to the detection of 14 nuclear recoils during 45.4 live-days of unshielded exposure of the DRIFT-IId detector. This first attempt is a demonstration of the capabilities of NITPC but the results obtained by DRIFT were limited by the size of the sample of events.

The Geant4 simulation presented in sec. 6.3 has shown that, if confronted with an environment with higher background level, NITPCs may be able to perform the first directional time-dependent measurements of the neutron flux in an underground laboratory. This measurement would constitute an improvement compared to capabilities of Bonner spheres, and could have a substantial impact on the search for dark matter if an annual modulation of the flux of fast neutrons is confirmed, especially if the two oscillations are, indeed, in phase. While it is unlikely that NITPCs will replace Bonner spheres for the measurement of neutron fluxes in high background areas (on the surface for example), the technology is still in its infancy.

Furthermore, the directional capabilities of NITPCs could make them direct competitors of manganese baths. While the measurement of an ambient flux requires being made in situ, radioactive sources can be brought to an underground laboratory where a NITPC can operate more easily. With sufficiently detailed Monte-Carlo simulations, a NITPC could eventually detect the anisotropy of a radioactive source as described in sec. 6.1. Although, while a manganese bath is limited to measuring the neutron fluence of the source, a NITPC might be able to extract a neutron energy spectrum based on the energy of the recoils. For example, simulations done for UNDER collaborators in Italy have shown that there may be a possibility to discriminate between He recoils and fluorine recoils at low pressure based on range.

However, the measurements performed by the DRIFT detector in [146] were only possible because the gamma rejection factor was high enough to exclude Compton scattering as a possible origin for the 14 events. In the following chapter, it will be shown that the intrinsic gamma background can become problematic for larger NITPCs. However, with regards to NITPCs as neutron detectors, the simulations have shown no justification to go beyond the m^3 scale, where DRIFT has demonstrated good gamma discrimination.

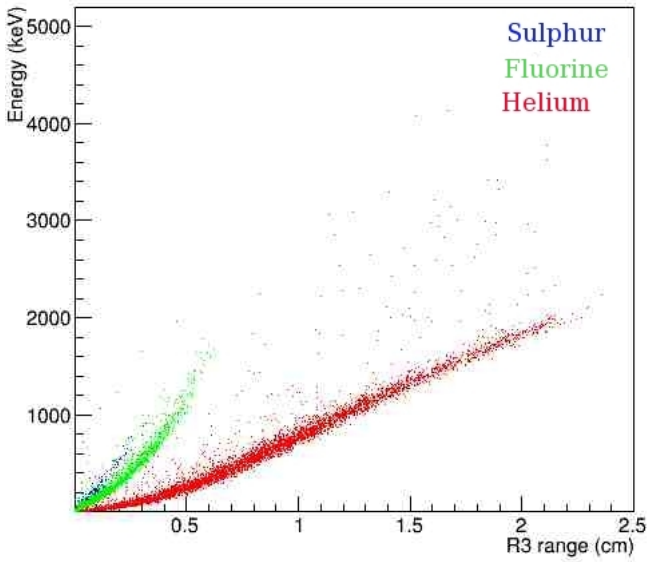

Figure 6.11: Energy vs Track length for nuclear recoils in a 90 : 10 He : SF_6 mixture.

7 Design simulations for the CYGNUS detectors

The CYGNUS proto-collaboration is working towards the development of a family of large scale directional dark matter detector based on the NITPC technology, with the potential inclusion of a nuclear emulsion component. The CYGNUS project originates from the realisation that the largest detectors are expected to reach the neutrino floor soon. For example, XENON-1T is expected to start being sensitive to solar neutrinos at 2 ton $\times$ year [127], while projection sensitivities for larger liquid xenon detector are predicting that sensitivity to atmospheric and supernova neutrinos is achievable with a 200 ton $\times$ year detector [270]. At these levels, new techniques will need to be employed in order to reject the neutrino background. Since neutrinos are weakly interacting, the conventional shielding techniques currently employed for neutrons or gamma rays are of no use. This is why new techniques based on data rejection rather a reduction of the background flux are being investigated. Some of these results are presented in sec. 7.1. The primary focus of this chapter is to evaluate the intrinsic background of a large scale gas TPC. The DRIFT detector has demonstrated in [131] and [146] that zero background can be achieved with a 1 m^3 NITPC. However, the background contribution of internal elements will scale as the size of the detector. Furthermore, lowering the detection threshold of the experiment will also increase the background levels as the detector becomes sensitive to a larger fraction of the incoming flux. In sec. 7.2, the different proposed designs for the CYGNUS detectors are reviewed, and the expected background levels are predicted

using Geant4 based on radio-background assays performed by several other dark matter experiments.

7.1 Potential for neutrino discrimination

A first review of the advantages of the directional direct detection principles was discussed in chapter 2. Most importantly, it was shown that directional detectors would be able to provide an independent assessment of the galactic origin of the signal observed by DAMA. Assuming that the DAMA signal is genuinely induced by WIMP recoils, directional detectors will be able to reconstruct the direction of the WIMP and prove that it is consistent with a WIMP-wind coming from the Cygnus constellation, based on the momentum transferred by the WIMP to a target nucleus. However, the directional capabilities of CYGNUS can also be employed to increase the background rejection efficiency of the experiment. One such example will be the measurement of the modulation of the fast neutron flux at LNGS with UNDER discussed in sec. 6.3. There is a possibility that the annual modulation of the fast neutron flux could account for the DAMA signal. Varying levels of dampness in the concrete could result in local disparities in the neutron flux. For a NITPC like CYGNUS, external neutrons can always be eliminated by increasing the thickness of the outer passive shielding. For neutrinos, however, this is not the case. Nonetheless, the discrimination technique remains the same as the strategy which will be employed by UNDER, especially for solar neutrinos.

A non-directional method is proposed in [271], where the author suggests that if a direct detection dark matter experiment records an annual modulation of its signal, then this signal could be decomposed into its component. This principle is illustrated in Fig. 7.1. In this approach, potential detected annual modulation signals (in blue and purple) can be decomposed as the sum of the annual modulation of the solar neutrino flux and the dark matter signal. This method relies on the fact that there is a phase between the neutrino cycle and the dark matter cycle. Assuming that

neutrinos are produced isotropically at the surface of the Sun, the neutrino flux is then proportional to the solid angle subtended by the Sun. The solar neutrino flux peaks when the Earth is at the perihelion of its orbit in January and is at its minimum when the Earth is at the aphelion of its orbit in July. The annual modulation of the dark matter signal relies on the fact that the Sun is moving through the dark matter halo and that the Earth is rotating around the Sun. In December, the Earth is moving the fastest in the opposite direction of the solar motion, while, in June, the Earth is moving the fastest in opposite direction. The change in the velocity of the Earth through the dark matter halo induces a small variation in the dark matter recoil rate as shown in equation 2.3. Since the two signals are almost out of phase, the author of [271] proposes that the temporal difference between the signal can be used to reject solar neutrino scattering.

This technique, however, inherits from the weaknesses of annual modulation experiments. First of all, the annual modulation effect is of the order of a few percent so very large detectors would be required to make this technique work efficienctly. Many Earth-based backgrounds also modulate throughout the year, one example was discussed with UNDER in sec. 6.3. However, certain background modulations can be harder to account for. For examples, changes in the flux of atmospheric neutrinos measured in the Super-Kamiokande experiment showed no clear seasonal pattern [272]. Using the phase difference between the dark matter event rate and the background signals can provide a way to discriminate events statistically, but as more modulating background are added to the model, the more difficult it will become to extract a clear dark matter signal.

Other studies have suggested that directionality can be used to distinguish between WIMP recoils and solar neutrinos [273, 274]. Directional detection below the neutrino floor is based on the realisation that for most the year, the Sun and Cygnus are not collinear, as illustrated in Fig. 7.2. This means that a directional detector with enough resolution could in principle distinguish between the two populations of recoils. The simulations done in [273] suggest that directional detection with a

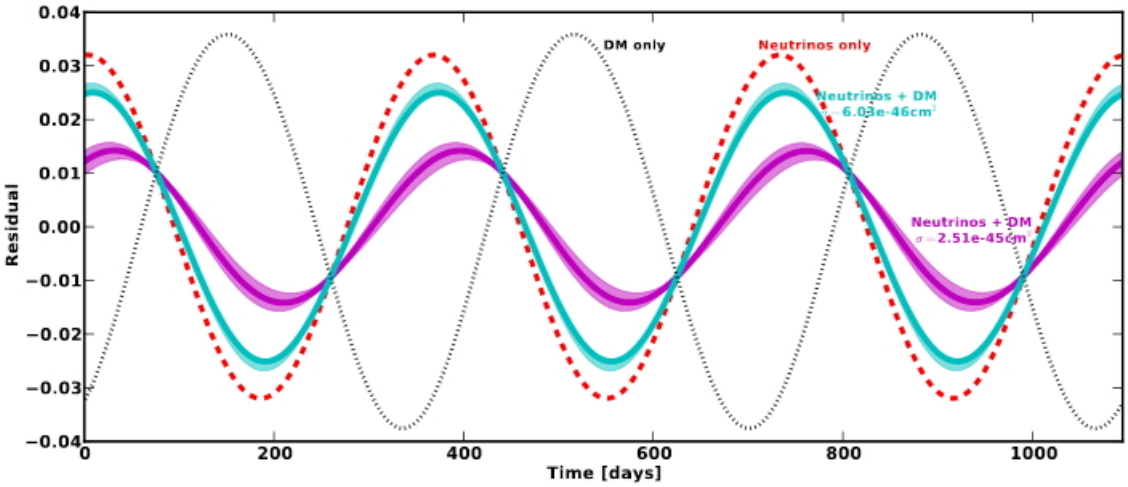

Figure 7.1: Annual modulation of a simulated WIMP and solar neutrino signal. From [271].

light target material can enhance sensitivity to low mass WIMPs, while there is only a marginal gain in the sensitivity to large mass WIMPs recoiling on a heavy target. This result is a confirmation of the interest of using an helium-rich mixture as proposed in sec. 6.3 and for the CYGNUS-10 detector presented in sec. 7.2.

The background rejection power of directional detection can be increased in two ways. Firstly, the detector can be orientated towards Cygnus. For detectors which have less than a full 3D readout, there is a preferred direction in which the head-tail effect of nuclear recoil track is the most prominent. In the DRIFT detector, for example, it was shown in [161] that head-tail can be detected in events collinear with the direction of fiducialisation, while the head-tail parameter for events orthogonal to the Z-direction was consistent with a null result. The results from DRIFT suggest that the properties of the detector can be enhanced if it is properly orientated. For small scale detectors, the TPC can be mounted on an equatorial mount in order to maintain adequate orientation. This method is already used in nuclear emulsion experiments. However, for very large directional TPCs capable of operating below the neutrino floor, this solution would require costly excavations of larger caverns to accommodate heavy equatorial mounts.

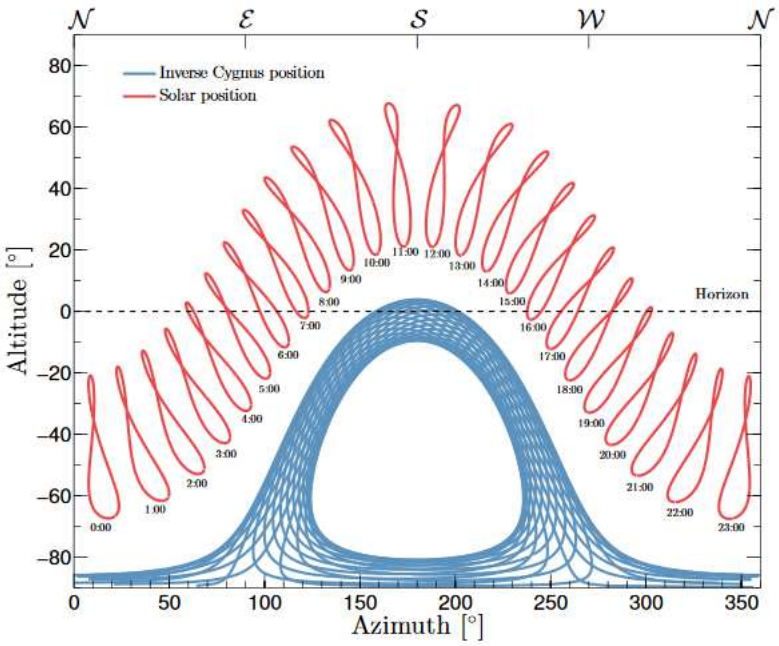

Figure 7.2: Position in the sky in terms of altitude and azimuth of the Sun (red) and Cygnus (blue) at Modane. From [274].

Instead, the second method to full use of directionality is to deploy an array of CYGNUS TPCs in different underground laboratories. The method implies a loss of individual efficiency in each detector since will be properly aligned only twice a day, but by comparing the data between detectors, directionality could increase the background rejection capabilities of an array of CYGNUS detectors. In particular, Fig. 7.3 demonstrates the interest of placing a CYGNUS detector in each hemisphere. Each day, the direction towards Cygnus revolves by 360 degrees with a phase proportional to the longitude of the underground site. For the northern hemisphere sites, the difference in longitude acts as a phase of the modulation of altitude. However, the symmetrical distribution in the southern hemisphere suggests that a directional array of detectors may be able to prove the galactic origin of a dark matter signal indisputably

Overall, the neutrino floor is not a “hard floor” and direct detection experiments can continue to search for dark matter below the neutrino floor. Nevertheless, strategies

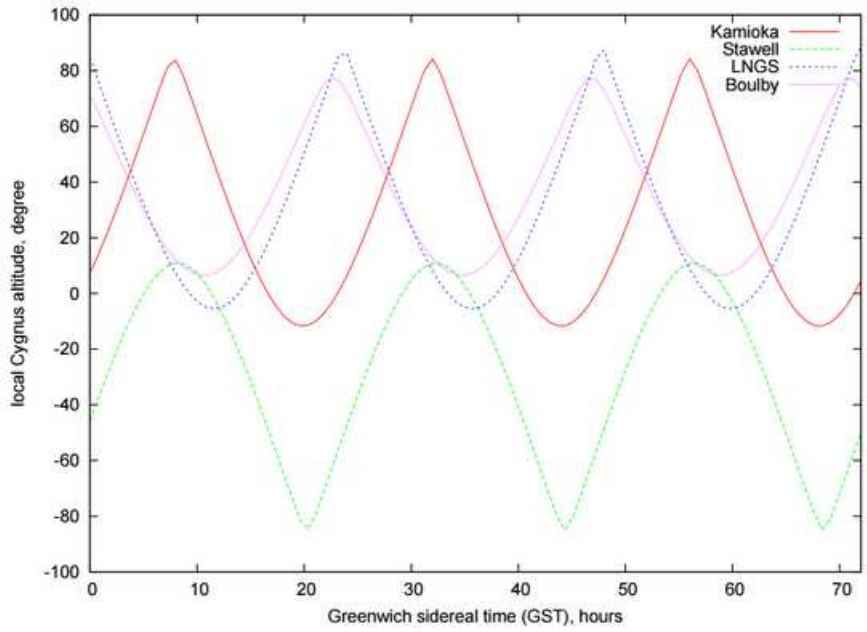

Figure 7.3: Altitude of the Cygnus constellation as a function of time at different underground laboratories.

must be employed to distinguish the two populations. This is particularly the case since the simulations in [275, 274] have shown that a 6 GeV WIMP is expected to produce nuclear recoils indistinguishable from ^{8}B neutrinos if the spin-independent cross section of the WIMP is around 5×10^{-45} cm^2. Nevertheless, there is effectively no neutrino floor for directional detectors due to solar neutrinos. This is due to the fact that the angular distance between the Cygnus constellation and the Sun undergo a sinusoidal modulation [274] between a maximum around 120 degrees and a minimum at 60 degrees. Therefore, directional detectors with sufficient resolution will be able to differentiate between the two origins, or at least during a significant fraction of the year.

7.2 Zero background feasibility in CYGNUS detectors

Neutrinos will be a source of background for the next generation of dark matter experiments. However, rare-event searches are already sensitive to gamma rays and fast neutrons from the radioactive decays of materials. For directional detectors, the additional identification properties from the reconstruction of the initial momentum allow the detectors to operate even with a non-zero level of isotropic nuclear recoils. One example is NEWAGE which can perform directional dark matter searches despite a high rate of nuclear recoil backgrounds as shown in Fig. 2.10. However, directional readout with 3D information rely on materials which high concentrations of radioisotopes compared to simpler readouts. This situation creates a trade-off between different backgrounds (for example, better gamma rejection at the cost of a higher rate of fast neutrons), as well as a balance between the size of the experiment and its background. In this section, the requirements for the purity of the detector materials are investigated in order to achieve an expected rate of less than 1 background event per anticipated exposure time for the different CYGNUS-TPC models.

7.2.1 CYGNUS Models

The simulations presented in the following paragraphs are based on three potential CYGNUS prototypes named after their volume of gas. Overall, five different designs had been envisaged, however, for conciseness only the three most advanced models are presented here. The first prototype called CYGNUS-24 originated from the discussions of the CYGNUS proto-collaboration at the CYGNUS-TPC meeting in Boulby in January 2016. The design consists of steel vessel 2 cm thick which accommodates a gas volume of 6 m (L) $\times$ 2 m (W) $\times$ 2 m (H). This prototype is inspired from the previous DRIFT-III proposal [276]. For example, CYGNUS-24 was

envisaged as a juxtaposition of DRIFT-like TPCs creating a detector which is modulable. This is partly because the structural properties of the salt rock at Boulby makes the excavation of long tunnels easier than the creation of large caverns. It was also estimated that CYGNUS-24 is as large as possible given the dimensions of the new laboratory at Boulby when the required thickness of external neutron shielding is accounted for. In the simulation presented below, CYGNUS-24 is filled with 100 Torr of SF_6. CYGNUS-24 was envisaged to be a demonstrator of the successful use of SF_6 in a dark matter detector. CYGNUS-24 also represented a first attempt at developing directional high-pressure TPCs for dark matter detection by increasing the gas pressure compared to DRIFT by about a factor 2. At the time of writing, the CYGNUS-24 design has been abandoned in favour of developing several smaller CYGNUS-10 detectors which would be deployed at different locations.

The second CYGNUS prototype considered, and referred to as CYGNUS-10 is a smaller 10 m^3 to test directional detection in 1 atmosphere of He and SF_6. The proposals for the CYGNUS-HD detector in the United States [277] and for the CYGNUS-Pathfinder detector in Europe are based on the background simulations presented here. Although the proposed gas mixtures differ slightly between the two proposals, the results presented here are for the CYGNUS-Pathfinder detector filled with 200 Torr of SF_6 and 560 Torr of He.

Finally, the third and largest CYGNUS prototype described in this work is a NITPC with a gas volume with dimensions $10 \times 10 \times 10$ m filled with 50 Torr of SF_6. While studies are underway to evaluate the potential of this detector with a gas mixture similar to CYGNUS-10, only the results of the simulation of the first variant of this detector are presented. It is expected that CYGNUS-1000 will be the first directional detector to reach below the neutrino floor.

7.2.2 Background simulations for the CYGNUS detectors

In this section, a comparison is made between the responses of the different CYGNUS when exposed to the different backgrounds. For internal backgrounds such as the readout materials, the simulations are done with the concentrations of ^{238}U, ^{232}Th and ^{40}K supplied by the different members of the collaboration, as well as rough approximations of the amount of materials required in each detector.

7.2.2.1 Background from the rock

This section discusses the simulation of neutrons and gammas rays originating from the rock of the cavern of the Boulby underground laboratory. Similarly to the simulation of fast rock neutrons for the DRIFT detector, Geant4 was used to sample neutrons from the energy spectrum produced with SOURCES and shown in Fig. 5.11. Neutrons represent a fundamental background for dark matter detectors as their interaction in the detector can mimic a dark matter signal. The flux of external neutrons can easily be reduced by using an external moderator such as the polypropene pellets utilised by DRIFT. For the CYGNUS detectors, the relevant simulation consists in increasing the thickness of the neutron shield until the nuclear recoil rate in the detector becomes less than 1 event/ exposure time. In this case, the exposure time is chosen to be 1 year.

Similarly to the DRIFT neutron simulations, it was found that there exists a linear relationship between the pressure of the gas and the nuclear recoil rate. This is because the probability of double scattering remains small. For instance, at 200 Torr of SF_6, the neutron mean free path of a background neutron is around 62 m. For 200 Torr of SF_6 and 560 Torr of ^{4}He, the neutron mean free path decreases to 55.5 m. However, for helium-based mixtures, rapid departures from the linear relationship between pressure and the nuclear recoil rate were found when comparing results between Geant4 simulations of the same detector. In 560 : 200 Torr of He : SF_6, the results differed by more than 1σ for pressure factors at or above 4 corresponding

to 3040 Torr. Comparatively, for DRIFT-like mixtures, no corrections are needed below 6000 Torr. Rather than to apply an artificial scaling to the Monte-Carlo results, all the neutron simulations presented in this chapter for He : SF6 mixtures are done at nominal pressure.

The DRIFT simulations presented in sec. 5.3.2 have shown that a 50 cm thick water shield is required to reduce the neutron background levels below 1 in 3 years. This result can be used as a starting point for the simulations. However, a thicker neutron shield is required. In sec. 5.3.2, it was shown that at least 75 cm are required in order to decrease the nuclear recoil rate below 1/year. The smaller CYGNUS detector may accept a smaller neutron shield. For example, it was found that the nuclear recoil rate for CYGNUS-24 is 0.7 ± 0.4 year^{-1} with a 62.5 cm thick water shield. The results between CYGNUS-24 and CYGNUS-1000 are approximately equivalent when the differences in mass and pressure are accounted for. This example is an illustration of the validity of the use of a pressure factor for the neutron background simulations in pure SF_6.

Water shield thickness	Detector (R.O.I)	
	CYGNUS-24 $(10 - 50$ keV)	CYGNUS-1000 $(1 - 100$ keV)
50 cm	6 ± 2 /year	57 ± 22 /year
75 cm	< 0.12 /year (90% CL)	< 0.93 /year (90% CL)

Table 7.1: Nuclear recoil rates in the region of interests due to rock neutrons in CYGNUS-24 and CYGNUS-1000 as a function of thickness of the water shield.

The DRIFT detector is an example of the way in which NITPCs can be made insensitive to gamma rays by raising the detector threshold. However, this technique reduces the efficiency of the experiment at detecting possible low mass WIMPs nuclear recoils. This is why preliminary gamma discrimination techniques have been investigated to be implemented in the CYGNUS detectors, these are discussed

in chapter 8. The flux of external gamma rays can be reduced by adding layers of high-Z materials in the shield. These extra materials are necessary since the water shielding has a weak gamma stopping efficiency. For example, the simulated gamma flux was measured in front of the neutron shielding as $(5.77 \pm 0.03) \times 10^{-2}/\mathrm{s/cm^2}$, after 75 cm of water, the gamma ray flux was reduced to $(1.12 \pm 0.02) \times 10^{-2}/\mathrm{s/cm^2}$. The small effect of the water can be explained by the slow, gradual moderation of the gamma rays due to multiple Compton scattering in the water. Effectively, the Compton scattered high energy gamma rays are gradually shifted to lower energies. In water, Compton scattering dominates as the main method of energy loss compared to the photoelectric effect, even at low energy [278]. Tab. 7.2 shows that the 75 cm of water shielding of the CYGNUS-24 detector only provides a factor 10 reduction of the scattering rate due to rock gammas. These results are coherent with the measurements of the simulated gamma flux in CYGNUS-10 before and after the water shield. The recoil rate in the shielded CYGNUS-24 detector about 20 times the gamma rejection factor obtained in DRIFT from the ^{60}Co exposure in sec. 6.2.2. This result shows the importance of developing proper gamma shields for large NITPC, especially since the background rate increases proportionally to the mass of the detector (because the active region of rock increases). In the CYGNUS-1000 detector, shielded with only 75 cm of water, it was found that the gamma background from the rock dominates all other sources in the region of interest with a simulated recoil rate of $(2.82 \pm 0.04) \times 10^{10}$/ year.

The results of the simulation of a graded-Z shield are now presented. This shield is incorporating the 75 cm of neutron shielding for CYGNUS-10. The results above have shown that the neutron shield alone is not providing sufficient gamma stopping power. The results below show the outcome of the simulations of the combined neutron and gamma shielding for CYGNUS-10. The shield is composed of an outer layer of 5 cm thick stainless steel, followed by the 75 cm thick water shield, and finally a 2 cm thick copper shield to intercept the gamma rays produced in the previous layers of the shield. For stainless steel, the GERDA experiment has re-

Isotope	Unshielded rate (year^{-1})	Shielded rate (year^{-1})
^{40}K	$(2.7 \pm 0.6) \times 10^9$	$(2.8 \pm 0.9) \times 10^8$
^{238}U	$(1.9 \pm 0.3) \times 10^9$	$(1.3 \pm 0.6) \times 10^8$
^{232}Th	$(8 \pm 2) \times 10^8$	$(6 \pm 3) \times 10^7$
Total	$(5.4 \pm 0.6) \times 10^9$	$(5 \pm 1) \times 10^8$

Table 7.2: Electron recoil rates between 10 and 50 keV in CYGNUS-24 due to gamma rays from the rock.

ported reaching purity levels which are around a factor 10 below the concentrations of the DRIFT vessels. The concentration of radioisotopes in the stainless steel are 0.081 ppb of uranium, 0.37 ppb of ^{232}Th and 0.026 ppm of ^{40}K [279]. Germanium measurements of the activity of tap water at Boulby [247] have returned concentrations of radioisotopes on par with polypropene pellets. The measurements found activity levels corresponding to 3.09 ppb of uranium, 1.99 ppb of ^{232}Th and 5.12 ppm of ^{40}K. The UKDM database [237] suggests that concentrations nearly two orders of magnitude below can be obtained if the distilled water replaces the tap water. For the results shown in Tab. 7.3, the simulation used distilled water with 0.008 ppb of ^{238}U, 0.009 ppb of ^{232}Th and 0.0084 ppm of ^{40}K.

The inner most section of the gamma shielding is made of copper. Copper has been widely used in rare event search for its high achievable purity and good gamma stopping power. Concentrations of radioisotopes similar to distilled water can be obtained using electroformed copper, for example, high purity materials made of electroformed copper with 0.012 ppb of ^{238}U, 0.011 ppb of ^{232}Th and 0.0056 ppm of ^{40}K are documented in [237]. For comparison, this is around a factor 50 below the concentrations levels of the copper used for the COSINE shield. An overview of the external gamma background for the CYGNUS-10 detectors is given in Tab. 7.3. The current lower limits are dominated by the rock due to its large amount of potassium

(1130 ppm). The limits shown in Tab. 7.3 can be decreased further but this is a long and CPU intensive process due to the sheer amount of active materials. The lack of a pressure factor also means that to decrease the upper-limit (of the gamma background from the rock, for example) by a factor 10^5, the number of simulated events must increase by 10^5. However, the contribution of one layer can always be decreased up to < 1 year^{-1} by increasing the thickness of the next inner layer. In this situation, there is little advantage to pursue a long simulation of the gamma background in the steel and water. Instead, the efforts were concentrated on the copper shield for which the gamma background rate is manageable, but the results shown in Tab. 7.3 benefit from the gamma stopping power of the copper vacuum vessel used in this instance. In the next section, the choice of material for the vacuum vessel will be discussed as well as its impact on the background rate.

Origin	Recoil rate in CYGNUS-10 (year^{-1})
Salt rock	$< 1.6 \times 10^5$ (90% C.L.)
Steel shield	$< 3.3 \times 10^3$ (90% C.L.)
Water shield	$< 1.7 \times 10^2$ (90% C.L.)
Copper shield	< 1.54 (90% C.L.)

Table 7.3: External gamma background for the CYGNUS-10 detector between 1 and 100 keV.

7.2.2.2 Background from the vacuum vessels

Several materials can be considered to design the CYGNUS vacuum vessels. A key consideration in the choice of material is the neutron and gamma background these materials creates. Besides, certain materials lack the structural strength to form a large scale TPC capable of withholding a vacuum. A solution to this problem is to design vessels based on two materials. For example, for a very large TPC such

as CYGNUS-1000, it will be shown that that steel remains too radioactive to be the only component of the vacuum vessel. On the other hand, an acrylic vacuum vessel of the size of CYGNUS-1000 would need important structural supports to withstand the inward pressure from 1000 m^3 of vacuum. A possible solution is to design a vacuum vessel made of acrylic panels placed on a steel skeleton. This option would reduce the mass of steel up to an acceptable vessel while limiting the stress on the acrylic panels. However, for this work, only the background requirements of the experiments are taken into account and only vacuum vessels made of a single material are considered.

Using the neutron production rates for stainless steel produced with SOURCES in Fig. 5.1, the neutron output from stainless steel was calculated for vacuum vessels corresponding to each CYGNUS detectors. For the CYGNUS-24 detector, a mass of 3.16 tonnes was estimated based on the averaged thickness of the DRIFT vacuum vessel and the dimension of the detector given in sec. 7.2.1. For the CYGNUS-1000 detector, the required mass of steel for a vacuum vessel of this size was estimated at 96.5 tonnes [280]. For the CYGNUS-10 detector, the mass of the detector was extrapolated from the mass of CYGNUS-1000. For the CYGNUS-10 simulation, it was assumed that the mass of the vessel scales as the gas volume, this is done because the structure of larger vessels needs to be able to withstand a stronger strain from the vacuum inside the detector. In this case, the steel vacuum vessel of CYGNUS-10 would weight 965 kg. SOURCES predicts that the neutron production rate in stainless steel are 1.48×10^{-10} neutron/s/cm^3/ppb (U) and 4.63×10^{-11} neutron/s/cm^3/ppb (^{232}Th). Assuming the GERDA concentrations of ^{238}U (0.081 ppb) and ^{232}Th (0.37 ppb) [279], the total neutron production rate is 1.15×10^{-5}neutron/s/cm^3. Tab. 7.4 shows that the current level of purity is not sufficient in order to develop large vacuum vessels for TPCs with lower threshold on the order of 1 to 10 keV_r. Simulations were done in order to test the possibility of adding internal acrylic shielding inside the CYGNUS-1000 detector in order to shield the fiducial volume from the neutron produced in the steel vacuum vessel.

However, it was found that nearly 10 cm of solid polypropene is required to bring the neutron background rate below 1/ year.

Detector	Energy range	He : SF_6 (Torr)	Neutron background rate ($year^{-1}$)
CYGNUS-10	$1 - 100$ keV_r	560 : 200	1.747 ± 0.006
CYGNUS-24	$10 - 50$ keV_r	0 : 100	$(6.537 \pm 0.003) \times 10^{-1}$
CYGNUS-1000	$1 - 100$ keV_r	0 : 50	$(2.870 \pm 0.002) \times 10^{2}$

Table 7.4: Nuclear recoil events in the CYGNUS detectors from neutrons from the stainless steel vacuum vessels.

Another option is to build a vacuum vessel made of titanium. The LZ collaboration has investigated several samples of titanium alloy [281] but found no significant improvement to the purity compared to the Ti used in LUX. Using the concentration levels of [281], the CYGNUS-1000 vacuum vessel was populated with neutrons obtained from SOURCES for 20.25 ppt of uranium and 49.2 ppt of ^{232}Th. The neutron production rates from SOURCES are 3.75×10^{-11} neutron/s/g/ppb (U) and 2.027×10^{-11} neutron/s/g/ppb (^{232}Th), in good agreement with the values quoted in [281]. Since the density of Ti is only 4.506 g/cm^3 compared to the 8.027 g/cm^{3}used for stainless steel, the mass the vacuum vessel was decreased to 54.17 tonnes. Using these results, it was found that the nuclear recoil rate in CYGNUS-1000 above the 1 keV_r threshold is 38.54 ± 0.06 $year^{-1}$. Although this result constitutes a real progress compared to the values obtained with stainless steel, the neutron background from Ti remains too high for a TPC of the size of CYGNUS-1000. The addition of acrylic inner shielding in the simulation showed that about 5 cm of inner shield were required in order to reduce the nuclear recoil rate below 1/ year. The Geant4 simulations of the various designs of vacuum vessels have shown that the concentration of U and Th remains too high and that plastic inner shielding is required to lower the nuclear recoil rates. In these simulations, it was assumed that

the acrylic is inert and does not contribute to the neutron flux.

This section will now consider vacuum vessels made of acrylic. As mentioned previously, the simulations presented here are focused on the background from the vacuum vessel and do not consider the issue of the structural strength. Several experiments have worked towards developing ultra-pure acrylic vessels for rare event searches. For example, the DEAP-3600 has reported levels of uranium in the bulk of its acrylic vessel as low as 0.3 ppt of U and 1.3 ppt of ^{232}Th [282]. The SNO+ collaboration has obtained 2.35 ppt of U , 9.60 ppt of ^{232}Th and 67.83 ppb of ^{40}K [283]. Although the DEAP experiment has reached lower concentrations values for uranium and thorium, the simulations presented below were done with the SNO+ values in order to keep the integrity of the data set when comparing with the gamma simulations.

Using SOURCES, its was found that the neutron production rate due to spontaneous fission and (α, n) reactions in perspex is 2.939×10^{-11} neutron/s/g/ppb (U) and 6.171×10^{-12} neutron/s/g/ppb (^{232}Th). For CYGNUS-24, a vacuum vessel of the same dimensions as the stainless steel vessel is expected to be 2.5 cm thick at the minimum [280], corresponding to a mass of approximately 1.7 tonnes. For CYGNUS-1000, an acrylic vacuum vessel capable to house a $10 \times 10 \times 10$ m^3 volume of gas is expected to weight around 47 tonnes. The mass of CYGNUS-10 acrylic vacuum vessel is extrapolated from the mass of CYGNUS-1000 by postulating that the mass of the vacuum vessel is proportional to the volume of gas. In that case, the calculated mass of the acrylic CYGNUS-10 vacuum vessel was 470 kg. Geant4 was used to sample neutrons from the neutron energy spectra produced with SOURCES. Tab. 7.5 shows that the neutron background from the vacuum vessel can be greatly reduced by using high purity acrylic. The background rate in CYGNUS-1000 is slightly above the self-imposed limit of < 1/year, the DEAP collaboration [282] has shown that the neutron background can be reduced by a further factor 10.

The principal argument against an acrylic vacuum vessel is its small contribution to the reduction of the flux of gamma rays and the structural issues it poses. For

Detector	Energy range	He : SF_6 (Torr)	Neutron background rate ($year^{-1}$)
CYGNUS-10	$1 - 100$ keV_r	560 : 200	0.661 ± 0.005
CYGNUS-24	$10 - 50$ keV_r	0 : 100	$(1.006 \pm 0.001) \times 10^{-3}$
CYGNUS-1000	$1 - 100$ keV_r	0 : 50	2.114 ± 0.004

Table 7.5: Neutron background for the acrylic CYGNUS vacuum vessels.

CYGNUS-10, the gamma background rate due to the acrylic TPC vessel was calculated as $(2.9 \pm 0.2) \times 10^6$/year in the $1-100$ keV region. In CYGNUS-1000, the larger vessel induces a gamma background rate of $(2.805 \pm 0.002) \times 10^7$/ year. These numbers are largely above the gamma discrimination potential already achieved by gas TPC experiments. A solution is to develop copper vacuum vessels. Electroformed copper can be manufactured with uranium and thorium concentrations similar to acrylic so the neutron background should remain manageable. However, the concentration of ^{40}K achievable in electroformed copper is around a factor 10 lower [237] than in the SNO+ acrylic, hence reducing the gamma background contribution. Furthermore, a vacuum vessel made of copper would act a further layer of gamma shielding against external radiations and also reduce its own contribution to the total gamma background through self-shielding of its bulk background.

The result of the simulation of a copper vacuum vessel for CYGNUS-10 are now presented. The dimensions of the vessel were assumed to be identical to the CYGNUS-10 stainless steel vacuum vessel, but its mass was increased to match the slightly higher density of copper. This resulted in a copper vacuum vessel with mass 993 kg and radioisotope concentration levels corresponding to the best high purity electroformed copper available at the time of writing: 0.9 ppt of uranium, 1.0 ppt of ^{232}Th and 2 ppb of ^{40}K [284]. The results of the simulations of the copper vessel are shown in Tab. 7.6. Overall, a copper vacuum vessel with purity levels similar to those obtained in [284] can reduce the gamma background rate by 3 orders of

magnitudes compared to a high purity acrylic vessel. Despite their substantial cost, copper vacuum vessels seem to be the best option for background mitigation. In particular, a copper vessel can participate to the reduction of the flux of external gamma rays by increasing the amount of copper in the graded-Z shield without the necessary addition of more materials. Furthermore, the simulations have shown that it is the material available with the smallest contribution to the total gamma background and, that its irreducible contribution is well below the gamma rejection factor obtained in DRIFT [146].

Isotope	Neutron background (year^{-1})	Gamma background (year^{-1})
^{238}U	$(8.0 \pm 0.5) \times 10^{-5}$	$(1.87 \pm 0.02) \times 10^{3}$
^{232}Th	$(1.00 \pm 0.03) \times 10^{-6}$	$(4.38 \pm 0.06) \times 10^{2}$
^{40}K	-	$(1.5 \pm 0.2) \times 10^{2}$
Total	$(8.1 \pm 0.5) \times 10^{-5}$	$(2.46 \pm 0.03) \times 10^{3}$

Table 7.6: Recoil rates due to the neutron and gamma backgrounds in the 1 to 100 keV region for the CYGNUS-10 copper vacuum vessel.

7.2.2.3 Internal and Readout backgrounds

Many of the current directional detectors have been built around different readout technologies. While the backgrounds from the rock and the vessel presented in the previous section are expected to dominate due to their relative size, the detector cannot be shielded from backgrounds originating in the readout materials. This, when added to the large mass of CYGNUS, may represent some limitation of the capabilities of the detector and call for the careful selection of readout materials. This section investigates the rate of background events caused by these materials. The development of the CYGNUS detectors is still at an early stage. Therefore, it is difficult to create a realistic detector with Geant4 in a similar manner to Fig. 4.4.

Also, this level of accuracy is not required to obtain benchmark values which will assist in the development of the future CYGNUS experiments. Instead, a sheet 1 m long $\times$ 1 m high can be drawn in Geant4 at the centre of the gas volume. The simulation is then repeated for the different materials of interest. The width of the sheet is also varied to represent the typical thickness of the material. This is done in order to account for the self-moderation of the background in the materials. Since the sheet is homogeneously populated with neutrons or nuclei, a single simulation is representing both the bulk and surface background. Finally, the results can be scaled to the estimated mass of the material in question. No particular readout was envisaged for CYGNUS-24 before the shift in attention from the collaboration towards the CYGNUS-10 and 1000 designs, therefore, in this section, the simulations are concentrated on the study on these two detectors. In particular, for the CYGNUS-1000 detector, the background levels associated with the different background strategies are investigated.

CYGNUS-1000

The first background to be simulated is the Micro Pixel Chamber readout (μPIC) as used in NEWAGE [285]. The μPIC readout is a pixelated 2D readout with sub-millimetre resolution [286]. The board (shown in yellow in Fig. 7.4) is made of an insulating plastic while the copper anodes (in brown) capture the drifting electrons with the 400 μm region. PCB boards are known to have a high concentration of ^{238}U and ^{232}Th. In particular, the glass polymid making the insulating boards of the NEWAGE μPICs has 1.2 ppm of ^{238}U and 5.8 ppm of ^{232}Th [287]. These concentrations have been a limiting factor since the high output of fast neutrons from the polymid has been overwhelming the detector and can especially be seen in Fig. 2.10. This is why the NEWAGE collaboration has developed a cleaner polymid with no glass cloth reinforcing the structural strength to reduce the radioactivity of the material. The new concentrations of radioisotopes achieved are 2.997 ppb of ^{238}U, 6.642 ppb of ^{232}Th and 13.243 ppm of ^{40}K [287]. In the simulation, an

0.8 mm thick polymid in the μPICs was assumed with a drift distance of 50 cm similar to DRIFT. In this case, based a mass of 1.12 kg/m^2 of readout in NEWAGE [287], it was estimated that nearly 2.2 tonnes of polymid are required to instrument the CYGNUS-1000 detector. In this setup, the neutron background between 1 and 100 keV$_r$ is 64.5 ± 0.3 year^{-1} and the gamma background is $(1.3586 \pm 0.0003) \times 10^8$ year^{-1} in the region of interest.

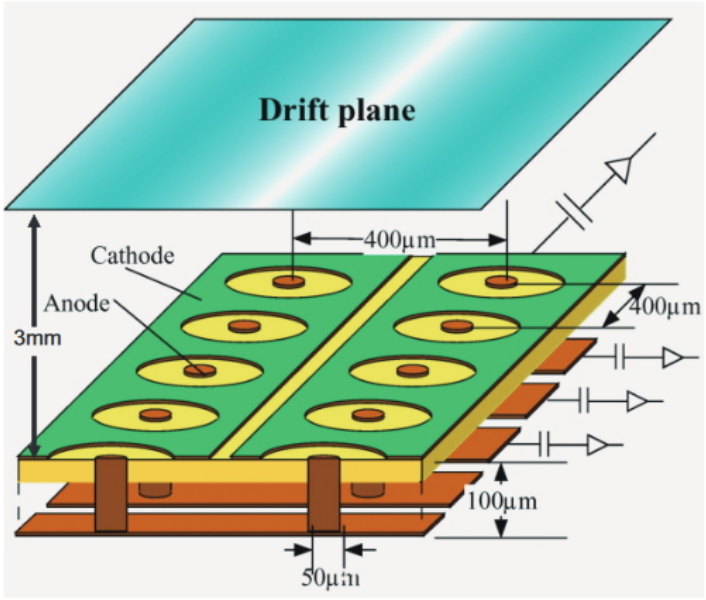

Figure 7.4: Schematic structure of the μPIC readout. From[288].

Secondly, the potential of the Gas Electron Multipliers (GEMs) readout is investigated. GEMs have been used in dark matter directional experiments (such as D^3 [153] or [289]) in conjunction with CCD cameras in order to increase gain in CF_4. They can, however, be used on their own as a simple 1D readout. This option is considered in further details for the CYGNUS-10 detector. This is illustrated in Fig. 7.5. The GEM is composed of a central layer of insulating material (in light grey) in between two thin layers of copper (in dark grey). A Lorentz force accelerates electrons passing through the holes of the GEM. This causes scintillation light through the Bremsstrahlung process, and this light can be collected by a photodiode or a CCD camera placed behind the GEM. On the other hand, the GEM can be used

on its own by reading the charge collecting on the anode of the GEM. In this case, the detector resolution is only as good as the pixelisation of the GEM panels. In the present simulation, a thick-GEM was simulated by summing the contribution of a 0.4 mm thick sheet of Kapton. Other insulating materials are used in GEMs such as FR4 or G10, but it was found that Kapton has lower concentrations of isotopes. On each side of the GEM, a 0.01 mm thick sheet of copper was simulated to represent the anode and cathode. Different experiments such as TREX [290] have looked at the background of copper-Kapton foil but it was found that the best background values for Kapton were 8 ppb of uranium, 9 ppb of ^{232}Th and 1.9 ppm of ^{40}K. In CYGNUS-1000, the estimated total mass of Kapton is 1136 kg. For copper on the other hand, the same concentration values were used as for the electroformed copper of the vessel 0.9 ppt of uranium, 1.0 ppt of ^{232}Th and 0.002 ppm of ^{40}K, with an estimated total mass of 358.4 kg. In this case, the Geant4 simulations suggest a neutron background rate between $1-100$ keV$_\mathrm{r}$ of $(2.292 \pm 0.003)\times10^{-4}$/year^{-1} for the copper and 22.4 ± 0.1/ year^{-1} for kapton. For the gamma background, the simulations predicts the following event rates in the region of interest $(2.785 \pm 0.001) \times 10^4$/ year^{-1} from the copper and $(2.515 \pm 0.001) \times 10^8$/ year^{-1}.

The third option considered is to instrument the CYGNUS-1000 detector with multi-wires proportional chambers (MWPCs) similar to DRIFT. In this case, 3D information can be extracted from the minority carriers and by instrumenting all 3 planes of wires of MWPC. The DRIFT detector and its components are discussed in sec. 4.1. A similar study has been done for wire-based TPCs in [187]. There the authors identified that field cage resistors constitute the main internal source of neutron background. The authors estimate that 70 resistors are needed to operate a DRIFT-like detector, corresponding to 22.6 g of aluminium oxide. However, the TREX collaboration, in their background assay [290], has reported on resistors with much lower background levels than [187]. The TREX values are consistent with concentration levels of 16 ppb of U , 2.80 ppb of ^{232}Th and 2.71 ppm of ^{40}K in aluminum oxide. Using the approximation that CYGNUS-1000 represents 1000 DRIFT

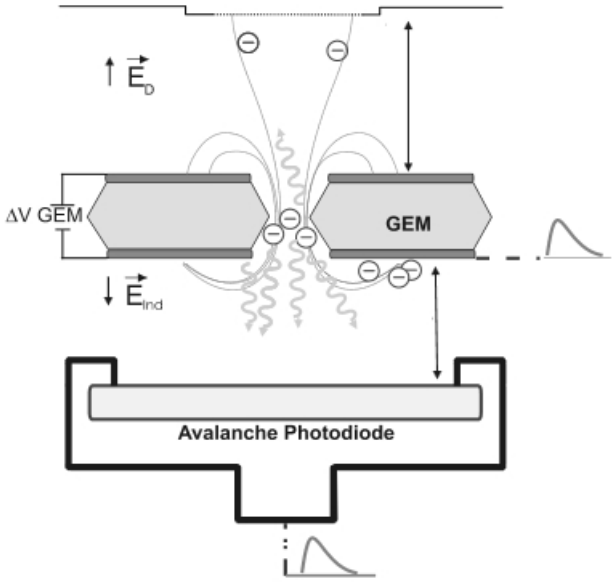

Figure 7.5: Schematic of a GEM based readout. Adapted from [291].

detectors, the amount of aluminium oxide was scaled to 22.6 kg and the associated neutron background rate in the region of interest amounted to 3.02 ± 0.01 year^{-1}, while the gamma background rate is $(2.24 \pm 0.01) \times 10^6$ year. Another possible source of background for MWPC readouts is the steel wires themselves. Although their mass is negligible compared to some other background, the mass of steel of each MWPC must be added for each TPC in CYGNUS-1000, and their combined contribution might add to a noticeable effect. Using the DRIFT detector as an example, it was estimated that each 1 m^2 TPC contains 1.94 g, therefore totaling to 3.9 kg of stainless steel in CYGNUS-1000. It is not entirely clear whether the fabrication process of ultra pure stainless steel such as the GERDA vacuum vessel [279] can be applied to thin steel wires with diameters between tens and hundreds of μm. For this reason, the concentrations of radioisotope measured on the DRIFT-I grid wires were used instead. These concentrations are 1.5 ppb of uranium, 5 ppb of ^{232}Th and 0.2 ppm of ^{40}K. In this case, the Geant4 simulations produced a nuclear recoil rate of $(2.26 \pm 0.01) \times 10^{-2}$ year^{-1} in the region of interest due neutrons originating

from the steel. The electron recoil rate due to the gamma ray emanating from the steel wires is $(7.853 \pm 0.003) \times 10^4$ year^{-1}.

Material	Readout	Neutron background rate in R.O.I. (year^{-1})	Gamma background rate in R.O.I. (year^{-1})
Rock	All	< 0.93 (90% C.L.)	$(2.82 \pm 0.04) \times 10^{10}$
Vessel (Acrylic)	All	2.114 ± 0.004	$(2.805 \times 0.002) \times 10^7$
Polymid	μPIC	64.5 ± 0.3	$(1.3586 \pm 0.0003) \times 10^8$
Copper	GEM	$(2.292 \pm 0.003) \times 10^{-7}$	$(2.785 \pm 0.01) \times 10^4$
Kapton	GEM	22.4 ± 0.1	$(2.515 \pm 0.001) \times 10^8$
Steel wires	MWPC	$(2.26 \pm 0.01) \times 10^{-2}$	$(7.583 \pm 0.003) \times 10^4$
Resistors	MWPC	3.02 ± 0.01	$(2.24 \pm 0.01) \times 10^6$

Table 7.7: Background summary for the CYGNUS-1000 detector.

To conclude on the readout simulation for CYGNUS-1000, it is important to say that the results presented here are simply based on a sample of a few materials, rather than a full detector design. Nonetheless, these figures can be used as benchmarks to orientate the effort to develop materials with lower concentrations of radioisotopes. A summary of the background event rates is given in Tab. 7.7. Overall, there is no particular obvious choice of readout based on the background levels, given the importance of the gamma background at the chosen 1 keV$_r$ threshold, it is likely that the final readout will be selected based on its gamma rejection capabilities and directional sensitivity (for dark matter search). The previous sections have shown that the contribution of external background sources can be reduced with the installation of sufficient graded-Z shielding. For the vessel and readout materials, background assays performed by other low background experiments are searching for materials with lower radioactivity levels. The CYGNUS collaboration is also involved in the development of more efficient readouts, one example being the development of

larger thick GEMs [292] or the significant reduction of the background levels in the NEWAGE μPICs [287]. Furthermore, most of the estimations of the required masses of materials were based on proportionality compared to a 1 m^3 detector. As the design effort for CYGNUS-1000 progresses, these numbers may be refined, or the design could be modified in a way that reduces the number of background emitters. For example, the design could consist of back to back TPCs such that each TPC either share a cathode or a readout plane. The readout electronic could be shielded from the gas volume or pushed outside of the vessel is possible as it planned for the CYGNUS-KM prototype [292]. Finally, the CYGNUS collaboration is working on Monte-Carlo models to find new parameters and veto cuts which could increase the gamma rejection capabilities of the detector. This effort is taking place in parallel in different institutions, but the current state of the Sheffield effort is presented in chapter 8.

CYGNUS-10

A detailed estimation of the amount of materials required for CYGNUS-10 was done for the proposed CYGNUS-Pathfinder detector already mentioned in sec. 7.2.1. This detector is based on a 1D thick GEM readout. Some of the results for this detector were already presented in the previous section, such as the graded-Z shield to reduce the flux of external gamma rays in sec. 7.2.2.1, or the overview of the background rate from the vacuum vessels made of different materials in sec. 7.2.2.2. This section deals with the results of the background simulations for the other materials contained in the detector and concludes on the total neutron and gamma background rates for CYGNYS-10.

The field cage is composed of 50 kg of acrylic for the cage frame and 100 g of copper for the field rings. For acrylic, the concentrations of radioisotopes obtained by the SNO+ collaboration were used [283], 2.35 ppt of uranium, 9.60 ppt of ^{232}Th and 67.83 ppb of ^{40}K, with the neutron production rates obtained from SOURCES for perspex 2.939×10^{-11} neutron/s/g/ppb (U) and 6.171×10^{-12} neutron/s/g/ppb (^{232}Th).

The rate of neutron background event in $1 - 10$ keV$_r$ region of interest was found to be $(3.0 \pm 0.1) \times 10^{-5}$ year^{-1}, while the rate of gamma background events is $(1.6 \pm 0.2) \times 10^{3}$ year^{-1}. For the copper field cage, the concentrations of radioisotopes for the electroformed copper found the NEXT experiment [284] were used, 0.9 ppt of uranium, 1.0 ppt of ^{232}Th and 2 ppb of ^{40}K, combined with the neutron production rates from SOURCES: 1.354×10^{-11}neutron/s/g/ ppb (U)and 4.605×10^{-13} neutron/s/g/ppb (^{232}Th). In this case, the rate of gamma background events in the region of interest is $(1.0 \pm 0.1) \times 10^{-2}$ year^{-1}, and the rate of neutron background events is $(3.56 \pm 0.06) \times 10^{-8}$ year^{-1}.

For the readout, 36 panels of thick GEMs were assumed, each measuring 35×35 cm^2, with the layer of Kapton being 0.13 mm corresponding to 814 g of Kapton, while the copper on each side of the GEMs is 0.5 μm thick which leads to 39.34 g of copper. Using the concentrations and neutron production rates for copper given above, the background rates in the region of interest were found to be $(1.36 \pm 0.02) \times 10^{-8}$ year^{-1} for neutrons and $(3.9 \pm 0.9) \times 10^{-3}$ year^{-1} for gamma rays. For Kapton, the UKDM [237] concentrations of isotopes were used, corresponding to 8 ppb of uranium, 9 ppb of ^{232}Th and 1.9 ppm of ^{40}K which gives a gamma background rate of $(8.9 \pm 0.5) \times 10^{2}$ year^{-1}. Using the neutron production rates from SOURCES, 3.457×10^{-11} neutron/s/g/ppb (U) and 8.945×10^{-12} neutron/s/g/ppb (^{232}Th), the rate of neutron background events is $(9.2 \pm 0.3) \times 10^{-5}$ year^{-1}.

In sec. 5.2, it was shown shown that the z-fiducialisation can be used to reject radon progeny recoils on the surface of the cathode with an efficiency much greater than the expected lifetime of the experiment. However, the decay of radon progeny on the cathode can produce gamma rays which will find their way into the fiducial volume. Similarly, RPRs are detected in the analysis since they appear as potential nuclear recoil events when the α particle is trapped inside the cathode. In this case, there is a chance the α particle could be absorbed and that a fast neutron is emitted through (α, n) reactions. This possibility will now be discussed. The DRIFT collaboration has developed a thin 0.9 μm cathode of aluminised Mylar [213]. Assuming a 1 m

DRIFT distance, the total mass of Mylar in the CYGNUS-10 detector was estimated to be 6.26 g. Concentrations of radioisotopes for the aluminised Mylar can be found in [237], and using 0.2 ppb of U, 3 ppb of ^{232}Th and 50 ppm of ^{40}K , the rate of gamma background events in the signal region is $(2.93 \pm 0.02) \times 10^3$ year^{-1}. It is not possible to draw the textures of the cathode in Geant4. However, it was measured in [214] that the probability of an α particle being absorbed in the 0.9 μm thick Mylar is 1.3%. This value has a small dependence of the α energy, but for this simulation, it was assumed to be constant. This probability was measured for a cathode with no textures. The comparison between a "straight" and textured cathode in [214] found that the probability of absorption is reduced by 23%. Therefore, a scaling factor of 0.772% was applied to the neutron production rates in Mylar obtained from SOURCES. The unscaled production rates are 2.789×10^{-11} neutron/s/g/ppb (U) and 5.590×10^{-12} neutron/s/g/ppb (^{232}Th). The Geant4 simulation of neutrons sampled from the energy spectra produced by SOURCES showed that the rate of neutron events between $1-10$ keV$_\mathrm{r}$ is $(1.17 \pm 0.03) \times 10^{-8}$ year^{-1}, when all correction factors are applied.

Finally, the gas mixture itself can be a source of background in the detector, although the gas cannot contribute to the neutron background. The radon in the gas disintegrates through α decays. For this α to produce a neutron, it must be absorbed by a nucleus which can then undergo an (α, n) reaction. However, this is not an instantaneous process, so the α particle will ionise the gas along its track and the neutron produced from the (α, n) reaction can be vetoed through a coincidence analysis. The only background contribution from the gas, therefore, comes from the β decays of the late thorium chain. Assuming secular equilibrium, Geant4 was used to simulate the gamma rays from the decay of ^{214}Pb and ^{214}Bi using the energies and branching ratios given in [293] and shown in Tab. 7.8. The concentration of ^{238}U used were measured in [237] for CS_2: 0.6 ppt and assumed firstly that the same levels of purity can be achieved for the He : SF_6 mixture of CYGNUS-10, secondly that there is secular equilibrium in the uranium chain. Finally, the contribution of

the gas to the gamma background is $< 3.5 \times 10^{-2}$ year^{-1} (90% C.L.) in the signal region.

Radionucleid	β Energy (MeV)	Branching ratio (%)
^{214}Pb	1.02	6
	0.70	42
	0.65	48
^{214}Bi	3.27	18
	1.54	18
	1.51	18

Table 7.8: Energies and branching ratios of the β decay of the ^{222}Rn chain. From [293].

To conclude the background simulations for the CYGNUS-10 detector, the results of the background simulation are summarised in Tab. 7.9. The neutron background is small enough such that background-free status is achievable under the condition that the gamma discrimination power of the detector is sufficient. External backgrounds originating from the rock and the shield can be shielded until the < 1 event/year is reached, at the cost of additional shielding. However, with no pressure factor to accelerate the simulation the gamma backgrounds, it will require a substantial amount of computing power to bring the Monte-Carlo rates to this level. Nonetheless, the total gamma background rate from the vessel and the internal components is well below the gamma rejection factor obtained with DRIFT [146] so it may be possible to reach background-free status at 1 atmosphere of He : SF_6 with CYGNUS-10. The ongoing effort to develop new gamma rejection cuts in SF_6 and SF_6 based mixtures are discussed in chapter 8.

Material	Neutron background rate in R.O.I. (year^{-1})	Gamma background rate in R.O.I. (year^{-1})
Boulby rock	< 0.9 (90% C.L.)	$< 1.6 \times 10^5$ (90% C.L.)
Graded-Z shield	$< 4.64 \times 10^{-5}$ (90% C.L.)	$< 3.5 \times 10^4$ (90% C.L.)
Copper Vessel	$(8.1 \pm 0.5) \times 10^{-6}$	$(2.46 \pm 0.03) \times 10^3$
Field cage copper	$(3.56 \pm 0.06) \times 10^{-8}$	$(1.0 \pm 0.1) \times 10^{-2}$
Field cage acrylic	$(3.0 \pm 0.1) \times 10^{-5}$	$(1.6 \pm 0.2) \times 10^3$
GEM copper	$(1.36 \pm 0.02) \times 10^{-8}$	$(3.94 \pm 0.9) \times 10^{-3}$
GEM Kapton	$(9.2 \pm 0.3) \times 10^{-6}$	$(8.9 \pm 0.5) \times 10^2$
Cathode	$(1.17 \pm 0.03) \times 10^{-8}$	$(2.93 \pm 0.02) \times 10^3$
Gas	-	$< 3.5 \times 10^{-2}$ year^{-1} (90% C.L.)

Table 7.9: Summary of the background simulations for the CYGNUS-10 detector.

7.2.2.4 Muon-induced neutrons

Muon-induced neutrons were simulated in the case of the salt rock at Boulby using the MUSUN Monte-Carlo code [294] for the CYGNUS-1000 detector. MUSUN takes into account the angular profile and the composition of the rock overburden for the transportation of cosmic ray muons as calculated by MUSIC. Muons tracks can be distinguished from nuclear recoils due to their length and the fact that muons (as charged particles) will ionise the gas along the track. However, muons can produce neutrons through two different processes. High energy muons interacting with nuclei can induce spallation. At lower energies, muons can interact with hydrogen atoms to produce fast neutrons [209]. For example, these interactions are the basis of muon-induced fusion experiments [295]. The Coulomb capture of the muons happens in the higher orbitals due to the muon energy. The muon may then move to the

ground state energy through electronic de-excitation. There is then a chance of fusion between the muon and the nucleus which can produce a neutron.

In the simulation, the muons are produced on the surface of a cube of 40 m of rock to allow for 20 m of rock on each side for the muons to interact. The rock is modeled as pure NaCl with density 2.17 g/cm^3. A cubic cavern filled with air with 13.5 m length on each side is placed at the centre of the rock. The CYGNUS-1000 detector and its neutron shielding are placed centrally in the cavern. Muons veto were added to the simulation on each side of the detector, excluding the bottom side. Since the muons originate in the atmosphere, it is expected that the overwhelming majority of muons are travelling downwards. Underground laboratories built under mountains may see an enhancement of the muon flux in the directions corresponding to the flanks of the mountain since the profile of the mountain is creating a variation of the overburden. This is not the case for Boulby as it is built under flatland. The CYGNUS-1000 muon veto is modelled as 1 cm thick sheet of plastic.

More than 200 million muons were produced with MUSUN with energies between 0 and 10^6 GeV. These muons are propagated through the remaining rock using Geant4. The mean muon energy is 269.3 GeV and the muon energy spectrum is shown in Fig. 7.6. Normalisation of the Monte-Carlo is achieved by counting the number of muons penetrating the cavern and by comparing this number to the flux of muons at Boulby $(4.09 \pm 0.15) \times 10^{-8}$ cm^{-2}s^{-1} measured in [296]. Using this technique, it was possible to verify the results of the simulation of [187] for a 1 m^3 DRIFT-like detector.

Several cuts were applied to the simulated data. First of all, any event in the gas which shares the same event number as a muon recorded in the veto volume is rejected. Secondly, some nuclear recoils were observed with very high energies. These events are induced by muons at the high energy end of the spectrum and would be outside of the signal if a cut on the maximum energy was installed, similarly to the NIPs < 6000 cut in DRIFT. The region of interest is therefore limited to $1 - 100$ keV$_\mathrm{r}$ as it is the case in the other simulations presented above for CYGNUS-

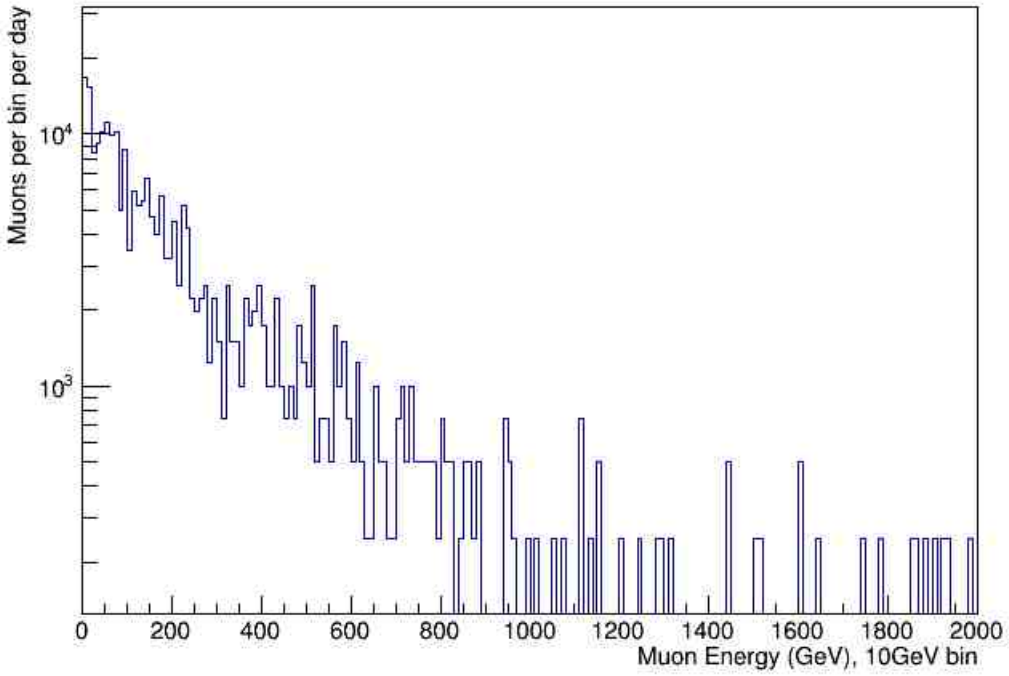

Figure 7.6: Simulated muon energy spectrum at Boulby.

1000. Thirdly, as discussed in sec. 7.2.2.1, the neutron mean free path is such that the probability of neutrons double scattering in the detector in negligible. However, a significant fraction of nuclear scattering events was accompanied by one or several other particles (generally an electron) with the same event number. This means that the same muon both produces the neutron causing this nuclear recoil and the detected electrons. This coincidence cut was able to reject about half of the events recorded in the detector. This result is in good agreement with the similar simulation done in [187]. However, since this veto cut relies on the detection of electrons, it was not possible to increase the pressure and use the proportionality between pressure and the nuclear recoil rate. Finally, using the comparison between the measured and simulation muon flux in the laboratory, it was calculated that the simulation corresponded to $(2.8 \pm 0.1) \times 10^7$ s or 324 ± 12 days during which no nuclear recoil event successfully passed through all 3 cuts. This result gives an

upper-limit on the rate of non-vetoed nuclear recoils due to muon-induced neutrons of $< 8.71 \times 10^{-8}$ s^{-1} (90% C.L.) or < 2.75 year^{-1} (90% C.L.). This rate is below or comparable to the rate of nuclear recoils due to the radioactivity of some of the readout materials in CYGNUS-1000. Overall, this simulation shows that by using discrimination techniques based on the coincidence of nuclear recoils with other forms of energy deposition, the muon background can be brought down to a manageable level.

7.3 Conclusions

This chapter presented a discussion of the difficulty that neutrinos pose to dark matter direct detection experiments. Despite its name, the neutrino floor is not a hard floor and direct detection experiment can continue to probe this region of the parameter space. However, since neutrinos are an irreducible background, new strategies must be employed to reject this veto. In [297], the authors suggest that the neutrino background can be subtracted from the data based only on the recoil energy due to the different tails of the recoil energy spectra. The weakness of this technique is that it requires extensive datasets to be effective. The study done in [271] shows that solar neutrinos can in principle be distinguished from WIMP interaction since both signals modulate with a phase difference. However, it is not obvious how well this method would fare when the annual (or biennial) modulation of the other background sources are taken into account in the model. It is likely that any discrimination done in this way would lead to a weak and unreliable dark matter signal.

On the other hand, the simulations in [273, 274] have shown that, effectively, there is no neutrino floor from solar neutrinos for directional detectors. This is because the angular separation between the Cygnus constellation and the Sun never drops below 60 degrees [274]. The CYGNUS proto-collaboration aims to seise this opportunity for directional detectors to really contribute in this region of the parameter space.

The goal of the collaboration is to develop a NITPC capable of reaching the neutrino floor. Both the CYGNUS-10 and CYGNUS-1000 are expected to reach this goal. However, it is not certain that diectionality can be achieved in CYGNUS-10 at 1 atm.

In order to reduce the hazards of going from operating a 1 m^3 detector directly to a 1000 m^3 detector, the collaboration has envisaged a series of smaller detectors acting as intermediate steps. The background simulations presented in this chapter for the different CYGNUS designs aimed at verifying whether directional TPCs of these scales could, in principle, achieve backgrounds low enough to reach its scientific goals. Each readout technology has a specific intrinsic background and discrimination capabilities. The task of the collaboration is to find the best trade off between the two aspects. In this chapter, the simulations focused on the background aspect of the problem. Overall, it was shown that provided that the materials are carefully chosen, the fast neutron background rate can be contained to acceptable levels, especially if the readout technology and installation are optimised to reduce the required amount of material, or use less radioactive materials. The simulations have shown that the radon background, in the form of cathode RPRs can be rejected such that less than one event is expected in the fiducial volume during the lifetime of the experiment. For the muon-induced neutron background, the use of muon veto panels and coincidence analysis are sufficient to keep the nuclear recoil rate under control. In fact, the difficulty of operating a 1000 m^3 NITPC with a low threshold is to maintain the gamma background in check. Efforts are underway in the collaboration to develop Monte-Carlo models capable of discriminating between electron and fluorine tracks. Nonetheless, the preliminary results of the simulation of electron and fluorine tracks in SF_6 suggest that discrimination factor up to 10^4 could be achieved even with a 1D readout below 10 keV_{ee}. An overview of the current state of the simulation is discussed in chapter 8.

8 Preliminary gamma discrimination strategies

The background simulations for the CYGNUS detectors have shown that the gamma background largely dominates over the other backgrounds. Especially for the case of CYGNUS-1000, Tab. 7.7 has shown that the gamma rejection factor which must be obtained in order to make the detector insensitive to gammas must be on the order of 10^{-8} at the 1 keV threshold. The gamma rejection factor for DRIFT calculated in this work is $< 2 \times 10^{-7}$ (90% C.L.) with a threshold around 30 keV. Each readout has a different resolution, and some readouts only produce 1D or 2D information. This means that the gamma rejection cuts may depend on various parameters specific to particular readouts. This is why the different groups within the CYGNUS collaboration are concentrating on different technologies. A first step is to demonstrate sufficient discrimination in the $1 - 10$ keV region for CYGNUS-10. This only required discrimination around 10^{-4} at 1 keV. This chapter presents an overview of the current situation of the ongoing Monte-Carlo simulations of electron and fluorine tracks in SF_6 or SF_6 based mixture and the search for efficient discrimination parameters for 1D gamma discrimination with a GEM readout.

8.1 Quartile integration method

The fluorine recoils are simulated using the SRIM package [298], while electrons are simulated using the CASINO software [299]. It was found that the simulation

of low energy electron tracks in Geant4 induced artefacts with both the Livermore and Shielding libraries. The objective of the simulations is to determine the electron track discrimination capabilities of a NITPC with 1D readout filled with SF_6. These simulations are therefore relevant for both the CYGNUS-10 and CYGNUS-1000 detector.

For the fluorine recoils, the detector is assumed to be aligned in the direction of CYGNUS such that the fluorine recoils are orientated in the Z-direction. This corresponds to an optimal scenario, but it is expected that this approximation could, for the moment, increase discrimination. For the electron recoils, CASINO is a beam simulation so once the output of the code is recorded, each electron track is assigned 3 random angles uniformly chosen between 0 and 360 degrees. The position vector of each track is then multiplied by 3 rotation matrices (one in each direction) where the rotation angle is one of the 3 random number generated.

In the ideal case where there is no diffusion of the charge in the track, electron tracks are statistically longer than fluorine recoil tracks as shown in Fig. 8.1. However, with diffusion, the two distributions are expected to overlap further. The simulation utilises a homemade diffusion code. This code contains two steps. Firstly, the code makes a transition between the unphysical steps of the Monte-Carlo and sums the energy loss in the steps until it reached the W-value. The W-value is defined as the energy required to form one electron / positive ion pair. For the simulation, the chosen W-value was W=35.45 eV based on the measurements done in [300]. Once the energy deposited in the gas becomes greater or equal to the W-value, an electron is placed into the gas. Its position is calculated as the barycentre of the corresponding section of the track. The longitudinal diffusion for $600 - 800$ V/cm in 20 Torr of SF_6 has been measured in [289] to be $\sigma_0 = 116.2\,\mu\text{m}/\sqrt{\text{cm}}$. The longitudinal diffusion is modelled by first assigning an absolute Z position to the track. A random number generator chooses this number with a flat distribution between 11 and 48 cm. These limits are chosen to emulate the z cuts in DRIFT. After this step, the z coordinate of each electron along the track is modified is a

function of the form

$$z' = z + \times f\left(z|0, \frac{\sigma_0}{2}\right),$$

where z' is the diffused z coordinate, z is the original z coordinate of the electron, and $f\left(z|0, \frac{\sigma_0}{2}\right)$ is a Gaussian distribution with mean 0 and standard deviation $\frac{\sigma_0}{2}$. The factor $1/2$ in the equation is added because $\sigma_z = \sigma_0 \times \sqrt{L}$ is the major axis of the diffused electron could. Since $f\left(z|0, \sigma_0\right)$ can take both negative and positive values the standard deviation of the distribution needs to be half of the semi-major axis of the ellipse.

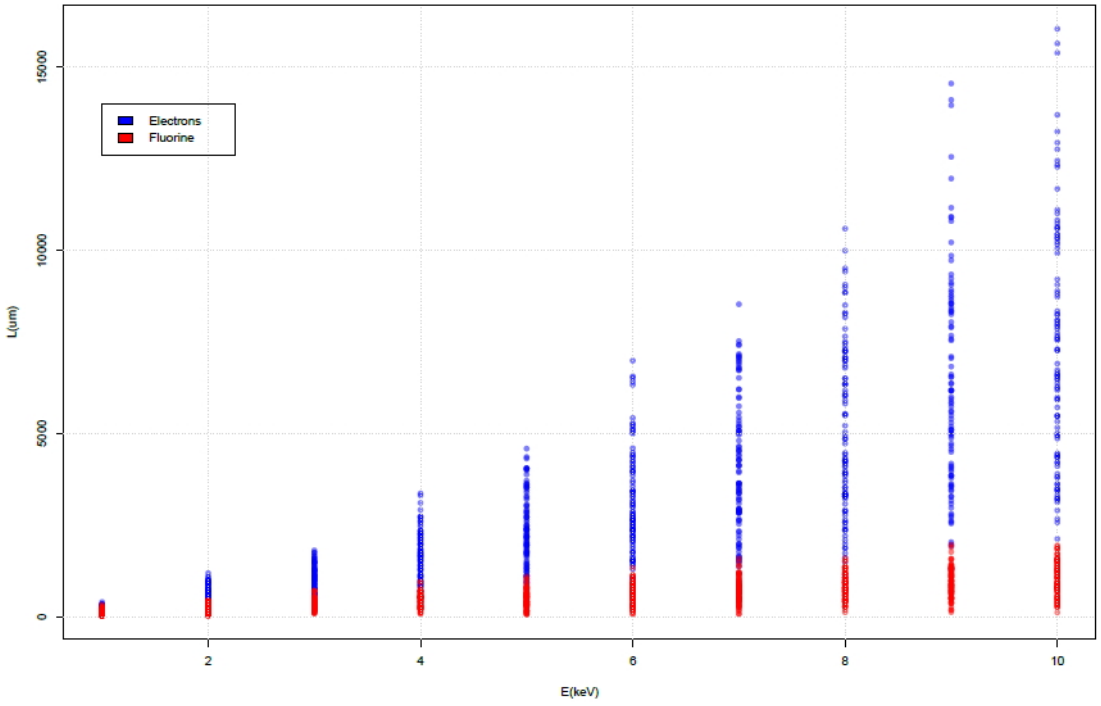

Figure 8.1: Track length vs energy for electron tracks (blue) and fluorine tracks (red) in 20 Torr of SF_6. From [301]

Fig. 8.2 shows a 10 keV electron track in 560 : 200 Torr of He : SF_6 before and after the diffusion function is applied. On average, there is more straggling for electron tracks than for nuclear recoils. These changes of directions are due elastic Møller scatterings ($e^- e^- \rightarrow e^- e^-$) [302]. An interesting result from the Monte-Carlo simulation is that the main structures of the electron tracks remain after diffusion.

This means that the variations in the shape of the electron track are potentially important. On the other-hand, the head-tail effect dominates for nuclear recoils. One of the tested method of discrimination, nicknamed quartile integration is based on this difference. This method consists in integrating the charge Q_i of each 1/4 of the z-projected pulse. For nuclear recoils, the head-tail effect means that there is more charge in the first half of the track than in the second half. The first step of the quartile integration method is to assign "head" to the most energetic charge 1/2 of the track. The second step is to compare the two quartiles of the "head" half of the track. If "head" is assigned to the beginning of the pulse then the second head-tail ratio is defined as $\frac{Q_2}{Q_1}$, while if "head" is the end of the pulse, the second head-tail ratio is defined as $\frac{Q_3}{Q_4}$. Overall, the quartile integration method is a measure associated to the skewness of the track.

Fig. 8.3 shows the second head-tail parameter for 100 electronic and fluorine tracks of 10 keV_e assuming a quenching factor of 0.4. The fluorine distribution is centred around 1 due to events such as the one shown in Fig. 8.4 where the integrated energy loss between the first two quartiles is nearly constant. The high-end tail of the fluorine distribution is due to events with a more pronounced rate of energy loss. For electrons, the sharp Bragg peaks simulated by CASINO at the end of the electron tracks create a large population with a small second head-tail parameter. Although the two populations follow different distributions, the significant overlap between them means that the gamma discrimination capabilities of this technique are below 1 in 100 at 10 keV_e.

8.2 Pulse length discrimination

Another possible route to develop 1D discrimination techniques for CYGNUS is to emulate the DAMA cuts shown in 3.4 used in the COSINE-100 analysis to eliminate the short pulses from the PMT noise. This technique is essentially based on the length of the projected pulse. Fig. 8.5 shows the difference between the averaged

energy loss along the z projection of the track for 100 4 keV$_e$ electrons and fluorine recoils. By defining the discrimination parameter D as

$$\mathrm{D} = \frac{\int_0^{\mathrm{z_{cut}}} \frac{\mathrm{dq}}{\mathrm{dz}} \mathrm{dz}}{\int_0^{\mathrm{20mm}} \frac{\mathrm{dq}}{\mathrm{dz}} \mathrm{dz}}, \tag{8.1}$$

where $\frac{\mathrm{dq}}{\mathrm{dz}}$ is the energy loss per bin, it is possible to select short pulse consistent with nuclear recoils and reject the longer electron tracks. A natural way of selecting of the parameter $\mathrm{z_{cut}}$ is the crossing point between the electron and the fluorine distribution. This value depends of the total energy of the recoil but this value is already calculated by the integral on the denominator. For fluorine recoils, the short duration of the pulse will give $\mathrm{D} \approx 1$ while most of the electron will have $\mathrm{D} \ll 1$ due to the fact that, on average, electrons have longer tracks. In this case, Fig. 8.6 shows that 10^2 discrimination is possible at 4 keV$_\mathrm{e}$ with 80% efficiency based on the preliminary sample of events simulated.

8.3 Conclusion

Geant4 simulations have shown that the background due to the presence of radionuclides in the detector's material is a key issue for the development of large scale dark matter NITPCs such as CYGNUS. In particular, the gamma background rate can be of the order of 10^3 events per year for the CYGNUS-10 detector as shown in Tab. 7.9. The only information recorded by a 1D readout is time and electric charge. With no position information, the options to develop new discrimination techniques are more limited than for full 3D readout. Nonetheless, the intrinsic difference between electron and nuclear recoil tracks can be used to distinguish between the two. Given the present preliminary results, the discrimination method based on the length of the track seems to have more potential than other methods based on the straggling of the electrons. The veto cut based on pulse length discussed in sec. 8.2 has shown that at 4 keV$_e$ 10^2 discrimination is possible with an 80% efficiency. Other methods have confirmed that a discrimination of 10^4 is achievable at 4keV$_e$ [303] with a full

3D readout, or a discrimination of $\sim 10^3$ at 10 keV_e with a 2D readout. Further simulations and modifications to the model may improve this technique further such that sufficient discrimination may be obtained for the CYGNUS-10 detector.

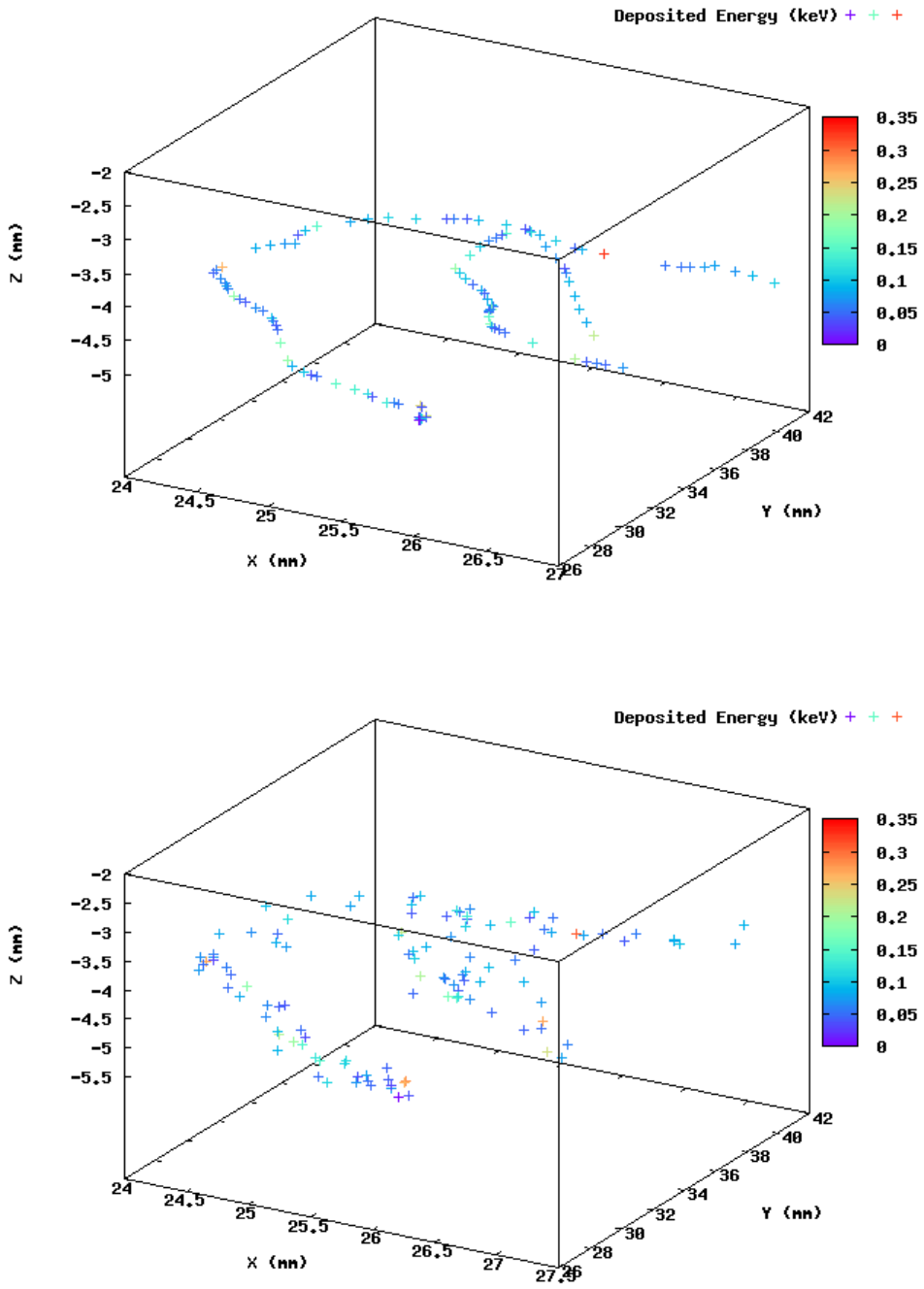

Figure 8.2: Undiffused (top) and diffused (bottom) track on a 10 keV electron in 20 Torr of SF_6.

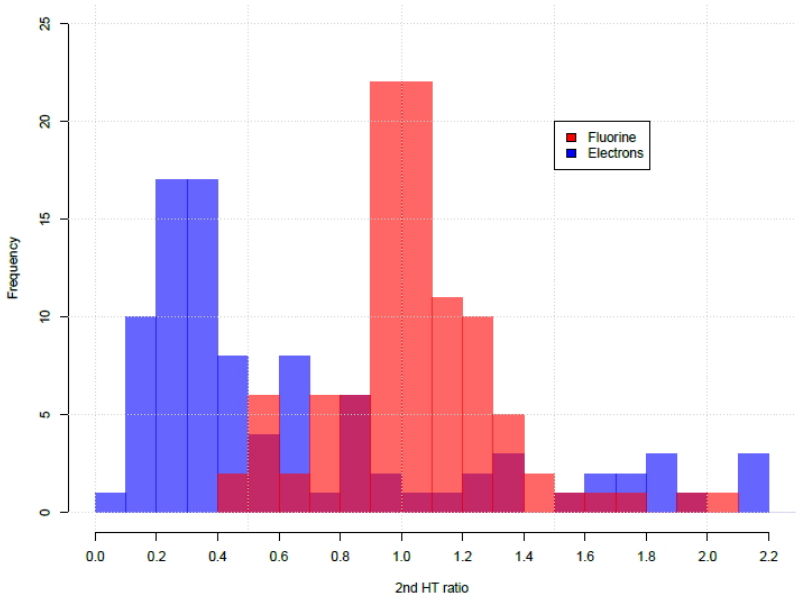

Figure 8.3: Second head-tail parameter for 100 10 keV$_e$ electrons and fluorine tracks if 20 Torr of SF_6. From [301].

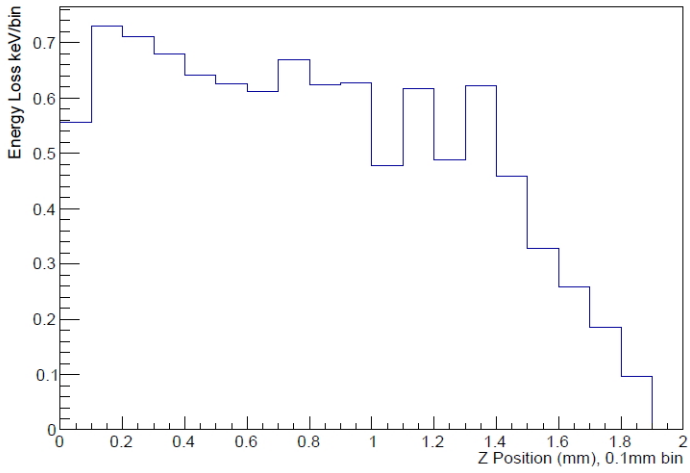

Figure 8.4: z-projected track from a10 keV$_e$ fluorine recoil in 20 Torr of SF_6. From [301].

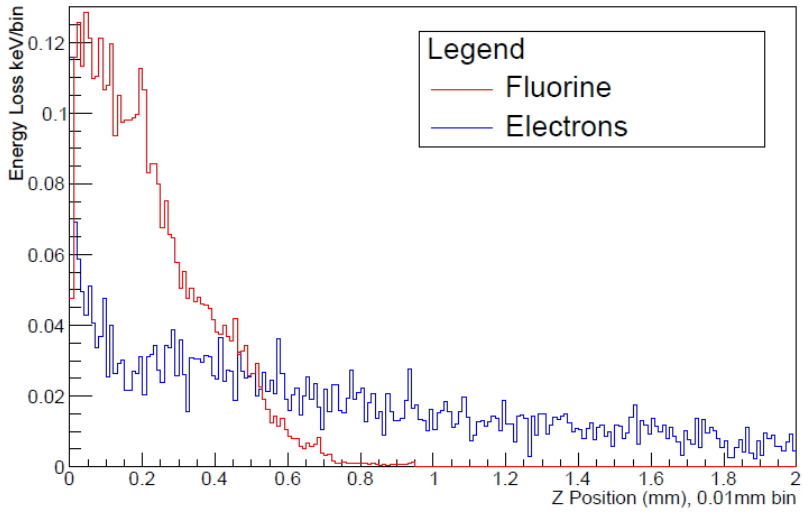

Figure 8.5: Averaged energy loss along the z-projected track for 100 4 keV$_e$ electrons and fluorine recoils. From [301].

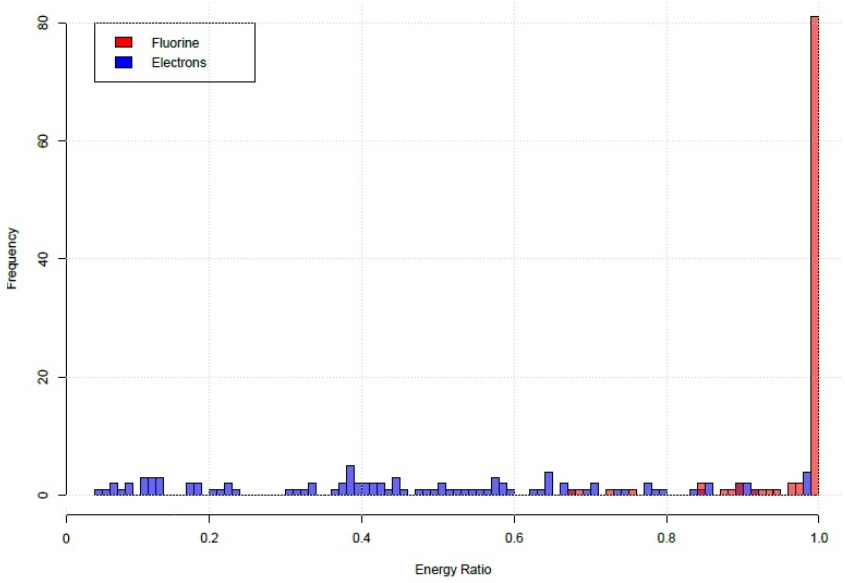

Figure 8.6: Pulse length discrimination of 100 4 keV$_e$ electrons and fluorine tracks in 20 Torr of SF_6. From [301].

9 Conclusions and Outlook

There now exist a whole range of compelling cosmological and astrophysical evidence that the Universe is dominated by a dark sector composed of dark energy (possibly in the form of a cosmological constant) and cold dark matter. Astrophysical evidence such as the Bullet Cluster point towards the existence of a weakly interacting dark matter particles. This WIMP particle is also well motivated by the extensions of the Standard Model such as supersymmetry or theories such as Kaluza-Klein based on more than 4 dimensions. At present, none of the proposed modification of general relativity has been able to explain all of the observations without the need to integrate the existence of this new particle in their models.

In chapter 2, the complementarity of the methods of dark matter detection was discussed. At the LHC, high energy proton-proton collisions seek to recreate energy conditions closer to the early universe and to produce dark matter particles. Indirect detection experiments are searching to detect the decay products of the annihilation of the dark matter particles, especially in the core region of the galaxy where this rate of this reaction is expected to be greater. Finally, direct detection experiments seek to detect the scattering of a WIMP particle off nuclei. The current most sensitive direct detection experiments are based on noble liquids cryogenically cooled-down. These experiments, however, are not specifically designed to demonstrate the galactic origin of their signals.

NaI (Tl) dark matter experiments have obtained a special status as galactic signature experiments. The annual modulation of the recoil rate reported by the DAMA,

then DAMA/LIBRA experiment is consistent with a dark matter above a 9σ significance level. However, this result is in disagreement with many other directional experiments. This is why the DM-Ice collaboration has deployed two crystals at the South Pole where the dark matter annual modulation could be distinguished from some of the Earth-based background whose phases are reversed.. In chapter 3, the recent effort to reduce the background levels in the DM-Ice experiment were discussed, particularly for the R&D run of DM-Ice37 at Boulby for which it was shown that the background levels were relatively well-understood at high energy thanks to a Geant4 simulation of the gamma backgrounds in the crystals and other materials. However, the development of a technique to discriminate between electron and nuclear recoils in KIMS is reinforcing the need to perform detailed simulations of the neutron backgrounds in NaI (Tl) experiments. This is especially true for the COSINE-100 experiment. This new NaI (Tl) experiment aims to verify the galactic origin of the DAMA signal. Projected sensitivities of the detector have shown that goal could be achieved with 3 years of exposure. Using the Geant4 and SOURCES packages, the fast neutron background from spontaneous fission and (α, n) reactions in the detectors and its surroundings was simulated. These simulations have shown that special care was taken in the choosing of materials for the construction of the detector and the total background rate per crystal as on the order of $10^{-6} - 10^{-8}$ event/kg/day . It has been proposed that the annual modulation observed by DAMA could potentially be explained by the detection of muon-induced neutrons and neutrino-induced neutrons. This claim has been disputed by several groups, including the DAMA collaboration. In the case of COSINE, it was found that the veto systems in place reduced the background rate from muon-induced neutrons below the targeted 3 events/ year.

Another form of searching for the galactic signature of dark matter is by using directionality. In chapter 2, it was shown that directionality can be achieved using different materials and technique. However, the current world-leading results are from the DRIFT detector, a gas NITPC. chapter 4 presented the demonstration

that background-free status can be achieved by mixing 1 Torr of oxygen in the gas mixture of the experiment. This addition resulted in the appearance of minority carriers, for which the temporal separation between the minority peaks and the mean ionisation peak is proportional to the drift distance. This method can be used to reject radon background events. It was shown in chapter 5 that this method of rejection can eliminate the radon background with an efficiency sufficient to expect less than 1 event in the duration of the experiment. This new background free status has allowed the collaboration of lower the threshold of the detector. In chapter 4, the nuclear recoil detector efficiency of the detector was measured and used to obtain the current world-leading spin-dependent directional dark matter results with 147.48 days of background-free exposure. The DRIFT detector will continue to search for WIMP interactions at its new location in a recently built new underground laboratory at Boulby. A new neutron shield is being assembled based on the simulation presented in chapter 5 to protect the detector from external background. This shielding is based on water rather than polypropylene shielding in order to provide the same level of protection in a more reduced volume.

In chapter 6, a NITPC was used for the first time to measure the radioactivity levels in an underground laboratory. This was done through the detection of 14 nuclear recoils-like events with the unshielded DRIFT detector in the JIF laboratory. Once the calculation of the gamma rejection efficiency had shown that the events could not be due to Compton scatterings in the gas, a Geant4 simulation of the neutron background in the rock was used to measure its uranium and thorium content. It was found that the uranium concentration in the vicinity of the JIF laboratory at Boulby is $77 \pm 20\,(\text{ stat}) \pm 7\,(\text{ sys})$ ppb and $150 \pm 40\,(\text{stat}) \pm 10\,(\text{sys})$ ppb of thorium, in good agreement with the previous independent measurements. This new pioneering technique has opened the way for more measurements of this kind in other low background areas. In particular, the preliminary Geant4 simulations of the UNDER experiment have shown that it will be able to measure the annual modulation of the fast and thermal flux at LNGS. If successful, these measurements will need

to be repeated in the other underground laboratories so that the modulation of the neutron flux can be taken into account by the dark matter experiments searching for annual modulation. Future developments of this technology may also benefit nuclear physics as a replacement of manganese baths and Bonner spheres to perform neutron measurements.

Finally, chapter 7 discussed the possibility of creating large scale NITPC capable of probing the parameter space up to and below the neutrino floor. This endeavour results from the realisation that the DRIFT detector is now limited by its target mass rather than its background. This was again confirmed in this thesis with the background-free dark matter search presented in chapter 4. The interest in large scale NITPCs is reinforced by the fact that the large non-directional detectors are soon expected to become sensitive to nuclear recoils from solar neutrinos. For directional detectors, however, there is no neutrino floor since the positions of the Sun and the Cygnus constellation never overlap. The background simulations in chapter 7 have shown that in order to develop ton scale NITPCs capable of operating background-free only materials with the highest levels of purity must be chosen. However, regarding the intermediate steps on the path towards this ton scale detector, the simulations have shown that neutron background rates inferior to 1 event/year can be achieved in CYGNUS-10. The internal gamma background, on the other-hand, has proven harder to reduce, despite the choice of low background materials. Nonetheless, background-free operation may very well be achievable in CYGNUS-10 thanks to the gamma rejection algorithms currently being developed by the CYGNUS collaboration in order to create gamma veto cuts, such as the gamma discrimination parameters presented in chapter 8.

Bibliography

[1] I. Newton. *The Principia: Mathematical Principles of Natural Philosophy*. University of California Press, 1999.

[2] Aristotle. *On the Heavens*. Loeb, 2006.

[3] K. Milton. The Casimir effect: recent controversies and progress. *J. Phys. A: Math. Gen.*, 37(38), 2004.

[4] J. H. Jeans. The motions of the stars in a Kapteyn-Universe. *Mon. Not. R. Astron. Soc.*, 82:122, 1922.

[5] F. Zwicky. Republication of: The redshift of extragalactic nebulae. *Gen. Relativ. Gravitation*, 41:207, 2009.

[6] V. Rubin and W. Ford. Rotation of the Andromeda Nebula from a spectroscopic survey of emission regions. *Astrophysical Journal*, 159:379, 1970.

[7] A. Klyping et al. LCDM-based models for the Milky Way and M31 I: Dynamical models. *Astrophys. J.*, 573(2):597, 2002.

[8] D. Lyth and A. Liddle. *The Primordial Density Perturbation: Cosmology, Inflation and the Origin of Structure*. Cambridge University Press, 2009.

[9] K. Oman et. al. The unexpected diversity of dwarf galaxy rotation curves. *Mon. Not. R. Astron. Soc.*, 452:3650, 2015.

[10] J. Navarro et al. A universal density profile from hierarchical clustering. *Astrophys. J.*, 490(2):493, 1997.

[11] J. Bovy and S. Tremaine. On the local dark matter density. *Astrophys. J.*, 756(1), 2012.

[12] M. Bidin et al. On the local dark matter density. *Astron. Astrophys.*, 573(A91), 2014.

[13] D. Weinberg et al. Cold dark matter: controversies on small scales. *PNAS*, 112(40):12249, 2014.

[14] C. Purcell et al. The dark disk of the Milky Way. *Astrophysical J*, 703(2):2275, 2009.

[15] M. Streff et al. Modeling dark matter subhalos in a constrained galaxy: Global mass and boosted annihilation profiles. *Phys. Rev.*, 95(6), 2017.

[16] A. Burkert. The structure of dark matter halos in dwarf galaxies. *Astrophysical Journal Letters*, 447(1):L25, 1995.

[17] J. Hjorth et al. Non-universality of dark matter halos: Cusps, cores and the central potential. *Astrophys. J.*, 811(1), 2015.

[18] A. Ludlow et al. The mass profile and accretion history of cold dark matter haloes. *Mon. Not. R. Astron. Soc.*, 432(2):1103, 2013.

[19] A. Cintio et al. A mass-dependent density profile for dark matter haloes including the influence of galaxy formation. *Mon. Not. R. Astron. Soc.*, 441(4):2985, 2014.

[20] R. Teyssier et al. Core-cusp transformations in dwarf- galaxies: observational predictions. *Mon. Not. R. Astron. Soc.*, 429(4):3068, 2013.

[21] J. Jardel and K. Gernhart. Variations in a universal dark matter profile for dwarf spheroidals. *Astrophys. J.*, 775(1):L30, 2013.

[22] S. McCaugh et al. A limit on the cosmological mass density and power spectrum from the rotation curves of low surface brightness galaxies. *Astrophys. J.*, 584(2):566, 2003.

[23] Planck Collaboration. Planck 2015 results xiii. cosmological parameters. *Astron. Astrophys.*, 594(A13), 2016.

[24] W. de Blok et al. Mass density profile of LSB galaxies. *Astrophys. J.*, 552(1):L23, 2001.

[25] D. Rodrigues et al. Evidence against cuspy dark matter halos in large galaxies. *Mon. Not. R. Astron. Soc.*, 470(2):2410, 2017.

[26] M. Roos. Dark matter in dwarf galaxies. *Preprint, arXiv:1701.05506*, 2017.

[27] A. Del Popolo. Non-baryonic dark matter in cosmology. *Int. J. Mod. Phys. D*, 23(3), 2014.

[28] S. Jaki. Johann Georg von Soldner and the gravitational bending of light, with an english translation of his essay on it published in 1801. *Found. Phys.*, 8(11-12):927, 1978.

[29] C. Grillo et al. Cosmological parameters from strong gravitational lensing and stellar dynamics in elliptical galaxies. *Astron. Astrophys.*, 477(2):397, 2013.

[30] M. Bartelman et al. Weak gravitational lensing. *Phys. Rep.*, 340(4):291, 2016.

[31] C. Alcock et al. The MACHO project: Microlensing results from 5.7 years of LMC observations. *Astrophys. J.*, 542(1):281, 2005.

[32] D. Clowe et al. A direct empirical proof of the existence of dark matter. *Astrophysical Journal Letters*, 648(2):109, 2006.

[33] M. Bradac et al. Revealing the properties of dark matter in the merging cluster MACS J0025.4-1222. *Astrophys. J.*, 687(2):959, 2008.

[34] M. Markevitch et. al. A textbook example of a bow shock in the merging galaxy cluster 1E 0657-56. *The Astrophysical Journal Letters*, 567(1):L27, 2002.

[35] H. Kragh and D. Lambert. The context of discovery: Lemaï¿œtre and the origin of the primeval-atom universe. *Annals of Science*, 64(4):445, 2007.

[36] W. de Boer. Grand unified theories and supersymmetry in particle physics and cosmology. *Prog. Part. Nucl. Phys.*, 33:201, 1994.

[37] D. Baumann and L. Macallister. *Inflation and String Theory.* Cambridge University Press, 2015.

[38] A. Riotto. Inflation and the theory of cosmological perturbations. *arXiv:hep-ph/0210162*, 2017.

[39] A. Penzias and R. Wilson. A measurement of excess antenna temperature at 4080 Mc/s. *Astrophys. J.*, 142(1):419, 1965.

[40] D. Wands et. al. Physics of the cosmic microwave background radiation. In SpringerLink, editor, *The Cosmic Microwave Background*, page 3, 2016.

[41] D. Fixen. The temperature of the cosmic microwave background. *Astrophys. J.*, 707(2):916, 2009.

[42] Planck Collaboration. Planck 2015 results XI. CMB power spectra, likelihoods, and robustness of parameters. *Astron. Astrophys.*, 594:A11, 2016.

[43] P. Fosalba et al. Detection of the integrated sachs-wolfe and sunyaev-zeldovich effects from the cosmic microwave background-galaxy correlation. *The Astrophysical Journal Letters*, 597(2):L89, 2003.

[44] Y. Rephaeli et al. The sunyaev zeldovich effect. *Riv.NuovoCim.*, 29(N12):1, 2006.

[45] K. Freese. Status of dark matter in the universe. *Int. J. Mod. Phys. D*, 26(6):1730012, 2017.

[46] M. Milgrom. A modification of the newtonian dynamics as a possible alternative to the hidden mass hypothesis. *Astrophys. J.*, 270:365, 1983.

[47] D. Bugg. A new perspective on MOND. *Can. J. Phys.*, 91(8):668, 2013.

[48] A. Hodson et al. Generalizing MOND to explain the missing mass in galaxy clusters. *Astron. Astrophys.*, 598:A127, 2017.

[49] J. Bekenstein. Relativistic gravitation theory for the modified newtonian dynamics paradigm. *Phys. Rev. D*, 70(8):083509, 2004.

[50] N. Mavromatos et al. Can the relativistic field theory version of modified newtonian dynamics avoid dark matter on galactic scales? *Phys. Rev. D*, 79(8):081301, 2009.

[51] M. Feix et al. Asymmetric gravitational lenses in TeVeS and application to the bullet cluster. *Astron. Astrophys.*, 480(2):313, 2008.

[52] E. di Valentino et al. Cosmological axion and neutrino mass constraints from Planck 2015 temperature and polarization data. *Phys. Lett. B*, 752:182, 2015.

[53] X. Xu et al. Testing the tensor-vector-scalar theory with the latest cosmological observations. *Phys. Rev. D: Part. Fields*, 92(8):83505, 2015.

[54] T. Sautirou et al. f(R) theories of gravity. *Rev. Mod. Phys.*, 82(1):451, 2010.

[55] T. Katsugarawa. Modified gravity explains dark matter ? *Phys. Rev.D*, 95(4):044040, 2017.

[56] S. Carroll et al. Can the dark energy equation-of-state parameter w be less than -1? *Phys. Rev. D: Part. Fields*, 68(2):23509, 2003.

[57] T. Biswas et al. Generalized ghost-free quadratic curvature gravity. *Classical Quantum Gravity*, 31(15):159501, 2014.

[58] Y Gong and A. Wang. Energy conditions and current acceleration of the universe. *Phys. Lett. B*, 652(2-3):63, 2007.

[59] A. Liddle et al. Triple unification of inflation, dark matter, and dark energy using a single field. *Phys. Rev.D*, 77(12):121301, 2008.

[60] S. Nojiri et al. Dark energy, inflation and dark matter from modified f(R) gravity. *Modern Theoretical Physics*, 2008.

[61] G. Bertone and D. Hooper. A history of dark matter. *FERMILAB-PUB-16-157-A*, 2016.

[62] P. Tisserand et al. Limits on the MACHO content of the galactic halo from the EROS-2 survey of the Magellanic Clouds. *Astron. Astrophys.*, 469(2):387, 2007.

[63] C. Alcock et al. EROS and MACHO combined limits on planetary-mass dark matter in the galactic halo. *Astrophys. J.*, 499(1):L9, 1999.

[64] G. Matthews et al. Introduction to big bang nucleosynthesis and modern cosmology. *Int. J. Mod. Phys. E*, 26(8):1741001, 2017.

[65] R. Cyburt et al. Big bang nucleosynthesis: Present status. *Rev. Mod. Phys.*, 88:15004, 2016.

[66] V. Mukhanov and S. Winitzki. *Introduction to Quantum Effects in Gravity.* Cambridge University Press, 2007.

[67] F. Capela et al. Constraints on primordial black holes as dark matter candidates from capture by neutron stars. *Phys. Rev. D*, 87(12):123524, 2013.

[68] K. Garrett and G. Duda. Dark matter: A primer. *Advances in Astronomy*, 2011:968283, 2011.

[69] D. Jeong. Silk damping at a redshift of a billion: New limit on small-scale adiabatic perturbations. *Phys. Rev. Lett.*, 113(6):061301, 2014.

[70] R. Peccei and H. Quinn. CP conservation in the presence of pseudoparticles. *Phys. Rev. Lett.*, 28(25):1440, 1977.

[71] M. Dine. Tasi lectures on the strong cp problem. *arXiv:hep-ph/0011376*, 2000.

[72] W. Wislicki. Direct CP violation in neutral kaon decays. *Pramana*, 62(3):601, 2004.

[73] L. Duffy and K. van Bibber. Axions as dark matter particles. *New Journal of Physics*, 11:105008, 2009.

[74] Y. Kim et al. New experimental limit on the electric dipole moment of the neutron. *Phys. Rev.D*, 91(10):102004, 2015.

[75] A. Paeyz et al. Revisiting the SN1987A gamma-ray limit on ultralight axion-like particles. *J. Cosmol. Astropart. Phys.*, 2015(6):1502, 2015.

[76] A. Arvanitaki et al. Discovering the QCD axion with black holes and gravitational waves. *Phys. Rev.D*, 91(8):084011, 2015.

[77] V. Skobelev. Primakoff effect: Synchrotron and coulomb mechanisms of axion emission. *Phys. At. Nucl.*, 63(11):1963, 2000.

[78] I. Stern. Admx status. *Proceedings of 38th International Conference on High Energy Physics*, 2017.

[79] A. Ringwald. Alternative dark matter candidates: Axions. *Proceedings of Science*, 2016.

[80] P. Agrawal et al. Opening up the QCD axion window. *Preprint arXiv:1708.05008*, 2017.

[81] A. Ibarra. Neutrinos and dark matter. *AIP Conf. Proc.*, 1666(1):140004, 2015.

[82] M. Lattanzi et al. Connecting neutrino physics with dark matter. *New J. Phys.*, 16:125012, 2014.

[83] O. Miranda and J. Valle. Neutrino oscillations and the seesaw origin of neutrino mass. *Nucl. Phys. B*, 908:436, 20016.

[84] M. Lindner et al. Seesaw mechanisms for dirac and majorana neutrino masses. *Phys. Rev.*, 65(15):053014, 2002.

[85] T. Fischer et al. Impact of active-sterile neutrino mixing on supernova explosion and nucleosynthesis. *Phys. Rev.*, 89(6):061303, 2014.

[86] K. Ng et al. Improved limits on sterile neutrino dark matter using full-sky Fermi Gamma-ray Burst Monitor data. *Phys. Rev.*, 92(4):043503, 2015.

[87] A. Riis et al. Detecting sterile neutrinos with KATRIN like experiments. *J. Cosmol. Astropart. Phys.*, 2011(2):011, 2011.

[88] G. Bertone. The moment of truth for WIMP dark matter. *Nature*, 468:389, 2010.

[89] G. Davli. A lecture on the hierarchy problem and gravity. *10.5170/CERN-2013-003.145*, 2013.

[90] T. Kimura et. al. Nonlocal N=1 supersymmetry. *J. High Energy Phys.*, 2016:22, 2016.

[91] G. Bertone et al. Particle dark matter: evidence, candidates and constraints. *Phys. Rep.*, 405(5-6):279, 2005.

[92] S. Martin. A supersymmetry primer. *Advanced Series on Directions in High Energy Physics*, 18:1, 1998.

[93] A. Cohen et al. (De)Constructing Dimensions. *Phys. Rev. Lett.*, 86(21):4757, 2001.

[94] S. Dimopoulos et al. Phenomenology, astrophysics, and cosmology of theories with submillimeter dimensions and TeV scale quantum gravity. *Phys. Rev.D*, 59(8):086004, 1999.

[95] A. Pasini. A conceptual introduction to the Kaluza-Klein theory. *Eur. J. Phys.*, 9(4):289, 1988.

[96] J. Long and J. Price. Current short-range tests of the gravitational inverse square law. *C. R. Phys.*, 4(3):337, 2003.

[97] H. Cheng. 2009 tasi lecture – introduction to extra dimensions. *arXiv:1003.1162*, 2009.

[98] J. Bonifacio and K. Hinterbichler. Kaluza-Klein reduction of massive and partially massless spin-2. *Phys. Rev.B*, 95(2):024023, 2017.

[99] J. Jaeckel et al. Hidden photons with Kaluza-Klein towers. *arXiv:1408.0019*, 2014.

[100] G. Servant and T. Tait. Is the lightest Kaluza Klein particle a viable dark matter candidate? *Nucl. Phys. B*, 650(1-2):391, 2003.

[101] C. Boehm et al. Light dark matter annihilations into two photons. *Nucl. Phys. B*, 641(3-4):247, 2006.

[102] C. Chen et al. Implications of the Little Higgs dark matter and T-odd fermions. *J. High Energy Phys.*, 2014(6):74, 2014.

[103] K. Harigaya et al. GUTzilla dark matter. *J. High Energy Phys.*, 2016(9):14, 2016.

[104] A. Chamseddine and V. Mukhanov. Mimetic dark matter. *J. High Energy Phys.*, 2013(11):135, 2013.

[105] F. Kahlhoefer. Review of LHC dark matter searches. *Int. J. Mod. Phys. A*, 32(13):1730006, 2017.

[106] S. Y. Hoh et al. Dark matter searches at the Large Hadron Collider. *AIP Conf. Proc.*, 1704(1):020005, 2016.

[107] P. Jean et al. Early SPI/INTEGRAL measurements of 511 keV line emission from the 4th quadrant of the galaxy. *Astron. Astrophys.*, 407(3):L55, 2003.

[108] A. Vincent et al. The galactic 511 keV line and the intergalactic positron density. *Physics Procedia*, 61:796, 2015.

[109] J. Knoedlseder et al. The all-sky distribution of 511 kev electron-positron annihilation emission. *Astron. Astrophys.*, 441(2):513, 2005.

[110] S. Baum et al. Dark matter capture, subdominant WIMPs, and neutrino observatories. *Phys. Rev.D*, 95(4):043007, 2017.

[111] R. Allahverdi. Probing dark matter annihilation to primary neutrinos with IceCube. *AIP Conf. Proc.*, 1664(1):5, 2014.

[112] M. G. Aartsen et al. First search for dark matter annihilations in the Earth with the IceCube detector. *Eur. J. Phys. C*, 77(2):82, 2016.

[113] P. Gondolo et al. Darksusy: computing supersymmetric dark matter properties numerically. *J. Cosmol. Astropart. Phys.*, 2004(7):8, 2004.

[114] E. Aprile. et al. Dark matter results from 225 live days of XENON100 data. *Phys. Rev. Lett.*, 109(18):181301, 2012.

[115] H. Silverwood. Sensitivity of IceCube-DeepCore to neutralino dark matter in the MSSM-25. *J. Cosmol. Astropart. Phys.*, 2013(3):27, 2013.

[116] L. Rauch et al. Dark matter direct-detection experiments. *J. Phys. G: Nucl. Phys.*, 43(1):013001, 2015.

[117] J. D. Lewin and P. F. Smith. Review of mathematics, numerical factors, and corrections for dark matter experiments based on elastic nuclear recoil. *Astropart. Phys.*, 6(1):87, 1996.

[118] M. C. Smith et al. The RAVE survey: constraining the local galactic escape speed. *Mon. Not. R. Astron. Soc.*, 379(2):755, 2007.

[119] M. Lisanti K. Freese and C. Savage. Annual modulation of dark matter: A review. *Rev. Mod. Phys.*, 2013.

[120] P. J. MacMillan and J. J. Biney. The uncertainty in galactic parameters. *Mon. Not. R. Astron. Soc.*, 402(2):934, 2010.

[121] Dark Matter Research Group University of Sheffield. Dark matter. `https://www.hep.shef.ac.uk/research/dm/intro.php`.

[122] A. Drukier et al. Detecting cold dark matter candidates. *Phys. Rev. D: Part. Fields*, 33(12):3495, 1986.

[123] D. Spergel. Motion of the Earth and the detection of weakly interacting massive particles. *Phys. Rev. D: Part. Fields*, 37(6):1353, 1987.

[124] C. O'Hare and A. Green. Directional detection of dark matter streams. *Phys. Rev.D*, 90(12):123511, 2014.

[125] R.G. Carlberg. Dark matter sub-halo counts via star stream crossings. *Astrophys. J.*, 748(1), 2012.

[126] A. Tan et al. Dark matter results from first 98.7 days of data from the PandaX-II experiment. *Phys. Rev. Lett.*, 117(12):121303, 2016.

[127] E. Aprile. et al. Physics reach of the XENON1T dark matter experiment. *J. Cosmol. Astropart. Phys.*, 2016(4):27, 2016.

[128] E. Bernabei et al. DAMA/LIBRA results and perspectives. *EPJ Web Conferences*, 136:5001, 2017.

[129] H. S. Lee et al. Search for low-mass dark matter with CsI(Tl) crystal detectors. *Phys. Rev.D*, 90(5):52006, 2014.

[130] M. Leyton. Directional dark matter detection with the DMTPC m3 experiment. *J. Phys. Conf. Ser.*, 718:42035, 2016.

[131] J. B. R. Battat et al. First background-free limit from a directional dark matter experiment: Results from a fully fiducialised DRIFT detector. *Phys. Dark Universe*, 9:1, 2015.

[132] N. S. Phan et al. The novel properties of SF6 for directional dark matter experiments. *J. Instrum.*, 12(2):P02012, 2017.

[133] D. Woods and D. Saxon. Diffuse surface optical model for nucleon-nuclei scattering. *Phys. Rev.*, 95(2):577, 1954.

[134] J. Engel. Nuclear form factors for the scattering of weakly interacting massive particles. *Phys. Lett. B*, 264(1-2):114, 1991.

[135] N. Anand et al. Model-independent WIMP scattering responses and event rates: A Mathematica package for experimental analysis. *Phys. Rev. C: Nucl. Phys.*, 89(6):65501, 2014.

[136] W. R. Leo. *Techniques for Nuclear and Particle Physics Experiments.* Springer-Verlag, 1993.

[137] R. Bernabei et al. Final model independent result of DAMA/LIBRA-phase1. *Eur. Phys. J. D*, 73:2648, 2013.

[138] R. Bernabei et al. The DAMA/LIBRA apparatus. *Nucl. Instr. Meth.*, 592(3):297, 2008.

[139] G. Adhikari et al. Understanding NaI(Tl) crystal background for dark matter search. *Eur. J. Phys.*, 77(7):437, 2017.

[140] C. Arina et al. Dark matter with pseudoscalar-mediated interactions explains the DAMA signal and the galactic center excess. *Phys. Rev. Lett.*, 114(1):11301, 2015.

[141] P. Fox and E. Poppitz. Leptophilic dark matter. *Phys. Rev.D*, 79(8):83528, 2009.

[142] G. Bellini et al. Cosmic-muon flux and annual modulation in Borexino at 3800 m water-equivalent depth. *J. Cosmol. Astropart. Phys.*, 2012(5):15, 2012.

[143] R. Bernabei et al. No role for muons in the DAMA annual modulation results. *Eur. Phys. J. C*, 72(7):2064, 2012.

[144] H. Wulandari et al. Neutron flux at the Gran Sasso underground laboratory revisited. *Astropart. Phys.*, 22(3-4):313, 2004.

[145] E. Barbossa de Souza et al. First search for a dark matter annual modulation signal with NaI(Tl) in the southern hemisphere by DM-Ice17. *Phys. Rev.D*, 95(3):32006, 2017.

[146] J. B. R. Battat et al. Low threshold results and limits from the DRIFT directional dark matter detector. *Astropart. Phys.*, 91:65, 2017.

[147] K. Abe. The XMASS experiment. *J. Phys. Conf. Ser.*, 120(4), 2008.

[148] K. Abe et al. Direct dark matter search by annual modulation in XMASS-I. *Phys. Lett. B*, 759:272, 2016.

[149] D.S. Akerib et al. First results from the LUX dark matter experiment at the Sanford underground research facility. *Phys. Lett. B*, 112(9):91303, 2014.

[150] R. Agnese et al. Search for low-mass weakly interacting massive particles with SuperCDMS. *Phys. Rev. Lett.*, 112(241302):24, 2014.

[151] F. Froborg et al. SABRE: WIMP modulation detection in the northern and southern hemisphere. *J. Phys. Conf. Ser.*, 718, 2016.

[152] D. Santos et al. MIMAC: A micro-tpc matrix for dark matter directional detection. *J. Phys. Conf. Ser.*, 460, 2013.

[153] S. Vahsen et al. The directional dark matter detector (D3). *EAS Publication Series*, 53:43, 2012.

[154] K. Miuchi et al. First underground results with NEWAGE-0.3a direction-sensitive dark matter detector. *Phys. Lett. B*, 686(11-17):1, 2010.

[155] H. Sekiya et al. Measurements of anisotropic scintillation efficiency for carbon recoil in a stilbene crystal for dark matter detection. *Phys. Lett. B*, 571(3-4):132, 2003.

[156] H. Sekiya et al. Dark matter search with direction sensitive scintillators. In *The Identification of Dark Matter*, page 378, 2004.

[157] V. Caracciolo et al. The ADAMO project and developments. *J. Phys. Conf. Ser.*, 718:42011, 2016.

[158] F. Cappella et al. On the potential of the ZnWO4 anisotropic detector to measure the directionality of dark matter. *Eur. J. Phys.*, 73:2276, 2013.

[159] P. Adrihaki et al. Understanding internal backgrounds of NaI(Tl) crystal towards a 200 kg array of KIMS-NaI experiment. *Eur. J. Phys.C*, 76(185), 2016.

[160] D. Dujmic et al. Observation of the head-tail effect in nuclear recoils of low-energy neutrons. *Nucl. Instrum. Methods Phys. Res., Sect. A*, 584(2):327.

[161] J. B. R. Battat et al. First measurement of nuclear recoil head-tail sense in a fiducialised WIMP dark matter detector. *J. Instrum.*, 11:10019, 2016.

[162] J. B. R. Battat et al. DMTPC: Dark matter detection with directional sensitivity. *Proceedings of Science*, 110, 2010.

[163] S. Joosten et al. Enhanced UV light detection using a p-terphenyl wavelength shifter. *Nucl. Instrum. Methods Phys. Res., Sect. A*, 870:110, 2017.

[164] N. Ishida et al. Attenuation length measurements of scintillation light in liquid rare gases and their mixtures using an improved reflection suppresser. *Nucl. Instrum. Methods Phys. Res., Sect. A*, 384(2-3):380, 1997.

[165] J. Nikkel et al. Index of refraction, Rayleigh scattering length, and Sellmeier coefficients in solid and liquid argon and xenon. *Nucl. Instr. Meth.*, 867:204, 2017.

[166] J. R. Nygren. Columnar recombination: a tool for nuclear recoil directional sensitivity in a xenon-based direct detection WIMP search. *J. Phys. Conf. Ser.*, 460:12006, 2013.

[167] J. Hernando. Status of NEXT-100 experiment. *Physics Procedia*, 61:251, 2015.

[168] G. Mohlabeng et al. Dark matter directionality revisited with a high pressure xenon gas detector. *J. High Energy Phys.*, 2015(7):92, 2015.

[169] M. Caddedu. A directional dark matter argon detector at LNGS. *J. Phys. Conf. Ser.*, 689:12015, 2015.

[170] J. Li. Directional dark matter by polar angle direct detection and application of columnar recombination. *Phys. Rev.D*, 92(4):43523, 2015.

[171] A. Green and B. Morgan. Optimizing WIMP directional detectors. *Astropart. Phys.*, 27(2-3):142, 2006.

[172] C. Lattes et al. Processes involving charged mesons. *Nature*, 159:694, 1947.

[173] T. Fukuda. The nuclear emulsion technology and the analysis of the OPERA experiment data. *arXiv:0910.3274*, 2009.

[174] N. D'Ambrosio et al. Nuclear emulsion as a very high resolution detector for directional dark matter search. *J. Instrum.*, 9(1):C01043, 2014.

[175] T. Naka et al. R&D status of nuclear emulsion for directional dark matter search. *EAS Publication Series*, 53:51, 2012.

[176] N. Natsume et al. Low-velocity ion tracks in fine grain emulsion. *Nucl. Instrum. Methods Phys. Res., Sect. A*, 575(3):439, 2007.

[177] T. Asada et al. The development of super fine-grained nuclear emulsion. *Progress of Theoretical and Experimental Physics*, 2017(6):063H01, 2017.

[178] A. Aleksandrov et al. NEWS: Nuclear emulsions for WIMP search. *arXiv:1604.04199*, 2016.

[179] A. Aleksandrov et al. Intrinsic neutron background of nuclear emulsions for directional dark matter searches. *Astropart. Phys.*, 80:16, 2016.

[180] S. Tilav et al. Atmospheric variations as observed by IceCube. *arXiv:1001.0776*, 2010.

[181] N. J. C. Spooner et al. NaI dark matter limits and the NAIAD array a detector with improved sensitivity to WIMPs using unencapsulated NaI. *Phys. Lett. B*, 473(3-4):330, 2000.

[182] M. G. Aartsen et al. South pole glacial climate reconstruction from multi-borehole laser particulate stratigraphy. *J. Glaciol.*, 59(218):1117, 2013.

[183] J. Cherwinka et al. First data from DM-Ice17. *Phys. Rev.D*, 90(9):92005, 2014.

[184] M. G. Aartsen et al. Determining neutrino oscillation parameters from atmospheric muon neutrino disappearance with three years of IceCube DeepCore data. *Phys. Rev.D*, 91(7):72004, 2015.

[185] K. W. Kim et al. Tests on NaI(Tl) crystal for WIMP search at the YangYang underground laboratory. *Astropart. Phys.*, 62:249, 2015.

[186] M. G. Aartsen et al. PINGU: a vision for neutrino and particle physics at the South Pole. *J. Phys. G: Nucl. Phys.*, 44(5):54006, 2017.

[187] M. J. Carson et al. Simulation of neutron background in a time projection chamber relevant to dark matter searches. *Nucl. Instr. Meth.*, 546(3):509, 2005.

[188] Hamamatsu R877 PMT. Technical details. `https://www.hamamatsu.com/jp/en/R877.html`.

[189] Hamamatsu R12669 PMT modified R6233. Technical details. `https://www.hamamatsu.com/us/en/R6233.html`.

[190] S. Agonstinelli et al. Geant4 –a simulation tookit. *Nucl. Instr. Meth. Phys. Res. A*, 506(3):250, 2003.

[191] R. Brun and F. Rademakers. ROOT – an object oriented data analysis framework. *Nucl. Instr. Meth. Phys. Res. A*, 389(1-2):81, 1997.

[192] Geant4 Physics List. FTFP BERT Physics list. `http://geant4.cern.ch/support/proc_mod_catalog/physics_lists/hadronic/FTFP_BERT.html`.

[193] E. Barbossa de Souza. Energy resolution of DM-Ice37 at Fermilab. *Internal DM-Ice memorandum.*

[194] K. W. Kim et al. Pulse shape discrimination of nuclear recoil and electron recoil events with a NaI(Tl) crystal for dark matter search. *IEEE Trans. Nucl. Sci.*, 63(2):534, 2016.

[195] S. C. Wu et al. Pulse shape discrimination techniques in scintillating CsI(Tl) crystals. *Nucl. Instrum. Meth.*, 523(1):116, 2004.

[196] G. Gerbier et al. *Sources and Detection of Dark Matter and Dark Energy in the Universe*, chapter Pulse Shape Discrimination and Dark Matter Search with NaI(Tl) Scintillator at the Laboratoire Souterrain de Modane, page 333. Springer, 2001.

[197] R. Bernabei et al. The DAMA/LIBRA apparatus. *Nucl. Instrum. Methods Phys. Res.*, 592(3):297, 2008.

[198] J. Cherwinka et al. Measurement of muon annual modulation and muon-induced phosphorescence in NaI(Tl) crystals with DM-Ice17. *Phys. Rev. D: Part. Fields*, 93(4):42001.

[199] E. J. Jeon and Y. D. Kim. A simulation-based study of the neutron backgrounds for NaI dark matter experiments. *Astropart. Phys.*, 73:28, 2016.

[200] J. Klinger and V. A. Kudryatsev. Can muon-induced backgrounds explain the DAMA data? *J. Phys. Conf. Ser.*, 718:42033, 2016.

[201] Geant4 Collaboration. Geant4 physics reference manual. *CERN*, 2004.

[202] W. B. Wilson et al. SOURCES 4C : a code for calculating (alpha,n), spontaneous fission, and delayed neutron sources and spectra. *Los Alamos Report LA-UR-02-1839*, 2002.

[203] Isotope Project, LBNL. Th232 isotopes. `http://ie.lbl.gov/education/parent/Th_iso.htm`.

[204] M. Lee et al. Radon environment in the Korea Invisible Mass Search experiment and its measurement. *JKPS*, 58:713, 2011.

[205] G. Feldman and R. Cousins. Unified approach to the classical statistical analysis of small signals. *Phys. Rev.D*, 57(7):3873, 1998.

[206] J. Davis. Fitting the annual modulation in DAMA with neutrons from muons and neutrinos. *Phys. Rev. Lett.*, 113(8):81302, 2014.

[207] C. Patrigani et al. Review of particle physics. *Chin. Phys.*, 40(10):100001, 2016.

[208] J. Zhu et al. Study on the muon background in the underground laboratory of KIMS. *High Energy Physics and Nuclear Physics*, 29(8):721, 2005.

[209] A. M. Short. Fast neutron production by muons underground. *Proceedings of the 9th International Cosmic Ray Conference*, 1:1009, 1965.

[210] K. Blum. DAMA vs. the annually modulated muon background. *arXiv:1110.0857*, 2011.

[211] H. Prihtiadi. Measurement of a muon flux at the Yangyang Underground Laboratory. *Internal COSINE memorandum*, 2017.

[212] J. B. R. Battat et al. Measurement of directional range components of nuclear recoil tracks in a fiducialised dark matter detector. *J. Instrum.*, 12:P10009, 2017.

[213] J. B. R. Battat et al. Reducing DRIFT backgrounds with a submicron Aluminized-Mylar cathode. *Nucl. Instr. Meth. Phys. Res. A*, 794:33, 2017.

[214] E. Miller. *Mitigating Backgrounds with a Novel Thin-Film Cathode in the DRIFT-IId Dark Matter Detector.* PhD thesis, University of New-Mexico, 2015.

[215] J. Monroe. Status and prespect of the DMTPC directional dark matter experiment. *AIP Conf. Proc.*, 1441:512, 2012.

[216] D. Snowden-Ifft. Discovery of multiple, ionization-created CS2 anions and a new mode of operation for drift chambers. *Rev. Sci. Instrum.*, 85(1):13303, 2014.

[217] F. Bloch and N. Bradbury. On the mechanism of unimolecular electron capture. *Phys. Rev.*, 48(8):689, 1935.

[218] H. Shimamori and Y. Hatano. Thermal electron attachment to O2 in the presence of various compounds as studied by a microwave cavity technique combined with pulse radiolysis. *Chem. Phys.*, 21(2):187, 1977.

[219] H. Shimamori and H. Hotta. Mechanism of thermal electron attachment to O2 as studied by observing isotope effects of attachment rates for 18-O2 systems. *J. Chem. Phys.*, 78(3):1318, 1982.

[220] A. Fridman. *Plasma Chemistry.* Cambridge University Press, 2008.

[221] K. Pushkin and D. Snowden-Ifft. Measurements of W-value, mobility and gas gain in electronegative gaseous CS2 and CS2 gas mixtures. *Nucl. Instrum. Methods*, 606(569-577):3, 2009.

[222] S. Burgos et al. Measurement of the range component directional signature in a DRIFT-II detector using 252Cf neutrons. *Nucl. Instr. Meth. Phys. Res. A*, 600(2):417, 2009.

[223] British Gypsum. Technical details. `http://www.british-gypsum.com/`.

[224] C. Ghag. *Simulation, Calibration & Exploitation of the DRIFT-II Directional Dark Matter Detector.* PhD thesis, University of Edinburgh, 2006.

[225] E. Daw. A review of the theory of WIMP scattering off target nuclei. *Private Communications*, 2012.

[226] M. Lisanti. Lectures on dark matter physics. *New Frontiers in Fields and Strings*, 85(4):1561, 2015.

[227] R. Catena and P. Ulio. The local dark matter phase-space density and impact on WIMP direct detection. *J. Cosmol. Astropart. Phys.*, 2012(5):5, 2012.

[228] T. Piffl et al. The RAVE survey: the galactic escape speed and the mass of the Milky Way. *Astron. Astrophys.*, 562:A91, 2014.

[229] D. R. Tovey et al. A new model-independent method for extracting spin-dependent cross section limits from dark matter searches. *Phys. Lett. B*, 488(1):17, 2000.

[230] D. M. Webber et al. Measurement of the positive muon lifetime and determination of the Fermi Constant to part-per-million precision. *Phys. Rev. Lett.*, 106(7):79901, 2011.

[231] S. Sadler. *Towards the DRIFT-III Directional Dark Matter Experiment.* PhD thesis, University of Sheffield, 2014.

[232] A. Ezeribe. *Towards a massive directional dark matter detector CYGNUS-TPC.* PhD thesis, University of Sheffield, 2016.

[233] B. Feldstein and F. Kahlhoefer. A new halo-independent approach to dark matter direct detection analysis. *J. Cosmol. Astropart. Phys.*, 2014:65, 2014.

[234] A. Scarff. *Developments towards a sscale-up one-dimensional directional dark matter detector.* PhD thesis, University of Sheffield, 2017.

[235] C. Amole et al. Dark matter search results from the PICO 60 C3F8 bubble chamber. *Phys. Rev. Lett.*, 118(25):251301, 2017.

[236] C. Savage et al. Compatibility of DAMA/LIBRA dark matter detection with other searches. *J. Cosmol. Astropart. Phys.*, 2009(4):10, 2009.

[237] UKDM Collaboration. Radioactivity test results. *hep-www.rl.ac.uk/ukdmc/Radioactivity/uk.html*.

[238] J. B. R. Battat et al. Radon in the DRIFT-II directional dark matter TPC: emanation, detection and mitigation. *J. Instrum.*, 9(11):P11004, 2014.

[239] Q. Riffard et al. First detection of radon progeny recoil tracks by MIMAC. *J. Instrum.*, 12(6):P06021, 2017.

[240] E. Aprile. et al. Online 222Rn removal by cryogenic distillation in the XENON100 experiment. *Eur. J. Phys.*, 77:358, 2017.

[241] K. Abe et al. Radon removal from gaseous xenon with activated charcoal. *Nucl. Instrum. Methods Phys. Res.*, 661(1):50, 2012.

[242] P. A. Amaudruz et al. Radon backgrounds in the DEAP-1 liquid-argon-based dark matter detector. *Astropart. Phys.*, 62:178, 2015.

[243] Q. Riffard et. Directional detection with MIMAC. *Cygnus 2015 Conference*, 2015.

[244] A. Scarff. Structure of the new laboratory at boulby. *DRIFT Internal document*, 2015.

[245] I. J. Vera-Marun et al. Direct electronic measurement of Peltier cooling and heating in graphene. *Nat. Commun.*, 1038:11525, 2016.

[246] A. Murphy. The Boulby underground laboratory. In *Proceedings of the Fifth International Workshop on The Identification of Dark Matter*, 2005.

[247] A. Cole. DRIFT shielding germanium measurements. *DRIFT Internal document*, 2016.

[248] N. J. Roberts et al. Commissioning of the new manganese bath suite at the National Physical Laboratory. *NPL Report IR11*, 2008.

[249] NPL. Manganese bath. `http://www.npl.co.uk/science-technology/neutron-metrology/research/manganese-bath`.

[250] V. Lacoste. Design of a new long counter for the determination of the neutron fluence reference values at the IRSN AMANDE facility. *Radiat. Meas.*, 45(10):1250, 2010.

[251] J. de Pangher and L. L. Nichols. Precision long counter for measuring fast neutron flux density. *PNNL Technical Report*, 1966.

[252] N. P. Hawkes et al. Measurement and calculation of the emission anisotropy of an X1 CF252 neutron source. *Radiat. Prot. Dosim.*, 126(1-4):78, 2007.

[253] M. C. Chu et al. Development of a Bonner sphere neutron spectrometer from a commercial neutron dosimeter. *J. Instrum.*, 11(11):P11005, 2016.

[254] H. H. Hsu et al. A new Bonner sphere set for high energy neutron measurement: Monte-Carlo simulation. *IEEE Trans. Nucl. Sci.*, 41(4):938, 1994.

[255] Q. Hu et al. Neutron background measurements at China Jinping underground laboratory with a Bonner multi-sphere spectrometer. *Nucl. Instrum. Methods Phys. Res., Sect. A*, 859:37, 2017.

[256] D. Snowden-Ifft. Results from 55 days of low threshold data. *Internal DRIFT memorandum*, May 2015.

[257] S. Burgos et al. Studies of neutron detection and backgrounds with the DRIFT-IIa dark matter detector. *Astron. Astrophys.*, 28(4):409, 2007.

[258] D. Maleczweski et al. Gamma background measurements in the Boulby Underground Laboratory. *J. Radioanal. Nucl. Chem.*, 291(3):1483, 2013.

[259] P. F. Smith et al. Simulation studies of neutron shielding, calibration and veto systems for gaseous dark matter detectors. *Astropart. Phys.*, 22(5-6):409, 2005.

[260] S. Plank. *The DRIFT dark matter project.* PhD thesis, University of Edinburgh, 2008.

[261] E. Tziaferi et al. First measurement of low intensity fast neutron background

from rock at the Boulby Underground Laboratory. *Astropart. Phys.*, 27(5):326, 2007.

[262] E. Belloti et al. New measurement of rock contaminations and neutron activity in the Gran Sasso tunnel. *INFN/TC-85-19*, 1985.

[263] P. Belli et al. Deep underground neutron flux measurement with large BF3 counters. *Il Nuovo Cimento A*, 101(6):959, 1989.

[264] Z. Debicki et al. Thermal neutrons at Gran Sasso. *Nucl. Phys. Proc.*, 101(6):959, 2009.

[265] A. Best et al. Low energy neutron background in deep underground laboratories. *Nucl. Instrum. Methods Phys. Res., Sect. A*, 812:1, 2016.

[266] R. Aleksan et al. Measurement of fast neutrons in the Gran Sasso laboratory using a Li6 doped scintillator. *Nucl. Instrum. Methods Phys. Res.*, 274(203-206):1, 1989.

[267] F. Arneodo et al. Neutron background measurements in the Hall C of the Gran Sasso Laboratory. *Il Nuovo Cimento A*, 112:819, 1999.

[268] M. Cribier et al. The neutron background in GALLEX. *Astropart. Phys.*, 4(1):23, 1995.

[269] A. Rindi et al. Underground neutron flux measurement. *Nucl. Instr. Meth.*, 272(3):871, 1988.

[270] M. Schumann et al. Dark matter sensitivity of multi-ton liquid xenon detectors. *J. Cosmol. Astropart. Phys.*, 2015(10):16, 2015.

[271] J. Davis. Dark matter vs neutrinos: the effect of astrophysical uncertainties and timing information on the neutrino floor. *J. Cosmol. Astropart. Phys.*, 2015(3):12, 2015.

[272] E. Richard et al. Measurements of the atmospheric neutrino flux by Super-Kamiokande: Energy spectra, geomagnetic effects, and solar modulation. *Phys. Rev.D*, 94(5):52001, 2016.

[273] P. Grothaus et al. Directional dark matter detection beyond the neutrino bound. *Phys. Rev. D*, 90(5):55018, 2014.

[274] A. Green. Readout strategies for directional dark matter detection beyond the neutrino background. *Phys. Rev. D*, 92(6):63518, 2015.

[275] J. Billard et al. Implications of neutrino backgrounds on the reach of the next generation dark matter direct detection experiments. *Phys. Rev. D*, 89(2):23524, 2014.

[276] F. Mayet et al. The DRIFT dark matter experiments. *European Astronomical Society Publications Series*, 53:11, 2012.

[277] M. Battaglieri et al. US Cosmic Visions: new ideas in dark matter 2017: community report. *arXiv:1707.04591*, 2017.

[278] D. McAlister. Gamma ray attenuation properties of common shielding materials. *PG Research Foundation*, 2013.

[279] W. Maneschg et al. Measurements of extremely low radioactivity levels in stainless steel in GERDA. *Nucl. Instr. Meth.*, 593(3):448, 2008.

[280] T. Gamble. Private communication. *University of Sheffield*, 2016.

[281] D. S. Akerib et al. LUX-ZEPLIN (LZ) conceptual design report. *LBNL-190005*, 2015.

[282] C. M. Nantais et al. Radiopurity measurement of acrylic for DEAP-3600. *AIP Conf. Proc.*, 1549:185, 2013.

[283] A. Hallin. Private communication. *University of Alberta*, 2017.

[284] V. Alvarez et al. Radiopurity control in the NEXT-100 double beta decay experiment: procedures and initial measurements. *J. Instrum.*, 8(1):T01002, 2013.

[285] K. Nakamura et al. NEWAGE - direction-sensitive dark matter search experiment. *Physics Procedia*, 61:737, 2015.

[286] K. Muichi et al. Performance of the TPC with Micro Pixel Chamber Readout: micro-TPC. *IEEE Trans. Nucl. Sci.*, 50:825, 2003.

[287] T. Hashimoto. Private conversation. *University of Kobe*, 2016.

[288] A. Ochi et al. Development of a Micro Pixel Chamber for the ATLAS upgrade. *Physics Procedia*, 37:554, 2012.

[289] N. S. Phan et al. GEM-based TPC with CCD imaging for directional dark matter detection. *Astropart. Phys.*, 84:84, 2016.

[290] F. J. Iguaz et al. TREX-DM: a low-background Micromegas based TPC for low mass WIMP detection. *Eur. J. Phys.*, 76:259, 2016.

[291] A. S. Conceicao et al. GEM scintillation readout with avalanche photodiodes. *J. Instrum.*, 2(9):P09010, 2007.

[292] J. Burns et al. Characterisation of large area THGEMs and experimental measurement of the Townsend coefficients for CF4. *J. Instrum.*, 12(10):T10006, 2017.

[293] Radon guide. Radon decay chain. `www.radonguide.com/radon-decay-chain.html`.

[294] V. A. Kudryatsev. Muon simulation code MUSIC and MUSUN for underground physics. *Comput. Phys. Commun.*, 180(3):339, 2009.

[295] N. Nagele et al. Experimental investigation of muon-induced fusion in liquid deuterium. *Nucl. Phys. A*, 493(3-4):397, 1989.

[296] M. Robinson et al. Measurements of muon flux at 1070 m vertical depth in the Boulby underground laboratory. *Nucl. Instrum. Methods Phys. Res., Sect. A*, 511(3):347, 2003.

[297] F. Ruppin et al. Complementarity of dark matter detectors in light of the neutrino background. *Phys. Rev.*, 90(8):83510, 2014.

[298] J. Ziegler et al. SRIM - The Stopping and Range of Ions in Matter. *Nucl. Instr. Meth.*, 268(11):1810, 2010.

[299] H. Demers et al. Three-dimensional electron microscopy simulation with the CASINO Monte Carlo software. *Scanning*, 33(3):135, 2011.

[300] Y. H. Hilal et al. The energy to produce an electron-ion pair in SF6 and SF6/N2 gas mixtures. *J. Phys. D: Appl. Phys.*, 20(7):975, 1987.

[301] W. Lynch and F. Mouton. Potential for electron discrimination in CYGNUS. *Internal CYGNUS memorandum*, 2017.

[302] J. McLellan et al. A method for the calculation of electron energy-straggling spectra. *Med. Phys.*, 21(3):367, 1994.

[303] J. Billard et al. Low energy electron recoil discrimination for directional dark matter detection. *J. Cosmol. Astropart. Phys.*, 2012(7):20, 2012.